

FOUR-DIMENSIONAL Q<sup>2</sup>PSK  
MODULATION AND CODING FOR  
MOBILE DIGITAL COMMUNICATION

VAN WYK, DANIEL JACOBUS

DANIEL JACOBUS VAN WYK

FOUR-DIMENSIONAL Q<sup>2</sup>PSK MODULATION AND CODING  
FOR MOBILE DIGITAL COMMUNICATION

Master of Engineering (Electronics)

MEng

UP

1996

ELECTRICAL AND ELECTRONIC ENGINEERING

FACULTY OF ENGINEERING

UNIVERSITY OF PRETORIA

SUPERVISOR: J. J. F. Van der Merwe

1996

# FOUR-DIMENSIONAL Q<sup>2</sup>PSK MODULATION AND CODING FOR MOBILE DIGITAL COMMUNICATION

by

DANIËL JACOBUS VAN WYK

A dissertation submitted as partial fulfilment  
of the requirements for the degree

Master of Engineering (Electronic)

in

ELECTRICAL AND ELECTRONIC ENGINEERING

in the

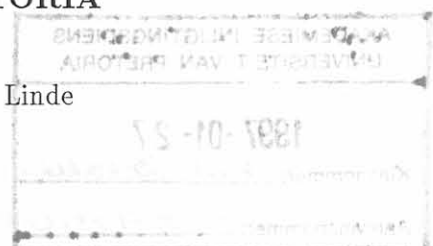
FACULTY OF ENGINEERING

at the

UNIVERSITY OF PRETORIA

SUPERVISOR: Prof. L.P. Linde

April 1996



## To my wife, Daleen

For all her support and love.  
Without her, this study would  
not have been possible.

### Key Words:

Phase-Shift Keying, Mobile Digital Communication, Multidimensional Signalling, Synchronisation and Forward Error Correction.

# SUMMARY

In this dissertation an indepth research into the design, implementation and evaluation of a digital four-dimensional modem for application to high speed mobile communication on the V/UHF channel has been carried out. The four-dimensional digital signalling employs Quadrature-Quadrature Phase-Shift Keying ( $Q^2PSK$ ) as modulation scheme, which was claimed to outperform two-dimensional modulation schemes in terms of spectral efficiency.  $Q^2PSK$  constitutes a relatively new modulation technique, and for this reason considerations of digital modulation and demodulation, synchronisation and error correction coding for this signalling scheme, are of utmost importance.

A conventional DSP based implementation of a  $Q^2PSK$  modulator/demodulator is considered in this thesis. Furthermore, key synchronisation strategies are considered, including new carrier phase and frequency tracking loops. A novel frame synchronisation strategy for  $Q^2PSK$ , employing complex correlation sequences, is presented. The excellent bandwidth efficiency of the  $Q^2PSK$  signalling strategy and elegant signal structure, facilitates the incorporation of sophisticated forward error correction strategies. For this reason the dissertation introduces new trellis codes for  $Q^2PSK$ , including classical, TCM and MTCM, for transmission over both the AWGN and mobile fading channels. Performance evaluations of the developed  $Q^2PSK$  digital modem are given from results obtained from computer simulations when operating on the static AWGN channel and mobile Rician or Rayleigh fading channels.

The research work can be summarised as follows:

- Realisation of a digital  $Q^2PSK$  mobile communication system simulation test facility, facilitating burst mode communication scenarios;
- Design and implementation of a novel frame synchronisation strategy employing complex correlation sequences, for the  $Q^2PSK$  system;
- Design and implementation of a  $Q^2PSK$  dual carrier phase and frequency Kalman estimator for carrier phase and frequency tracking;
- Novel application of classical convolutional error correction codes to  $Q^2PSK$ . In addition, the derivation of theoretical upper bounds to bit error probability are presented;
- Design and application of trellis codes for transmission over the AWGN channel are presented;
- Design and application of multiple trellis codes for transmission over the Rician fading channel are presented with some new results;
- Not only are the extensive evaluations presented, but the performance bounds derived, are benchmarked against actual simulation curves.

# ACKNOWLEDGEMENTS

I would like to thank my Creator, to Him all the praise !

I am indebted to many people for their advice and assistance towards the successful completion of this dissertation.

In particular to my supervisor, Professor Louis Linde for directing this research and his constant and enthusiastic encouragement. His superb supervision and most professional approach, in every way, has benefited me tremendously.

For financial assistance and unique opportunities I thank Armscor, the Foundation for Research Development (FRD) and the Laboratory for Advanced Engineering (LGI).

I would like to thank Professor Ezio Biglieri and Dr. Giorgio Taricco from the Politecnico Di Torino (Italy) for answering my questions and for the invaluable discussions and suggestions on TCM and MTCM.

To my research colleagues and friends Jacques Cilliers, Frans Marx, Emlyn Davies, Gert Veale, Roelf du Toit and Etiënne Pretorius my sincere thanks for being at my disposal at all times to help me with many computing and other technical problems and solutions. I would also like to thank David Joubert, previously of LGI, for his assistance and many discussions during the development of the Q<sup>2</sup>PSK modem platform. A special word of gratitude is expressed to Jacques Cilliers for the many hours of discussions on Trellis Coded Modulation and also his patience in teaching me the finer details concerning Object Oriented Programming.

To my parents, parents in-law and sisters for their unselfish support. Finally, I would also express my deepest gratitude to my wife, Daleen for her continuous support and love.

# CONTENTS

GLOSSARY OF ABBREVIATIONS	v
LIST OF SYMBOLS	vii
1 INTRODUCTION	1
1.1 INTRODUCTION AND OVERVIEW . . . . .	1
1.2 LITERATURE SURVEY . . . . .	3
1.2.1 Multidimensional modulation . . . . .	3
1.2.2 Error correction techniques . . . . .	5
1.2.3 Trellis codes for Q <sup>2</sup> PSK . . . . .	7
1.3 DISSERTATION ORGANISATION . . . . .	8
I FOUR-DIMENSIONAL Q <sup>2</sup> PSK: Theory and Application to mobile communication	11
2 FOUR-DIMENSIONAL Q <sup>2</sup> PSK SIGNALLING: THEORETICAL FOUNDATION	12
2.1 FOUR-DIMENSIONAL SIGNALLING . . . . .	12
2.2 Q <sup>2</sup> PSK SIGNALLING . . . . .	14
2.2.1 Q <sup>2</sup> PSK Modulation . . . . .	15
2.2.2 Q <sup>2</sup> PSK Demodulation . . . . .	17
2.2.3 Spectral efficiency analysis of Q <sup>2</sup> PSK . . . . .	18
2.2.4 BER performance . . . . .	21
2.3 ON THE CAPACITY OF Q <sup>2</sup> PSK FOR BANDLIMITED AWGN CHANNELS . . . . .	25
2.4 CONCLUDING REMARKS: CHAPTER 2 . . . . .	27

<b>3</b>	<b>Q<sup>2</sup>PSK — MOBILE COMMUNICATION SYSTEM</b>	<b>29</b>
3.1	GENERAL SYSTEM ARCHITECTURE . . . . .	30
3.1.1	Transmitter . . . . .	30
3.1.2	Receiver . . . . .	33
3.2	FADING CHANNEL . . . . .	34
3.2.1	Fading channel model . . . . .	35
3.2.2	Noise in the Mobile Channel . . . . .	36
3.2.3	Mobile Channel Simulator . . . . .	37
3.3	SYSTEM SPECIFICATION . . . . .	38
3.4	CONCLUDING REMARKS: CHAPTER 3 . . . . .	41
<b>4</b>	<b>DIGITAL Q<sup>2</sup>PSK — Modulation, Demodulation and Synchronisation</b>	<b>42</b>
4.1	MODEM REALISATION . . . . .	42
4.1.1	Digital Q <sup>2</sup> PSK Modulator . . . . .	42
4.1.2	Digital Q <sup>2</sup> PSK Demodulator . . . . .	45
4.1.3	Modem waveforms and spectra . . . . .	48
4.2	BLOCK TRANSMISSION STRATEGY . . . . .	49
4.3	Q <sup>2</sup> PSK SYNCHRONISATION . . . . .	54
4.3.1	Frame Synchronisation . . . . .	54
4.3.2	Carrier and Symbol Synchronisation . . . . .	56
4.3.3	Effect of Carrier Phase and Frequency Errors on BER . . . . .	58
4.3.4	Kalman Phase and Frequency Estimation . . . . .	59
4.4	CONCLUDING REMARKS: CHAPTER 4 . . . . .	66
<b>II</b>	<b>TRELLIS CODING WITH APPLICATION TO Q<sup>2</sup>PSK</b>	<b>67</b>
<b>5</b>	<b>DESIGN FOR AWGN CHANNELS</b>	<b>68</b>
5.1	INTRODUCTION TO ERROR CORRECTION . . . . .	68
5.2	CLASSICAL ERROR CORRECTION . . . . .	69
5.2.1	Convolutional Channel Coding . . . . .	69
5.2.2	Maximum Likelihood Decoding . . . . .	71

5.2.3	Performance Estimates . . . . .	73
5.3	TRELLIS CODED MODULATION . . . . .	76
5.3.1	Rate 3/4 Q <sup>2</sup> PSK/TCM . . . . .	80
5.3.2	Rate 2/4 Q <sup>2</sup> PSK/TCM . . . . .	82
5.3.3	Q <sup>2</sup> PSK/TCM code performance . . . . .	84
5.3.4	Analytical upper performance bounds for Q <sup>2</sup> PSK/TCM . . . . .	85
5.4	CONCLUDING REMARKS: CHAPTER 5 . . . . .	86
<b>6 DESIGN OF TCM AND MTCM FOR FADING CHANNELS . . . . . 88</b>		
6.1	MULTIPLE TRELLIS CODED MODULATION . . . . .	89
6.1.1	Ungerboeck Set Partitioning: From <i>Root-to-Leaf</i> . . . . .	90
6.2	Q <sup>2</sup> PSK/MTCM CODE DESIGN . . . . .	94
6.2.1	Design of 4-State Rate 6/8 codes . . . . .	94
6.3	PERFORMANCE ANALYSIS . . . . .	95
6.3.1	TCM for fading channels . . . . .	95
6.3.2	MTCM for fading channels . . . . .	96
6.4	CONCLUDING REMARKS: CHAPTER 6 . . . . .	96
<b>III Q<sup>2</sup>PSK Modulation and Coding: PERFORMANCE EVALUATION . . . . . 98</b>		
<b>7 PERFORMANCE EVALUATION . . . . . 99</b>		
7.1	INTRODUCTION . . . . .	99
7.1.1	SNR versus $E_b/N_o$ . . . . .	99
7.1.2	Simulation software . . . . .	101
7.2	EVALUATION ON AWGN CHANNELS . . . . .	101
7.2.1	Mobile Channel effects in AWGN . . . . .	105
7.2.2	Phase/Frequency Tracking and Correction . . . . .	111
7.2.3	DSP implementation . . . . .	113
7.2.4	Classical and TCM error correction in AWGN . . . . .	115
7.3	EVALUATION ON FADING CHANNELS . . . . .	118
7.3.1	Trellis Coded Q <sup>2</sup> PSK . . . . .	124
7.4	CONCLUDING REMARKS: CHAPTER 7 . . . . .	127



<b>8</b>	<b>CONCLUSIONS AND FUTURE RESEARCH</b>	<b>129</b>
8.1	FUTURE RESEARCH . . . . .	130
8.1.1	Design and implementation of a multidimensional equaliser . . . . .	130
8.1.2	Application of a burst-error correcting Viterbi decoder . . . . .	131
8.2	Design of Ungerboeck-type codes for fading channels . . . . .	131
8.3	CONCLUDING REMARKS: CHAPTER 8 . . . . .	132
<b>A</b>	<b>A TUTORIAL ON TCM</b>	<b>135</b>
A.1	INTRODUCTION . . . . .	135
A.1.1	Fundamentals of TCM . . . . .	136
A.2	HEURISTIC AND ANALYTIC REPRESENTATION OF TCM . . . . .	138
A.2.1	Ungerboeck Codes . . . . .	138
A.2.2	Calderbank—Mazo Codes . . . . .	139
A.3	PERFORMANCE EVALUATION . . . . .	140
A.3.1	Analytical Upper Bound to the Error Probability of Q <sup>2</sup> PSK . . . . .	140
A.3.2	Lower Bound to Error Probability . . . . .	142
A.3.3	Union Bound techniques . . . . .	142
A.4	DECODING TCM . . . . .	143
A.5	CONCLUDING REMARKS: APPENDIX A . . . . .	145
<b>B</b>	<b>TCM CODE DESIGN — Utility Software</b>	<b>146</b>
B.1	Calderbank—Mazo Description of trellis codes . . . . .	146
B.2	Mulligan—Wilson Algorithm for computation of $d_{free}$ . . . . .	150
<b>C</b>	<b>TRANSFER FUNCTION DERIVATION</b>	<b>156</b>
<b>D</b>	<b>SET PARTITIONING FOR Q<sup>2</sup>PSK/MTCM CODE DESIGN</b>	<b>159</b>
D.1	CODE CARDINALITY OF 16 . . . . .	159
D.2	CODE CARDINALITY OF 8 . . . . .	161

# GLOSSARY OF ABBREVIATIONS

1D	— One-Dimensional
2D	— Two-Dimensional
4D	— Four-Dimensional
ACI	— Adjacent Channel Interference
AFC	— Automatic Frequency Control
ASK	— Amplitude-Shift Keying
AWGN	— Additive White Gaussian Noise
B-E	— Bandwidth-Efficiency
BEP	— Bit Error Probability
BER	— Bit Error Rate
BPF	— Bandpass Filter
BSC	— Binary Symmetric Channel
CC	— Cross-Correlation
CCI	— Co-Channel Interference
CCRM8	— Convolutional Codes over Ring Modulo-8
CDMA	— Code-Division Multiple-Access
CE-Q <sup>2</sup> PSK	— Constant Envelope Q <sup>2</sup> PSK
C/N	— Carrier-to-Noise Ratio
CSI	— Channel State Information
DPFKE	— Dual Phase-Frequency Kalman Estimator
DMC	— Discrete Memoryless Channel
DS	— Distance Spectrum
DSP	— Digital Signal Processing
EEP	— Error Event Path
ED	— Euclidean Distance
EKF	— Extended Kalman Filter
EM	— Electromagnetic
E-E	— Energy-Efficiency
FDMA	— Frequency-Division Multiple-Access
FEC	— Forward Error Correction
FH	— Frequency Hopped
FPM	— Frequency Phase Modulation
FIR	— Finite Impulse Response
FSK	— Frequency-Shift Keying
GMSK	— Gauss Minimum-Shift Keying
HT	— Hilbert Transform(er)
IF	— Intermediate Frequency
ISI	— Intersymbol Interference

---

LCR	— Level Crossing Rate
LMC	— Land Mobile Channel
LMSC	— Land Mobile Satellite Channel
LO	— Local Oscillator
LOS	— Line-of-Sight
LPF	— Lowpass Filter
M-PSK	— M-ary Phase-Shift Keying
MED	— Minimum Euclidean Distance
MFD	— Mean Fade Duration
ML	— Maximum Likelihood
MSE	— Minimum Square Error
MSED	— Minimum Squared Euclidean Distance
MSK	— Minimum Shift-Keying
MTCM	— Multiple Trellis-Coded Modulation
NEP	— Negative Equally Probable
PCS	— Personal Communication Services
PDF	— Probability Density Function
PLL	— Phase-Locked Loop
PSK	— Phase-Shift Keying
PSD	— Power Spectral Density
QASK	— Quadrature Amplitude-Shift Keying
QPSK	— Quadrature Phase-Shift Keying
$\pi/4$ -QPSK	— $\pi/4$ Quadrature Phase-Shift Keying
Q <sup>2</sup> PSK	— Quadrature-Quadrature Phase-Shift Keying
Q <sup>2</sup> PSK/TCM	— Trellis Coded Q <sup>2</sup> PSK
Q <sup>2</sup> PSK/MTCM	— Multiple-Trellis Coded Q <sup>2</sup> PSK
RHS	— Right Hand Side
RI	— Rotational Invariant
RF	— Radio Frequency
SEP	— Symbol Error Probability
SFH	— Slow Frequency Hopping
SKF	— Scalar Kalman Filter
SNR	— Signal-to-Noise Ratio
S/P	— Serial-to-Parallel
TCM	— Trellis-Coded Modulation
TDMA	— Time-Division Multiple-Access
VA	— Viterbi Algorithm
V/UHF	— Very- and Ultra-High Frequency

# LIST OF SYMBOLS

$C$	— Channel capacity
$D$	— Dimensions per second
$d_{free}$	— Minimum Euclidean Distance
$d_{free}^2$	— Minimum Squared Euclidean Distance
$\eta_f$	— Bandwidth Efficiency ( <i>bits/s/Hz</i> )
$E_b/N_o$	— Ratio of Energy per bit to Noise spectral density
$f$	— Frequency
$f_c$	— Carrier frequency ( <i>Hz</i> )
$f_d$	— Deviation frequency ( <i>Hz</i> )
$f_D$	— Doppler frequency ( <i>Hz</i> )
$f_e$	— Frequency error
$G_c$	— Coding gain
$\gamma_c$	— Asymptotic coding gain
$h$	— Deviation ratio
$k$	— MTCM multiplicity
$K$	— Rician factor
$L_c$	— Constraint length
$M$	— Number of symbols per signal set
$N$	— Dimensionality
$N_s$	— Number of trellis coder states
$P_b$	— Bit Error Probability
$P_s$	— Symbol Error Probability
$\psi_i$	— $i$ -th Orthonormal basis
$Q$	— Number of quantisation bits
$R_b$	— Bit Rate ( <i>bits/s</i> )
$R_c$	— Code rate ( $k/n$ )
$R_s$	— Symbol Rate ( <i>Symbols/s</i> )
$s(t)$	— Function of time
$S(f)$	— Function of frequency
$t$	— Time ( <i>seconds</i> )
$T_b$	— Bit Duration ( <i>seconds</i> )
$T_s$	— Symbol Duration ( <i>seconds</i> )
$T(D)$	— Transfer function
$\theta_e$	— Phase error ( <i>radians</i> )
$\theta_D$	— Doppler angle ( <i>radians</i> )
$\theta_o$	— Phase offset ( <i>radians</i> )
$W$	— Bandwidth ( <i>Hz</i> )

# LIST OF FIGURES

1.1	Modulator with 2D/Polarisation and frequency-reuse. . . . .	4
1.2	Dissertation organisation. . . . .	8
2.1	16-ary constellations in Two-Dimensions (2D): (a) Optimal 16-ary design. (b) Standard 16-QASK design. . . . .	13
2.2	Quadrature-Quadrature Phase-Shift Keying (Q <sup>2</sup> PSK) modulator. . . . .	15
2.3	Power spectral densities of MSK, QPSK and Q <sup>2</sup> PSK modulated signals. . . . .	20
2.4	Power captured as function of bandwidth of MSK, QPSK and Q <sup>2</sup> PSK signals. . . . .	20
2.5	Power spectral densities of Q <sup>2</sup> PSK, CP-Q <sup>2</sup> PSK and 4-CPFSK modulated signals. . . . .	22
2.6	Power captured as function of bandwidth for Q <sup>2</sup> PSK and CP-Q <sup>2</sup> PSK signals. . . . .	22
2.7	Signals on vertices of $N = 3$ dimensional hypercube. . . . .	24
2.8	Channel capacity $C^*$ of 2D M-PSK ( $M = 4, 8$ and $16$ , denoted by dashed lines) and 4D Q <sup>2</sup> PSK modulation for bandlimited AWGN channels. . . . .	26
3.1	Basic communication system model. . . . .	30
3.2	Detailed transmitter block diagram. . . . .	31
3.3	Detailed receiver block diagram. . . . .	33
3.4	Non-frequency selective Rician fading channel model. . . . .	35
3.5	V/UHF mobile channel simulator block diagram. . . . .	37
3.6	Power spectral density of fading process when an omnidirectional antenna is employed. . . . .	38
3.7	Overall radio channel response. . . . .	39
4.1	Q <sup>2</sup> PSK Transmitter block diagram. . . . .	43
4.2	Fourier Transform of basic data pulse, $a(t)$ ; with amplitude $\pm 1$ , width $T_s$ , and centered on the origin. . . . .	44
4.3	Visualisation of first quadrature modulation in the frequency domain, producing in-phase digital signal, $I(nT_{smp})$ . . . . .	44
4.4	Visualisation of final modulation process in the frequency domain, producing Q <sup>2</sup> PSK transmitter output, $s(nT_{smp})$ . . . . .	45

4.5	Q <sup>2</sup> PSK DSP based receiver block diagram . . . . .	46
4.6	Non-optimum demodulator decision devices for (a) Q <sup>2</sup> PSK, and (b) CE-Q <sup>2</sup> PSK. . . . .	48
4.7	Decoupled Q <sup>2</sup> PSK signal space. . . . .	49
4.8	An illustrative timing diagram showing the waveforms involved in generating the Q <sup>2</sup> PSK signal. . . . .	50
4.9	An illustrative timing diagram showing the waveforms involved in generating the CE-Q <sup>2</sup> PSK signal. . . . .	50
4.10	Power spectral densities of Q <sup>2</sup> PSK, CE-Q <sup>2</sup> PSK and CP-Q <sup>2</sup> PSK. . . . .	51
4.11	Basic frame structure. . . . .	52
4.12	Block signalling format for symbol rate of $R_s = 5.0 \text{ ksymbols/s}$ for the different hopping rates, (a) 25 (b) 50 (c) 100 <i>hops/s</i> , utilising an 8 symbol header. . . . .	53
4.13	Proposed Q <sup>2</sup> PSK frame synchronisation procedure. . . . .	55
4.14	Complex correlator block diagram. . . . .	56
4.15	Saha synchronisation circuit for Q <sup>2</sup> PSK. . . . .	57
4.16	Saha synchronisation circuit for CE-Q <sup>2</sup> PSK. . . . .	57
4.17	BEP sensitivity of Q <sup>2</sup> PSK to a Tikhonov-distributed phase error. . . . .	60
4.18	Optimum recursive scalar Kalman estimator. . . . .	62
4.19	Dual Frequency and Phase Kalman Estimator (DPFKE). . . . .	64
5.1	Rate-3/4 encoding scheme for Q <sup>2</sup> PSK. . . . .	70
5.2	Half rate encoding scheme for Q <sup>2</sup> PSK. . . . .	70
5.3	Half rate encoding scheme for CE-Q <sup>2</sup> PSK. . . . .	71
5.4	Decoding scheme for rate-3/4 Q <sup>2</sup> PSK. . . . .	72
5.5	Decoding scheme for rate-1/2 Q <sup>2</sup> PSK. . . . .	72
5.6	Decoding scheme for rate-1/2 CE-Q <sup>2</sup> PSK. . . . .	73
5.7	Bit error probability, $P_b$ for Rate-1/2 codes with Viterbi decoding (Hard quantisation) and Q <sup>2</sup> PSK modulation. . . . .	74
5.8	Bit error probability for Rate-2/3 codes with Viterbi decoding (Hard quantisation) and Q <sup>2</sup> PSK modulation. . . . .	75
5.9	Bit error probability for Rate-3/4 codes with Viterbi decoding (Hard quantisation) and Q <sup>2</sup> PSK modulation. . . . .	75
5.10	Group $B_0 = \{C_0, C_1, C_2, C_3\}$ : Even Parity . . . . .	78
5.11	Group $B_1 = \{C_4, C_5, C_6, C_7\}$ : Odd Parity . . . . .	79
5.12	Q <sup>2</sup> PSK signal space partition tree. . . . .	80

5.13	Inputs and state variables for the half-connected 8-state code. . . . .	81
5.14	Half-connected $R = 3/4$ 8-state trellis code. . . . .	81
5.15	Inputs and state variables for fully-connected 8-state code. . . . .	82
5.16	Fully-connected $R = 3/4$ 8-state trellis code. . . . .	82
5.17	Code structures for half-rate trellis coders. . . . .	83
5.18	Half-connected $R = 2/4$ 8-state trellis code. . . . .	83
5.19	Quarter-connected $R = 2/4$ 16-state trellis code. . . . .	84
5.20	Half-connected $R = 2/4$ 8-state trellis code for Constant Envelope (CE) Q <sup>2</sup> PSK. . .	85
5.21	Upper bounds to bit error probabilities for 8-state rate-3/4 Q <sup>2</sup> PSK/TCM. . . . .	86
6.1	Generalised MTCM transmitter. . . . .	89
6.2	Set partitioning method for multiple ( $k = 2$ ) trellis codes on the fading channel. . . .	93
6.3	Set partitioning method for multiple ( $k = 4$ ) trellis codes on the fading channel. . . .	93
6.4	Rate-6/8 4-state Q <sup>2</sup> PSK/MTCM . . . . .	94
7.1	Power spectral densities of unfiltered and filtered Q <sup>2</sup> PSK (CE-Q <sup>2</sup> PSK). . . . .	101
7.2	Q <sup>2</sup> PSK operating at 2.0 <i>bits/s/Hz</i> in AWGN with $E_b/N_o = 25.0$ dB. . . . .	102
7.3	Q <sup>2</sup> PSK operating at 2.0 <i>bits/s/Hz</i> in AWGN with $E_b/N_o = 5.0$ dB. . . . .	102
7.4	Q <sup>2</sup> PSK signal under static channel conditions (X-axis: samples, Y-axis: volt). . . . .	103
7.5	CE-Q <sup>2</sup> PSK signal under static channel conditions. . . . .	103
7.6	BEP curves for MSK, QPSK, Q <sup>2</sup> PSK, and CE-Q <sup>2</sup> PSK. . . . .	104
7.7	BEP curves for Q <sup>2</sup> PSK and CE-Q <sup>2</sup> PSK, operating at 2.0 and 2.4 <i>bits/s/Hz</i> , respectively. . . . .	105
7.8	Q <sup>2</sup> PSK signal constellations for phase offset, $\theta_o = 0.05$ rad. . . . .	106
7.9	Q <sup>2</sup> PSK signal constellations for phase offset, $\theta_o = 0.1$ rad. . . . .	106
7.10	Q <sup>2</sup> PSK signal constellations for phase offset, $\theta_o = 0.2$ rad. . . . .	106
7.11	Q <sup>2</sup> PSK signal constellations for Doppler frequency of 25 <i>Hz</i> at RF frequency of 900 <i>MHz</i> . . . . .	107
7.12	Q <sup>2</sup> PSK signal constellations for Doppler frequency of 50 <i>Hz</i> . . . . .	107
7.13	Q <sup>2</sup> PSK signal constellations for Doppler frequency of 100 <i>Hz</i> . . . . .	107
7.14	CE-Q <sup>2</sup> PSK signal constellations for phase offset, $\theta_o = 0.01$ rad. . . . .	108
7.15	CE-Q <sup>2</sup> PSK signal constellations for phase offset, $\theta_o = 0.1$ rad. . . . .	108
7.16	CE-Q <sup>2</sup> PSK signal constellations for phase offset, $\theta_o = 0.2$ rad. . . . .	108

7.17 CE-Q <sup>2</sup> PSK signal constellations for Doppler frequency of 25 Hz at RF frequency of 900 MHz. . . . .	109
7.18 CE-Q <sup>2</sup> PSK signal constellations for Doppler frequency of 50 Hz. . . . .	109
7.19 CE-Q <sup>2</sup> PSK signal constellations for Doppler frequency of 100 Hz. . . . .	109
7.20 BEP curves for Q <sup>2</sup> PSK for $\theta_o = 0.1$ rad and Doppler frequencies of 25, 50 and 100 Hz, compared to the ideal Q <sup>2</sup> PSK modem transmission in AWGN. . . . .	110
7.21 BEP curves for CE-Q <sup>2</sup> PSK for $\theta_o = 0.1$ rad and Doppler frequencies of 25, 50 and 100 Hz, compared to the ideal CE-Q <sup>2</sup> PSK modem transmission in AWGN. . . . .	110
7.22 Minimum Squared Errors for DPFKE estimator tracking carrier phase and frequency uncertainties over the header period (a) Frequency MSE, $\rho_k$ (b) Phase MSE, $\rho_l$ . . . . .	112
7.23 Frequency MSE for DPFKE estimator tracking carrier frequency uncertainties over the data period. . . . .	112
7.24 BEP curves for Q <sup>2</sup> PSK and CE-Q <sup>2</sup> PSK with DPFKE activated. . . . .	113
7.25 Q <sup>2</sup> PSK constellations (cosine-carrier information) under static AWGN channel conditions (a) $E_b/N_o = 20.0$ dB (b) $E_b/N_o = 15.0$ dB. . . . .	114
7.26 Q <sup>2</sup> PSK constellations (cosine-carrier information) under mobile channel impairments for $E_b/N_o = 25$ dB (a) carrier phase offset $\theta_o = 0.1$ rad (b) Doppler frequency $f_D = 100.0$ Hz. . . . .	114
7.27 Q <sup>2</sup> PSK constellations for a constant phase offset $\theta_o = 0.1$ rad, a Doppler frequency $f_D = 50.0$ Hz and $E_b/N_o = 15.0$ dB (a) cosine-carrier information (b) cosine-sine-carrier information. . . . .	115
7.28 BEP graphs 8- and 16-state rate-2/4 Q <sup>2</sup> PSK, compared to uncoded Q <sup>2</sup> PSK and the upper bounds to BEP. . . . .	116
7.29 BEP graphs 8- and 16-state hybrid rate-2/4 Q <sup>2</sup> PSK employing a single rate-2/3 convolutional coder, compared to uncoded CE-Q <sup>2</sup> PSK and the upper bounds to BEP. . . . .	116
7.30 BEP graphs 8- and 16-state rate-3/4 Q <sup>2</sup> PSK employing a single rate-3/4 convolutional coder, compared to uncoded Q <sup>2</sup> PSK and the upper bounds to BEP. . . . .	117
7.31 BEP graphs 8- and 16-state rate-2/4 Q <sup>2</sup> PSK/TCM and CE-Q <sup>2</sup> PSK/TCM compared to uncoded Q <sup>2</sup> PSK. . . . .	119
7.32 BEP graphs 8- and 16-state rate-3/4 Q <sup>2</sup> PSK/TCM, compared to uncoded Q <sup>2</sup> PSK. . . . .	119
7.33 Q <sup>2</sup> PSK under Rician fading channel conditions, $K = 10$ dB. . . . .	120
7.34 CE-Q <sup>2</sup> PSK under Rician fading channel conditions, $K = 10$ dB. . . . .	120
7.35 Q <sup>2</sup> PSK under Rayleigh fading channel conditions, $K = 0$ dB. . . . .	121
7.36 CE-Q <sup>2</sup> PSK under Rayleigh fading channel conditions, $K = 0$ dB. . . . .	121
7.37 Q <sup>2</sup> PSK operating at 2.0 bits/s/Hz under Rician fading channel conditions with $K = 5$ dB and $E_b/N_o = 25$ dB. . . . .	122
7.38 Q <sup>2</sup> PSK operating at 2.0 bits/s/Hz under Rayleigh fading channel conditions with $K = 0$ dB and $E_b/N_o = 25$ dB. . . . .	122



7.39	BER results for Q <sup>2</sup> PSK modem operating on AWGN, Rician and Rayleigh fading channel. . . . .	123
7.40	BER results for CE-Q <sup>2</sup> PSK modem operating on AWGN, Rician and Rayleigh fading channel. . . . .	123
7.41	BER results for 4-state rate-6/8 and rate-5/8 Q <sup>2</sup> PSK/MTCM operating on Rician ( $K = 10$ dB) fading channel. . . . .	125
7.42	BER results for 4-state rate-6/8 and rate-5/8 Q <sup>2</sup> PSK/MTCM modem operating on Rician ( $K = 5$ dB) fading channel. . . . .	125
7.43	BER results for 4-state rate-5/8 Q <sup>2</sup> PSK/MTCM modem operating on Rician ( $K = 5$ dB) fading channel without and with CSI based on the correlation-magnitude of the frame and symbol synchronisation process. . . . .	126
A.1	General model for TCM. . . . .	137
A.2	Block diagram of an Ungerboeck code ( $m = \log_2 M$ ). . . . .	138
A.3	General structure of the Calderbank—Mazo analytical description . . . . .	139
C.1	Fully-connected $R = 3/4$ 8-state trellis code. . . . .	157

# LIST OF TABLES

2.1	Comparison of required SNR to achieve a symbol-error probability, $P_s = 10^{-5}$ . . . .	26
2.2	Bandwidth comparison of MSK, QPSK, 4-CPFSK, Q <sup>2</sup> PSK and CP-Q <sup>2</sup> PSK signalling as a function of power containment. . . . .	27
3.1	Channel specifications . . . . .	39
3.2	Modem specifications . . . . .	40
4.1	Block transmission format for hopping rates of $R_{HOP} = 25, 50$ , and $100 \text{ hops/s}$ . . . .	52
4.2	SFH design summary for hopping rates of $R_{HOP} = 25, 50$ , and $100 \text{ hops/s}$ . . . . .	53
5.1	Minimum squared Euclidean distances between all pairs of Q <sup>2</sup> PSK code words. . . .	77
6.1	Interdistances between partitioned subsets, with $A_0 \otimes B_0$ used as reference. . . . .	91
6.2	Interdistances between partitioned subsets, with $C_0 \otimes D_{0a}$ used as reference. . . . .	92
6.3	Design summary for Q <sup>2</sup> PSK/MTCM. . . . .	95
7.1	Comparison of trellis codes for Q <sup>2</sup> PSK at a BEP of $P_e = 10^{-5} \text{ dB}$ . . . . .	127

---

---

# FOUR-DIMENSIONAL Q<sup>2</sup>PSK MODULATION AND CODING FOR MOBILE DIGITAL COMMUNICATION

CHAPTER 1  
INTRODUCTION

---

---

In this chapter, the motivation for the research is given. The scope of the research is defined and the structure of the thesis is outlined. The outline of the thesis is as follows:

## 1.1 INTRODUCTION AND OVERVIEW

In its basic definition, communication is the exchange of information. The history of communication is long and varied. In the eighteenth century, the telegraph was invented. In the nineteenth century, the telephone was invented. In the early twentieth century, the radio was invented. In the mid-twentieth century, the transistor was invented. In the late twentieth century, the satellite was invented. The invention of the transistor and the satellite has made possible the development of modern communication systems. The invention of the transistor has made possible the development of modern communication systems. The invention of the satellite has made possible the development of modern communication systems. Truly, the invention of the transistor and the satellite has made possible the development of modern communication systems. Truly, the invention of the transistor and the satellite has made possible the development of modern communication systems. Truly, the invention of the transistor and the satellite has made possible the development of modern communication systems.

## CHAPTER 1

---

# INTRODUCTION

---

---

In this chapter an overview of the research and a formulation of the problem that is addressed in this study are given. Importantly, most of this chapter is concerned with the extensive literature study which was carried out. This is followed by a section in which the contributions of this study are highlighted and placed in perspective. The chapter closes with a schematic representation and a written outline of the dissertation.

### 1.1 INTRODUCTION AND OVERVIEW

In its basic electrical sense, the term *communication* refers to the sending, receiving and processing of information by electric means. As such, it started with *wire telegraphy* perfected by Samuel Morse in the eighteen-forties, followed by the development of *telephony*, conceived by Alexander Graham Bell some decades later, and *radio* at the beginning of this century [1]. *Radio communications*, made possible by the invention of the triode tube, was greatly stimulated by the work done during World Wars I and II. Then, after a long pause, *digital radio* (i.e., digital communications by radio) experienced a renaissance in the early 1970s. Renewed interest in microwave radio as a transmission medium for digital communications was largely due to the introduction of digital switching at that time. It subsequently became even more widely used and refined through the invention and use of the transistor, integrated circuits and other semiconductor devices [2]. More recently, the use of satellites has made radio communications even more widespread [3, 4].

Truly, the invention of the telegraph and telephone in the 19th century was the first steps towards shattering the barriers of space and time in communication between individuals. The second step was the successful deployment of radio communications. To date, however, the location barrier has not been completely surmounted: people are less tied to telephone sets or "fixed wireline" equipment for communication. With an annual growth rate of 40% per year, wireless (mobile) communication is the fastest growing sector of the communications sector [5]. The ultimate goal of

Personal Communication Services (PCS) is to provide instant communication between individuals located anywhere in the world, and at any time. In mobile digital radio communications, however, both the available frequency spectrum and the transmitter power are limited. In order to cope with the ever-increasing amount of data traffic which has to be accommodated in the already overcrowded electromagnetic spectrum and the demand for more efficient transmission, improved modulation techniques are needed. This increasing demand for digital transmission channels in the radio frequency band creates a challenging problem for the communications engineer.

In recent years, the emphasis has been placed on the development of signalling strategies for digital communication that conserve both available power and bandwidth. An example of a spectrally efficient modulation scheme is  $\pi/4$ -QPSK, which has been selected as the standard for the new U.S. digital cellular system. This nonconstant envelope linear modulation scheme has a higher spectral efficiency (1.62 *bits/s/Hz*) than constant envelope modulation schemes such as MSK, GMSK (0.83 *bits/s/Hz*) and digital FM (0.67 *bits/s/Hz*) previously employed in mobile radio systems [6, 7, 8, 9, 10]. Due to the increasing demand for mobile communication services more efficient modulation techniques than  $\pi/4$ -QPSK need to be investigated for future mobile communication systems.

The foregoing discussion is the motivation for the research carried out at the University of Pretoria, the main objective being to investigate spectrally efficient signalling strategies to be employed in mobile digital communication systems. With this objective in mind, a multidimensional QPSK modulation scheme, known as Quadrature-Quadrature Phase-Shift Keying ( $Q^2$ PSK) [11, 12] has been selected as a platform. This scheme has a theoretical bandwidth efficiency of 4.0 *bits/s/Hz* and an elegant signal structure which facilitates the incorporation of sophisticated forward error correction strategies.

The dissertation objectives can be summarised as follows:

- Design and realisation of a mobile digital  $Q^2$ PSK communication system.
- Design and simulation of sophisticated error correction strategies.
- Performance evaluation under typical mobile fading V/UHF channel conditions.

Within the framework of the objectives, this research study has set out to investigate the design, implementation and evaluation of a digital  $Q^2$ PSK modem for application to mobile communication on typical V/UHF channels. Key aspects, such as digital modulation and demodulation, block signalling format and synchronisation, including carrier tracking strategies, are addressed. In addition, the design and implementation of sophisticated error correction strategies, including classical convolutional codes, trellis codes and multiple trellis codes are considered. Although, most of the concepts of multidimensional modulation and particularly four-dimensional signalling are not new, the utilisation, actual implementation and evaluation of these techniques in the digital communication environment are of crucial importance. The final objective of the dissertation is to evaluate the performance of the digital  $Q^2$ PSK (uncoded as well as trellis coded) communication system under typical static and mobile fading channel conditions.

## 1.2 LITERATURE SURVEY

In this section attention is focused on a literature survey of published technical material concerning the two main topics of this dissertation; namely multidimensional modulation and the application of coding to these modulation schemes.

### 1.2.1 Multidimensional modulation

Motivation for the use of multidimensional signals for digital transmission dates back to the work of Shannon [13]. Shannon showed that it is theoretically possible to have error-free transmission over a noisy channel if the transmission rate does not exceed the capacity of the channel. In this classical paper Shannon related the information capacity of a communication channel to bandwidth and Signal-to-Noise Ratio (SNR), as follows:

$$C = \frac{1}{2} \log_2 \left( 1 + \frac{P_s}{P_n} \right) \quad (1.1)$$

where  $C$  represents the number of error-free bits per second that can be transmitted in a per hertz  $Hz$  bandwidth,  $P_s$  is the received average signal power and  $P_n$  the average noise power added to the signal. Any communication system attempts to transmit the maximum number of information bits in the minimum time and at the minimum expense of signal energy [14]. In his celebrated analysis of the limiting performance available in digital communication over a given channel, Shannon also recognised that the performance of a signal constellation used to transmit digital information over a Additive White Gaussian Noise (AWGN) channel can be improved by increasing  $N$ , the dimensionality of the signal set used for transmission. In particular, as the dimensionality grows to infinity, the performance tends to an upper limit defined as the capacity of the channel in (1.1) [13, 15].

Heuristically, as the number of dimensions grows more space becomes available to accommodate the signals, and hence the Euclidean distance between signal points increases. In turn, a greater distance between signal points means (at least for high-enough signal-to-noise ratios) a smaller error probability. The price paid for an improvement in performance when the dimensionality is increased is essentially the increase in complexity of the modulator and demodulator.

#### 1.2.1.1 Four-Dimensional Signalling

The notion for Four-Dimensional (4D) signalling was first considered by Wilson and Sleeper [16], employing a technique known as "frequency-reuse". Frequency-reuse is a technique which utilises two spatially-orthogonal electric field polarisations for communicating on the same carrier frequency to double the apparent spectral capacity of a satellite communication system. Provided that the two fields can be kept orthogonal (admittedly a problem on land mobile channels due to depolarisation), the spectrum efficiency is twice that of a non-frequency strategy, and the energy efficiency is exactly that of a single channel at the same energy requirement level. A typical application would perform Quadrature Phase-Shift Keying (QPSK) on each polarisation, providing a theoretical spectral efficiency of 4.0 *bits/s/Hz*. Figure 1.1 illustrates the block diagram of such a modulator with Two-Dimensional (2D) polarisation and frequency-reuse, forming a 4D signalling scheme.

The 4D receiver employs quadrature carrier demodulation on each of the polarisations, followed by matched filtering and decision making. The problem with the foregoing scheme is that the space

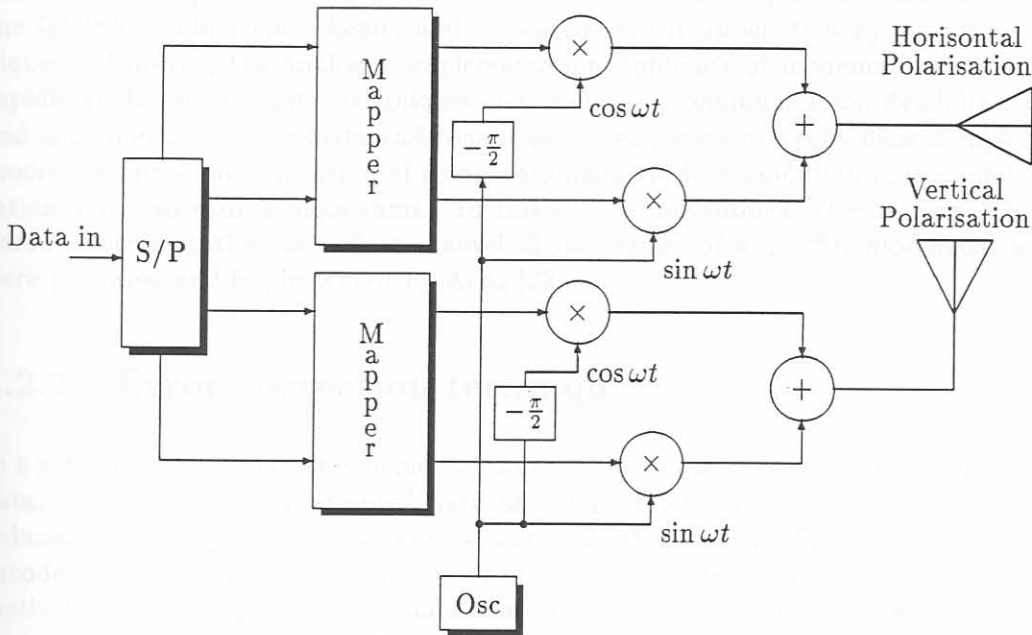


Figure 1.1: Modulator with 2D/Polarisation and frequency-reuse.

polarisation would be difficult, even impossible, when considering application to a land mobile communication scenario.

An overview of the current papers available on multidimensional modulations are summarised, with specific reference to 4D modulations: Uncoded Four-Dimensional (4D) signal sets were considered by Welti and Lee [17], Zetterberg and Brändström [18], Wilson et al. [19], and Biglieri and Elia [20]. Welti-Lee codes are essentially subsets or translations of the lattice consisting of the points in the 4D space whose integer components have an even sum. Zetterberg-Brändström designs are based on quaternary groups, and their signals are constrained to have an equal energy. Wilson *et al.* consider 4D signal sets based on subsets of lattice packings. Gersho and Lawrence [21] consider four- and eight-dimensional signal sets with two information bits per dimension. Their designs show a 1.2 to 2.4 dB gain in noise margin over conventional (two-dimensional) quadrature amplitude modulations.

### 1.2.1.2 Four-Dimensional Q<sup>2</sup>PSK

A measure of spectrally efficient modulation lies in the notion of effective use of available space dimensions. This notion of effective use of available signal space, was considered by Saha [11, 12]. In Quadrature Phase-Shift Keying (QPSK) and Minimum Shift Keying (MSK), the symbol duration  $T_s$  is  $2T_b$ , where  $T_b$  is the bit interval of the incoming data stream. If one supposes that the channel is strictly bandlimited to  $1/T_b$  on either side of the carrier, then the two-sided bandwidth occupancy is  $W = 2/T_b$ , and the number of available signal space dimensions is  $T_s W = 4$  [22]. Only two of these dimensions or degrees of freedom are utilised in QPSK and MSK.

Saha observed the shortcomings of the existing modulation schemes in the utilisation of avail-

able signal space dimensions and proposed the development of the new class of digital modulation scheme named Quadrature-Quadrature Phase-Shift Keying (Q<sup>2</sup>PSK). Saha developed the basis of the Q<sup>2</sup>PSK modulation scheme, and he suggested the application by traditional analogue techniques. However, the analogue implementation approach of modems is out-dated and is being rapidly replaced by digital techniques, for reasons of communication flexibility, power efficiency, and implementation simplicity and consistency. Realisation of a fully digital implementation of the modem requires the utilisation of computationally efficient modulation, demodulation, synchronisation and also coding algorithms. To this end, a conventional Digital Signal Processing (DSP) based implementation as well as a novel digital design of a Q<sup>2</sup>PSK modulator and demodulator were proposed and implemented by Acha [23].

## 1.2.2 Error correction techniques

In a general error correction scheme the *channel encoder* adds controlled *redundancy* to the message data, thereby producing encoded data at a higher bit rate. The *channel decoder* exploits the redundancy to decide which message was actually transmitted. The two main goals of the channel encoder, in a Land Mobile Channel (LMC) and Satellite Mobile Channel (SMC) scenario are firstly to minimise the effect of channel noise, and secondly to minimise the effects of the fading channel. That is, the number of errors between the channel encoder input and the channel decoder output must be minimised. The use of coding adds complexity to the system, especially for the implementation of the decoding operation at the receiver. Thus, the design trade-offs in the use of error-control coding in order to achieve acceptable error performance, are considerations of bandwidth and system complexity.

Coding techniques are generally divided into two main types: *block coding* and *convolutional coding* [24, 25]. Convolutional coding was first proposed by Elias for use over discrete memoryless channels. Its superior performance over block coding, for a given amount of system complexity, has gained its success in many communication systems. Although, at first the application of convolutional coding to bandlimited channels was not originally thought of as being practical. In 1967, Viterbi derived an error exponent for convolutional codes using an asymptotically optimum decoding algorithm, known as the Viterbi Algorithm (VA), which constitutes the basis of new coding techniques.

### 1.2.2.1 Combined Coding and Modulation

In classical digital communications systems, the functions of modulation and error correction were separated, but in 1974 Massey advocated the viewpoint of regarding channel coding and modulation as an entity [26]. This view was later pursued by Ungerboeck in the design of his well-known multi-level/phase convolutional codes with asymptotic coding gains of up to 6.0 dB [27, 28, 29]. Ungerboeck's originality was the use of an expanded signal constellation and a *set partitioning technique* to accommodate the redundant bits introduced by coding. This coding technique is nowadays known as Trellis Coded Modulation (TCM).

The advantages offered by Ungerboeck's technique is twofold: First high coding gains may be obtained and, secondly information rate is maintained without expanding the required bandwidth. Over the last 2 decades TCM has emerged as an efficient and reliable coding scheme used for data communication with the purpose of improving the reliability of a digital transmission system without increasing the transmitted power or the required bandwidth.



The definition of TCM given by Biglieri *et al.* [30] can be stated as follows:

*The trellis code solution combines the choice of a higher-order modulation scheme with that of a convolutional code, while the receiver, instead of performing demodulation and decoding in two separate steps, combines the two operations into one.*

A different description of trellis codes was formulated by Calderbank and Mazo [31]. The description is known as the analytical description, where the trellis code is seen as a *sliding window* method of encoding a binary data stream as a sequence of real or complex numbers that are sent over the transmission channel. The main characteristics of the analytical description is that the codes may be described very simply, and strict bounds on performance can be obtained.

### 1.2.2.2 Design for AWGN channels

In the design of TCM schemes for the AWGN channel, the most significant parameter is the Euclidean distance of the code, which must be maximised in order to ensure an optimum code. It is known, that asymptotically, the error probability is upper- and lower-bounded by a function that decreases monotonically when the Minimum Squared Euclidean Distance (MSED), increases. The free Euclidean distance is thus the most significant single parameter useful for comparing TCM schemes employed for transmission over the AWGN when the Signal-to-Noise Ratio (SNR) is large enough [30].

In 1983, Fang claimed that an improved error performance was achieved by Four-Dimensional (4D) channel coding, with the expanded signal set similar to Ungerboeck's set partitioning method [32]. In a later publication, Biglieri analysed some of the codes developed by Ungerboeck on non-linear channels [33], where he showed that the codes were particularly attractive for application in the band-limited environment. In the same year Wei discovered the use of non-linear trellis codes, with the incorporation of a 90° invariant property which gives the coded system immunity against 90° phase jumps at the demodulator [34, 35]. Rate 3/4 convolutional coding for 16-PSK was analysed by Wilson [19], who demonstrated that trellis coded 16-PSK was preferable to trellis coded 16-Quadrature Amplitude Shift Keying (QASK) on non-linear satellite channels.

TCM systems traditionally used symmetric constellations, with uniformly spaced signal points. Symmetric systems are optimum for uncoded signals, but in a paper by Divsalar [36] it was shown that trellis codes with asymmetric constellation may offer a better performance than those with symmetric constellations on AWGN. Calderbank published a paper where new trellis codes based on lattices and cosets were presented [37]. A good review of TCM systems may be found in a paper of Benedetto [38], where theoretical aspects of the encoding process are investigated.

### 1.2.2.3 Design for Fading channels

All the references given in the foregoing section dealt with design and analysis of trellis codes for AWGN channels, where the parameter to be maximised is the Euclidean distance of the code. This criteria is valid for AWGN channels, however in practical channel other parameters do also have to be taken into account. There is presently a large amount of work being done on coding for fading channels.

The first papers concerned with the design and application of TCM for fading channels were published by Divsalar and Simon [39, 40, 36, 41, 42]. In these papers the authors established that depending on the Rician factor of the channel, the diversity of the code will be the parameter to be maximised rather than the Euclidean Distance (ED). Performance criteria for the set partitioning of trellis coded MPSK for fading channels are shown by Divsalar and Simon. In the same paper the authors suggest the use of Multiple TCM (MTCM), wherein more than one channel symbol is assigned to each trellis branch. The main conclusions of this work were that for the design of the multiple trellis codes for optimum performance on the fading channel, the length of the shortest Error Event Path (EEP) and the product of branch distances along that path must be maximised. It is noted that the latter design objectives differ from the design of TCM schemes for AWGN channels, where maximisation of the free Euclidean distance of the code is the primary objective.

Other coding techniques for fading channels have been reported by Farrell [43] and Zehavi [44]. In his paper Farrell summarises the basic methods for combating fading with TCM systems. In a very recent paper by Zehavi, an alternative to the method for MPSK proposed by Divsalar and Simon, is presented. The approach is based on a convolutional code followed by bit interleavers, yielding a better coding gain over Rayleigh channels compared to when MTCM is employed.

An interesting paper of trellis codes for Frequency-Phase Modulated (FPM) signals was presented by Peryalwar [45], who showed that the optimum set partitioning of trellis coded FPM signals for fading channels also provides asymptotically optimum performance on AWGN channels.

### 1.2.3 Trellis codes for $Q^2$ PSK

In this section the most important references, which dealt specifically with the design of trellis codes for  $Q^2$ PSK are given. It is surprising that only a few publications by Saha and Acha were found. In his first paper Saha proposed 7/8 rate trellis codes on the  $Q^2$ PSK signal space [46]. In this paper coding gains of 2.43 dB and 5.45 dB were calculated. In his second paper dealing with trellis coded  $Q^2$ PSK signals, Saha presented four main types of codes [47]. Analysis of these codes have shown that they are catastrophic. That is, if no redundant information is introduced it is not possible to obtain any coding gain. The first code presented by Saha, called rate unity, does not expand the original set and does not introduce any coding information in the signal. For the second code, being a 3/4 rate code, Saha proposed the utilisation of an 8 point constellation, which will not allow any redundant information to be introduced.

Different trellis codes for  $Q^2$ PSK have been developed by Acha. Trellis codes for AWGN channels were developed and evaluated in [48]. Four different types of trellis codes were designed. Rotationally invariant trellis codes have been designed for  $Q^2$ PSK signals by using multidimensional coding and double multi-level Convolutional Codes over Ring Modulo-8 (CCRM8). In the same paper half-rate constant envelope codes for  $Q^2$ PSK signals and double Ungerboeck codes for 8-PSK were presented and evaluated [48, 49].

### 1.3 DISSERTATION ORGANISATION

Figure 1.2 contains a schematical representation of this dissertation. The general background and topic of this study, as well as an overview of the relevant papers in the literature are presented in this chapter. The rest of the dissertation is divided into three parts following the main objectives. In the first part, Chapters 2 to 4, a theoretical analysis and the application of four-dimensional Q<sup>2</sup>PSK to mobile digital communication are presented. In the second part, Chapters 5 and 6, the design and application of different trellis codes to the digital Q<sup>2</sup>PSK modem is presented. Part III concentrates on the performance evaluation results, and the dissertation summary and conclusions. The original work of this study is presented in Chapters 4 to 6, and also in Chapter 7, containing a multitude of simulation results. Finally, four appendices are included at the end of the dissertation.

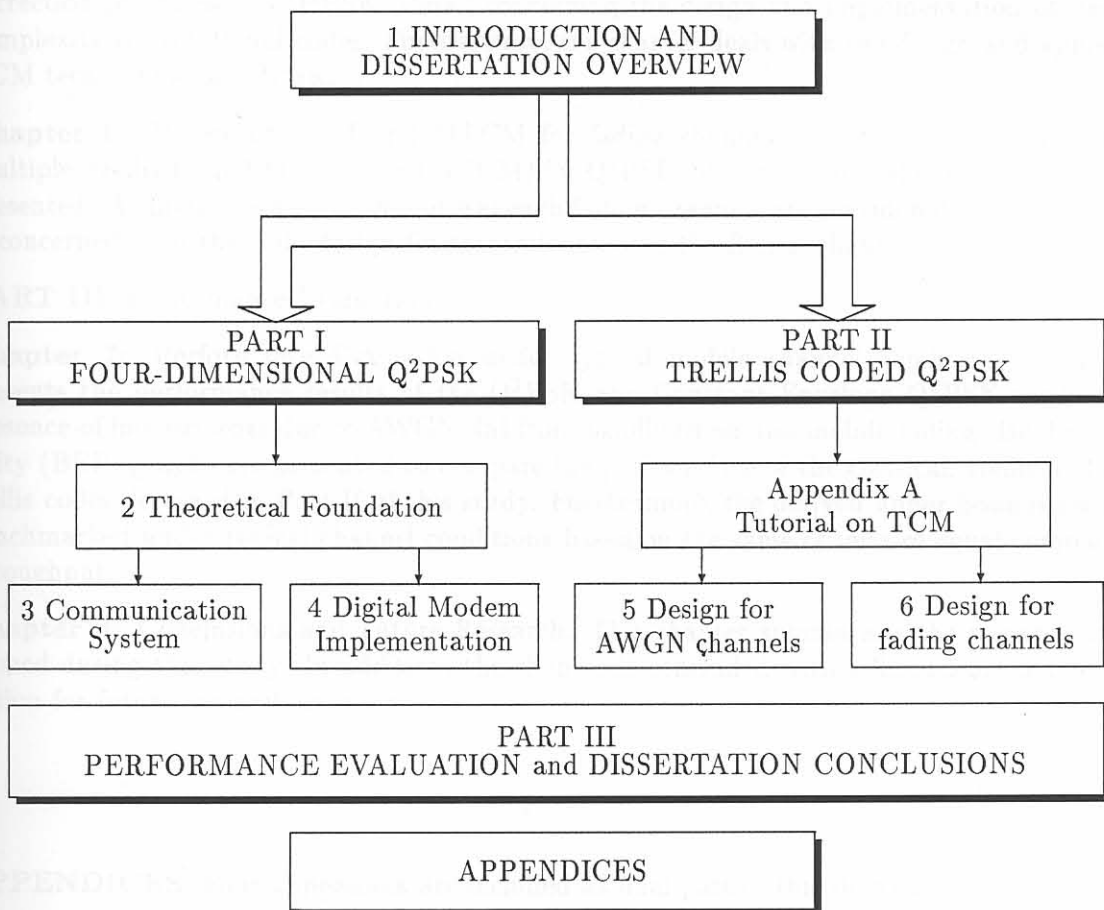


Figure 1.2: Dissertation organisation.

The dissertation is outlined as follows:

**PART I: Four-Dimensional Q<sup>2</sup>PSK** — Theory and Application to mobile digital communication.

**Chapter 2: Theoretical Foundation:** In this chapter the concepts of four-dimensional signalling are considered. Furthermore, investigations into the constraints imposed by finite bandwidth and

energy on the dimensionality and capacity of Q<sup>2</sup>PSK are carried out.

**Chapter 3:** Communication System Concepts: This chapter is concerned with the introduction of the general architecture of the communication system under investigation. It is devoted to the study of the communication environment, including the channel model and link budget analysis. The chapter is concluded with a summary of the channel and modem specifications.

**Chapter 4:** Digital Q<sup>2</sup>PSK Modulation, Demodulation and Synchronisation: In this chapter detail is presented concerning the design and implementation of the Q<sup>2</sup>PSK modulation and demodulation processes.

**PART II:** Trellis Coding with application to Q<sup>2</sup>PSK.

**Chapter 5:** Design for AWGN channels. This chapter is concerned with the design of trellis codes for AWGN channels, with specific reference to the application of classical and TCM forward error correction techniques to Q<sup>2</sup>PSK. Detail concerning the design and implementation of simple low-complexity convolutional codes. Furthermore, the chapter deals with the design and application of TCM techniques for Q<sup>2</sup>PSK.

**Chapter 6:** Design of TCM and MTCM for fading channels. In this chapter, the design of Multiple-Trellis Coded Modulation (MTCM) for Q<sup>2</sup>PSK when transmitted over a fading channel is presented. Although, both Rician and Rayleigh fading channels are considered, most of this section is concerned with the code design for transmission over the Rician channel.

**PART III:** Performance Evaluation.

**Chapter 7:** Performance Evaluation under typical mobile channel conditions: This chapter presents the performance results of the Q<sup>2</sup>PSK and Constant Envelope Q<sup>2</sup>PSK modems in the presence of impairments due to AWGN, ISI from bandlimiting and mobile fading. Bit Error Probability (BEP) graphs are presented to compare the performance of the classical, trellis and multiple trellis codes designed in Part II of this study. Furthermore, the derived upper bounds on BEP are benchmarked under typical channel conditions based on the same criteria of equal complexity and throughput.

**Chapter 8:** Conclusions and Future Research: This chapter summarises the research work performed during this study. In addition, the chapter is concluded with a discussion and recommendation for future research avenues.

---

**APPENDICES:** Four appendices are included as final part of this dissertation.

**Appendix A:** Tutorial on TCM: This appendix presents a tutorial on the theory of TCM required in Part II of the dissertation, concerned with trellis code design for Q<sup>2</sup>PSK. Specifically, the general concepts of trellis coded modulation, including the fundamentals, presentation, decoding and evaluation are discussed.

**Appendix B:** Code design — Utility software. This appendix presents the utility software developed in the design of trellis coded systems. The evaluation of the coefficients of the analytical description and the establishment of  $d_{free}$  are the two main tasks in the design procedure that must be carried out. The Calderbank—Mazo analytical presentation of TCM and MTCM is discussed. The general concepts and software developed to derive the analytical presentation are presented.

Furthermore, the software for evaluation of the minimum free Euclidean distance,  $d_{free}$  is discussed, based on the computational algorithm by Mulligan and Wilson.

**Appendix C:** Chan—Norton Algebraic algorithm. In this appendix the algebraic algorithm proposed by Chan and Norton for generating the transfer function,  $T(D)$  of a trellis encoder is presented.

**Appendix D:** Set-partitioning for Q<sup>2</sup>PSK/MTCM code design. In this appendix the complete partitioned Q<sup>2</sup>PSK/MTCM subsets evaluated in Chapter 6 are given, for code cardinality of 16 and 8, respectively.

---

---

## PART I

---

---

# FOUR-DIMENSIONAL Q-PSK Theory and Application to communication

---

---

CHAPTER 2

FOUR-DIMENSIONAL Q<sup>2</sup>PSK

## PART I

---

---

SIGNALING THEORETICAL

FOUNDATION

# FOUR-DIMENSIONAL Q<sup>2</sup>PSK: Theory and Application to mobile communication

---

---

2.1. THEORETICAL FOUNDATION

The text of the document is very faint and mostly illegible. It appears to be a technical document related to digital communication systems, specifically focusing on Q<sup>2</sup>PSK modulation.

where  $d$  is the minimum distance between any two signal points in the signal space. The average energy per signal point is  $E_s$ . The energy per bit is  $E_b$ . The number of bits per signal point is  $k$ . The minimum distance between any two signal points is  $d$ .

## CHAPTER 2

---

# FOUR-DIMENSIONAL Q<sup>2</sup>PSK SIGNALLING: THEORETICAL FOUNDATION

---



---

In this chapter the concepts of four-dimensional Quadrature Quadrature Phase-Shift Keying (Q<sup>2</sup>PSK) are considered, as a means of improving communication efficiency on the bandlimited Gaussian channel. Investigations into the constraints imposed by finite bandwidth on the dimensionality of the spectrally and power efficient Q<sup>2</sup>PSK modulation strategy are carried out. In particular, attention is focused on the derivation of a suitable four-dimensional orthonormal set of basis functions for, and channel capacity of Q<sup>2</sup>PSK. The capacity is then compared to that of two-dimensional Multiple Phase-Shift Keying (M-PSK) signals.

### 2.1 FOUR-DIMENSIONAL SIGNALLING

The term signal constellation is defined as the geometric arrangement of symbols within a given signal space. The power efficiency of a signal constellation is defined as

$$\Lambda = \frac{d_{free}^2 \cdot R_s}{E_s} \quad (2.1)$$

where  $d_{free}^2$  is the minimum squared Euclidean distance between any pair of signals,  $E_s$  is the average energy per symbol, and  $R_s$  is the symbol rate. The energy efficiency largely depends on the signal space geometry. The main objective of a digital communication system design is to minimise the average energy requirement. Specifically, the Four-Dimensional (4D) design problem is

to locate  $M$  signal points in 4D space,  $\mathbf{R}^4$ , so that for a given minimum Euclidean distance between signals,  $d_{free}$ , the average (or peak) energy is minimised. Letting  $\bar{s}_i$  denote signal locations and  $|\cdot|$  the norm, the problem to be solved is

$$\text{minimise } \frac{1}{M} \sum_{i=1}^M |\bar{s}_i|^2 \quad (2.2)$$

subject to  $|s_i - s_j| \geq d_{free}$ ,  $i \neq j$ . This is the classical sphere packing problem for which ample previous work has been done [16, 50]. For illustrative purposes, a Two-Dimensional (2D) arrangement is considered. For large  $M$  the best arrangement in 2D places signal points on vertices of equilateral triangles, which tessellate the plane. This is sometimes referred to as a hexagonal lattice, as the decoding regions are hexagons centered at each signal point. For finite  $M$  in 2D, the paper by Foschini *et al.* [50] provides optimal constellations as well as symmetrical constellations. For example, the optimum  $M = 16$  constellation in 2D has the arrangement shown in Figure 2.1a, while Figure 2.1b illustrates the standard symmetric 16-point Quadrature Amplitude-Shift Keying (16-QASK) design, which may be visualised as a Cartesian product of two One-Dimensional (1D) 4-level Amplitude Modulation (AM) systems.

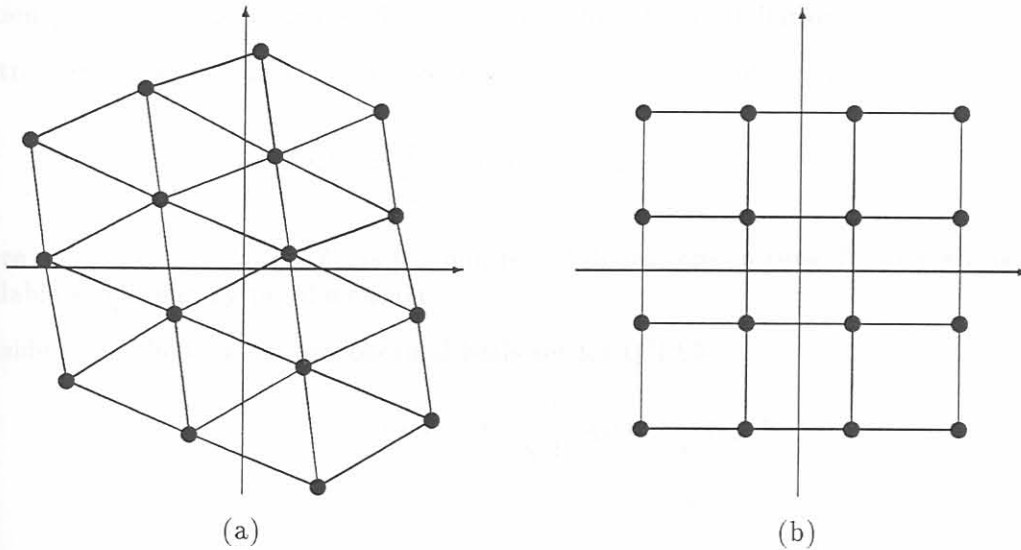


**Figure 2.1:** 16-ary constellations in Two-Dimensions (2D): (a) Optimal 16-ary design. (b) Standard 16-QASK design.

The optimal constellation is more complicated to implement, especially as far as the receiver is concerned. The concepts of the foregoing example may be extended to three and four dimensions, as illustrated in [51]. Related work may be found on Four-Dimensional (4D) modulation in the papers by Welti and Lee [17] and of Zetterberg and Brändström [18]. The Zetterberg and Brändström codes have the property that signal vectors lie on a 4D sphere (equal-energy), whereas Welti and Lee codes are allowed to consume all of the 4D space within the sphere. The equal-energy constraint constitutes a significant penalty as  $M$  becomes large, in the same way as  $M$ -ary PSK become less efficient than  $M$ -ary amplitude/phase modulation in 2D signal space. For the rest of the chapter specific 4D designs are considered, where the symbols coincide with the vertices of a hypercube. A detailed analysis and discussion of these signalling schemes can be found in the book by Wozencraft and Jacobs [22].



## 2.2 Q<sup>2</sup>PSK SIGNALLING

In general, the available number of dimensions per second,  $D$ , is larger or equal to the symbol rate  $R_s$ ,  $D \geq R_s$ , since the number of vertices on a hypercube of  $N = DT_s$  dimensions is  $2^{DT_s}$  and the number of signals required is  $M = 2^{R_s T_s}$ . It is clear that not all the vertices need be used.

The Q<sup>2</sup>PSK signal space provides a 16-ary constellation in 4D with signals of the normalised form  $(\pm 1, \pm 1, \pm 1, \pm 1)$ , i.e. the vertices of a hypercube centered at the origin of the signal space [12, 11]. Since the usual association of each of the four bits with  $\pm 1$  modulation on a particular dimension applies for detection, minimum bit error probability demodulation can be achieved by means of sign detection in each coordinate direction. As stated in [16], it is difficult to find a 16-ary design that outperforms 4D hypercube signalling, when evaluated in terms of spectral and energy efficiency, as well as implementation complexity.

The double-sided Nyquist-sense definition of bandwidth is adopted throughout this dissertation [22]. It states that theoretically a 4D modulation can transmit  $\log_2 M$  bits per symbol with a pass band signal bandlimited to a total bandwidth of  $W = 2/T_s$ , where  $T_s$  is the 4D symbol duration. The theoretical spectral efficiency for Q<sup>2</sup>PSK with  $M = 16$ , is therefore  $\eta_f = \log_2 M = 4$  bits/s/Hz. The spectral efficiency depends only on  $M$  and not upon the constellation, whereas the energy efficiency does depend on a specific geometry within the constellation.

Restricting the signals  $s_i(t)$  to the vertices of a hypercube implies that each signal has the form

$$s_i(t) = \sum_{j=1}^N s_{ij} \psi_j(t), \text{ for } i = 0, 1, \dots, M - 1 \quad (2.3)$$

where  $s_{ij} = \pm \sqrt{E_N}$ ,  $N = DT_s$ , is the number of dimensions in time  $T_s$ , and  $E_N$  is defined as the available signal energy per dimension.

Consider the following 4D orthonormal basis set for Q<sup>2</sup>PSK:

$$\begin{aligned} \psi_1(t) &= \frac{2}{\sqrt{T_s}} q_1(t) \cos 2\pi f_c t \\ \psi_2(t) &= \frac{2}{\sqrt{T_s}} q_2(t) \cos 2\pi f_c t \\ \psi_3(t) &= \frac{2}{\sqrt{T_s}} q_1(t) \sin 2\pi f_c t \\ \psi_4(t) &= \frac{2}{\sqrt{T_s}} q_2(t) \sin 2\pi f_c t \end{aligned} \quad (2.4)$$

defined over  $|t| < T_s/2$ , and zero outside this interval, where

$$\begin{aligned} q_1(t) &= \cos 2\pi f_d t \\ q_2(t) &= \sin 2\pi f_d t \end{aligned} \quad (2.5)$$

are the quadrature shaping pulses. Here  $f_c$  and  $f_d$  are the carrier and deviation frequencies, respectively. In general the deviation frequency is related to  $T_s$  as:

$$f_d = \frac{h}{T_s} \quad (2.6)$$

where  $h$  is the so-called *deviation ratio*, and  $T_s = 1/f_s$  the symbol duration. The basis set  $\{\psi_i(t)\}$  forms an orthonormal basis under the restriction

$$f_c = n f_d = \frac{nh}{T_s}, \quad n \in \mathbf{I} \geq 2. \quad (2.7)$$

The minimum value of  $h$  is 0.5, corresponding to the minimum frequency deviation necessary for signals to remain orthogonal. In general, any other four mutually orthonormal waveforms could be utilised, provided they conveniently represent the  $M = 16$  signals in the 4D signal space.

A difficulty in transmitting sequences of orthonormal pulses is that most physical channels introduce distortion, for instance when undistorted pulses that do not overlap tend to be "smeared", i.e., spread over time greater than  $T_s$ . The result, called Intersymbol Interference (ISI), causes loss of orthogonality, leading to a smaller value of  $D$  attainable in practice. In practice, the maximum number of essentially orthogonal waveforms that can be transmitted in time  $T_s$  through a channel with bandwidth  $W$  is limited to between  $T_s W$  and  $3/2 T_s W$ , where  $T_s W$  is the so-called *time-bandwidth product*. With our previous definition of bandwidth ( $W = 2/T_s$ ), the number of orthogonal waveforms is limited between 2 and 3 waveforms.

The orthogonality of the basis set remains invariant under the translation of the origin by multiples of  $T_s$ . In other words, if the basis set defined in (2.4) is translated, then orthogonality will be maintained over every interval of  $T_s$  centered around  $t = mT_s$ , with  $m$  an integer [12].

### 2.2.1 Q<sup>2</sup>PSK Modulation

The orthogonality of  $\{\psi_i(t - mT_s)\}$  suggests the modulation scheme which is shown in Figure 2.2 [11, 12]. Data from a binary source at rate  $1/T_b$  is demultiplexed into four streams  $\{a_i(t)\}$ ,  $i = 1, \dots, 4$ , with the duration of each data pulse equal to  $T_s = 4T_b$ . Each data stream is multiplied by the outputs of the basis signal generator  $\{\psi_i(t)\}$ , producing four mutually orthogonal data streams which are summed to form the modulated Q<sup>2</sup>PSK signal.

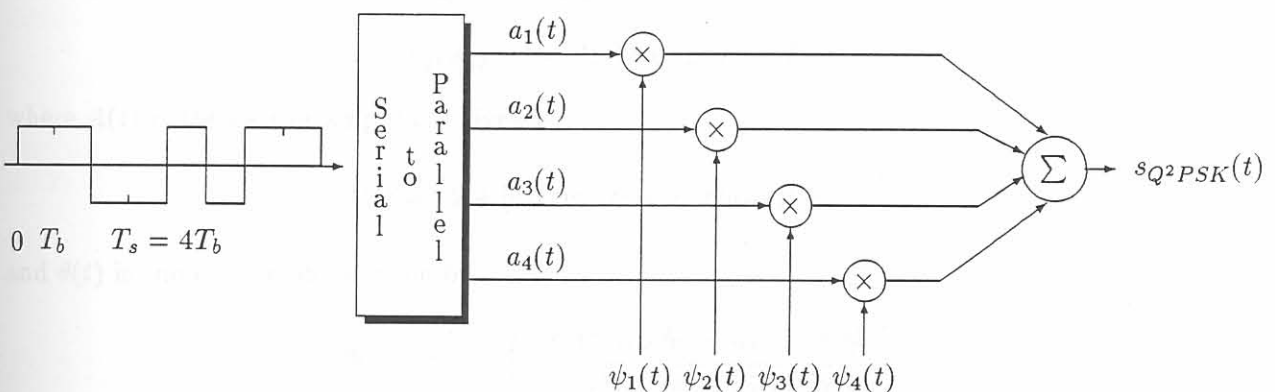


Figure 2.2: Quadrature-Quadrature Phase-Shift Keying (Q<sup>2</sup>PSK) modulator.

From Figure 2.2 and (2.4), one can represent the Q<sup>2</sup>PSK signal as

$$s_{Q^2PSK}(t) = \frac{\sqrt{T_s}}{2} \{a_1(t)\psi_1(t) + a_2(t)\psi_2(t) + a_3(t)\psi_3(t) + a_4(t)\psi_4(t)\} \quad (2.8)$$

$$\begin{aligned}
&= a_1(t)q_1(t) \cos 2\pi f_c t + a_2(t)q_2(t) \cos 2\pi f_c t \\
&+ a_3(t)q_1(t) \sin 2\pi f_c t + a_4(t)q_2(t) \sin 2\pi f_c t \quad (2.9)
\end{aligned}$$

$$= a_c(t) \cos [2\pi f_c + b_c(t)2\pi f_d] t + a_s(t) \sin [2\pi f_c + b_s(t)2\pi f_d] t \quad (2.10)$$

where the additional  $\sqrt{T_s}/2$  is a normalising factor. Recall, that the deviation ratio is defined as  $h = f_d T_s = 1/2$ . The relationships between binary quantities  $a_c(t), a_s(t), b_c(t), b_s(t)$  and the information data streams,  $\{a_i(t)\}_1^4$ , are given by

$$\begin{aligned}
a_c(t) &= a_1(t), & b_c(t) &= -a_4(t)/a_1(t) \\
a_s(t) &= a_3(t), & b_s(t) &= +a_2(t)/a_3(t)
\end{aligned} \quad (2.11)$$

The modulating signals  $\{\psi_i(t)\}$  affects the bit streams  $\{a_i(t)\}$  in two ways. Firstly shaping of the symbol pulse. The second effect is to translate the baseband spectrum to a pass band region. It should be noted that the two pulse trains associated with either of the two carrier are orthogonal over any interval of duration  $T_s$  centered around  $mT_s$ . Two of the dimensions come from the orthogonality of the carriers, while the other two come from the orthogonality of the data shaping pulses,  $q_1(t)$  and  $q_2(t)$  (defined in (2.5)). In other words, two carriers and two data shaping pulses are pairwise quadrature in phase. Hence, the name Quadrature-Quadrature Phase-Shift Keying.

At any instant the Q<sup>2</sup>PSK signal can be analysed as consisting of two signals: the one cosinusoidal with frequencies  $(f_c \pm f_d)$ , and the other sinusoidal with frequencies  $(f_c \pm f_d)$ . The separation between the two frequencies associated with either of the two signals is  $1/T_s$ . This is the minimum spacing that one needs for coherent orthogonality of two FSK signals, as in MSK. The Q<sup>2</sup>PSK signalling can be thought of as consisting of two minimum shift keying signalling schemes in parallel, which are in quadrature with respect to each other. Since the two schemes are in quadrature, it follows that the bandwidth efficiency will be twice that of conventional MSK.

### 2.2.1.1 Constant Envelope Q<sup>2</sup>PSK

One can write the Q<sup>2</sup>PSK signal, given in (2.8) as

$$s_{Q^2PSK}(t) = A(t) \cos(2\pi f_c t + \theta(t)) \quad (2.12)$$

where  $A(t)$  is the carrier amplitude given by,

$$A(t) = \left( 2 + [a_1(t)a_2(t) + a_3(t)a_4(t)] \sin \frac{2\pi t}{T_s} \right) \quad (2.13)$$

and  $\theta(t)$  is the carrier phase given by,

$$\theta(t) = \tan^{-1} \left( -\frac{a_3(t) \cos \frac{2\pi t}{T_s} + a_4(t) \sin \frac{2\pi t}{T_s}}{a_1(t) \cos \frac{2\pi t}{T_s} + a_2(t) \sin \frac{2\pi t}{T_s}} \right) \quad (2.14)$$

The Q<sup>2</sup>PSK signal, in the absence of any additional constraint, does not maintain a constant envelope. It is well known that constant envelope modulation techniques are desirable, as it makes the modulated signal relatively immune to channel non-linearities. In other words, *hard-limiting* should not degrade phase information. In addition, constant envelope techniques enable the use of automatic gain controllers at the demodulators, and can even tolerate hard-limiting without spectral degradation.

A simple block coding prior to modulation, proposed by Saha [11, 12], provides a constant envelope. The block coding scheme can be described as follows: The coder accepts serial input data and for every three information bits  $\{a_1, a_2, a_3\}$ , it generates a codeword  $\{a_1, a_2, a_3, a_4\}$ , such that the fourth bit is an odd parity check for the three information bits, represented by

$$a_4(t) = -\frac{a_1(t) \cdot a_2(t)}{a_3(t)} \quad (2.15)$$

The constant envelope feature is, however, achieved at the expense of a 25% decrease in bandwidth efficiency. This Constant Envelope (CE) Q<sup>2</sup>PSK scheme will be considered in more detail in Chapter 4.

### 2.2.1.2 Continuous Phase Q<sup>2</sup>PSK

In designing a modulation scheme, continuity of phase of the Radio Frequency (RF) carrier may be an additional desirable feature in certain situations apart from the minimum energy and bandwidth constraints. With continuity in phase, high frequency content, i.e., secondary sidelobes of the power spectral density may be significantly reduced. This will bring about a sharper spectrum fall-off, and relaxation of the restrictions on subsequent bandlimiting filters. This is desirable in certain situations where the cost of filtering after modulation is prohibitive and out of band radiation needs to be restricted at a low level. Also, in a bandlimited situation, faster spectral fall-off of the signal itself may result in less ISI and hence, a lower average bit energy requirement for a specified bit error rate.

Considering the expression for the carrier phase of Q<sup>2</sup>PSK in (2.14), it is noted that the carrier phase does not maintain continuity in phase. The foregoing continuous phase benefits motivates an investigation into the possibilities of achieving phase continuity in the Q<sup>2</sup>PSK signal. A wide variety of continuous phase modulations are found in the open literature [52, 53, 54]. Many of the better-known techniques, employ some sort of correlative coding which introduces finite memory into the modulated signal. In order to achieve phase continuity, it is necessary only to modify one of the two data shaping pulses,  $q_1(t)$  or  $q_2(t)$ . In other words phase continuity can be achieved without the use of any modulation with memory.

The conventional Q<sup>2</sup>PSK scheme uses two data shaping pulses. One of them is a half cosinusoid,  $q_1(T)$ , and the other is a half sinusoid,  $q_2(t)$ . If one replaces the half sinusoid by a full sinusoid over the same signalling interval,  $|t| \leq T_s/2$ , the RF carrier will display phase continuity [12], but at the expense of more bandwidth.

## 2.2.2 Q<sup>2</sup>PSK Demodulation

### 2.2.2.1 Analogue implementation

Implementation of a Q<sup>2</sup>PSK analogue demodulator was proposed by Saha and Birdsall [11] and later on by De Gaudenzi and Luise [55], where traditional analogue techniques were considered. At the demodulator, four identical coherent generators are available, and the orthogonality of the orthonormal basis set is used to separate the four information bit streams,  $\{a_i(t)\}$ . In the presence of AWGN, a correlation receiver will perform the process of demodulation in the optimum sense of minimum probability of error sense.

However, the tendency in communication systems is for the utilisation of digital techniques and algorithms for the implementation of more efficient modems; direct translation of analogue techniques to a digital implementation are far from being an optimal approach. Realisation of a fully digital implementation of the modem requires the utilisation of computationally efficient modulation, demodulation, synchronisation and also coding algorithms.

### 2.2.2.2 Digital implementation

Feiz and Soliman followed DSP techniques to derive a Maximum Likelihood (ML) demodulator for four dimensional modulation schemes. The work of Feiz and Soliman was developed having a Q<sup>2</sup>PSK modem in mind, and resulted in a DSP solution with reasonable complexity. To this end a conventional DSP based implementation of the Q<sup>2</sup>PSK modulator and demodulator is considered in this study, proposed and implemented by Acha [23]. In Chapter 4 more detail concerning the realisation of the digital Q<sup>2</sup>PSK modem will be given.

### 2.2.3 Spectral efficiency analysis of Q<sup>2</sup>PSK

The data streams  $a_i(t)$   $i = 1, \dots, 4$  used in (2.8) are assumed to be independent and at any instant each stream can take on either the value  $+1$  or  $-1$  with a probability of one half. This implies that in each  $T_s = 4T_b$  (second) interval the Q<sup>2</sup>PSK signal can be one of  $M = 16$  possible equally probable waveforms. Let  $s_i(t)$ ,  $i = 0, \dots, M - 1$  represent these waveforms. Probability of occurrence of  $s_i(t)$  is  $\rho_i = 1/M$  for all  $i$ . The signal set constituted by  $\{s_i(t)\}$  has the following characteristics:

- for each signal waveform  $s_i(t)$  of the set, there is also a negative waveform  $-s_i(t)$
- the stationary probabilities of  $s_i(t)$  and  $-s_i(t)$  are equal, and
- the transition probability between any two waveforms is the same.

Such a signalling source is set to be Negative Equally Probable (NEP) [56]. Its overall spectrum is characterised by the absence of a line spectrum and furthermore is independent of the transition probabilities themselves. The overall spectral density is given by [56]

$$S_{Q^2PSK}(f) = \sum_{i=0}^{M-1} \rho_i |S_i(f)|^2 \quad (2.16)$$

where  $S_i(f)$  is the Fourier transform of  $s_i(t)$  and is given by

$$S_i(f) = \int_{-\infty}^{\infty} s_i(t) e^{-j2\pi ft} dt \quad (2.17)$$

#### 2.2.3.1 Conventional Q<sup>2</sup>PSK

The time limited pulse shaping waveforms can be written in the following equivalent signal forms:

$$\begin{aligned} q_1(t) &= \sqrt{\frac{2}{T_s}} \cos\left(\frac{\pi t}{T_s}\right) \quad ; \quad 0 \leq t \leq T_s \\ &= \sqrt{\frac{2}{T_s}} \text{rect}\left(\frac{t}{T_s}\right) \cos\left(\frac{\pi t}{T_s}\right) \end{aligned} \quad (2.18)$$

$$(2.19)$$

$$\begin{aligned}
 q_2(t) &= \sqrt{\frac{2}{T_s}} \sin\left(\frac{\pi t}{T_s}\right) \quad ; \quad 0 \leq t \leq T_s \\
 &= \sqrt{\frac{2}{T_s}} \operatorname{rect}\left(\frac{t}{T_s}\right) \sin\left(\frac{\pi t}{T_s}\right)
 \end{aligned} \tag{2.20}$$

Suppose  $Q_1(f)$  and  $Q_2(f)$  are the Fourier transforms of the normalised timelimited pulse shaping waveforms,  $q_1(t)$  and  $q_2(t)$ , respectively. Then, it can be shown, using results in [56, 57, 12], that the equivalent baseband version of the Power Spectral Density (PSD) is given by

$$S_{Q^2PSK} = \frac{1}{2} \left[ |Q_1(f)|^2 + |Q_2(f)|^2 \right] \tag{2.21}$$

where

$$Q_1(f) = \frac{\sqrt{8T_s}}{\pi} \left( \frac{\cos \pi f T_s}{4f^2 T_s^2 - 1} \right) \tag{2.22}$$

$$Q_2(f) = -j \frac{\sqrt{32T_s^3} f}{\pi} \left( \frac{\cos \pi f T_s}{4f^2 T_s^2 - 1} \right) \tag{2.23}$$

Substituting (2.22) and (2.23) into (2.21), the baseband power spectral density,  $S_{Q^2PSK}(f)$ , and accordingly its Constant Envelope (CE) version, is given by

$$S_{Q^2PSK}(f) = \left( \frac{8T_s}{\pi^2} \right) (1 + 4f^2 T_s^2) \left( \frac{\cos \pi f T_s}{4f^2 T_s^2 - 1} \right)^2 \tag{2.24}$$

Expressed in terms of bit duration,  $T_b = 1/f_b$

$$S_{Q^2PSK}(f) = \left( \frac{32T_b}{\pi^2} \right) (1 + 64f^2 T_b^2) \left( \frac{\cos 4\pi f T_b}{64f^2 T_b^2 - 1} \right)^2 \tag{2.25}$$

To provide a means of comparison, the PSDs of MSK and QPSK (with rectangular symbols) signalling schemes, as functions of  $T_b$ , are given by [57]:

$$S_{QPSK}(f) = \frac{2T_b}{\pi^2} \left( \frac{\sin 2\pi f T_b}{2f T_b} \right)^2 \tag{2.26}$$

$$S_{MSK}(f) = \frac{16T_b}{\pi^2} \left( \frac{\cos 2\pi f T_b}{16f^2 T_b^2 - 1} \right)^2 \tag{2.27}$$

The power spectral densities of MSK, QPSK and Q<sup>2</sup>PSK are shown in Figure 2.3, as functions of normalised frequency,  $fT_b$ .

From these graphs, it is observed that MSK has a wider main lobe (the first null is at  $0.75/T_b$ ), than QPSK (the first null is at  $0.5/T_b$ ), and also wider than Q<sup>2</sup>PSK (the first null is at  $0.375/T_b$ ). However, the PSD of MSK has lower sidelobes than QPSK and Q<sup>2</sup>PSK at frequencies removed from the main spectral lobe.

In order to obtain quantitative information about the spectral compactness, a measure of the percentage of total power captured in a specified bandwidth has to be performed. This is plotted in Figure 2.4. For a small specified bandwidth, the percentage power captured in Q<sup>2</sup>PSK is larger than that in QPSK and MSK, when operating at the same bit rate. Beyond a bandwidth of  $1.2/T_b$ , the spectral behavior of QPSK and Q<sup>2</sup>PSK becomes almost identical.

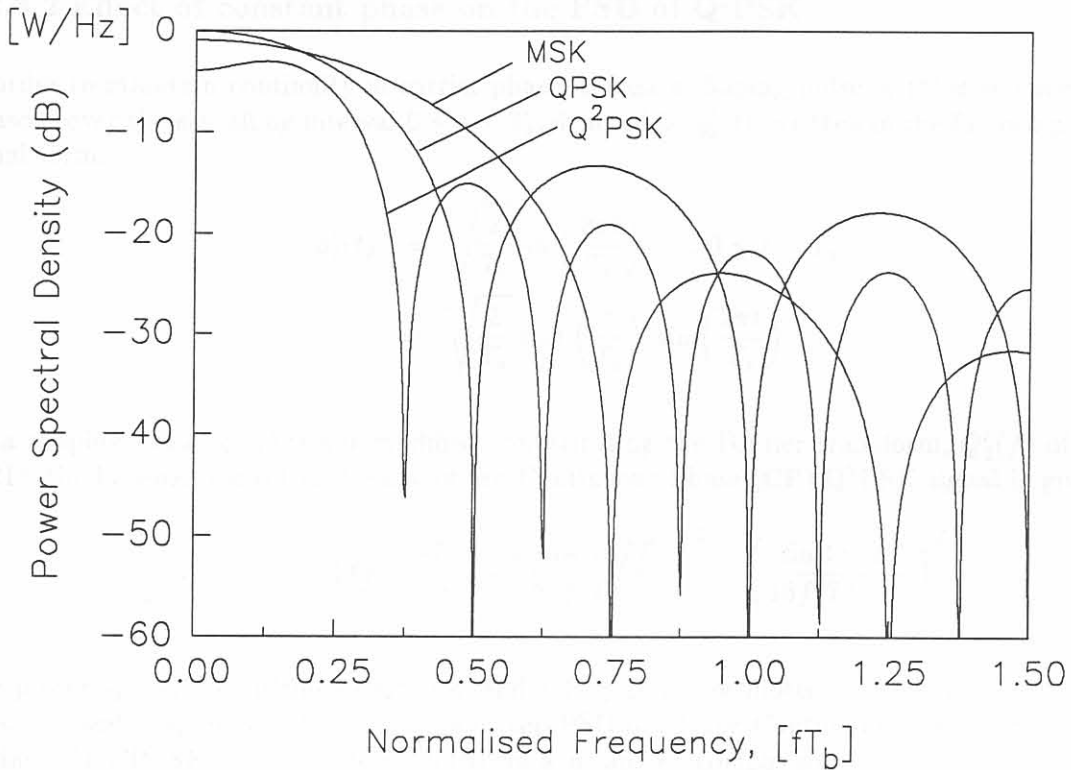


Figure 2.3: Power spectral densities of MSK, QPSK and Q<sup>2</sup>PSK modulated signals.

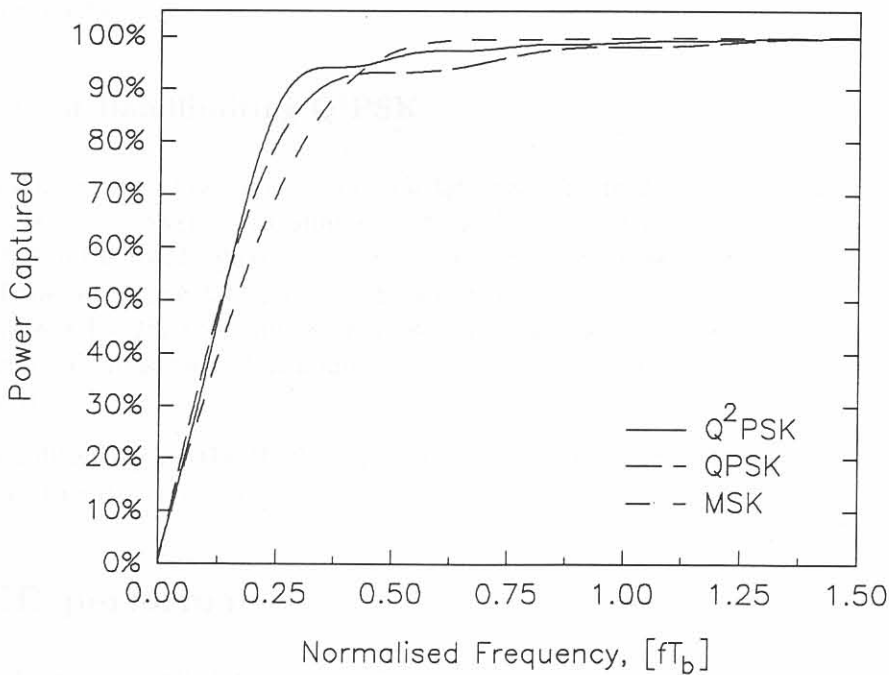


Figure 2.4: Power captured as function of bandwidth of MSK, QPSK and Q<sup>2</sup>PSK signals.

### 2.2.3.2 Effect of constant phase on the PSD of Q<sup>2</sup>PSK

In order to maintain continuity in carrier phase, the data shaping pulse,  $q_2(t)$  is replaced by a full sinusoid over the signalling interval  $0 \leq t \leq T_s$ , denoted by  $q'_2(t)$ , written in the following equivalent signal form:

$$\begin{aligned} q'_2(t) &= \sqrt{\frac{2}{T_s}} \sin\left(\frac{2\pi t}{T_s}\right) \quad ; \quad 0 \leq t \leq T_s \\ &= \sqrt{\frac{2}{T_s}} \operatorname{rect}\left(\frac{t}{T_s}\right) \sin\left(\frac{2\pi t}{T_s}\right) \end{aligned} \quad (2.28)$$

Data shaping pulse,  $q_1(t)$  is not modified. Substituting the Fourier transform,  $Q'_2(f)$  of  $q'_2(t)$  into (2.21), the baseband spectral density of the Continuous Phase (CP) Q<sup>2</sup>PSK signal is given by

$$S_{CP-Q^2PSK}(f) = \frac{4T_b}{\pi^2} \left\{ 4 \left( \frac{\cos 4\pi f T_b}{64f^2 T_b^2 - 1} \right)^2 + \left( \frac{\sin 4\pi f T_b}{16f^2 T_b^2 - 1} \right)^2 \right\} \quad (2.29)$$

The power spectral densities of Q<sup>2</sup>PSK and CP-Q<sup>2</sup>PSK are plotted in Figure 2.5, as functions of normalised frequency,  $fT_b$ . In addition, the PSD of  $M$ -ary Continuous Phase Frequency Shift Keying ( $M$ -CPFSK,  $M = 4$ ) is included as a means of comparison. Figure 2.6 illustrates the percentage of total power captured in a specified bandwidth for Q<sup>2</sup>PSK, CP-Q<sup>2</sup>PSK and 4-CPFSK.

In spite of the sharper asymptotic spectrum fall-off, the continuous phase version Q<sup>2</sup>PSK signal, for a finite bandwidth, captures almost the same power as the original one. The continuous phase version, therefore, does not seem to render any improvement with respect to conventional Q<sup>2</sup>PSK in terms of energy efficiency.

### 2.2.3.3 Effects of Bandlimiting Q<sup>2</sup>PSK

When the spectral compactness of conventional Q<sup>2</sup>PSK (Figure 2.4) is considered, it is noted that only 90.7% of the total power is transmitted within the Nyquist bandwidth,  $W = 2/T_s = 1/(2T_b)$ . Thus, nearly 10% of the total signal power will be lost in the process of band pass filtering, resulting in spreading of the baseband data pulses, which in turn causes ISI. For the same finite bandwidth, Continuous Phase (CP) Q<sup>2</sup>PSK, captures only 88.3% of the radiated power. When a MSK signalling scheme is considered, it is seen that almost the entire signal power (99.05%) is contained within the bandwidth  $W$ .

The effect of bandlimiting on the BEP of Q<sup>2</sup>PSK will be evaluated by means of simulation in Part III, Chapter 7 of this dissertation.

## 2.2.4 BER performance

The ultimate objective of all data communication systems is to achieve the minimum Bit Error Rate (BER) with a minimum amount of average energy per bit,  $E_b$ . In practice, BER performance is usually evaluated under the assumption of a bandlimited channel corrupted by AWGN. The



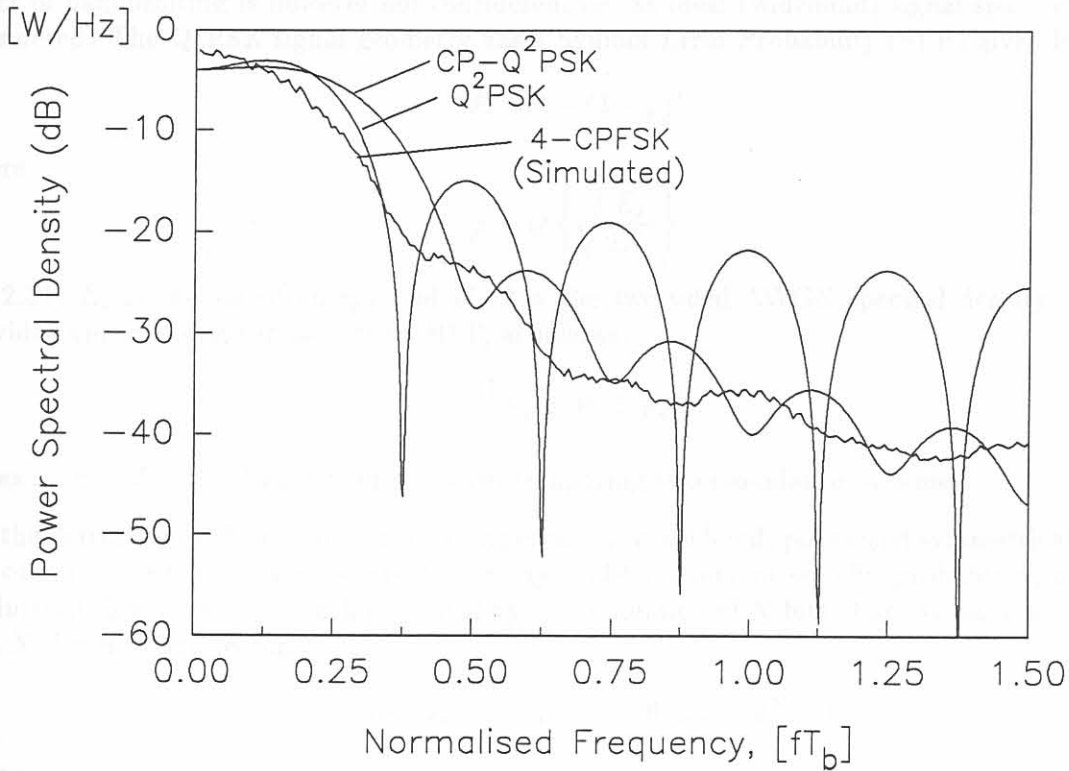


Figure 2.5: Power spectral densities of Q<sup>2</sup>PSK, CP-Q<sup>2</sup>PSK and 4-CPFSK modulated signals.

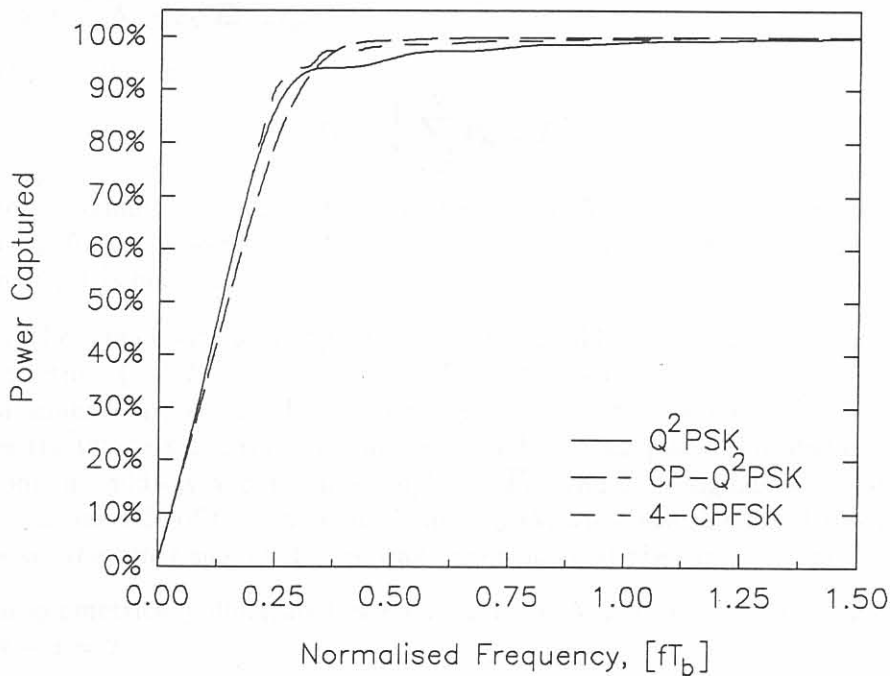


Figure 2.6: Power captured as function of bandwidth for Q<sup>2</sup>PSK and CP-Q<sup>2</sup>PSK signals.

effect of bandlimiting is however not considered, i.e. an ideal (wideband) signal space geometry is considered. The Q<sup>2</sup>PSK signal geometry has a Symbol Error Probability (SEP) given by [22]:

$$P_s = 1 - (1 - \rho)^4 \quad (2.30)$$

where

$$\rho = Q \left\{ \sqrt{\frac{E_s}{2N_o}} \right\} \quad (2.31)$$

In (2.31)  $E_s$  is the signal energy and  $N_o/2$  is the two-sided AWGN spectral density. The SEP provides upper and lower bounds on BEP, as follows:

$$\frac{1}{4}P_s \leq P_b \leq P_s \quad (2.32)$$

An exact calculation of  $P_b$  is required when comparing two modulation schemes.

For the derivation of  $P_b$  a  $N$ -dimensional hypercube is considered, positioned symmetrically around the origin to minimise the average bit energy. The number of equally probable signals in the modulated signal set is  $2^N$ , each presented by a combination of  $N$  bits. Each signal may be written as a  $N$ -dimensional vector:

$$s_i = (s_{i1}, s_{i2}, \dots, s_{iN}), \quad i = 0, 1, \dots, 2^N - 1 \quad (2.33)$$

where

$$s_{ij} = \begin{cases} +d/2 \\ \text{or} \\ -d/2 \end{cases} \quad \text{for all } i, j \quad (2.34)$$

represent the projections of the  $i$ -th symbol  $s_i$  onto the  $N$  basis vectors of the  $N$ -dimensional signal space, and  $d = 2\sqrt{E_s/N} = 2\sqrt{E_b}$  [22].

The average BEP is given by

$$P_b = \frac{1}{N} \sum_{i=1}^N P_{bi} = P_{bi} \quad (2.35)$$

where  $P_{bi}$  is the probability of error in the  $i$ -th bit position. The last equality in (2.35) comes from the equality of  $P_{bi}$  for all  $i$ , because of the symmetry in signal space geometry. In order to derive an equation for  $P_b$ , it is necessary to calculate  $P_{bi}$ .

To calculate  $P_{bi}$ , the signals within the signal space are divided into two sets:  $\{+d/2, s_{i2}, s_{i3}, \dots, s_{iN}\}$  and its image partner  $\{-d/2, s_{i2}, s_{i3}, \dots, s_{iN}\}$ . These two sets of signals will lie on two parallel hyper planes of dimension  $(N - 1)$ . The midway hyper plane of the same dimension is considered, which separates the two sets and is equidistant from each original plane. The distance of any signal in either set from the midway hyper plane is  $d/2 = \sqrt{E_b}$ . Thus, the signals with  $+d/2$  in the first bit position are on one side of this plane at distance  $\sqrt{E_b}$ , while the signals with  $-d/2$  in the first bit position are on the other side of the midway hyper plane at the same distance.

The foregoing is geometrically illustrated in Figure 2.7, for  $N = 3$ , with midway hyper plane being of dimension  $N - 1 = 2$ .

An error in the first bit position occurs when the noise component  $n_0$ , associated with the first bit position, displaces a signal to the other side of the midway hyper plane. The probability of such

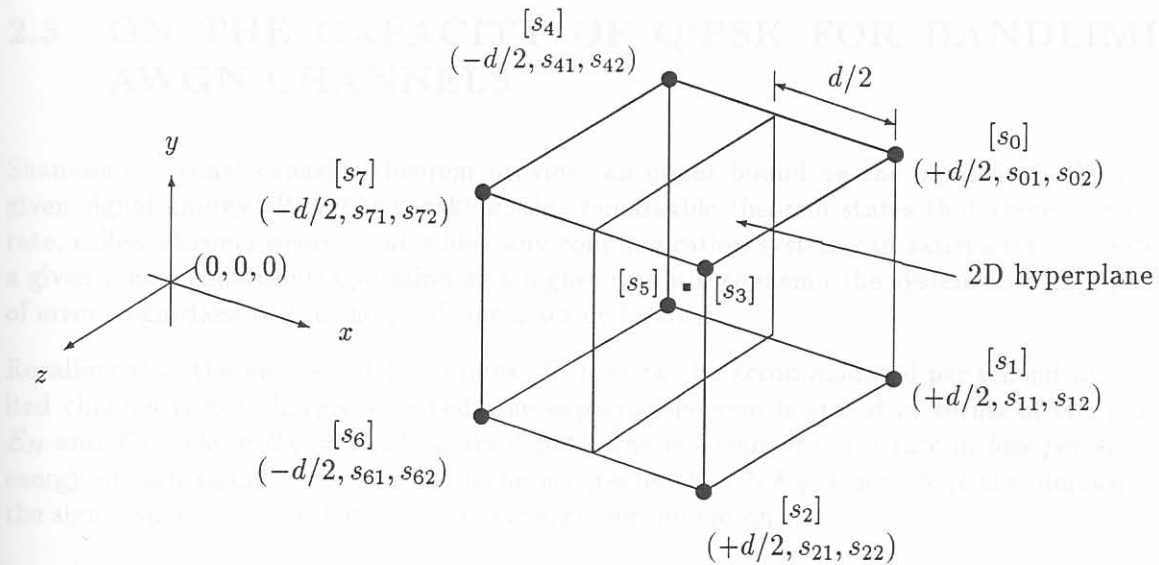


Figure 2.7: Signals on vertices of  $N = 3$  dimensional hypercube.

an event is

$$\begin{aligned}
 P_{b1} &= \int_{-\infty}^{\infty} \rho_{n0}(x) \cdot dx \\
 &= Q \left\{ \sqrt{\frac{2E_b}{N_o}} \right\}
 \end{aligned} \tag{2.36}$$

where  $p_{n0}(x)$  is the probability density function of Gaussian noise with variance per dimension  $N_o/2$ , the overall BEP simplifies to

$$\begin{aligned}
 P_b &= P_{b1} \\
 &= Q \left\{ \sqrt{\frac{2E_b}{N_o}} \right\}
 \end{aligned} \tag{2.37}$$

since the conditional probability  $P_{bi}$  is equal for all  $i$ . This probability of error holds for a hypercube of any dimension  $N$ .

Recall, that the BEP of Binary Phase-Shift Keying (BPSK) is exactly the same as the BEP for Q<sup>2</sup>PSK, given by (2.37). BPSK uses two antipodal signals that can be considered as the vertices of a hypercube of dimension one. Similarly, QPSK and MSK, which use a set of four biorthogonal signals, can be considered as using the vertices of a hypercube of dimension two. Further, it was shown that Q<sup>2</sup>PSK uses the vertices of a 4D hypercube. Thus, BPSK, QPSK, MSK and Q<sup>2</sup>PSK belong to the same class of signalling schemes using the vertices of 1D, 2D and 4D hypercubes, respectively. Also, each of them requires the same energy per bit,  $E_b$ , to maintain a specific level of communication reliability. The latter is true when the channel is not bandlimited, and corrupted only by AWGN.

In a practical situation channel bandlimiting causes ISI, which has a different effect on each of these schemes. Since the signal space of the hypercube no longer remains ideal, the energy efficiency is degraded in the case of Q<sup>2</sup>PSK.

## 2.3 ON THE CAPACITY OF Q<sup>2</sup>PSK FOR BANDLIMITED AWGN CHANNELS

Shannon's channel capacity theorem provides an upper bound on the bandwidth efficiency for a given signal energy. Roughly speaking, this remarkable theorem states that there is a maximum rate, called *channel capacity*, at which any communication system can satisfactorily operate within a given power constraint; operation at a higher rate will condemn the system to a high probability of error, regardless of the choice of signal set or receiver.

Recalling that the number of dimensions,  $D$ , that can be accommodated per second by a bandlimited channel is not sharply specified, the capacity theorem is stated in terms of the parameters  $E_N$  and  $R_N$ , where  $R_N = R_b/D$  again denotes the transmitter input rate in *bits per second*. The energy of each signal is constrained to be no greater than  $NE_N$ , where  $N$  is the dimensionality of the signal space and  $E_N$  is the average energy per dimension,

$$E_N = \frac{\text{joules/s}}{\text{dimensions/s}} \quad (2.38)$$

In the particular case of transmission over an AWGN channel, the capacity theorem may be expressed in the form

$$C_N = \frac{1}{2} \log_2 \left( 1 + 2 \frac{E_N}{N_o} \right) \quad (2.39)$$

$C_N$  is called the *Gaussian channel capacity*, measured in *bits/dimension*.

Let us examine the limits in performance gains that may be achieved when Q<sup>2</sup>PSK is considered, excluding the effects of ISI (i.e., wideband transmission in AWGN). With perfect timing and carrier-phase synchronisation, samples are taken at time instants  $iT_s + \tau_s$ , where  $\tau_s$  the appropriate sampling phase. The output of the modulation channel becomes

$$\bar{z}_i = \bar{a}_i + \bar{w}_i \quad (2.40)$$

where  $\bar{a}_i$  denotes a  $N$ -dimensional discrete channel signal vector transmitted at modulation time  $iT$ , and  $\bar{w}_i$  is an independent normally distributed noise sample with zero mean and variance  $\sigma^2$  along each dimension. The average SNR is defined as

$$\text{SNR} = \frac{E\{|\bar{a}_i|^2\}}{E\{|\bar{w}_i|^2\}} = \frac{E\{|\bar{a}_i|^2\}}{N\sigma^2} \quad (2.41)$$

where  $N = 4$  for Q<sup>2</sup>PSK. When normalised average signal power is assumed ( $E\{|\bar{a}_i|^2\} = 1$ ), the SNR is simply given by  $1/4\sigma^2$ .

The capacity,  $C^*$  of a Discrete Memoryless Channel (DMC) in the case of a continuous-valued output, assuming AWGN and equiprobable code occurrence, can be written as [27]:

$$C^* = \log_2(M) - \frac{1}{M} \sum_{k=0}^{M-1} E \left\{ \log_2 \sum_{i=0}^{M-1} \exp(A_{ik}) \right\} \quad (2.42)$$

where

$$A_{ik} = -\frac{|\bar{a}^k + \bar{w} - \bar{a}^i|^2 - |\bar{w}|^2}{N\sigma^2} \quad (2.43)$$

Using a Gaussian random generator,  $C^*$  has been evaluated by Monte Carlo averaging of (2.42) for Q<sup>2</sup>PSK and Constant Envelope (CE) Q<sup>2</sup>PSK. Also, the results presented by Ungerboeck [27] for 2D M-PSK modulations are repeated here for comparison purposes. In Figure 2.8,  $C^*$  is plotted as a function of SNR. The value at which an uncoded symbol-error probability  $P_s = 10^{-5}$  is achieved is also indicated for 4-PSK (QPSK), Q<sup>2</sup>PSK and its constant envelope version, CE-Q<sup>2</sup>PSK. These results are summarised in Table 2.1.

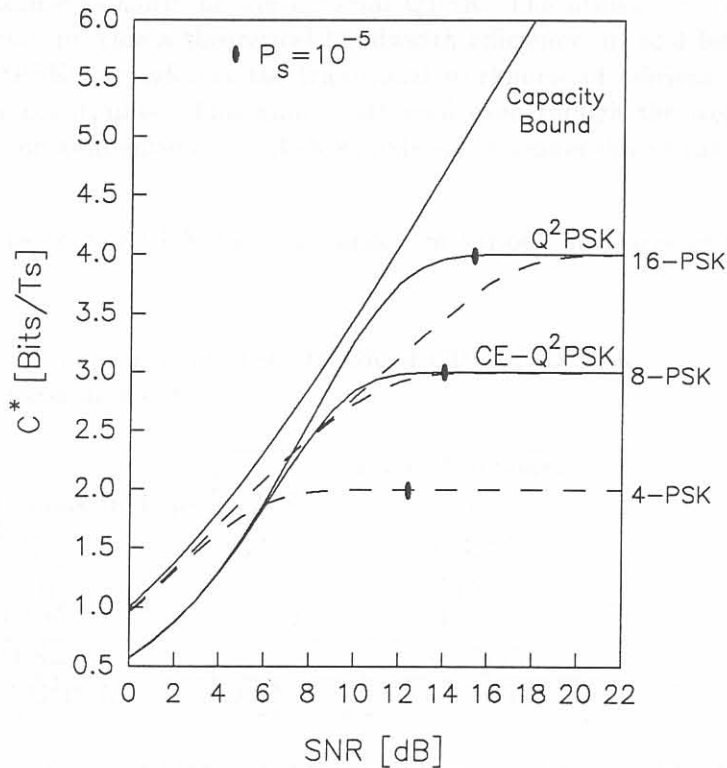


**Figure 2.8:** Channel capacity  $C^*$  of 2D M-PSK ( $M = 4, 8$  and  $16$ , denoted by dashed lines) and 4D Q<sup>2</sup>PSK modulation for bandlimited AWGN channels.

**Table 2.1:** Comparison of required SNR to achieve a symbol-error probability,  $P_s = 10^{-5}$ .

Modulation	Required SNR
QPSK	12.9 dB
Q <sup>2</sup> PSK	14.5 dB
CE-Q <sup>2</sup> PSK	13.9 dB

To interpret Figure 2.8, consider uncoded 4-PSK operating at  $2.0 \text{ bits}/T_s$  where  $P_s = 10^{-5}$  occurs at  $SNR = 12.9 \text{ dB}$ . If the modulation is changed from 2D to 4D, it is clear that by considering either Q<sup>2</sup>PSK or CE-Q<sup>2</sup>PSK, error-free transmission at  $2.0 \text{ bits}/T_s$  is theoretically possible at  $SNR = 6.9 \text{ dB}$ , constituting a gain of  $6.0 \text{ dB}$  compared to QPSK.

The latter observation indicates that if the modulation is changed from 2D to 4D, exploitation of the extra dimensions for coding, can lead to a theoretical gain in the order of  $4.8 \text{ dB}$ . The net result is a coding gain, achieved without alteration of the data throughput. The preceding discussion provides the motivation for 4D modulation.

## 2.4 CONCLUDING REMARKS: CHAPTER 2

The search for more effective modulation schemes, both from the energy and bandwidth saving viewpoint, is unquestionably one of the relevant trends in modern communication system research. As mentioned before, the key novelty of Q<sup>2</sup>PSK is the efficient use of degrees of freedom in an expanded multidimensional (4D) signal space. The modulated signal bears a four-fold dimensionality as opposed to the bidimensionality of conventional QPSK. The utilisation of a four-dimensional modulation scheme may provide a theoretical bandwidth efficiency,  $\eta_f$  of 4 *bits/s/Hz*. In terms of spectral efficiency Q<sup>2</sup>PSK outperforms the traditional workhorse of efficient modulations, MSK, within similar energy constraints. This gain is attained even though the well-known features of phase-continuity and constant envelope of MSK-signals are no longer shared (at least in the uncoded case) by Q<sup>2</sup>PSK.

These observations are supported in the comparison of various measures of bandwidth listed in Table 2.2.

**Table 2.2:** Bandwidth comparison of MSK, QPSK, 4-CPFSK, Q<sup>2</sup>PSK and CP-Q<sup>2</sup>PSK signalling as a function of power containment.

Modulation Type	Power Containment		
	77%	90%	99%
MSK	$0.29/T_b$	$0.39/T_b$	$0.59/T_b$
QPSK	$0.23/T_b$	$0.34/T_b$	$1.24/T_b$
4-CPFSK	$0.2/T_b$	$0.25/T_b$	$0.45/T_b$
Q <sup>2</sup> PSK	$0.2/T_b$	$0.27/T_b$	$1.0/T_b$
CP-Q <sup>2</sup> PSK	$0.32/T_b$	$0.338/T_b$	$1.25/T_b$

Comparing the curves of Figure 2.4 it is noted for a small specified bandwidth, the percentage power captured in Q<sup>2</sup>PSK is larger than that in QPSK and MSK, when operating at the same bit rate. Beyond a bandwidth of  $1.2/T_b$ , the asymptotic behavior of QPSK and Q<sup>2</sup>PSK (also CE-Q<sup>2</sup>PSK) became almost identical. The continuous phase version CP-Q<sup>2</sup>PSK signal (see Figure 2.6), in spite of the sharper asymptotic spectrum fall-off, captures almost the same power as the conventional one for a finite bandwidth. For the CP-Q<sup>2</sup>PSK version the latter is achieved at a 25% decrease in throughput. For this reason it does not seem feasible to pursue this technique further, with respect to conventional Q<sup>2</sup>PSK in terms of energy efficiency.

When the bandwidth utilisation of conventional Q<sup>2</sup>PSK is compared to that of 4-CPFSK (depicted in Figures 2.5 and 2.6), it is noted that these techniques exhibit very similar spectrum utilisation within a specified bandwidth. Considering the asymptotic behavior, it is clear that the continuous phase 4-CPFSK definitely provides a better solution in terms of spectral fall-off. However, the inherent phase trellis as a result of the memory employed, restricts the degrees of freedom provided in 4-CPFSK. For this reason, the code structure of Q<sup>2</sup>PSK is better suited for the application of sophisticated error correction techniques, without having to cope with restrictions on the availability of the extra dimensions.

Considerations of channel capacity of Q<sup>2</sup>PSK for bandlimited AWGN channels have shown that a theoretical gain of 6.0 *dB* in SNR can be expected when 4D modulation is used in the place of 2D modulation. The latter observation is in effect an indication of the expected theoretical gain when coding is employed. That is, changing the modulation from 2D to 4D and exploiting the extra

dimensions to add coding, a theoretical gain in the order of 6.0 dB will result, without altering the data throughput. The 4D Q<sup>2</sup>PSK signalling scheme can thus be used as a basis to implement coded transmission.

In the following chapter the Q<sup>2</sup>PSK digital communication system is introduced and discussed in detail, including the fading channel model and primary system specifications.

---



---

## CHAPTER 3

### Q<sup>2</sup>PSK MODEL

## COMMUNICATION SYSTEM

---



---

There are a number of key performance indicators (KPIs) that are used to evaluate the performance of a communication system. These KPIs are used to compare different communication systems and to determine the most suitable system for a given application. The KPIs are defined as follows:

- Maximum throughput
- Minimum error rate
- Minimum latency
- Minimum cost
- Maximum reliability
- Minimum power consumption

## CHAPTER 3

---

# Q<sup>2</sup>PSK — MOBILE COMMUNICATION SYSTEM

---

---

This chapter introduces the general architecture of the Q<sup>2</sup>PSK communication system proposed for spectrally efficient ( $\eta_f \geq 2.0$  bits/s/Hz) V/UHF mobile digital communications. A study of the communication environment is undertaken, including the fading channel model. This chapter is concluded with a summary of the primary system specifications.

There are a multitude of modulation/demodulation schemes available to the designer of a digital communication system required for data transmission over a band-pass channel. Each scheme offers *system trade-offs* of its own. The final choice made by the designer is determined by the way in which the available primary communication resources, *transmitted power* and *channel bandwidth*, are to be best exploited. In particular, the choice is made in favor of the scheme that attains as many of the following design goals as possible [1, 57]:

- Maximum data rate.
- Minimum probability of symbol error.
- Minimum transmitted power.
- Minimum channel bandwidth.
- Maximum rejection of interference.
- Minimum circuit complexity.



### 3.1 GENERAL SYSTEM ARCHITECTURE

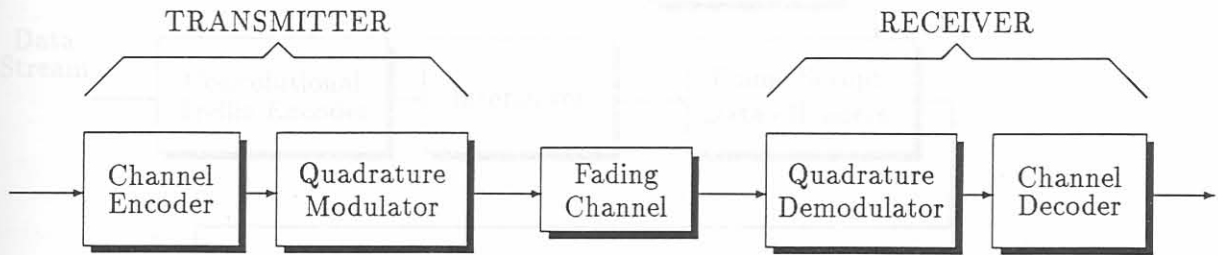


Figure 3.1: Basic communication system model.

Figure 3.1 presents the most basic block diagram of the system model under investigation. The *Transmitter* is identified as consisting of the channel encoder and quadrature modulator; the *Receiver*, consisting of the quadrature demodulator and channel encoder; and a fading channel that links the transmitter and receiver.

In the following subsections the different system building blocks are introduced in some detail.

#### 3.1.1 Transmitter

The transmitter can be further subdivided. This detailed transmitter block diagram is illustrated in Figure 3.2.

##### 3.1.1.1 Information source

A data stream is obtained from an information source where the output elements can take on only binary (1s or 0s) values. A desirable source is random so that it has maximum information. If the probabilities of occurrence of 1<sup>s</sup> and 0<sup>s</sup> are the same, its entropy is maximised. If for some reason or other, the source is not random (for example in a video image), it will necessitate the implementation of a source encoder. The role of the latter is to randomise the source. In our system a random information source is employed, canceling out the need for a source encoder and the associated source decoder at the receiver.

##### 3.1.1.2 Channel encoder

The goal of the channel encoder is to introduce an error detection and correction capability into the information source to combat channel transmission errors. To achieve this goal, some redundancy must be added to the information carrying data stream. The detection of errors is also a key item in channel coding since retransmissions of a code word containing errors can be requested, when a feedback channel is utilised.

In this dissertation the techniques of trellis coding will be applied, for adding redundancy to the information stream so that efficient channel utilisation can be achieved. The basic idea involves no change in data transmission rate; rather, the number of points in the signal constellation is increased

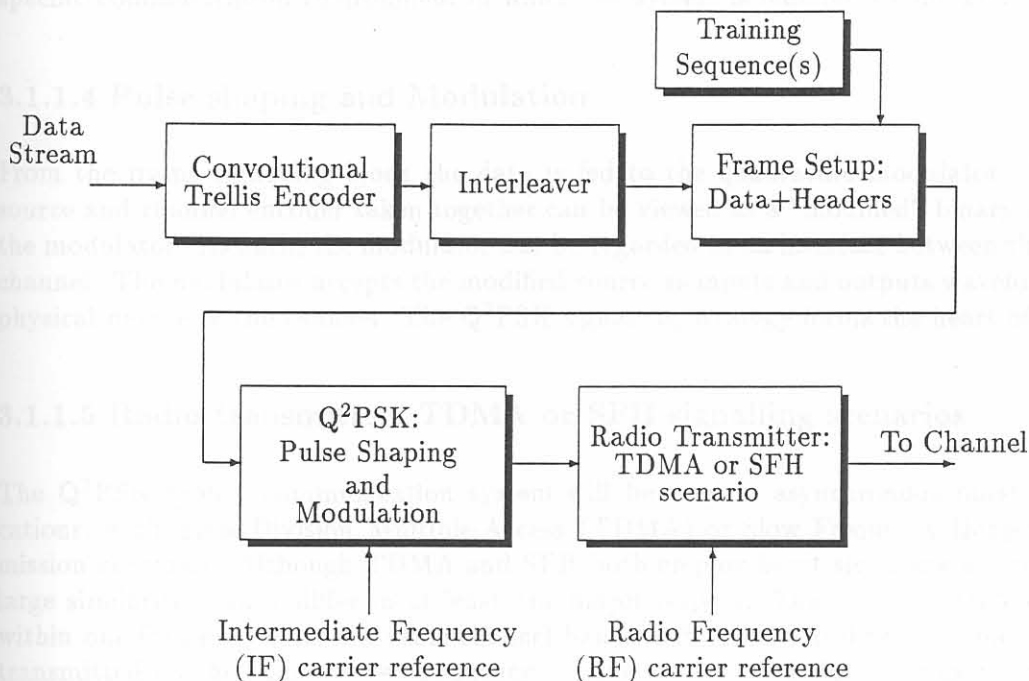


Figure 3.2: Detailed transmitter block diagram.

to achieve the required redundancy. The concepts of trellis coding or Trellis-Coded Modulation (TCM) and its application to four-dimensional Q<sup>2</sup>PSK signalling will be discussed in detail in Part II of this dissertation.

After the encoding of the data, it is sent through an interleaver which is included for *burst error* protection when a transmission over a *multipath* channel with *memory* is considered. Two types of interleavers are commonly used, *block interleavers* and *convolutional interleavers* [1, 58]. An example of a channel with memory is a fading channel, particularly when the fading varies slowly compared to the duration of one data symbol. Multipath impairments involves signal arrivals at the receiver over two or more paths of different lengths, resulting in a distorted resultant received signal.

Under the assumption that the channel has memory, the errors can no longer be characterised as being random and independent. Most convolutional codes are designed to combat random independent errors. The result of a channel having memory on such coded signals is to cause degradation in system error performance.

### 3.1.1.3 Frame transmission strategy

Almost all digital communication systems have some sort of frame structure. This is to say that the data stream is organised into uniformly sized groups of bits. Furthermore, for the receiver to make sense of the incoming data stream, the receiver needs to be synchronised with the data stream's frame structure. Frame synchronisation is therefore accomplished by organising the data transmitted in a special signalling format at the transmitter. Hence the need for a *frame transmission strategy*. In general the signalling procedure may become fairly complex depending on the

specific communication environment in which the system is required to operate.

#### 3.1.1.4 Pulse shaping and Modulation

From the frame signalling block the data is fed to the quadrature modulator. The information source and channel encoder taken together can be viewed as a "modified" binary source that feeds the modulator. As such, the modulator can be regarded as an interface between the source and the channel. The modulator accepts the modified source as inputs and outputs waveforms that suit the physical nature of the channel. The Q<sup>2</sup>PSK signalling strategy forms the heart of the modulator.

#### 3.1.1.5 Radio transmitter: TDMA or SFH signalling scenarios

The Q<sup>2</sup>PSK mobile communication system will be used in asynchronous burst-mode communications, with Time-Division Multiple-Access (TDMA) or Slow Frequency-Hopping (SFH) transmission scenarios. Although TDMA and SFH both employ burst signalling strategies and exhibit large similarities, they differ in at least one major respect. That is, in TDMA successive bursts within one frame all share the same channel bandwidth (albeit, at different time instants) and are transmitted on the same carrier frequency. In the case of SFH signalling each successive burst is transmitted on a different carrier frequency and therefore experiences completely different channel conditions.

The primary consequences of the foregoing difference between TDMA and SFH are as follows:

- In TDMA, carrier phase and Doppler frequency offset information obtained from one burst can be transferred to the next (i.e., *burst-to-burst* control is possible), whereas in SFH, carrier phase and frequency information gathered from one specific burst (or hop) cannot be used in successive bursts. This is true, since the channel conditions corresponding with these bursts may be totally different from the former and subsequent bursts by virtue of the nature of the variation of the channel response with frequency.
- In SFH systems, carrier phase and frequency control can therefore be regarded as truly bursty in nature, i.e., control is exclusively limited to the burst and must be obtained and exercised strictly within the burst period. Carrier information associated with one particular burst is only applicable to that burst and must be reacquired for each successive burst.

One of the advantages of frequency hopping systems is that when the hopping rate is fast enough the "spread spectrum" signals produced show strong resistance to interference and frequency selective (multipath) fading [59].

### 3.1.2 Receiver

The receiver follows the channel in the block diagram of Figure 3.1. Here, the transmitter fulfills the task of matching the source to the channel, whereas the receiver performs the inverse of this operation and recover the source symbols. The inverse of the detailed transmitter block diagram shown in Figure 3.2, is illustrated in Figure 3.3, constituting the receiver block diagram.

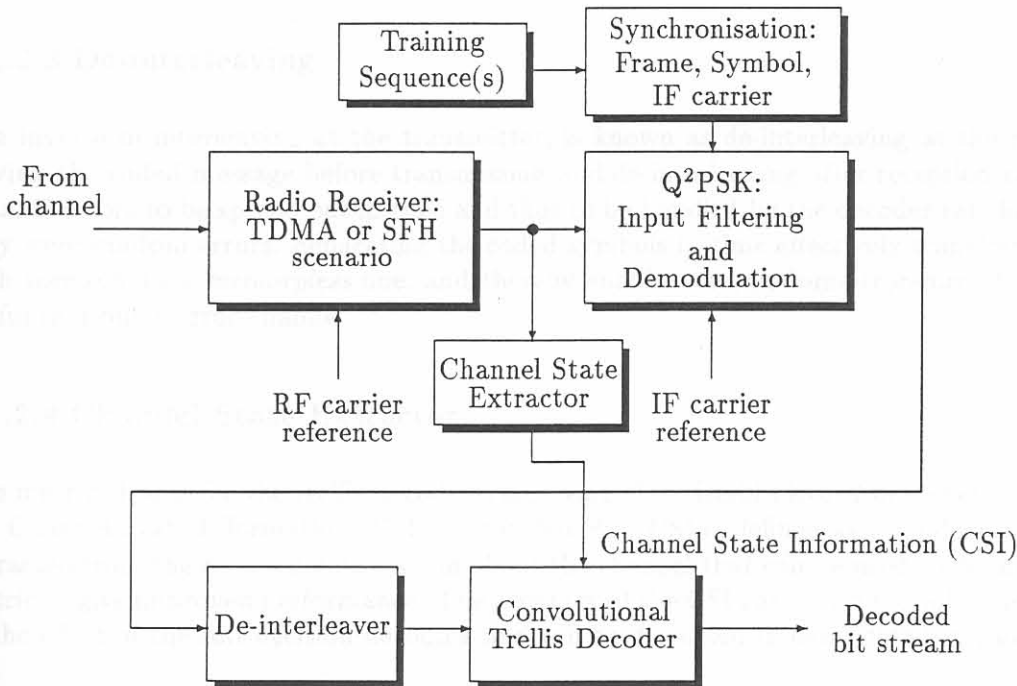


Figure 3.3: Detailed receiver block diagram.

#### 3.1.2.1 Frame synchronisation

A *synchronisation sequence* is sent as part of the *message header* to enable rapid synchronisation acquisition at the receiver. The header should provide buffer time to accommodate any timing uncertainty as well as any information required for equaliser training (when included) and information to provide frequency hopping or TDMA signalling. The synchronisation sequence is known at the receiver, which is constantly searching for it in the data stream. Detection of the synchronisation word normally involves the utilisation of a correlator. In chapter 4 a novel multidimensional frame synchronisation procedure will be described, specifically designed for the four-dimensional Q<sup>2</sup>PSK modem employing complex correlation sequences [60]. The advantage of this synchronisation procedure lies in the effective use of all the available dimensions to ensure that frame acquisition will be immediate with low probability of false detection.

### 3.1.2.2 Q<sup>2</sup>PSK: Input filtering and demodulation

At the output of the radio receiver, the modem receiver front-end consists of the input filter and demodulation subsystem. The demodulator is the inverse of the modulation process, where the faded, noise-corrupted channel signal are demodulated. The demodulated in-phase and quadrature signal components are fed to the de-interleaver (block or convolutional).

### 3.1.2.3 De-interleaving

The inverse of interleaving at the transmitter, is known as de-interleaving at the receiver. Interleaving the coded message before transmission and de-interleaving after reception causes bursts of channel errors to be spread out in time and thus to be handled by the decoder (at the receiver) as if they were random errors. Separating the coded symbols in time effectively transforms the channel with memory to a *memoryless* one, and thereby enables the random-error-correcting codes to be useful in a burst-error channel.

### 3.1.2.4 Channel State Extractor

The metric chosen for the trellis decoder, employing the Viterbi algorithm, depends on whether or not Channel State Information (CSI) is provided [61]. CSI is defined as the information derived or extracted from the received data stream about the channel that can be used to design the decoding metric to give improved performance. The accuracy of the CSI has only a secondary effect compared to the effect of the soft decision decoding and will be discussed in more detail in Chapters 6 and 7.

## 3.2 FADING CHANNEL

The most important channel constraints come from the variations of mobile radio propagation. In this study, only the effects of *flat* or *non-frequency* selective fading are investigated. These effects are common to narrowband channels, in which the transmitted signal frequency spectrum is narrow enough to ensure that all the frequency components are affected in a similar way by the fading process.

Two distinct types of flat fading can be defined, namely *fast* and *slow* fading.

- Fast Fading:

Fast fading is the short term fading caused by the local scatters like buildings and other obstructions and is observed over distances of half a wavelength and less. Fades with depths of less than 20 dB occur frequently, while deeper fades of 30 dB and more appear less frequently. The mobile unit can move through several fades in a second and communication can become extremely difficult under these circumstances.

- Slow Fading:

Slow fading originates as a result of slow movement of the mobile unit, causing the particular terrain configuration to change from one form to a new configuration, over a period of several seconds and even minutes. Another form of slow fading is known as *shadowing*, which is

manifested in the form of an EM attenuation, caused by "shadowing" by hills, buildings, foliage, etc. in a mobile communications scenario.

An exact mathematical model of this type of fading is not available, but measurements indicate that the mean path loss closely fits a log-normal distribution with standard deviation that depends on the carrier frequency and environment [62].

### 3.2.1 Fading channel model

In this dissertation the effects of a Land Mobile Satellite Channel (LMSC), modeled as a non-frequency selective Rician fading channel, is considered as primary communication scenario. The received signal is a linear combination of a large number of carrier signals spread in time and frequency, each corrupted by AWGN. In typical mobile communication systems, having symbol rates of  $R_s < 20 \text{ ksymbols/s}$  (*kbaud*), the time delay spread among these signal paths is frequently a negligible fraction of the symbol duration  $T_s$ . In this fading model, two signal paths are considered, namely a Line-of-Sight (LOS) component (excluding the effects of shadowing), and a scatter component, which is modeled as Rayleigh distributed envelope [63, 30, 62]. Figure 3.4 shows a basic schematic representation of the fading model.

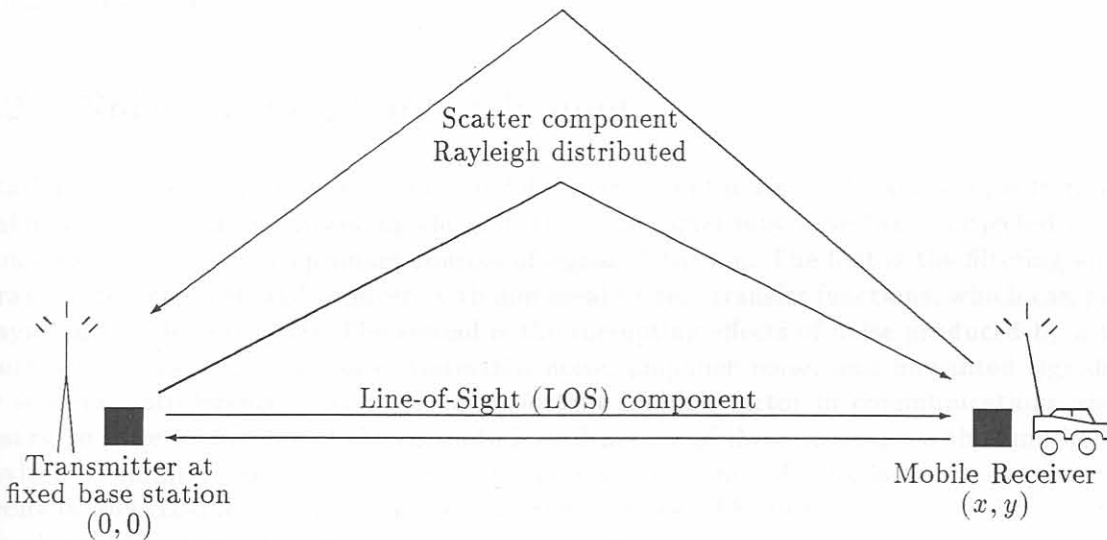


Figure 3.4: Non-frequency selective Rician fading channel model.

The amplitude of the modulated signal is multiplied by the output,  $r$  of a random process, normalised so that  $E\{r^2\} = 1$ . This is done in order to ensure that the average transmitted signal energy remains unaffected by the channel model. The latter simplification is suggested by the fading channel model proposed by Jakes [63]. The probability density function of the amplitude  $r$  may therefore be expressed as

$$\rho(r) = \frac{r}{\sigma^2} \exp\left(-\frac{r^2 + s^2}{2\sigma^2}\right) \text{I}_0\left(\frac{r s}{\sigma^2}\right) \quad (3.1)$$

where  $s^2$  denotes the average energy (power) of the direct LOS component, and  $\sigma^2$  is the average power the resultant scattered signal components. In (3.1)  $\text{I}_0(\cdot)$  is the modified Bessel function of the first kind and zero order.

Two limiting cases of special interest occur when  $\sigma^2 = 0$  (channel reduces to just an AWGN channel), and when  $s^2 = 0$  (channel is reduced to a Rayleigh fading channel). Therefore, in those cases where the direct LOS component is totally blocked out, the scatter (diffuse) component dominates and the received signal envelope exhibits a Rayleigh distribution (From (3.1)). The probability density function of the amplitude of a Rayleigh fading channel is simply given by

$$\rho(r) = \frac{r}{\sigma^2} \exp\left(-\frac{r^2}{2\sigma^2}\right) \quad (3.2)$$

However, if in addition to a portion of the reflected (scattered) signal component, the direct LOS component is also present at the receiver's antenna, the envelope of the received signal follows a Rician distribution; the channel is then called a Rician fading channel, with amplitude probability density function given by (3.1). In order to specify the characteristics of the Rician fading channel one has to define the so called Rician parameter,  $K$ . It is defined as the ratio of the power in the direct LOS to the scatter components present at the receiver, i.e.,

$$K = \frac{s^2}{2\sigma^2} \quad (3.3)$$

Thus, for a Rayleigh channel  $K = 0$ , and for the AWGN channel,  $K = \infty$ , constituting the two extremal propagation modes.

### 3.2.2 Noise in the Mobile Channel

The task facing the receiver is to retrieve the bit stream from the received waveform, with minimum probability of error, notwithstanding the distortion the signal may have been subjected to during transmission. There are two primary sources of signal distortion. The first is the filtering effects of the transmitter, channel, and receiver, with non-ideal system transfer functions, which can produce Intersymbol Interference (ISI). The second is the corrupting effects of noise produced by a variety of sources, such as galactical noise, terrestrial noise, amplifier noise, and unwanted signals from other sources (interference). Noise is an important limiting factor in communications and it is necessary to have knowledge of the magnitude and nature of these sources, so that methods may be devised to eliminate or suppress them. An unavoidable cause of noise is the thermal motion of electrons in any conducting media, known as *thermal noise*. The primary statistical characteristic of the global effects of all sources of noise is that the resultant noise amplitudes may be closely approximated by a Normal or Gaussian distribution, with probability density function (assuming zero-mean) expressed as

$$\rho(n) = \frac{1}{\sigma\sqrt{2\pi}} \exp\left[-\frac{1}{2}\left(\frac{n}{\sigma}\right)^2\right] \quad (3.4)$$

where  $\sigma^2$  is the noise variance [58, 14]. The primary spectral characteristic of white noise is that its two-sided power spectral density is flat for all frequencies of interest for the radio communication system. In other words, thermal noise, on the average, contains as much power per  $Hz$  in low-frequency fluctuations as in high-frequency fluctuations — up to a frequency of about  $10^{12}$   $Hz$ . The Additive White Gaussian Noise (AWGN) model is therefore often used to model the noise in the detection process and in the design of optimum receivers.

### 3.2.3 Mobile Channel Simulator

The block diagram of the channel simulator utilised in this study is shown in Figure 3.5, based on the model proposed by Jakes [63], implemented in software by Opperman [62].

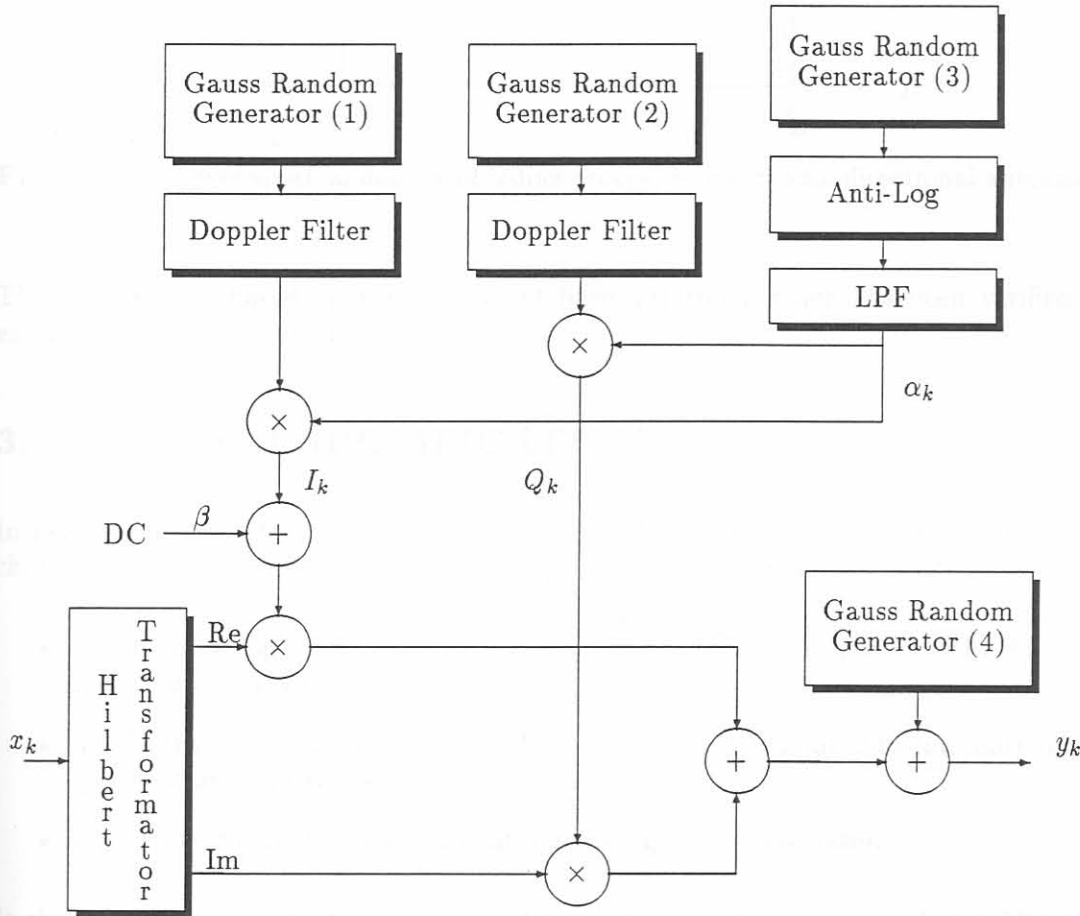


Figure 3.5: V/UHF mobile channel simulator block diagram.

The V/UHF channel simulator is capable of emulating both Rayleigh or Rician distribution envelopes with uniform phase distribution. The PSD of the foregoing, when an omnidirectional antenna is employed, is given by

$$S(f) = \begin{cases} \frac{1}{\pi\sqrt{1-(f/f_D)^2}} & |f| \leq f_D \\ 0 & \text{otherwise} \end{cases} \quad (3.5)$$

which is depicted graphically in Figure 3.6.

These characteristics can be effectively realised by a filtering process, since linear filtering of an input sequence modifies the spectrum, but not the phase and amplitude distributions of the sequence.



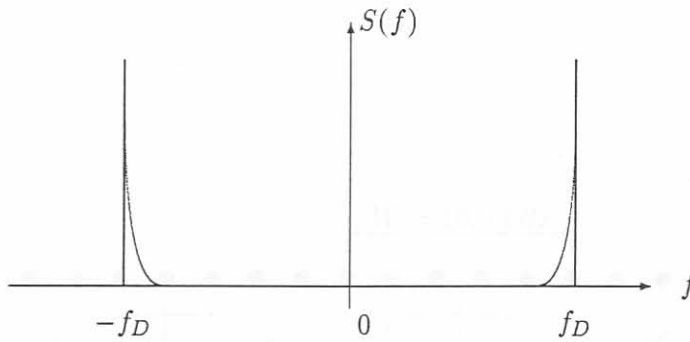


Figure 3.6: Power spectral density of fading process when an omnidirectional antenna is employed.

The simulator is based on this important basic principle, which has been verified by means of extensive computer simulation in [62].

### 3.3 SYSTEM SPECIFICATION

In general, the selection of modulation and coding formats for transmission on the mobile radio channel is based on the optimum selection of the following design parameters,

- $R_b$ , the information rate, i.e., the maximum number of bits per second achievable within an allocated channel bandwidth.
- $W$ , the transmission bandwidth in *Hertz*, usually strictly limited by international transmission specifications and radio filter limitations.
- The error probability achievable at a given signal-to-noise ratio.

It should be observed that the value of  $W$  depends on the definition of bandwidth that has been adopted for the specific application. Note that  $\eta_f$  is inevitably degraded by the presence of guard bands between adjacent channels within the allocated transmission bandwidth.

The primary limitations and specifications of the proposed Q<sup>2</sup>PSK digital V/UHF radio communication system are summarised below.

The allocated 30 *MHz* to 2.5 *GHz* frequency band covers most of the VHF and UHF frequency bands. Figure 3.7 depicts a typical multi-channel V/UHF radio channel response.

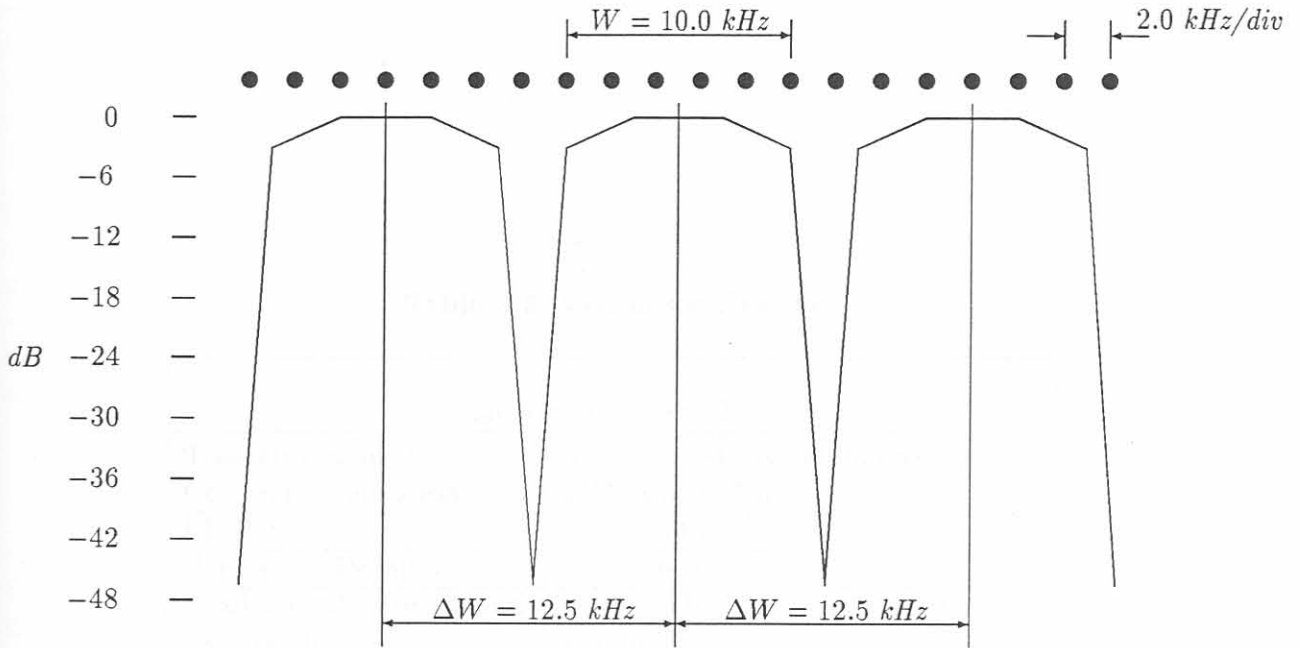


Figure 3.7: Overall radio channel response.

Table 3.1: Channel specifications

Channel characteristics	
Frequency band	VHF/UHF (30 MHz - 2.5 GHz)
Communication mode	Semi-stationary/mobile
Maximum distance	$50 \text{ km} \leq d_{max} \leq 150 \text{ km}$ (typical)
Fading	Rician and Rayleigh
Maximum Doppler	$f_D \leq 2 \text{ kHz}$ at 1.0 GHz (typical)
Expected time spread	Negligible, ( $\tau \approx 10 \mu\text{s}$ , typical)

Table 3.2: Modem specifications

Modem characteristics	
Transmission mode	Asynchronous bursts (block) data
Communication scenarios	TDMA and SFH
FH Rates	25, 50 and 100 <i>hops/s</i>
Bandwidth Definition	90% of power
Available effective channel bandwidth	$W = 10$ kHz ( $\Delta W = 12.5$ kHz channel spacing)
Maximum data rate	$R_{max} = 24$ kb/s
Samples per symbol	$I = 10, 16$ , depending on the FH rate
Symbol rate	$f_s = 5, 6$ ksymbols/s
Spectral efficiency	$\eta_f \leq 2.4$ b/s/Hz
IF subcarrier frequency	$f_{IF} = 25$ kHz
Sampling frequency	$f_{samp} = 100$ kHz
Subcarrier modulation	coherent Q <sup>2</sup> PSK
Bit Error Probability	
Uncoded	$P_b < 10^{-5}$ @ $E_b/N_o < 15.0$ dB
Coded	$P_b < 10^{-7}$ @ $E_b/N_o < 15.0$ dB
Error correction type	Convolutional Coding TCM and MTCM
Equalisation	To be determined

### 3.4 CONCLUDING REMARKS: CHAPTER 3

In order to achieve a minimum bit rate of  $f_b = 24 \text{ kb/s}$  in a V/UHF communications scenario with  $\Delta W = 12.5 \text{ kHz}$  channel spacing, a modulation technique with post-modulation bandwidth efficiency of  $\eta_f \geq 1.92 \text{ bits/s/Hz}$  is required. It will be shown in Chapter 4 that this radio response does not provide for excessive Doppler shift in a mobile communication scenario. The radio receiver will therefore have to eliminate most of the Doppler before the signal is passed on to the modem receiver. If this is not done, serious signal distortion will be caused by the misalignment of the received signal within the narrowband radio IF bandpass filters.

The proposed modem must meet the typical uncoded Bit Error Rate (BER) target specification of  $10^{-3}$  for digital speech under fading conditions. The chosen modulation method must be capable of supporting an appropriate coherent detector.  $E_b/N_o$  is the ratio of energy per bit to noise power spectral density and is the standard figure-of-merit by which digital modulation and coding schemes are compared. It is analogous to Carrier-to-Noise (C/N) ratio for analog FM modulation. Recall, the lower  $E_b/N_o$  the lower is the requirement of transmitter output power.

---

---

## CHAPTER 4

---

# DIGITAL Q<sup>2</sup>PSK — Modulation, Demodulation and Synchronisation

---

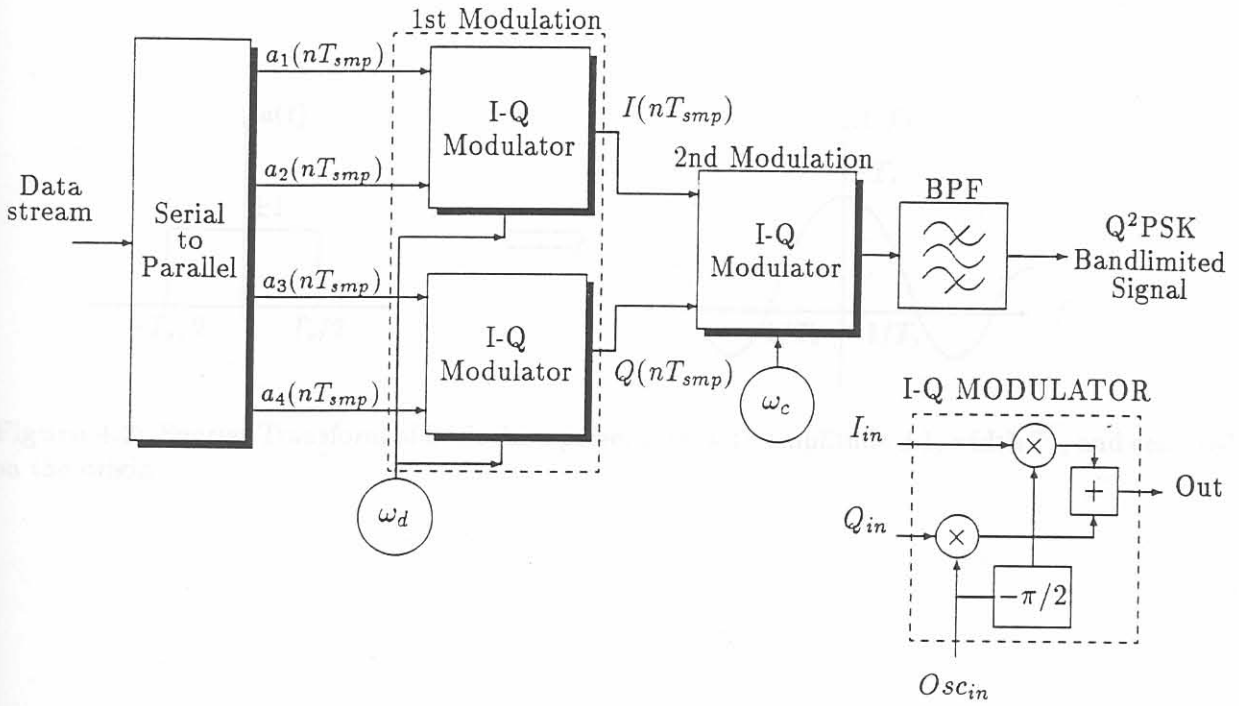
---

In this chapter the DSP design and implementation of the Q<sup>2</sup>PSK modulator, demodulator and synchronisation processes are considered. Furthermore, detail concerning the block transmission strategy adopted is presented. The different levels of synchronisation, namely carrier, symbol and frame synchronisation are considered. In addition, the sensitivity of the demodulator to phase and frequency synchronisation errors is discussed. The final part of this chapter is concerned with the analysis and design of carrier tracking algorithms. Specifically, for carrier frequency (Doppler) and phase tracking, the recursive scalar Kalman estimator is proposed and analysed. Two methods are proposed. The first method employs the Kalman estimator directly to estimate the carrier frequency information. The second method, the so-called Dual Phase and Frequency Kalman Estimator (DPFKE), employs two scalar Kalman estimators to simultaneously track both carrier frequency and phase information.

### 4.1 MODEM REALISATION

#### 4.1.1 Digital Q<sup>2</sup>PSK Modulator

The digital modulator implemented is shown in Figure 4.1 and can be viewed as two parallel quadrature modulations, followed by another quadrature modulation. The first set of modulations is related to data shaping pulses,  $q_1(t)$  and  $q_2(t)$  as defined in Chapter 2, equation (2.5). The second modulation translates the outputs of the first modulation onto quadrature carriers at a carrier frequency of  $f_c = \omega_c/2\pi$  Hz.


 Figure 4.1: Q<sup>2</sup>PSK Transmitter block diagram.

The Serial-to-Parallel (S/P) converter accepts serial data and following parallel conversion, the information bits are multiplied by the data shaping pulses, which are expressed as:

$$\begin{aligned} I(nT_{smp}) &= [a_1(nT_{smp}) - ja_2(nT_{smp})] e^{j2\pi f_d nT_{smp}} \\ Q(nT_{smp}) &= [a_3(nT_{smp}) - ja_4(nT_{smp})] e^{j2\pi f_d nT_{smp}} \end{aligned} \quad (4.1)$$

where  $\{a_i(nT_{smp})\}$  represents the discrete time signal of  $\{a_i(t)\}$  (from Chapter 2), and  $T_{smp}$  is the transmitter output sample period. In general,  $T_s = I \times T_{smp}$ , where  $T_s$  denotes the symbol duration, and  $I$  is the integer interpolation factor.

The basic data pulse, with amplitude  $\pm 1$  (each with probability one half), width  $T_s$ , and centered at the origin, is expressed as

$$a(t) = \text{rect}\left(\frac{t}{T_s}\right) = \begin{cases} \pm 1 & |t| < T_s/2 \\ 0 & |t| > T_s/2 \end{cases} \quad (4.2)$$

Letting  $A(f)$  denote the Fourier transform of  $a(t)$ , as illustrated in Figure 4.2, the first data shaping modulation process (denoted by 1st modulator in Figure 4.1), can be visualised in the frequency domain as illustrated in Figure 4.3 for the transmitted data sequence  $\{a_1, a_2, a_3, a_4\} = \{+1, +1, +1, +1\}$ . Note, that the sidelobes are omitted to facilitate easier and clearer graphical representation of  $I(nT_{smp})$  given in (4.1). An equivalent process is carried out for  $Q(nT_{smp})$ .

After the first modulations, the components of the in-phase and quadrature-phase digital signals  $I(nT_{smp})$  and  $Q(nT_{smp})$  respectively (given in (4.1)), are digitally translated by the second (2nd) modulator onto a carrier frequency,  $f_c$ . This second modulation process is visualised in the frequency domain as illustrated in Figure 4.4, resulting in the final digital modulator output  $s(nT_{smp})$ , similar to (2.8) given in Chapter 2 with  $t$  replaced by  $nT_{smp}$ . Finally, the signal generated is band-pass filtered before transmission.

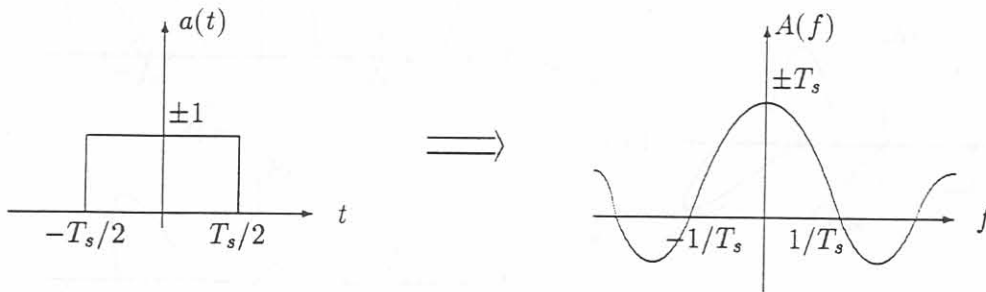


Figure 4.2: Fourier Transform of basic data pulse,  $a(t)$ ; with amplitude  $\pm 1$ , width  $T_s$ , and centered on the origin.

Figure 4.3: Visualisation of first quadrature modulation in the frequency domain, producing in-phase digital signal,  $I(nT_{smp})$ .

4.1.2 DQPSK Modulation

The in-phase and quadrature components of the signal are given by

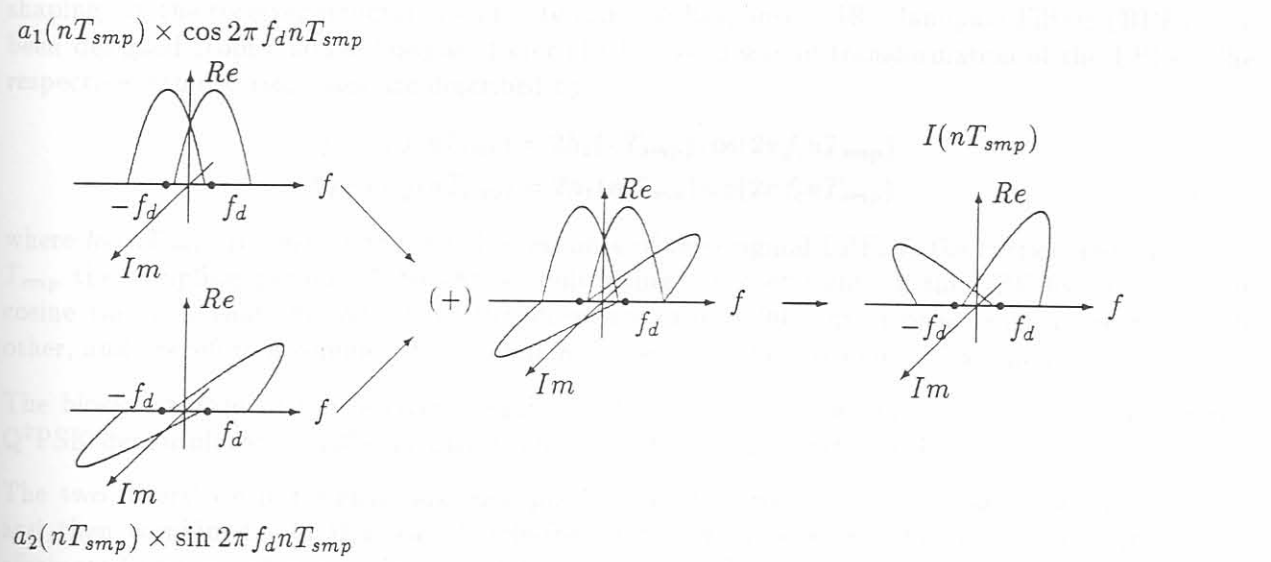


Figure 4.3: Visualisation of first quadrature modulation in the frequency domain, producing in-phase digital signal,  $I(nT_{smp})$ .

Similarly, the quadrature component is given by

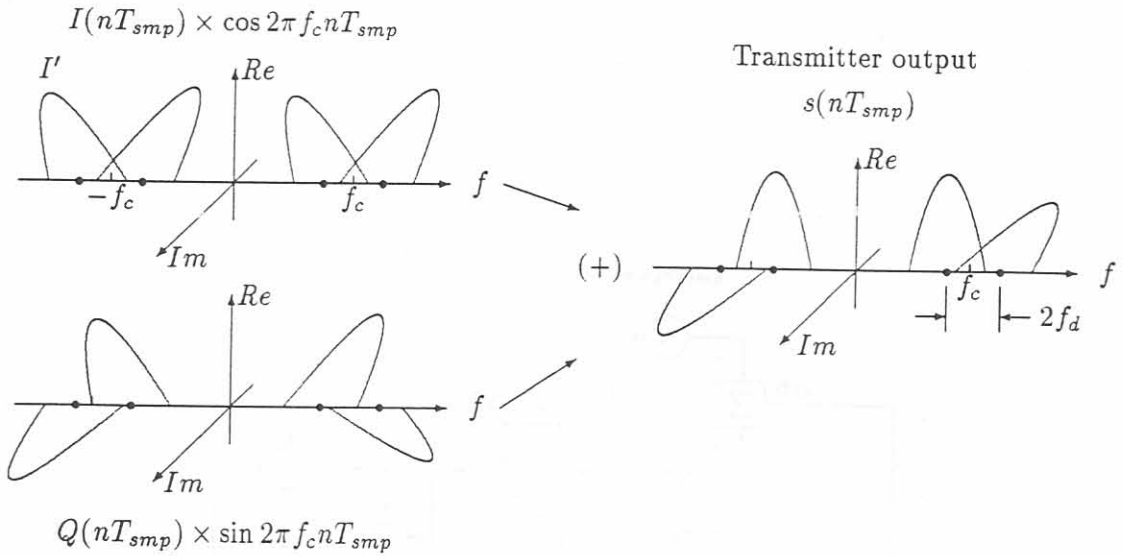


Figure 4.4: Visualisation of final modulation process in the frequency domain, producing Q²PSK transmitter output,  $s(nT_{smp})$ .

#### 4.1.2 Digital Q²PSK Demodulator

The basic structural blocks of the Q²PSK modem receiver are the input bandpass filters, the carrier,  $f_c$  demodulator, the second bank of filters and the demodulation associated with the data pulse shaping. In the receiver structure two Finite Impulse Response (FIR) Bandpass Filters (BPF) have been designed from a single Lowpass Filter (LPF), by means of transformation of the LPFs. The respective impulse responses are described by:

$$\begin{aligned} h_{BPF1,I}(nT_{smp}) &= 2h_1(nT_{smp}) \cos(2\pi f_c nT_{smp}) \\ h_{BPF1,Q}(nT_{smp}) &= 2h_1(nT_{smp}) \sin(2\pi f_c nT_{smp}) \end{aligned} \quad (4.3)$$

where  $h_1(nT_{smp})$  represents the impulse response of the original LPF,  $f_c$  the carrier frequency and  $T_{smp}$  the sampling period. A benefit of multiplying the coefficients of the LPF by the sine and cosine values is that the outputs of the filters are exactly 90° out of phase with respect to each other, and therefore a complex demodulation process may be implemented at the receiver.

The block diagram of the receiver is shown in Figure 4.5. (Note that the block diagram of the Q²PSK demodulator in [23] is incorrect, and should be as illustrated in Figure 4.5.)

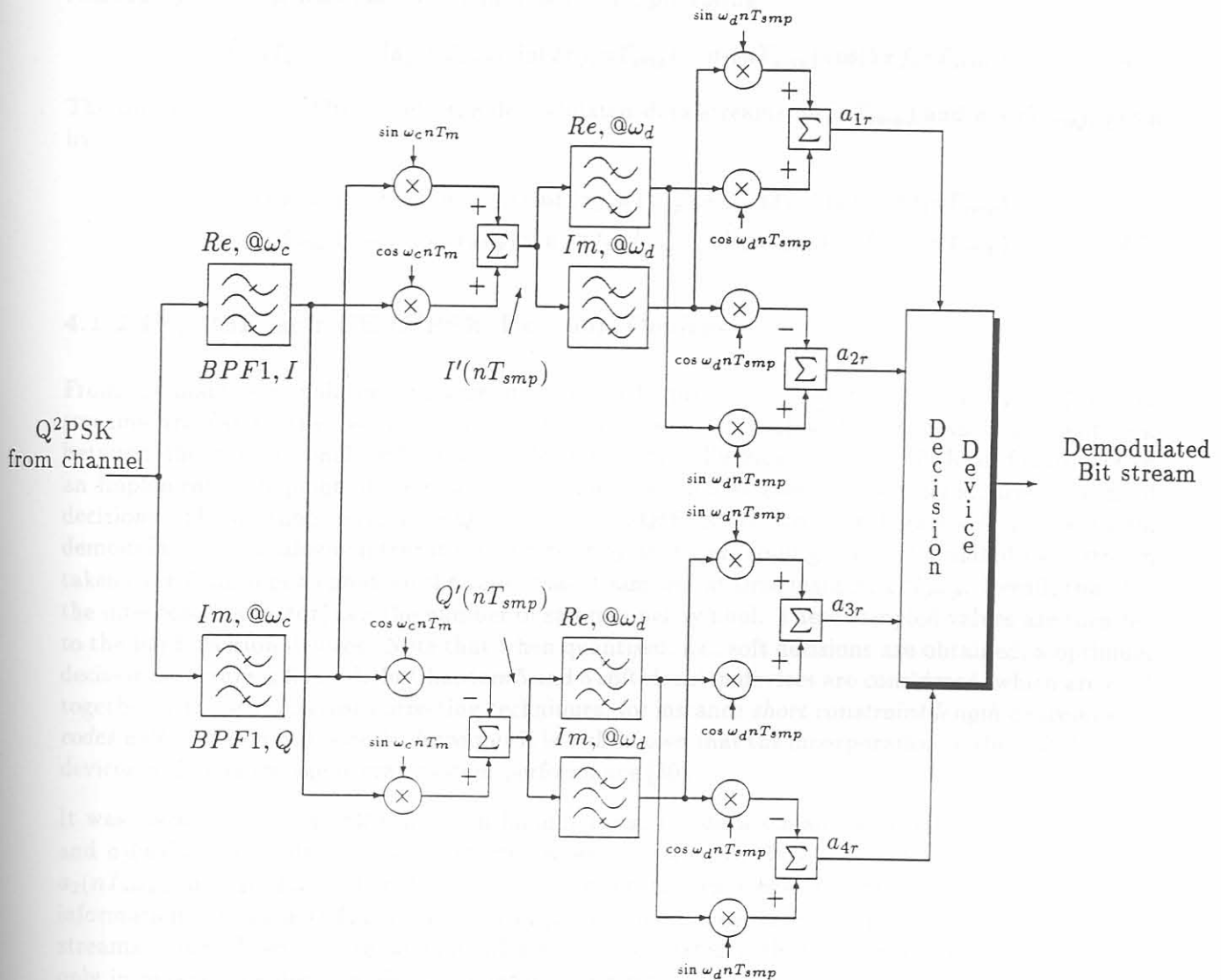
The two filters' output signals are multiplied by both a cosine and sine signal of frequency  $f_c$  and then combined. In this way double-frequency terms generated by the multiplications are eliminated and no subsequent low-pass filtering is needed to recover the baseband signals [64]. The real and imaginary components of the Q²PSK signal can be obtained by means of a single complex demodulation. The real part of the Q²PSK is given by the following expression:

$$\begin{aligned} I'(nT_{smp}) &= [a_1(nT_{smp}) - ja_2(nT_{smp})] e^{j2\pi f_d nT_{smp}} \\ &= a_1(nT_{smp}) \cos(2\pi f_d nT_{smp}) + a_2(nT_{smp}) \sin(2\pi f_d nT_{smp}) \end{aligned} \quad (4.4)$$

Similarly, the imaginary part is given by:

$$Q'(nT_{smp}) = [a_3(nT_{smp}) - ja_4(nT_{smp})] e^{j2\pi f_d nT_{smp}} \quad (4.5)$$



Figure 4.5: Q<sup>2</sup>PSK DSP based receiver block diagram

The method to recover the baseband signals  $\{a_i(nT_{smp})\}$ , from  $I'(nT_{smp})$  and  $Q'(nT_{smp})$  is to implement a new complex demodulator scheme for each quadrature signal component obtained from the carrier demodulation system. Only the demodulation of the  $I'(nT_{smp})$  given by (4.4) signal will be shown. The demodulation of the information available in  $Q'(nT_{smp})$  is obtained by identical means.

The demodulated signal  $I'(nT_{smp})$  is applied to a pairs of Hilbert Transformers (HT), which are realised by two FIR bandpass filters in quadrature, producing

$$\hat{I}'(nT_{smp}) = j[a_1(nT_{smp}) \sin(2\pi f_o nT_{smp}) - a_2(nT_{smp}) \cos(2\pi f_o nT_{smp})] \quad (4.6)$$

The outputs of these filters yield the demodulated data streams,  $a_{1r}(nT_{smp})$  and  $a_{2r}(nT_{smp})$ , given by

$$\begin{aligned} a_{1r}(nT_{smp}) &= I'(nT_{smp}) \cos(2\pi f_d nT_{smp}) + \hat{I}'(nT_{smp}) \sin(2\pi f_d nT_{smp}) \\ a_{2r}(nT_{smp}) &= I'(nT_{smp}) \sin(2\pi f_d nT_{smp}) - \hat{I}'(nT_{smp}) \cos(2\pi f_d nT_{smp}) \end{aligned} \quad (4.7)$$

#### 4.1.2.1 Q<sup>2</sup>PSK and CE-Q<sup>2</sup>PSK Decision Devices

From the main demodulator structure, depicted in Figure 4.5, the estimates  $\{a_{ir}(nT_{smp})\}_1^4$  of data streams are fed to the decision device. It is here where the only difference in implementation between the conventional Q<sup>2</sup>PSK and coded Constant Envelope (CE) Q<sup>2</sup>PSK is found. From an implementation point of view, a non-optimum decision strategy is considered, based on hard decisions. The decision devices for Q<sup>2</sup>PSK and CE-Q<sup>2</sup>PSK are shown in Figure 4.6. In the digital demodulator the analogue integrator is replaced by an adder, adding the demodulated data stream taken over  $I$  samples to produce the value that is sampled at time instant,  $kIT_{smp}$ . Recall, that  $I$  is the interpolation factor, i.e., the number of samples per symbol. These sampled values are then fed to the hard decision devices. Note that when quantised, i.e., soft decisions are obtained, a optimum decision structure is formed. In Chapters 5 and 6 soft-decision devices are considered, which are used together with forward error-correcting techniques, for instance *short constraint length convolutional codes with soft-decision Viterbi decoding*. It is well-known that the incorporation of the soft-decision devices will enhance the overall system performance [30].

It was shown in [12, 11, 23] that upon bandlimiting, the data streams associated with  $a_1(nT_{smp})$  and  $a_3(nT_{smp})$  are relatively less distorted when compared to those associated with data streams  $a_2(nT_{smp})$  and  $a_4(nT_{smp})$ . For this reason, in the constant envelope decision device, decisions about information bits in  $a_1(nT_{smp})$  and  $a_3(nT_{smp})$  are made independently from the respective data streams alone. Then, the redundant information associated with data stream  $a_4(nT_{smp})$ , is used only in making the decision about the information bits in data stream  $a_2(nT_{smp})$ . In other words, in order to make a decision about  $a_2(nT_{smp})$ , a simplifying assumption is made that  $a_1(nT_{smp})$  and  $a_3(nT_{smp})$  are decoded correctly. In his PHD thesis [12], Saha has shown that this decision is the random variable  $V$ , given by

$$V = a_{2r}(nT_{smp}) - \frac{a_1(nT_{smp})}{a_3(nT_{smp})} a_{4r}(nT_{smp}) \quad (4.8)$$

A decoder, which is optimum in the sense of minimising the probability of error, will make a  $\pm 1$  decision, depending on the sign of  $V$  ( $V \geq 0$  or  $V < 0$ ). However, information of the correct decision statistic,  $V$  is subject to the correctness of the decisions about  $a_1(nT_{smp})$  and  $a_3(nT_{smp})$ .

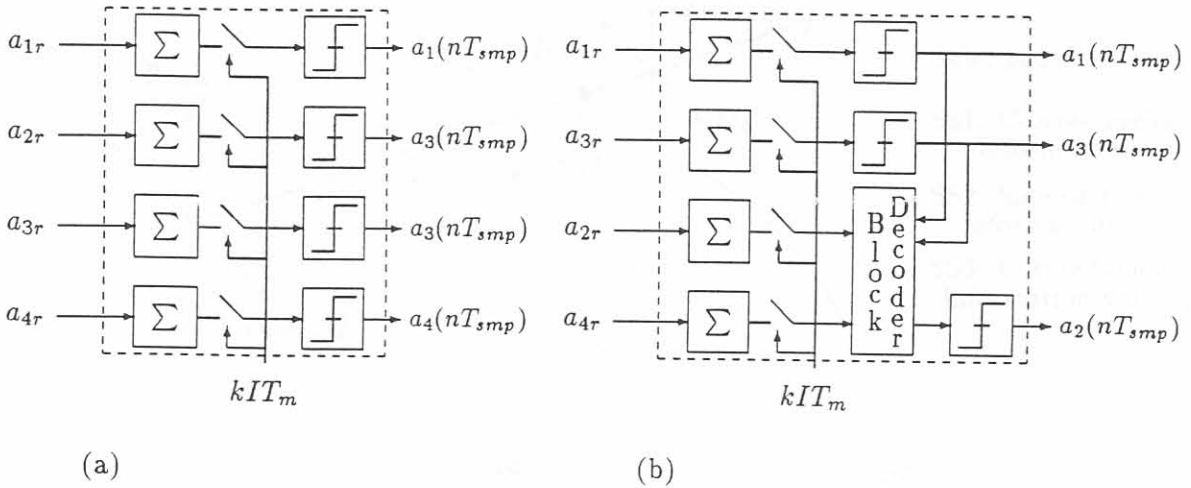


Figure 4.6: Non-optimum demodulator decision devices for (a)  $Q^2PSK$ , and (b)  $CE-Q^2PSK$ .

#### 4.1.2.2 Decoupled $Q^2PSK$ signal space

The constellation of a  $Q^2PSK$  signal consists of the vertices of a hypercube of dimension  $N = 4$  centered around the origin. The difficulty of representing a four-dimensional space leads one to decouple it into three two-dimensional (2D) subspaces, the first associated with the cosine-carrier, the second with the sine-carrier, and the third with the combination of the sine- and cosine-carrier information associated with data shaping pulse,  $q_1(t)$ , as illustrated in Figure 4.7.

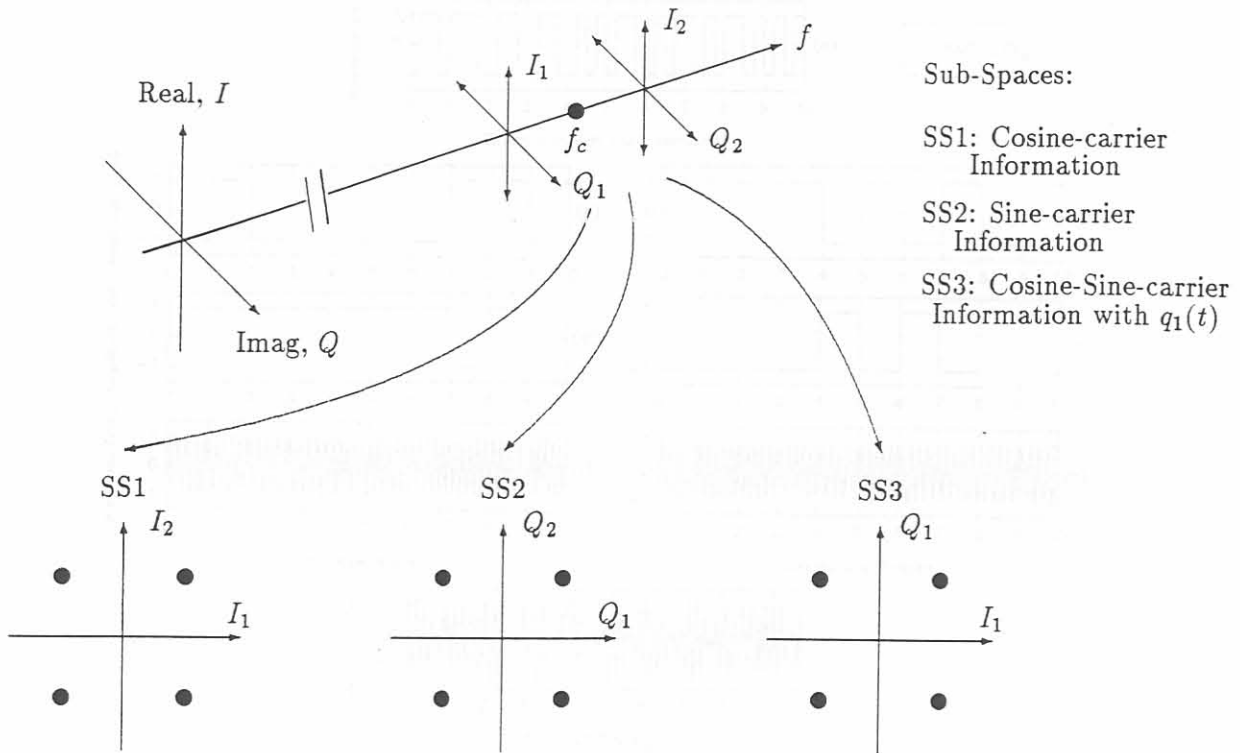
Recall, that two of the hypercube dimensions come from the orthogonality of the data shaping pulses  $q_1(t)$  and  $q_2(t)$ , and the other from the orthogonal carriers. One may therefore consider the vertices of the hypercube as the Cartesian product of two sets of biorthogonal, or 4-PSK signal points  $\{a_i\}$  and  $\{b_i\}$  [23].

The geometry of the hyper cube is, however, lost in extremely bandlimited situations, because the pulses,  $q_1(t)$  and  $q_2(t)$  chosen do not remain perfectly orthogonal under these circumstances. Alternative pulse shapes which are not affected by Intersymbol Interferences (ISI) and remain perfectly orthogonal in bandlimited situations are shown by Saha [11, 12]. However, these pulses suffer from other problems such as physical realisability. If, on the other hand, the data shaping pulses used are not minimum-bandwidth (i.e., Nyquist) signals, the modulation scheme suffers from ISI, resulting in degradation of the system performance.

#### 4.1.3 Modem waveforms and spectra

The generation of the  $Q^2PSK$  signal is illustrated in Figures 4.8, for the case where  $h = 1.0$ . It is assumed that the binary random data sequence  $\{a_n\}$ ,  $n = 1, 2, \dots$ , represented in Figure 4.8(a) as a rectangular unit pulse stream  $a_n(t)$ , is divided into four subsequences  $\{a_i\}_1^4$ . The subsequences illustrated in Figures 4.8(b) and 4.8(d) are fed to the first (upper) quadrature modulator of Figure 4.1, while subsequences illustrated in Figures 4.8(c) and 4.8(e) are fed to the bottom quadrature modulator. The final output, illustrated in Figure 4.8(h), are formed by the summation of the outputs obtained from the two quadrature modulators.

Similarly, the generation of the  $CE-Q^2PSK$  is illustrated in Figure 4.9, with the only difference

Figure 4.7: Decoupled Q<sup>2</sup>PSK signal space.

being that the original information data sequence is coded by the rate-3/4 block coder given by (2.15) to facilitate a constant envelope signal.

Figure 4.10 shows the simulated power spectral densities of unfiltered Q<sup>2</sup>PSK (CE-Q<sup>2</sup>PSK) and CP-Q<sup>2</sup>PSK, with the Intermediate Frequency (IF) chosen as 25.0 kHz. Note the faster spectral fall-off of the constant phase CP-Q<sup>2</sup>PSK system, with the latter being achieved at the expense of an increase of 25% in bandwidth requirement.

In the analysis so far, the assumption was made that the reference signal used for demodulation is perfectly frequency and phase synchronised to the transmitted signal. In a practical receiver, imperfect carrier frequency and phase results in performance degradation [65, 66]. Since the carrier recovery system forms its demodulation reference from a *noise- and interference-perturbed* version of the transmitted signal, the phase and frequency errors are random processes. This is even more prominent in SFH systems, where the large FH bandwidths may cause the FH synthesisers to lose frequency and phase coherence over successive hops. The degradation is a function of the rate of variation of the phase and frequency error over the symbol interval, and for a SFH application, over the *hop interval*,  $T_{HOP}$ .

## 4.2 BLOCK TRANSMISSION STRATEGY

As stated in paragraph 3.1.1.3, in Slow Frequency Hopped (SFH) or Time-Division Multiple Access (TDMA) applications a bursty signalling strategy is adopted, requiring that data be transmitted in short bursts or blocks, corresponding for instance with the time dwelt at each hopping frequency or time slot. Furthermore, proper synchronisation is needed to allow for any amount of timing

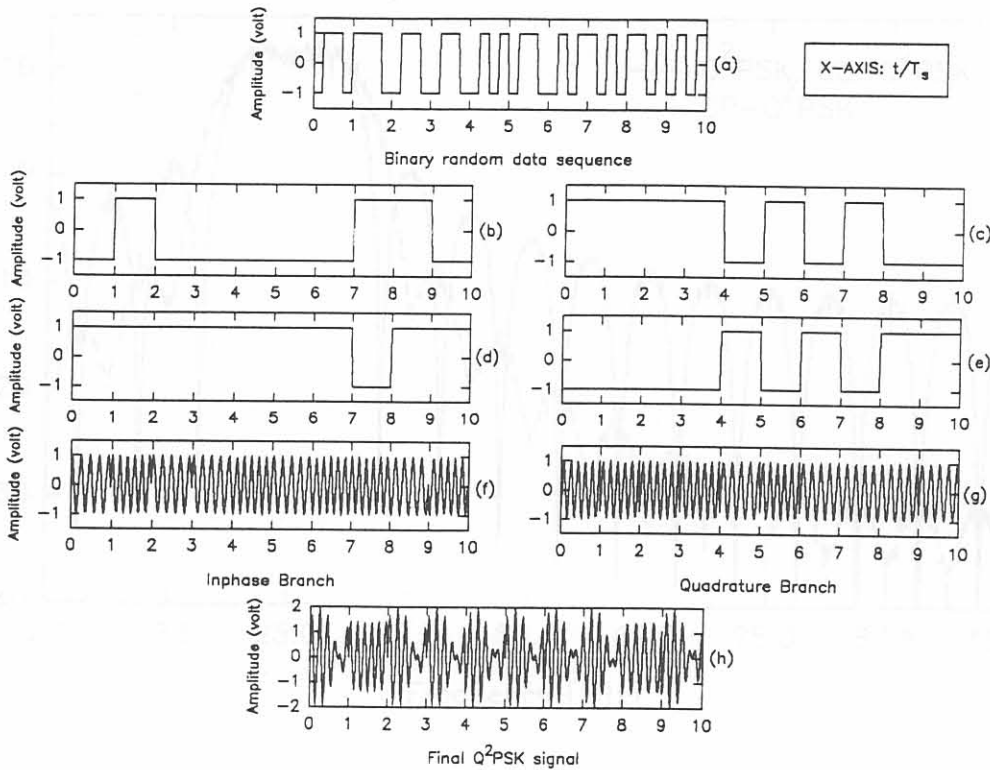


Figure 4.8: An illustrative timing diagram showing the waveforms involved in generating the  $Q^2PSK$  signal.

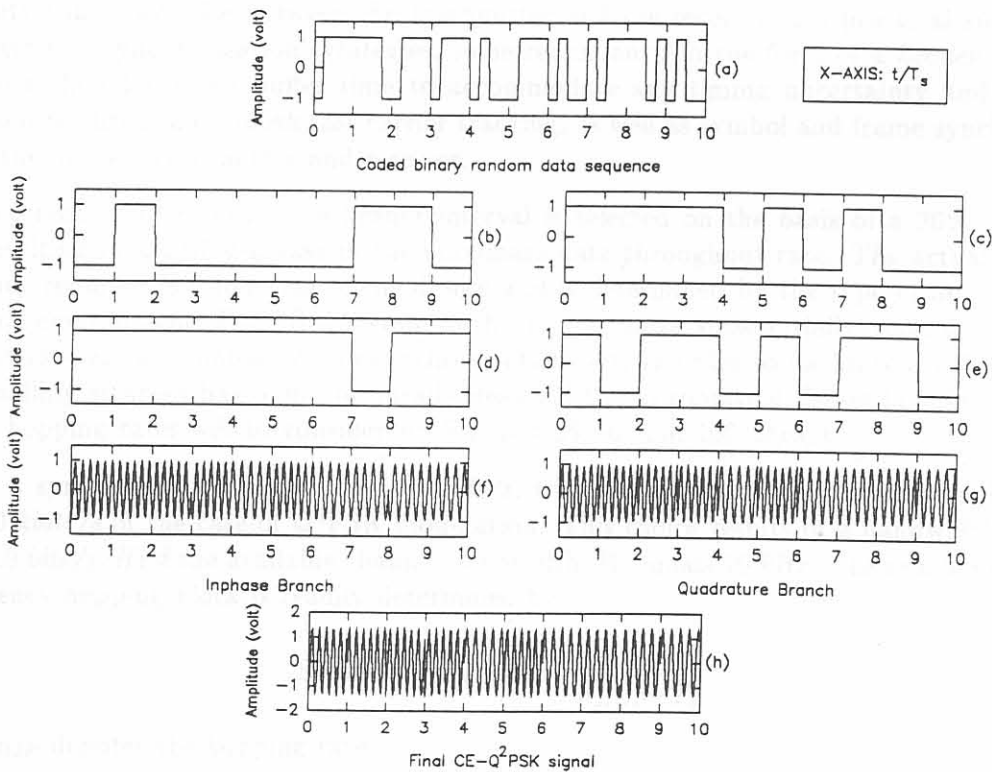


Figure 4.9: An illustrative timing diagram showing the waveforms involved in generating the  $CE-Q^2PSK$  signal.

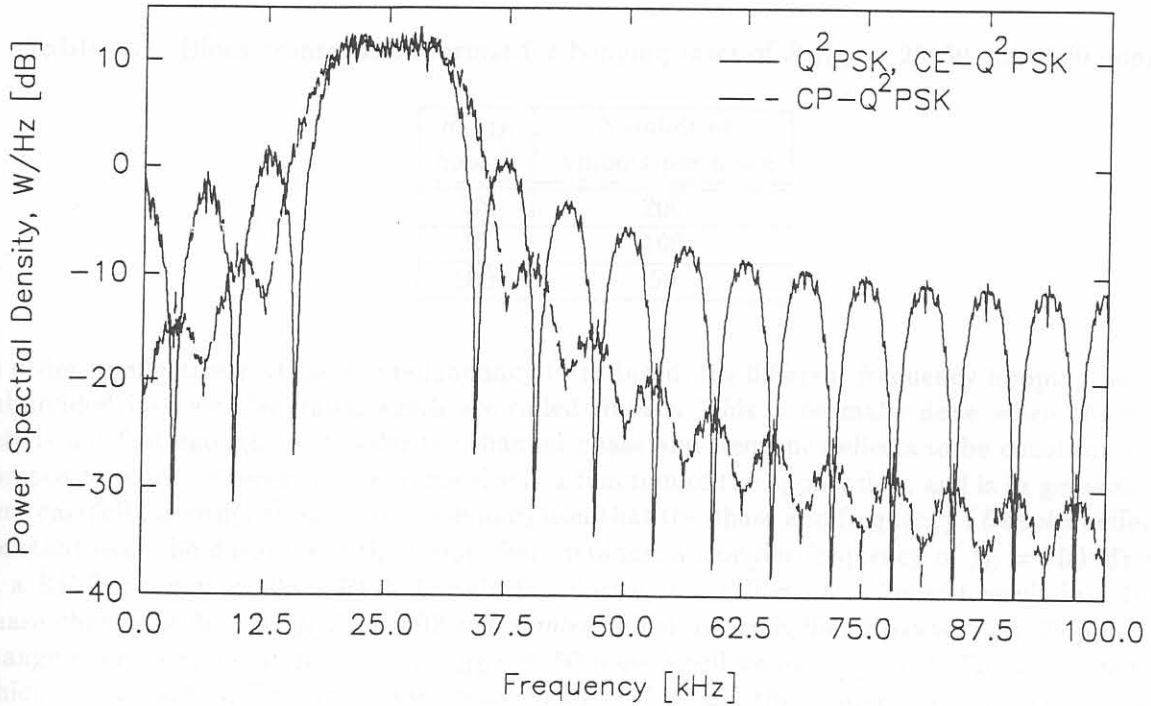


Figure 4.10: Power spectral densities of Q<sup>2</sup>PSK, CE-Q<sup>2</sup>PSK and CP-Q<sup>2</sup>PSK.

uncertainty that may arise between the transmitter and the receiver in a practical situation. To incorporate this synchronisation strategies, some redundancy in the form of a *header* is required. The header should provide buffer time to accommodate any timing uncertainty and to include information required to establish fast carrier tracking, as well as symbol and frame synchronisation between the modem transmitter and receiver.

For the current system design the header interval is selected on the basis of a 20% redundancy factor, resulting in a 20% decrease in the maximum data throughput rate. The actual amount of redundancy required is a function of the design and is determined by the type of application and operational environment. For TDMA systems this factor can be substantially lower due to the fact that all users share a common system synchronisation slot. In order to facilitate a FH system, the block signalling strategy has to be specifically designed to incorporate different hopping rates. The following hopping rates will be considered:  $R_{HOP} = 25, 50, \text{ and } 100 \text{ hops/s}$ .

Consider a symbol rate of  $R_s = 5.0 \text{ ksymbols/s}$ , which corresponds to a maximum bit rate of  $R_b = 20.0 \text{ kbits/s}$  in the case of Q<sup>2</sup>PSK modulation. This choice results in a bandwidth efficiency of  $\eta_f = 2.0 \text{ bits/s/Hz}$  if the available channel bandwidth,  $W$  equals  $10 \text{ kHz}$ . The number of symbols per frequency hopping block is readily determined by

$$\text{Symbols per Block} = \frac{1}{R_{HOP} \cdot T_s} \quad (4.9)$$

where  $R_{HOP}$  denotes the hopping rate.

For the chosen symbol rate,  $R_s$ , the symbol duration,  $T_s$  is  $200 \times 10^{-6} \text{ s}$ . The number of symbols per block can now be calculated for the different hopping rates,  $R_{HOP}$ . These are summarised in the table below.

Table 4.1: Block transmission format for hopping rates of  $R_{HOP} = 25, 50,$  and  $100 \text{ hops/s}$ .

$R_{HOP}$ <i>hops/s</i>	Number of symbols per block
25	200
50	100
100	50

In order to effectively utilise the redundancy introduced, the different frequency hopping blocks are subdivided into smaller units, which are called *frames*. This is normally done when the hopping rate is not fast enough to consider the channel phase and frequency effects to be constant over one composite block. Therefore, the frame size is a function of the application, and is in general chosen very carefully in order to support the assumption that the phase and frequency (*Doppler*) effects are constant over the duration of the frame. For instance, a Doppler frequency of  $f_D = 100 \text{ Hz}$  results at a RF frequency of  $900 \text{ MHz}$  if the vehicle velocity,  $v = 120 \text{ km/h}$ . This will result in a Doppler phase change of  $\theta_{D,T_s} = f_D T_s = 0.02 \text{ rad/symbol}$ , which is negligible. However, the Doppler phase change over an block at  $R_{HOP} = 1/T_{HOP} = 50 \text{ hops/s}$  will be  $\theta_{D,T_{HOP}} = f_D T_{HOP} = 2 \text{ rad/block}$ , which is substantial. This is however reduced by 80% if only the header interval is considered, i.e.,  $0.4 \text{ rad/header interval}$ .  $T_{HOP}$  denotes the block duration. In order to provide information about the channel to establish fast and effective synchronisation, the redundant information associated with each block, is included in each frame. The basic frame structure is shown in Figure 4.11, where  $T_H$  and  $T_D$  denote the header and data intervals respectively.

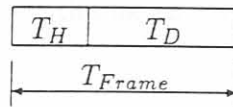


Figure 4.11: Basic frame structure.

In order to maintain the throughput rate, and to support practical header lengths of 8 and 16 symbols, it is assumed for the current design that a maximum allowable frame duration of  $T_{Frame} = 10 \text{ ms}$  and  $20 \text{ ms}$ , for the length 8 and 16 header sequences respectively. The block signalling strategy is depicted in Figure 4.12, shown for the different hopping rates,  $R_{HOP} = 25, 50,$  and  $100 \text{ hops/s}$ , utilising an 8 symbol header. Note, that an amount of "dead time" is included in the form of guard symbols, inserted at the beginning and end of the SFH signalling block. These are inserted to ensure that data will not be lost at the begin/end of the frame when a longer/shorter transmission path suddenly appears. In the situation where more than 8 symbols of header information is lost at the beginning of a block, due to multipath phenomena which causes loss of synchronisation, the loss of a total hopping frame will be inevitable.

The designs for the SFH application were extended to support two different symbols rates,  $R_s = 5.0, 6.0 \text{ ksymbols/s}$ , for the hopping rates of 25, 50, and 100 *hops/s*. These designs are summarised in Table 4.2.

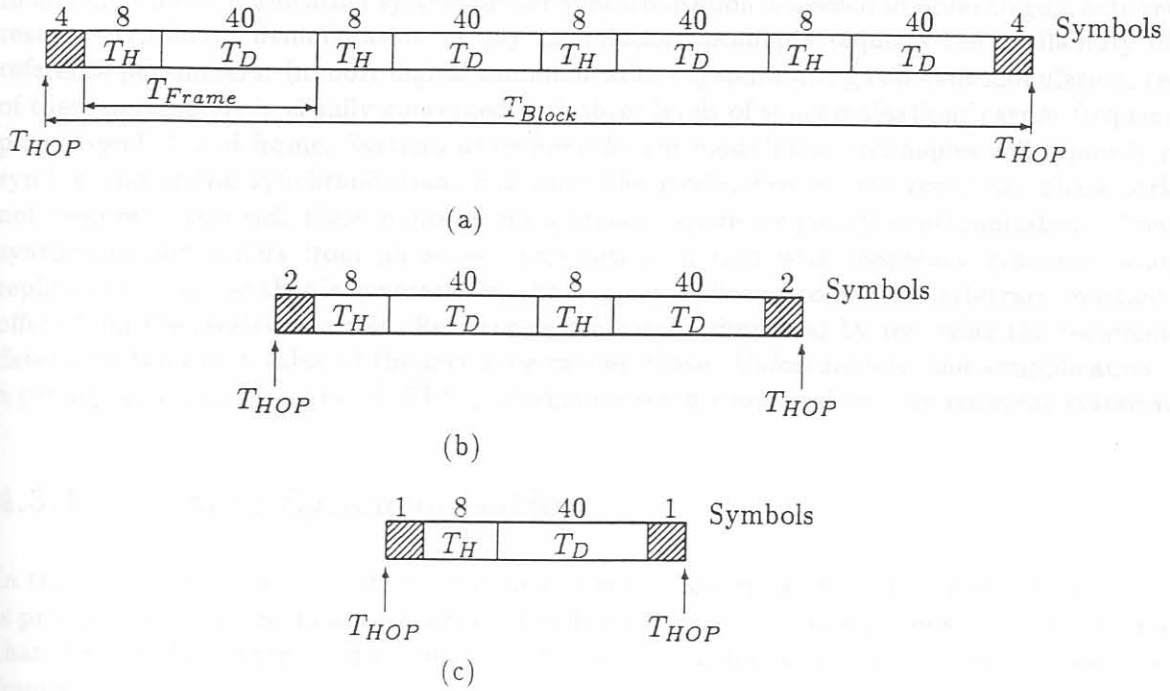


Figure 4.12: Block signalling format for symbol rate of  $R_s = 5.0$  *ksymbols/s* for the different hopping rates, (a) 25 (b) 50 (c) 100 *hops/s*, utilising an 8 symbol header.

Table 4.2: SFH design summary for hopping rates of  $R_{HOP} = 25, 50,$  and  $100$  *hops/s*.

Hopping Rate	Symbol Rate, $R_s$	Effective Bit Rate	Header Length, $L$	Symbols per Block	Symbols per Frame	Frame(s) per Block	Guard Symbols
25 <i>hops/s</i>	5.0 <i>kSymb/s</i>	16.0 <i>kbits/s</i>	8	200	40 + 8	4	8
			16	200	80 + 16	2	8
	6.0 <i>kSymb/s</i>	19.2 <i>kbits/s</i>	8	240	48 + 8	4	16
			16	240	96 + 16	2	16
50 <i>hops/s</i>	5.0 <i>kSymb/s</i>	16.0 <i>kbits/s</i>	8	100	40 + 8	2	4
			16	100	80 + 16	1	4
	6.0 <i>kSymb/s</i>	19.2 <i>kbits/s</i>	8	120	48 + 8	2	8
			16	120	96 + 16	1	8
100 <i>hops/s</i>	5.0 <i>kSymb/s</i>	16.0 <i>kbits/s</i>	8	50	40 + 8	1	2
			16	50	—	—	—
	6.0 <i>kSymb/s</i>	19.2 <i>kbits/s</i>	8	60	48 + 8	1	4
			16	60	—	—	—



### 4.3 Q<sup>2</sup>PSK SYNCHRONISATION

In any digital communication system proper synchronisation is needed in order to guarantee efficient results. Optimum demodulation of any modulation technique requires the availability of some reference parameters. In most digital communications systems using coherent modulation, recovery of these parameters is usually concerned with three levels of synchronisation: carrier frequency and phase, symbol, and frame. Systems using noncoherent modulation techniques will typically require symbol and frame synchronisation, but since the modulation is not coherent, phase locking is not required. Instead, these noncoherent systems require frequency synchronisation. Frequency synchronisation differs from phase synchronisation in that with frequency synchronisation, the replica of the carrier that is generated by the receiver is allowed to have an arbitrary constant phase offset from the received carrier. Receiver design can be simplified by removing the requirement to determine the exact value of the incoming carrier phase. Unfortunately, this simplification causes a penalty in terms of degraded BER performance when compared to fully coherent systems.

#### 4.3.1 Frame Synchronisation

In this section a novel multidimensional double complex correlation frame synchronisation strategy is proposed for Q<sup>2</sup>PSK. In asynchronous (burst) communication applications, e.g. FH, it is required that the data be transmitted in bursts or frames corresponding to the time spent at each hopping frequency.

The frame synchronisation procedure is closely related to the radio FH process. It is assumed that appropriate control signals are provided by the radio receiver to signify the start and end of the hopping sequence at each hopping frequency. Although these signals could be used to control the modem data block transmission process at every hopping frequency, it was decided to derive an independent Frame Synchronisation control signal from a special header preceding the data block in the block transmission scheme proposed in section 4.2.

In traditional quadrature modems, for instance QPSK, a single complex correlation is performed, requiring a relatively long correlation sequence to keep the probability of false detection low. In 4D Q<sup>2</sup>PSK, by exploiting the multidimensional signal space effectively, shorter correlation sequences can be used by performing two complex correlations to achieve the same probability of false detection. The delay introduced by this synchronisation strategy will be less than that resulting from a single long correlation sequence. Furthermore, since the complexity of the synchronisation procedure is proportional to the length of the codeword sequences, the complexity of the double complex correlation process will be comparable to a single long correlation process.

In an attempt to utilise the available dimensions within the Q<sup>2</sup>PSK signal space effectively, a novel frame synchronisation procedure is proposed using two synchronisation sequences or codewords, which are included as the header of each message frame [60]. The synchronisation sequences are selected from a family of complex correlation sequences of equal length  $L$ , exhibiting perfect periodic and near-perfect aperiodic correlation characteristics [67, 68]. From equation (2.8) binary data sequences  $a_1$  and  $a_4$  are used to form the real and imaginary parts of the first correlation sequence  $X_{14} = a_1 + ja_4$ , while data sequences  $a_2$  and  $a_3$  are used to form the real and imaginary parts of the second correlation sequence  $X_{23} = a_2 + ja_3$ . Each complex sequence occupies one distinct pair of two available pairs of dimensions within the Q<sup>2</sup>PSK signal space. By using all available dimensions of the Q<sup>2</sup>PSK signal space a form of synchronisation diversity is introduced

whereby a significant frame synchronisation improvement can be gained relative to existing (2D) QPSK techniques.

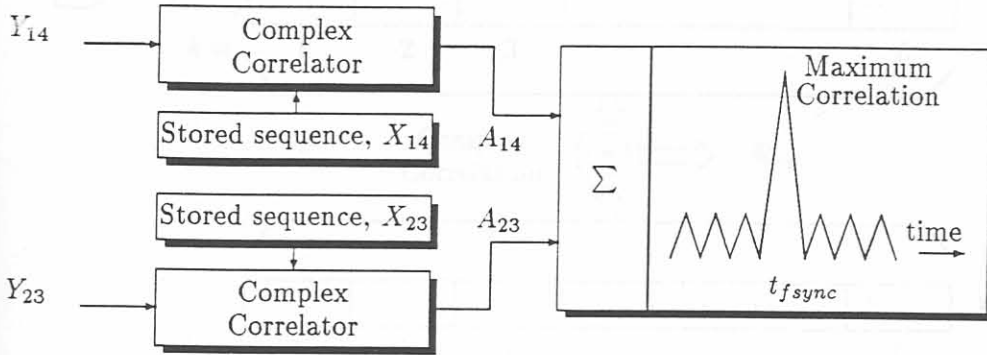


Figure 4.13: Proposed Q<sup>2</sup>PSK frame synchronisation procedure.

The proposed Q<sup>2</sup>PSK frame synchronisation procedure is illustrated in Figure 4.13. Two complex correlations are performed between the received (possibly distorted)  $S$  times oversampled synchronisation sequences,  $Y_{pq}$  and one sample per symbol local replicas of the reference sequences,  $X_{pq}$ , respectively, where  $p \in \{1, 2\}$  and  $q \in \{3, 4\}$ . The complex correlation processes yield  $S$  complex correlation outputs  $\Re_{pq}(n, i)$ ,  $i = 1, 2, \dots, S$ , where  $i$  denotes the sampling index and  $n = 1, \dots, N$  is the range in symbol periods over which the optimum correlation peak is sought, starting from symbol interval  $n = 1$  to typically  $N = L$ .

The complex correlation procedure illustrated in Figure 4.14 produces the following output sequences:

$$\Re_{pq}(n, i) = E[X_{pq}^* Y_{pq}] = \Re_{pq}^R(n, i) + j \Re_{pq}^I(n, i) \quad (4.10)$$

with  $p \in \{1, 2\}$ ,  $q \in \{3, 4\}$  and  $j = \sqrt{-1}$ , where

$$\begin{aligned} \Re_{pq}^R(n, i) &= \sum_{k=1}^L [X_{pq}^R(k)Y_{pq}^R(k+n, i) + X_{pq}^I(k)Y_{pq}^I(k+n, i)] \\ \Re_{pq}^I(n, i) &= \sum_{k=1}^L [X_{pq}^R(k)Y_{pq}^I(k+n, i) - X_{pq}^I(k)Y_{pq}^R(k+n, i)] \\ &p \in \{1, 2\}, q \in \{3, 4\}; \\ &i = 1, \dots, S, \text{ and } n = 1, \dots, N \end{aligned} \quad (4.11)$$

where  $R$  and  $I$  denote the real and imaginary parts of the complex sequences, respectively.

Note that the reference sequences' samples  $X_{pq}(k)$  are spaced by the symbol period  $T_s$ , whereas the received sequences  $Y_{pq}(k)$  are  $S$  times oversampled, as illustrated in Figure 4.14.

The magnitudes of the correlator outputs, denoted by  $A_{pq}(n, i)$  are given by:

$$\begin{aligned} A_{pq}(n, i) &= \sqrt{[\Re_{pq}^R(n, i)]^2 + [\Re_{pq}^I(n, i)]^2} \\ \text{where } &i = 1, \dots, S \text{ and } n = 1, \dots, N \end{aligned} \quad (4.12)$$

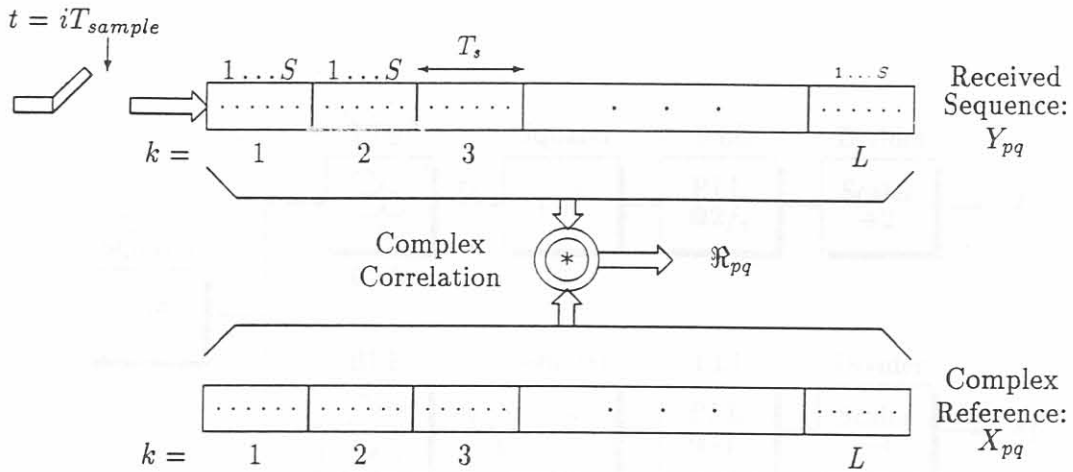


Figure 4.14: Complex correlator block diagram.

The resulting magnitudes are summed to produce the correlation magnitude,  $A(n, i) = A_{14}(n, i) + A_{23}(n, i)$ . By comparing these magnitudes to a fixed threshold, the optimum symbol and frame synchronisation instant  $t_{fsync}$  is obtained as that sampling instant  $i_m = i$  within the symbol period corresponding with  $n = n_{opt} \in \{1, 2, \dots, N\}$  producing the maximum correlation peak. In this way frame and symbol synchronisation are obtained to within  $1/S$  of a symbol period  $T_s$ . The optimum symbol samples for the rest of the FH frame are obtained by incrementing the sampling index  $i$  by  $S$ , starting from  $i_m = t_{fsync}$ , expressed as  $t_o = t_{fsync} + (i_m - 1)T_s$ .

In addition, the carrier phase rotation,  $\theta_o$ , can be obtained from

$$\theta_o = \theta_o(i_m) = \arctan \left[ \frac{\Re_{pq}^R(n, i)}{\Re_{pq}^I(n, i)} \right] \quad (4.13)$$

It is assumed that the initial phase change is set to zero, so that any other value of  $\theta_o$  corresponds to the carrier phase offset induced by the channel.

### 4.3.2 Carrier and Symbol Synchronisation

Since Q<sup>2</sup>PSK, and its constant envelope counterpart utilise all the available signal space dimensions, non-coherent operation is not feasible. For coherent or matched filter detection one needs to have carrier phase and clock timing information. As in an MSK receiver, the Q<sup>2</sup>PSK timing information is also derived from the received signal itself. The self-synchronising property of Q<sup>2</sup>PSK is most easily explained by reference to Sunde's FSK. The timing information signals are derived from the Q<sup>2</sup>PSK modulated signal by a nonlinear operation, such as a frequency doubler (squaring), and appropriate filtering.

In 1989 Saha proposed a carrier synchronisation procedure for Q<sup>2</sup>PSK signals, based on traditional carrier recovery methods utilising nonlinear squaring devices, filters and Phase Locked Loops (PLL). A variation of Saha's synchronisation scheme was analysed by De Gaundenzi [55], employing a fourth power generator device instead of a square device. A detailed diagram of the Saha synchronisation circuit for Q<sup>2</sup>PSK and CE-Q<sup>2</sup>PSK are shown in Figures 4.15 and 4.16.

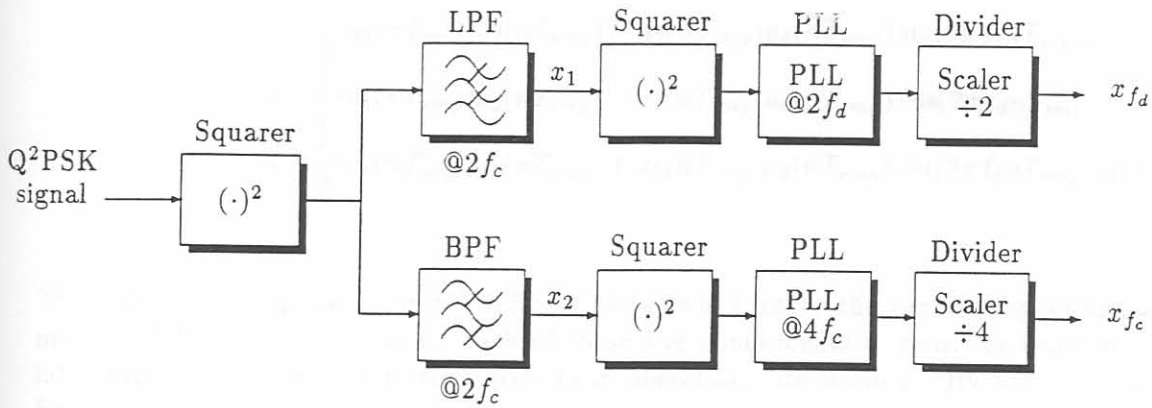


Figure 4.15: Saha synchronisation circuit for Q<sup>2</sup>PSK.

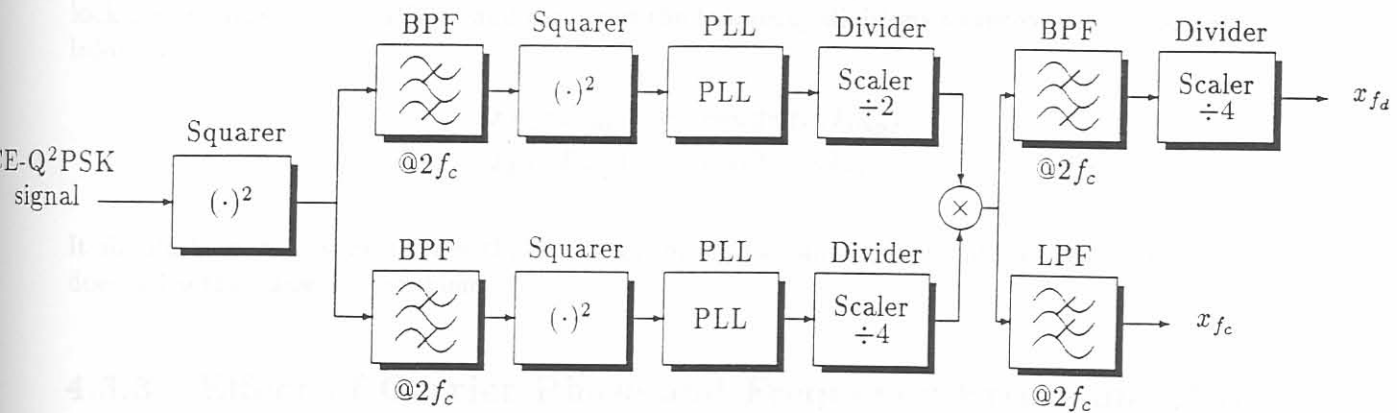


Figure 4.16: Saha synchronisation circuit for CE-Q<sup>2</sup>PSK.

If the sampled Q<sup>2</sup>PSK signal is passed through a squaring device, one obtains the following signal

$$\begin{aligned}
 s_{Q^2PSK}^2(nT_{smp}) &= 1 + \frac{1}{2}(a_1(nT_{smp})a_2(nT_{smp}) + a_3(nT_{smp})a_4(nT_{smp}) \sin(2\pi f_d nT_{smp})) \\
 &+ \frac{1}{2}(a_1(nT_{smp})a_2(nT_{smp}) - a_3(nT_{smp})a_4(nT_{smp}) \sin(2\pi f_d nT_{smp}) \cos(4\pi f_c nT_{smp})) \\
 &+ \frac{1}{2}(a_1(nT_{smp})a_3(nT_{smp}) + a_2(nT_{smp})a_4(nT_{smp}) \sin(4\pi f_c nT_{smp})) \\
 &+ \frac{1}{2}(a_1(nT_{smp})a_3(nT_{smp}) - a_2(nT_{smp})a_4(nT_{smp}) \cos(2\pi f_d nT_{smp}) \sin(4\pi f_c nT_{smp})) \\
 &+ \frac{1}{2}(a_1(nT_{smp})a_4(nT_{smp}) + a_2(nT_{smp})a_3(nT_{smp}) \sin(2\pi f_d nT_{smp}) \sin(4\pi f_c nT_{smp}))
 \end{aligned} \tag{4.14}$$

There are five components on the RHS of (4.14) which carry the required synchronisation information. The expected value of each of these five components is zero. In order to recover the information, filtering and further non-linear operations are needed. By lowpass and bandpass filtering of the squared signal, one may construct the two signals  $x_1(t)$  and  $x_2(t)$ , given by:

$$x_1(nT_{smp}) = \frac{1}{2}(a_1(nT_{smp})a_2(nT_{smp}) + a_3(nT_{smp})a_4(nT_{smp}) \sin(4\pi f_d nT_{smp})) \tag{4.15}$$

$$x_2(nT_{smp}) = \frac{1}{2}(a_1(nT_{smp})a_3(nT_{smp}) + a_2(nT_{smp})a_4(nT_{smp}) \sin(4\pi f_c nT_{smp})) \tag{4.16}$$

After squaring and taking the expectation (average), one obtains

$$E\{x_1^2(nT_{smp})\} = \frac{1}{4}(1 - \cos 4\pi f_d nT_{smp}) \tag{4.17}$$

$$E\{x_2^2(nT_{smp})\} = \frac{1}{4}(1 - \cos 8\pi f_c nT_{smp}) \tag{4.18}$$

Thus, on average,  $x_1^2(t)$  and  $x_2^2(t)$  contain spectral lines at  $2f_d$  and  $4f_c$ . One can use these lines to lock phase-locked loops (PLLs) and carry out the frequency divisions to recover the synchronisation information as

$$x_{f_d}(nT_{smp}) = \cos(2\pi f_d nT_{smp}) \tag{4.19}$$

$$x_{f_c}(nT_{smp}) = \cos(2\pi f_c nT_{smp}) \tag{4.20}$$

It should be noted, that neither the circuit proposed by Saha, nor the proposed by De Gaundenzi, does solve the hang-up<sup>1</sup> problem.

### 4.3.3 Effect of Carrier Phase and Frequency Errors on BER

Lets consider the effect of an imperfect carrier recovery, due to Doppler and channel effects, on the BEP performance of the Q<sup>2</sup>PSK demodulator. The effect of bandwidth-limiting will, however, not be taken into account. In other words it is assumed that the IF receiver bandpass filter has a wide enough bandwidth so that the received signal is not appreciably distorted.

<sup>1</sup>Hang-up is defined as the prolonged dwelling at large phase errors.

In order to evaluate the effect of static phase error,  $\theta_e$  and static frequency error,  $f_e$ , the channel input signal,  $s_{Q^2PSK}(t)$  to the demodulator is mixed with the "coherent" references at the IF carrier frequency,  $f_c$ , resulting in the synchronisation information given in (4.19) and (4.20) to be modified to

$$\begin{aligned} x_{f_d}(nT_{smp}) &= \cos(2\pi(f_c + f_e)nT_{smp} + \theta_e) \\ x_{f_c}(nT_{smp}) &= \cos(2\pi(f_c + f_e)nT_{smp} + \theta_e) \end{aligned} \quad (4.21)$$

The effect of the static carrier phase error,  $\theta_e$ , is considered, by eliminating the frequency error component,  $f_e$  from (4.21). Assuming the non-optimum integrate-and-dump decision device for Q<sup>2</sup>PSK depicted in Figure 4.6(a), the expression for average BEP conditioned on a fixed value of phase error  $\theta_e$ , is found to be [55]:

$$\begin{aligned} P_e(\theta_e) &= \frac{1}{2} \left\{ Q \left[ (\cos \theta_e + \sin \theta_e) \sqrt{2 \frac{E_b}{N_o}} \right] \right. \\ &\quad \left. + Q \left[ (\cos \theta_e - \sin \theta_e) \sqrt{2 \frac{E_b}{N_o}} \right] \right\} \end{aligned} \quad (4.22)$$

where  $E_b$  denotes the average transmitted energy per bit. Assuming a Tikhonov-distributed phase error [56, 30] the value of the average BEP of the demodulator for a given phase error variance  $\sigma_{\theta_e}^2$  is given as

$$P_e = \frac{2}{\pi I_o \left( \frac{1}{16\sigma_{\theta_e}^2} \right)} \int_{-\pi/4}^{\pi/4} \exp \left( -\frac{\cos 4\theta_e}{16\sigma_{\theta_e}^2} \right) P_e(\theta_e) d\theta_e \quad (4.23)$$

For a discrete carrier synchronisation loop, the Tikhonov PDF is given by

$$\rho(\phi) = \begin{cases} \frac{\exp(\rho \cos M\phi)}{(2\pi/M)I_o(\rho)} & |\phi| \leq \pi/M \\ 0 & \text{otherwise} \end{cases} \quad (4.24)$$

where  $\rho$  is the SNR in the system bandwidth.  $M$  is the number of phases for a  $M$ -phase Costas loop, and  $M = 1$  for PLL-type synchronisers.

Figure 4.17 illustrates the BEP curves of the receiver in the presence of the Tikhonov-distributed phase errors. Note that  $\sigma = \sigma_{\theta_e}$ , is the phase error variance. From these curves the sensitivity of the Q<sup>2</sup>PSK signal with respect to imperfect carrier references can be deduced. A possible explanation of this behavior is that the effect of a phase misalignment on the Q<sup>2</sup>PSK signal is two-fold. On one side the timing error induces adjacent-symbol interference, and on the other hand, the error on the initial phase of the demodulation subcarriers produces a *loss in orthogonality* between the data symbols. All these effects produces excess crosstalk between the parallel data streams, resulting in a degradation in BER noticeable in the graphs of Figure 4.17.

#### 4.3.4 Kalman Phase and Frequency Estimation

The first step after frame and symbol synchronisation has been obtained, is to establish the magnitude of any phase and frequency offset that may be present in the received Q<sup>2</sup>PSK modem signal.

A feed-forward, DSP based frequency estimation strategy for channels with both frequency and phase uncertainty, will be presented, based on the techniques presented in [69, 70]. The proposed

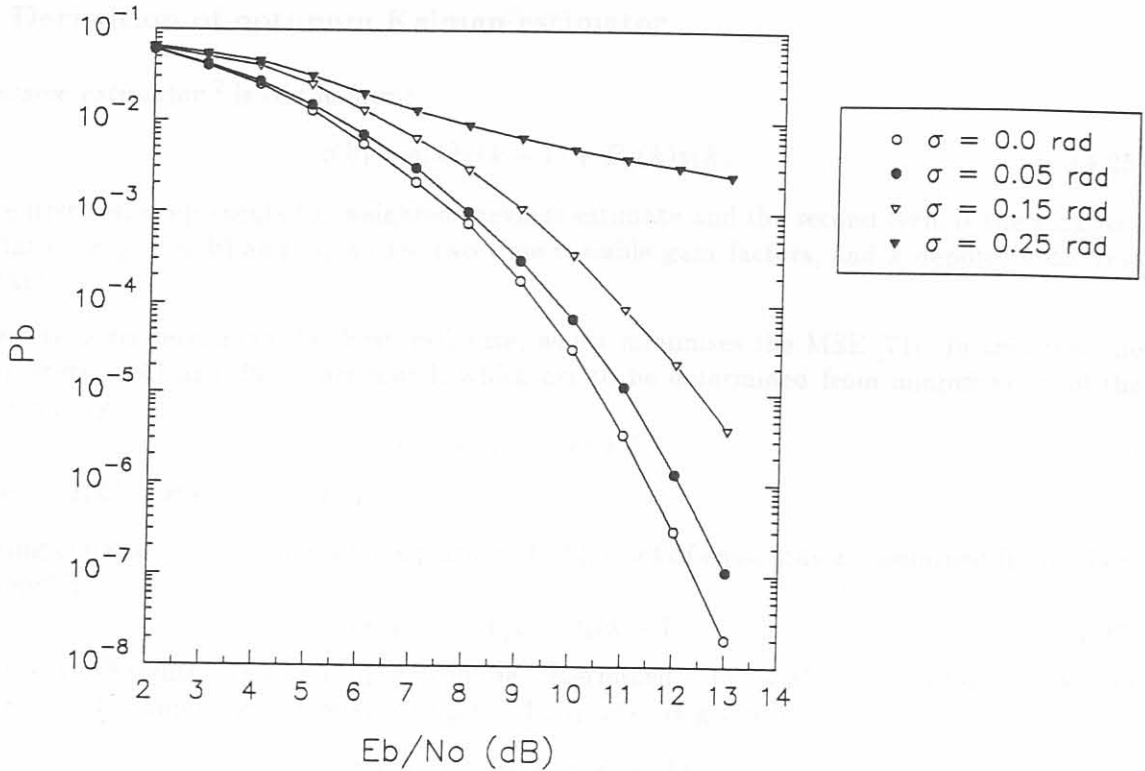


Figure 4.17: BEP sensitivity of Q<sup>2</sup>PSK to a Tikhonov-distributed phase error.

method is ideally suitable for application in burst-mode communications, where rapid acquisition is required.

Kalman filters have been used for applications in the signal processing field, when very fast identification or estimation of parameters is needed. It is known that the Kalman filter is a minimum Mean Square Error (MSE) estimator when the received signal is contaminated by Gaussian noise, and the observables and the parameters to be estimated are linearly related.

In this section two different, but indeed similar, phase and frequency correction procedures will be analysed.

Firstly the derivation of a optimum Scalar Kalman Estimator (SKE) is considered, which is capable of estimating a scalar time-varying process. In the following section a carrier phase and frequency correction strategy is introduced, which first of all eliminates the phase error and then tracks the frequency information with the derived SKE. In general, a tracking mechanism that unwraps the phase modulated incoming signal before attempting to estimate the unknown phase offset, may result in a better phase estimator than the one that estimates the phase information too. Finally, a dual phase and frequency tracking mechanism, based on the method of Kim [69], will be analysed. For both these correction strategies a step-by-step procedure will be presented.

#### 4.3.4.1 Derivation of optimum Kalman estimator

The *recursive estimator*<sup>2</sup> is of the form:

$$\hat{x}(k) = a(k)\hat{x}(k-1) + B_k(k)y(k) \quad (4.25)$$

where the first term represents the weighted previous estimate and the second term is the weighted current data sample.  $a(k)$  and  $B_k(k)$  are two time-variable gain factors, and  $k$  denotes a discrete time instant.

The objective is to determine the 'best' estimate, which minimises the MSE [71]. In this case the two parameters,  $a(k)$  and  $B_k(k)$  are found, which are to be determined from minimisation of the MSE,  $\epsilon$ , given by

$$\epsilon = p(k) = E[e^2(k)] \quad (4.26)$$

where  $e(k) = \hat{x}(k) - x(k)$  is the error.

Substituting equation (4.25) for  $\hat{x}(k)$  in equation (4.26), a set of equations are obtained from which the relationship

$$a(k+1) = A[1 - B_k(k+1)] \quad (4.27)$$

between the coefficients  $a(k)$  and  $B_k(k)$  can be determined. In (4.27),  $A$  denotes the system parameter [71]. By applying this relationship to (4.25),  $\hat{x}(k)$  is given by

$$\hat{x}(k) = A\hat{x}(k-1) + B_k(k)[y(k) - A\hat{x}(k-1)] \quad (4.28)$$

The first term,  $A\hat{x}(k-1)$ , represents the best estimate of  $\hat{x}(k)$  without any additional information, and it is therefore a *prediction* based on past observations. The second term is a *correction* term depending on the difference between the new data sample and the observation estimate,  $\hat{x}(k) = A\hat{x}(k-1)$ , multiplied with a variable gain factor,  $B_k(k)$ .

The realisation of equation (4.28) is depicted in Figure 4.18.

Derivation of expressions for  $B_k(k)$  and  $p(k)$  are derived in [71]. These expressions are repeated here for sake of convenience:

The variable Kalman gain factor

$$\begin{aligned} B_k(k) &= \frac{p(k-1)}{p(k-1) + \sigma_v^2} \\ &= \frac{1}{1 + \sigma_v^2/p(k-1)} \end{aligned} \quad (4.29)$$

and the MSE,

$$p(k) = \sigma_v^2 \cdot B_k(k) \quad (4.30)$$

where  $\sigma_v^2$  denotes the noise variance (or power). Finally, equations (4.28), (4.29) and (4.30) constitute a complete computationally viable estimation algorithm. Substituting  $\theta_I(k)$  for  $y(k)$ , the current input sample, and  $\hat{\theta}(k)$  for  $\hat{x}(k)$ , the best estimate, this estimator can be summarised as follows:

- Estimate over one symbol period:

$$\hat{\theta}(k) = \hat{\theta}(k-1) + B_k(k) [\theta_I(k) - \hat{\theta}(k-1)] \quad (4.31)$$

<sup>2</sup>Also known as recursive filter.



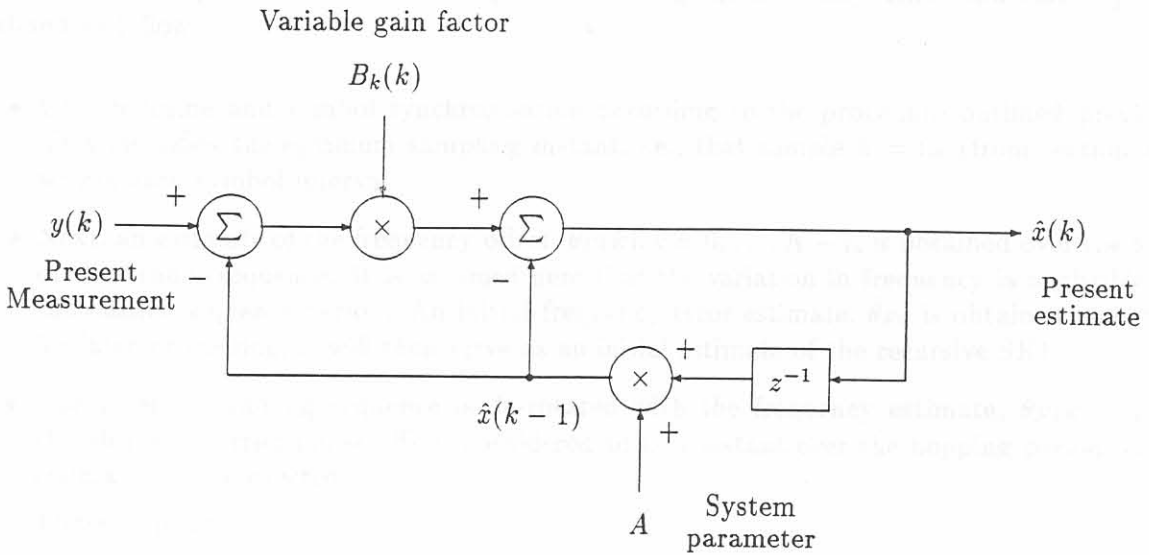


Figure 4.18: Optimum recursive scalar Kalman estimator.

- Calculate the variable Kalman gain:

$$\begin{aligned} B_k(k) &= \frac{p_1(n)}{p_1(n) + \sigma_v^2} \\ &= \frac{p(0)}{k \cdot p(0) + \sigma_v^2} \end{aligned} \quad (4.32)$$

where

$$p_1(k) = p(k-1) = p(k | k-1) \quad (4.33)$$

- Derive the MSE:

$$p(k) = p_1(k)[1 - B_k(k)] \quad (4.34)$$

Note that, with  $k \rightarrow \infty$ ,  $B_k(k) \rightarrow 0$  and  $\hat{\theta}(k) = \hat{\theta}(k-1)$ , which indicates that the estimator has stabilised on the best estimate of the required parameter,  $\theta$ , i.e., further measurements will not improve this estimate.

Equations (4.31-4.34) together form the recursive algorithm. The procedure is to find  $B_k(k)$  from equation (4.32). Then, from the stored previous value  $\hat{\theta}(k-1)$  and the new data sample  $\theta_I$ , calculate  $\hat{\theta}(k)$  from equation (4.31). This procedure continually generates the best linear estimation of  $\hat{\theta}(k)$ , and at the same time it provides the corresponding MSE,  $p(k)$ , which can be monitored to assess the convergence of the recursive algorithm. Note that  $p(k) \rightarrow 0$  for  $m$  very large.

#### 4.3.4.2 Correction Strategy A: Single Estimator

This method has been proposed by Aguirre and Hinedi [72], where the phase information is removed by manipulating the samples in a direct manner. This is done by performing a simple cross-product between the in-phase and quadrature sample, producing modified samples which are then fed into a recursive SKE, which estimates the time-varying frequency information.

The step-by-step procedure in estimating and correcting the frequency offset and carrier phase is outlined as follows:

- Obtain frame and symbol synchronisation according to the procedure outlined previously. This identifies the optimum sampling instant, i.e., that sample  $k = i_m$  (from section 4.3.1) within each symbol interval.
- Next, an estimate of the frequency offset,  $\hat{\theta}_F(k)$ ,  $k = 0, \dots, K - 1$ , is obtained over the length of the header sequence. It is assumed here that the variation in frequency is negligible over the header sequence period. An initial frequency error estimate,  $\hat{\theta}_{F0}$  is obtained and stored for later processing; it will then serve as an initial estimate of the recursive SKE.
- The received training sequence is de-rotated with the frequency estimate,  $\hat{\theta}_F(k)$ , so that the absolute carrier phase offset, considered to be constant over the hopping period, can be estimated and corrected.

These steps are:

- Repeat the correlation process, by using the de-rotated received training sequences with the reference training sequence. This corresponds to a correlation between the received training sequence and absolute phases of the reference training sequence. The initial carrier phase rotation,  $\theta_o(i_m)$ , is then calculated from (4.13) in section 4.3.1. This value is stored and later utilised in the establishment of decision boundaries of the Q<sup>2</sup>PSK detection scheme.
- All samples of the received I and Q baseband signals, associated with each two-dimensional modulator, are de-rotated with the fixed carrier phase offset,  $\theta_o(i_m)$ .
- Finally, after having obtained an initial Doppler estimate during the preamble period, the recursive SKE, can be initiated in order to track and improve the possibly time-variant frequency error during the data period of the FH burst.

#### 4.3.4.3 Correction Strategy B: Dual Estimator

In this section the analysis of a adaptive dual phase and frequency tracking loop will be carried out. This loop was introduced by Kim [69], an *adaptive dual digital phase-locked loop* DPPLL. By close investigation of the tracking loop (Figure 2, [69]), one can identify two separate loops, each in the form of a recursive Scalar Kalman Estimator (SKE) depicted in Figure 4.18, for tracking the phase and frequency variations, respectively. The first SKE is used to track frequency variation, while the second, utilising the estimated frequency is used to track phase variation.

The block diagram in Figure 2, [69] is repeated in Figure 4.19, but redrawn to indicate the two estimators more clearly. Henceforth, the name Dual Phase Frequency Kalman Estimator (DPFKE) is adopted for this configuration.

From Figure 4.19, the closed loop transfer function of the DPFKE loop is given by

$$\frac{\theta_P(z)}{\theta_I(z)} = \frac{(B_l(t) + B_k(t)(z - 1) + B_l(t)B_k(t))}{z - (1 - B_l(t))(z - (1 - B_k(t)))} \quad (4.35)$$

From equation (4.35), it is clear that the loop is stable as long as  $0 < B_k(t), B_l(t) < 1$ . The time-varying parameters (Kalman gain factors)  $B_k(t)$  and  $B_l(t)$ , control the bandwidth of the frequency detection and phase detection loops, as well as the overall bandwidth of the DPFKE.

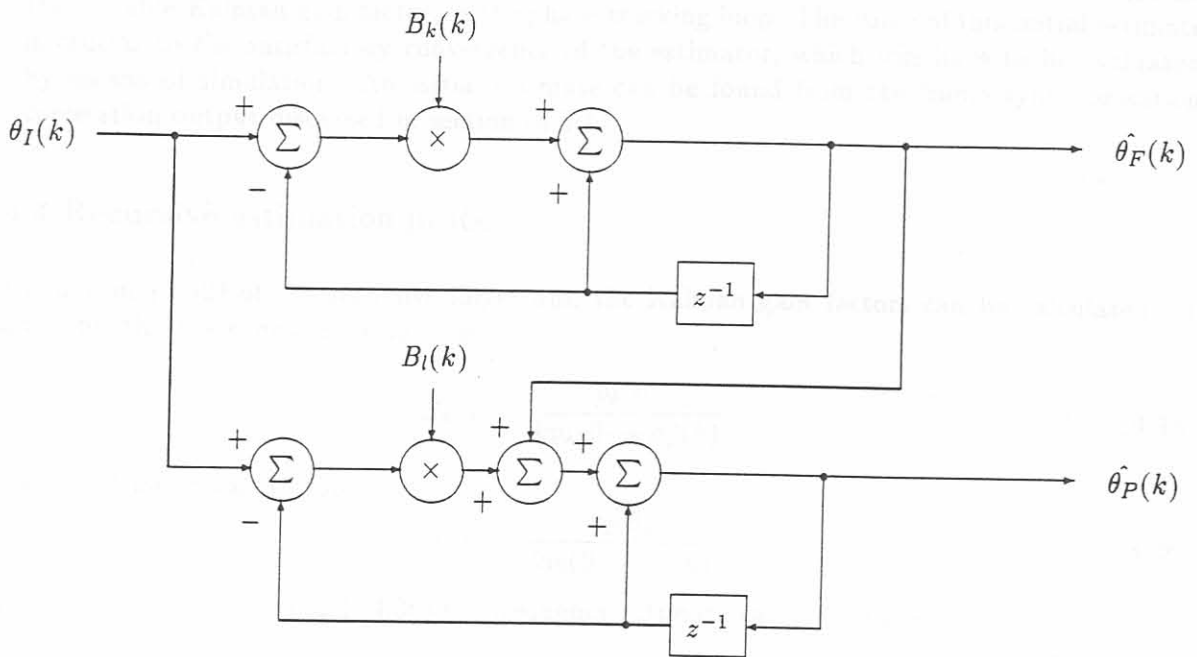


Figure 4.19: Dual Frequency and Phase Kalman Estimator (DPFKE).

From Figure 4.19, the dual frequency and phase estimator outputs at time instant,  $k$ , can be expressed as

$$\hat{\theta}_F(k) = \hat{\theta}_F(k-1) + B_k(k) [\theta_I(k) - \hat{\theta}_F(k-1)] \quad (4.36)$$

and

$$\hat{\theta}_P(k) = \hat{\theta}_P(k-1) + \hat{\theta}_F(k) + B_l(k) [\theta_I(k) - \hat{\theta}_P(k-1)] \quad (4.37)$$

The DPFKE has the capability of estimating the input frequency immediately, without any limitation in pull-in range. After the initial phase and frequency acquisition, it requires a short header period, since it aligns its phase adaptively based on the minimum MSE criterion at each given time instant [73].

Next, a step-by-step procedure will be given in estimating the phase and frequency offsets by means of the DPFKE. This dual estimator is very similar to the previous single Kalman estimator and almost the same steps are followed, with only slight changes concerning the phase estimation.

- Obtain frame and symbol synchronisation according to the procedures previously outlined.
- Next, an estimate of the frequency offset,  $\hat{\theta}_F(k)$ ,  $k = 0, \dots, K-1$ , is obtained over the length of the preamble sequence. Furthermore, an initial frequency error estimate,  $\hat{\theta}_{F0}$  is obtained and stored for later processing. It will be used to initialise the recursive DPFKE.
- The received training sequence is de-rotated with the frequency estimate,  $\hat{\theta}_F(k)$ , so that the absolute carrier phase offset, considered a constant over the hopping period, can be estimated and corrected. Recall, from the previous method that a second cross-correlation was needed to estimate this carrier phase offset. However, in this estimator the tracking of this information is interleaved with that of the frequency estimation. The problem is that no initial estimate

of the phase information is available at this stage. This is needed to obtain an initial value for the variable Kalman gain factor, in the phase tracking loop. The value of this initial estimate is crucial to the satisfactory convergence of the estimator, which will have to be evaluated by means of simulation. An initial estimate can be found from the frame synchronisation correlation output discussed in section (4.3.1).

#### 4.3.4.4 Recursive estimation process

From equation (4.32) of the recursive algorithm, the Kalman gain factors can be calculated, at instant  $k$ , for the frequency tracking loop:

$$B_k(k) = \frac{p_k(0)}{kp_k(0) + \sigma_v^2(k)} \quad (4.38)$$

and for the phase tracking loop:

$$B_l(k) = \frac{p_l(0)}{kp_l(0) + \sigma_v^2(k)} \quad (4.39)$$

Then from equations (4.31) and (4.36) the frequency estimate can be obtained:

$$\hat{\theta}_F(k) = \hat{\theta}_F(k-1) + B_k(k) [\theta_I(k) - \hat{\theta}_F(k-1)] ; k = 1, 2, \dots \quad (4.40)$$

with MSE from equation(4.34):

$$p_k(k) = \frac{p_k(0)}{1 + kp_k(0)/\sigma_v^2} \quad (4.41)$$

Similarly equations (4.31) and (4.37) produce the phase estimate:

$$\hat{\theta}_P(k) = \hat{\theta}_P(k-1) + \hat{\theta}_F(k) + B_k(k) [\theta_I(k) - \hat{\theta}_P(k-1)] ; k = 1, 2, \dots \quad (4.42)$$

with MSE from equation(4.34):

$$p_l(k) = \frac{p_l(0)}{1 + kp_l(0)/\sigma_v^2} \quad (4.43)$$

By plotting  $p_k(k)$  and  $p_l(k)$  as a functions of the iteration index  $k$ , an indication of the convergence of the recursive loops of the estimators can be obtained. These MSE curves can be smoothed by calculating the running average:

$$\bar{p}_k(k) = \beta \bar{p}_k(k-1) + (1 - \beta)p(k)_k \quad (4.44)$$

and

$$\bar{p}_l(k) = \beta \bar{p}_l(k-1) + (1 - \beta)p(k)_l \quad (4.45)$$

starting with  $\bar{p}_k(k-1) = \bar{p}_l(k-1) = p(0)$  at instant,  $k = 1$ .

This concludes the discussion of the proposed carrier phase and Doppler frequency error estimation and correction procedures for the Q<sup>2</sup>PSK modem. The carrier phase and frequency tracking procedures designed and analysed in the foregoing sections have been presented in [74].

#### 4.4 CONCLUDING REMARKS: CHAPTER 4

The research presented in the foregoing was motivated by the need for carrier frequency and phase recovery for  $Q^2PSK$  in a mobile communications environment. One of the main shortcomings of the Kalman based carrier estimators is that the acquisition characteristics of these estimators are highly dependent on the initial estimate. The question now is to what extent the initial estimates will be suitable for effective operation. To answer this question, a thorough performance evaluation is needed to verify the correctness and also the effectiveness of these procedures. In Chapter 7, these tracking procedures will be evaluated by means of simulation.

---

---

PART II

WORLDWIDE CODING WITH  
APPLICATION TO  $Q^2PSK$

## CHAPTER 5

---

# DESIGN FOR AWGN CHANNELS

---

---

This chapter is concerned with the design of trellis codes for AWGN channels, with specific reference to the application of classical and TCM forward error correction techniques to  $Q^2$ PSK. The first section of this chapter considers the classical techniques. The final sections deal with the design and application of TCM techniques for  $Q^2$ PSK.

### 5.1 INTRODUCTION TO ERROR CORRECTION

The task facing the communications engineer is that of providing a cost-effective system for transmitting information (data or voice) from a sender to a user at a specific rate and an acceptable level of reliability. Practical considerations usually place a limit on the value that can be assigned to  $E_b/N_o$ . In other words, in practice, we may find that a specific modulation scheme may not provide acceptable performance. For a fixed  $E_b/N_o$ , the only practical option available for improving data quality to an acceptable level is to resort to coding techniques. The use of Forward Error Correcting (FEC) codes is well suited to channels that can be modeled as Additive White Gaussian Noise (AWGN) channels [22, 75, 76].

In a general FEC scheme the *channel encoder* accepts message bits and adds controlled *redundancy* according to a prescribed encoding rule, thereby producing encoded data at a higher bit rate. The *channel decoder* exploits the redundancy to decide which message bit was actually transmitted. In FEC systems, the motivation is to achieve a *coding gain*, defined as the difference in  $E_b/N_o$  required for coded and uncoded systems to provide a specified BER when operating on an AWGN channel. Moreover, the use of coding adds complexity to the system, especially for the implementation of the decoding operation at the receiver. Thus, the design trade-offs in the use of error-control coding are considerations of bandwidth and system complexity.

## 5.2 CLASSICAL ERROR CORRECTION

In the following sections low-complexity sub-optimal convolutional encoding schemes are proposed for Q<sup>2</sup>PSK. The first scheme employs a single rate-3/4 convolutional encoder, yielding an effective data rate equal to that of 3/4, the rate of uncoded Q<sup>2</sup>PSK, operating at  $R_b$ . A Maximum-Likelihood (ML) soft-decision Viterbi decoder is utilised at the receiver. The second encoding scheme, with so called *dual-use* of conventional 2D signals, employs two rate-1/2 convolutional encoders. At the receiver two soft-decision Viterbi decoders are utilised in parallel. The resulting bit rate is reduced by a factor of two, compared to that achieved with the uncoded transmission, to yield an effective bit rate equal to that of conventional 2D-QPSK.

Since the envelope of the Q<sup>2</sup>PSK signal in the absence of any additional constraint is non-constant, a third encoding scheme is proposed, employing a hybrid convolutional-block coding scheme. The encoder consists of a rate-2/3 convolutional encoder, followed by a simple block encoding scheme to facilitate a constant envelope. At the receiver a single soft-decision Viterbi decoder, together with a block decoding scheme, is employed.

### 5.2.1 Convolutional Channel Coding

Convolutional codes differ from block codes in that the encoder contains  $m$  memory elements, and the  $n$  encoder outputs at any given time unit depend not only on the  $k$  input bits at that time, but also on  $m$  previous input bits. A convolutional code is generated by passing the information sequence to be transmitted through a linear finite-state shift register. In general, the shift register consists of  $L_c$  ( $k$ -bit) stages and  $n$  linear algebraic function generators, called *generator sequences*. The parameter  $L_c$  is called the *constraint length* of the convolutional code, and can be interpreted as the maximum number of encoder outputs that can be affected by a single information bit. The number of states  $N_s$ , of the convolutional encoder which generates  $n$  encoded bits is a function of  $L_c$  and  $k$  input bits, given by  $N_s = 2^{k(L_c-1)}$ .

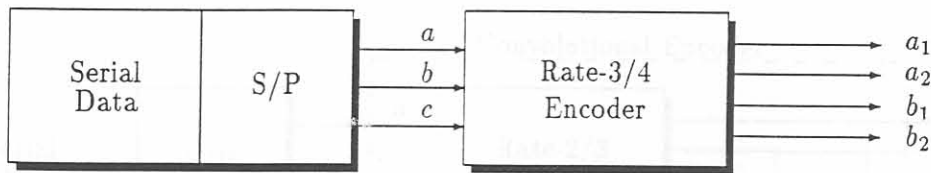
An  $(n, k, L_c)$  convolutional code can be implemented with a  $k$ -input,  $n$ -output linear shift register with input memory,  $m = kL_c$ , and at most  $knL_c$  modulo-2 adders. For each of the  $n$  outputs, a generator sequence of length  $kL_c$  is needed, describing the connections of the  $kL_c$  shift register stages to the modulo-2 adder of that output stage.

For our application, rate- $\frac{k}{k+1}$  trellis encoders, introduced by Ungerboeck [28, 29], are employed to select  $2^n$  ( $n = k + 1$ ) equally likely channel symbols.

#### 5.2.1.1 Rate-3/4 encoder for Q<sup>2</sup>PSK

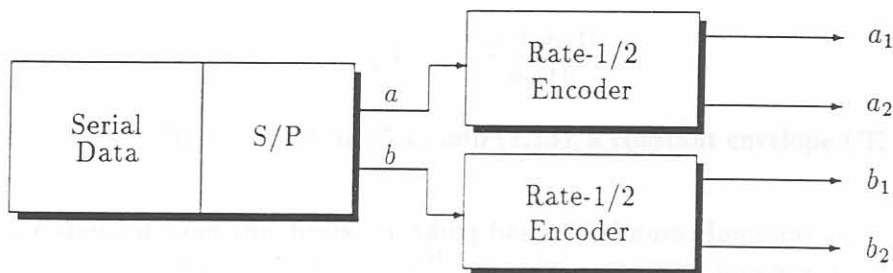
The first encoding strategy proposed for Q<sup>2</sup>PSK consists of a single rate-3/4 convolutional encoder, as illustrated in Figure 5.1. The serial data bit stream is Serial-to-Parallel (S/P) converted, producing three parallel bit streams,  $a$ ,  $b$  and  $c$ . These uncoded bit streams are then fed to the rate-3/4 encoder, producing a coded signal set  $A$  consisting of four coded bit streams  $\{a_1, a_2, b_1, b_2\}$ . Signal set  $A$  therefore consists of  $2^4$  equally likely signal symbols.

Since the ratio between the number of input bits to the number of output bits is 3/4, the effective code rate is reduced by 1/4 compared to that of uncoded transmission.

Figure 5.1: Rate-3/4 encoding scheme for  $Q^2$ PSK.

### 5.2.1.2 Rate-1/2 Encoder for $Q^2$ PSK

In the coding scheme proposed for  $Q^2$ PSK, two rate-1/2 ( $k = 1$ ) convolutional encoders, i.e., *dual-use* of 2D encoders, are employed as depicted in Figure 5.2. The serial data bit stream is S/P converted, producing two parallel bit streams,  $a$  and  $b$  at a rate  $R'_b = R_b/2$ . Recall that  $R_b$  is the original data rate. The uncoded bit streams,  $a$  and  $b$ , are then fed to the two rate-1/2 convolutional encoders, each producing two sets,  $A$  and  $B$ , consisting of two encoded data streams  $\{a_1, a_2\}$  and  $\{b_1, b_2\}$ , respectively. The two sets of encoded data streams each produce a signal set consisting of  $2^2 = 4$  symbols, resulting in a total signal set of  $M = 16$  symbols given by the Cartesian products of the sets  $A$  and  $B$ .

Figure 5.2: Half rate encoding scheme for  $Q^2$ PSK.

Since the ratio between the number of input bits to the number of output bits is one half, this is a true *half rate* convolutional encoding scheme.

### 5.2.1.3 Encoder for CE- $Q^2$ PSK

The coding scheme proposed for constant envelope CE- $Q^2$ PSK employs a hybrid convolutional-block coding scheme. The block encoding scheme is incorporated to force a constant envelope signal.

The front-end of this encoder is formed by a single rate-2/3 ( $k = 2$ ) convolutional encoder as depicted in Figure 5.3. As for the  $Q^2$ PSK encoder, the serial data bit stream is S/P converted,



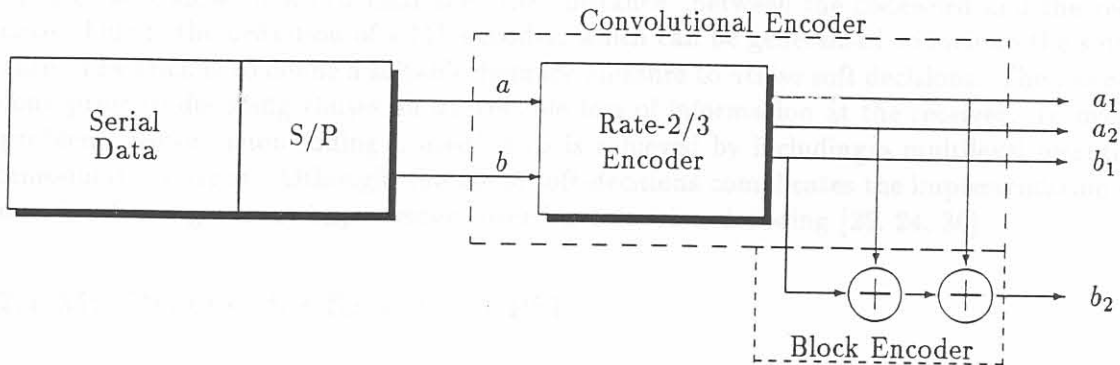


Figure 5.3: Half rate encoding scheme for CE-Q<sup>2</sup>PSK.

producing two parallel bit streams,  $a$  and  $b$ . These uncoded bit streams are then fed to the rate-2/3 convolutional encoder, which produces a single symbol set,  $C$ , consisting of the three encoded data streams,  $a_1, a_2$  and  $b_1$ , respectively. Note, that this set consists of  $2^3 = 8$  equally likely symbols.

The block coding scheme used to achieve a constant envelope Q<sup>2</sup>PSK signal can be described as follows: the coder accepts serial input data and for every three information bits  $\{a_1, a_2, b_1\}$ , it generates a codeword  $\{a_1, a_2, b_1, b_2\}$  such that the first three bits in the codeword are the encoded information and the fourth one is an odd parity check bit. The parity check bit  $b_2(t)$  is given by

$$b_2(t) = -\frac{a_1(t)b_1(t)}{a_2(t)} \quad (5.1)$$

in agreeing with (2.15). By substituting (5.1) into (2.13), a constant envelope CE-Q<sup>2</sup>PSK signal is obtained.

The resulting codeword from this block encoding has a minimum Hamming distance of  $d_{min}^H = 2$ . Recall from block coding theory that  $t = \lfloor (d_{min}^H - 1)/2 \rfloor$  errors can be corrected, where  $\lfloor x \rfloor$  is the largest integer less than or equal to  $x$ , implying that the added extra data bit,  $b_2(t)$ , can not be used for error correction. Instead, the redundancy in the resulting signal set can be used to improve the BER performance of the modulation scheme.

### 5.2.2 Maximum Likelihood Decoding

In Appendix A (section A.4) it is stated that Maximum Likelihood (ML) decoding implies finding the path with largest metric through the trellis by comparing the metrics of all branch paths entering each state with the corresponding received sequence in an iterative manner. The general Viterbi algorithm can be described as follows: In the decoding process, if at some level it is found that a path cannot possibly yield the largest metric, then the path is discarded by the decoder [77, 24]. In this manner, a decoder that compares the metrics of all paths entering a state and keeps only the survivor at that state, will yield a most likely path if the operation is repeated for all distinct states at each level.

In a coded system one would normally wish to structure the decoder such that for a given code the probability of error is minimised. In the hard decision case the optimum decoding procedure is to pick the codeword which differs from the received sequence in the smallest number of positions, i.e., choose the codeword which minimises the "distance" between the codeword and the received sequence. This is the definition of a ML decoder, which can be generalised to include the soft decision case. The trick is to define a suitable distance measure to utilise soft decisions. The use of hard decisions prior to decoding causes an irreversible loss of information at the receiver. To overcome this problem, *soft-decision* coding is used. This is achieved by including a multilevel quantiser at the demodulator output. Although, the use of soft-decisions complicates the implementation of the decoder, it offers significant improvement over hard-decision decoding [25, 24, 30].

### 5.2.2.1 ML Decoder for Rate-3/4 $Q^2$ PSK

Figure 5.4 depicts the decoding procedure for rate-3/4  $Q^2$ PSK, consisting of a  $Q$ -bit multi-level soft-quantiser and a Viterbi decoder. The  $Q$ -bit quantiser accepts serial input data and produces serial output data quantised into  $2^Q$  levels. These quantised outputs are then fed into the Viterbi decoder, where the data is decoded and the output data stream formed.

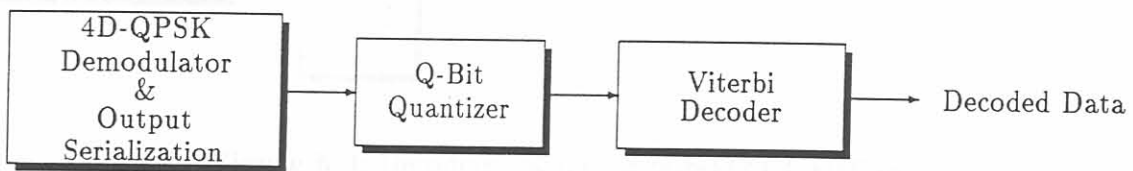


Figure 5.4: Decoding scheme for rate-3/4  $Q^2$ PSK.

### 5.2.2.2 ML Decoder for Rate-1/2 $Q^2$ PSK

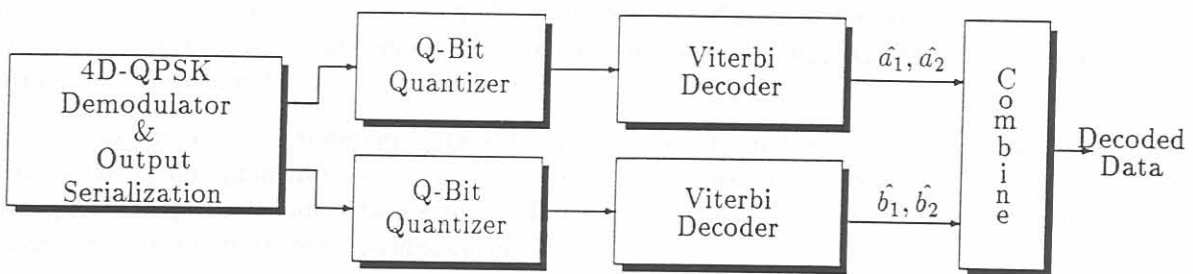


Figure 5.5: Decoding scheme for rate-1/2  $Q^2$ PSK.

Figure 5.5 depicts the decoding procedure for  $Q^2$ PSK, consisting of two  $Q$ -bit multi-level soft-quantisers and two ML decoders, employing the Viterbi algorithm. Each of the two  $Q$ -bit quantisers accepts serial input data and produces serial output data quantised into  $2^Q$  levels. These quantised outputs are then fed into the Viterbi decoders, where the data is decoded. From the decoders the output data streams are combined to form the decoded output data stream.

### 5.2.2.3 ML Decoder for Constant Envelope CE-Q<sup>2</sup>PSK

Figure 5.6 depicts the decoding scheme for CE-Q<sup>2</sup>PSK, consisting firstly of a block decoding procedure, and secondly, of a ML Viterbi decoder.

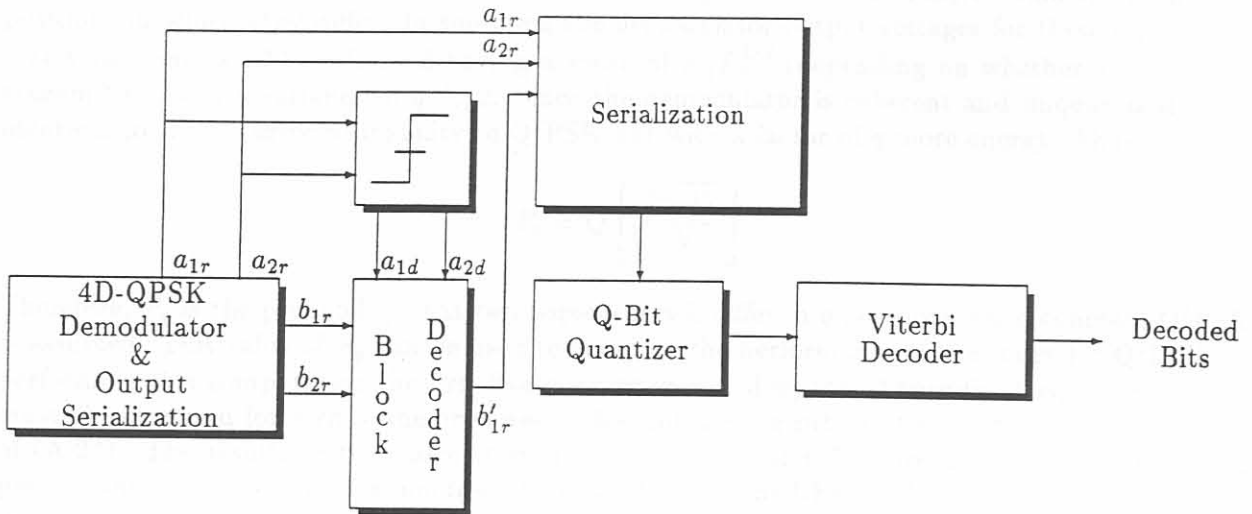


Figure 5.6: Decoding scheme for rate-1/2 CE-Q<sup>2</sup>PSK.

Decisions about demodulator outputs  $a_{1r}$  and  $a_{2r}$  associated with pulse trains  $a_1(t)$  and  $a_2(t)$  respectively, are made from the other Q<sup>2</sup>PSK demodulator outputs to produce the decoded information streams,  $a_{1d}$  and  $a_{2d}$ . These two streams, together with the redundant information associated with  $b_2(t)$ , are used only in making the decision about the information bit in  $b_1(t)$ . To make a decision about  $b_1(t)$ , a simplifying assumption that  $a_{1d}$  and  $a_{2d}$  are decoded correctly has to be made. These decoded information streams, along with the estimates  $b_{1r}$  of  $b_1$  and its redundant version  $b_{2r}$  of  $b_2$ ; observing a decision estimate about  $b_1$ , given by:  $b'_{1r} = b_{1r} - (a_{1d}/a_{2d})b_{2r}$  (in agreement with the discussion in section 4.1.2.1), is made.

The decision estimate,  $b'_{1r}$  together with estimates  $a_{1r}$  of  $a_1$  and  $a_{2r}$  of  $a_2$ , are then serialised and fed to the Q-bit quantiser. From here the serial quantised data stream is fed to the Viterbi decoder, producing the decoded data stream. The code classical trellis code designs carried out in the foregoing sections have been published in [78].

## 5.2.3 Performance Estimates

The most useful techniques of estimating the performance of convolutional coding are the union bound technique and computer simulation. This section will try to quantify the expected performance of the Forward Error Correction (FEC) coders presented in the foregoing sections. Most of the performance evaluation will, however be based on extensive computer simulations. The usefulness of computer simulation is limited by the long execution times required to obtain a good statistical sample (it may take several hours to yield a single point on the error graph). The union

bound approach for convolutional codes is virtually identical to that of block codes, and it provides performance estimates accurate within a small fraction of a decibel for all SNR large enough to give an error rate of  $10^{-3}$  or less.

Assume that coherent Q<sup>2</sup>PSK is used with a hard quantised demodulator output. Then to apply the union bound (presented in Appendix A, section A.3.3) we must calculate the probability that the distance between the received sequence and a weight- $q$  codeword is less than the distance to the transmitted all-zero word. Call this probability,  $P_q$ .  $P_q$  is a function of  $E_s/N_o$  and the number of positions in which they differ. In summing the demodulator output voltages for these  $q$  positions, a new random variable is formed having a mean of  $\pm qE_s^{1/2}$  (depending on whether a 1 or 0 was transmitted) and a variance of  $qN_o/2$ . Since the demodulator is coherent and unquantised,  $P_b$  is identical to the bit error probability of Q<sup>2</sup>PSK but with a factor of  $q$  more energy. Thus,

$$P_q = Q \left[ \sqrt{\frac{2qE_b}{N_o}} \right] \quad (5.2)$$

Therefore,  $P_q$  is the probability that two sequences will differ in  $q$  positions when coherent Q<sup>2</sup>PSK is assumed. This value of  $P_q$  can be used to compute the performance of the codes for Q<sup>2</sup>PSK. In performing this computation the first five nonzero values of  $w_q$  (see Appendix A equation (A.24)) must be computed for each of the proposed codes and then be substituted in the truncated version of (A.24). The results of this calculation are shown in Figures 5.7 through 5.9, where the BER performance  $P_b$  is plotted as a function of  $E_b/N_o$  (in dB). The BER performance curves are for the code rates of 1/2, 2/3 and 3/4, respectively and include the constraint lengths  $L_c$ . In Chapter 7 these performance curves will be benchmarked against graphs obtained by means of simulation.

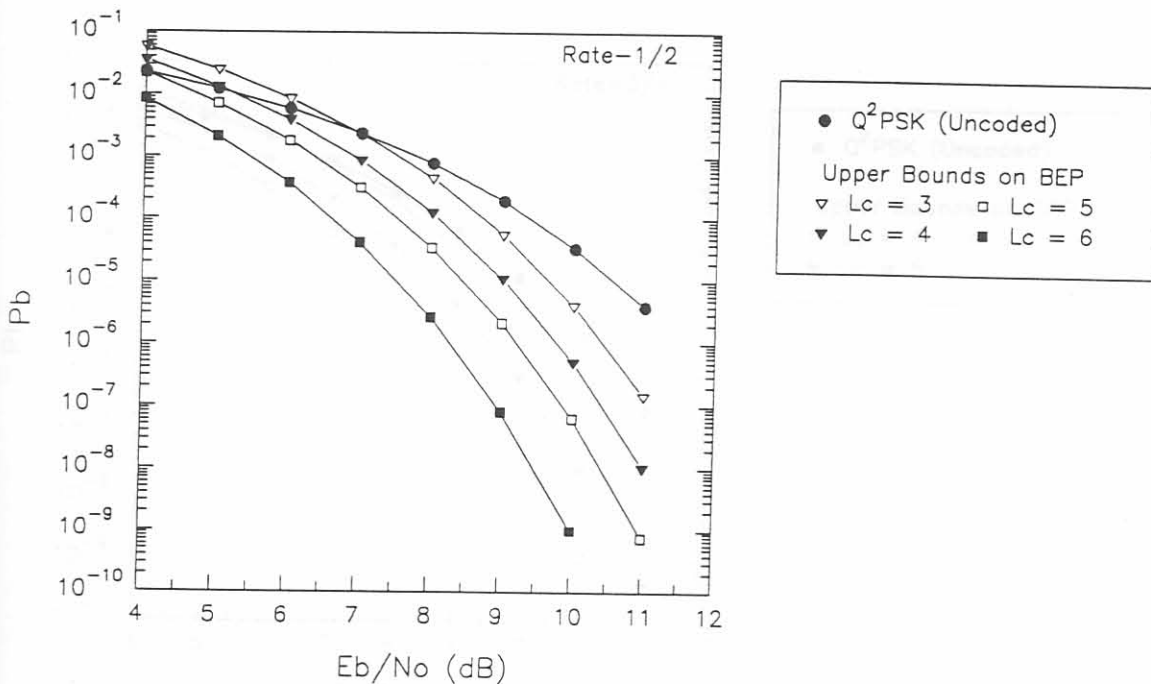


Figure 5.7: Bit error probability,  $P_b$  for Rate-1/2 codes with Viterbi decoding (Hard quantisation) and Q<sup>2</sup>PSK modulation.

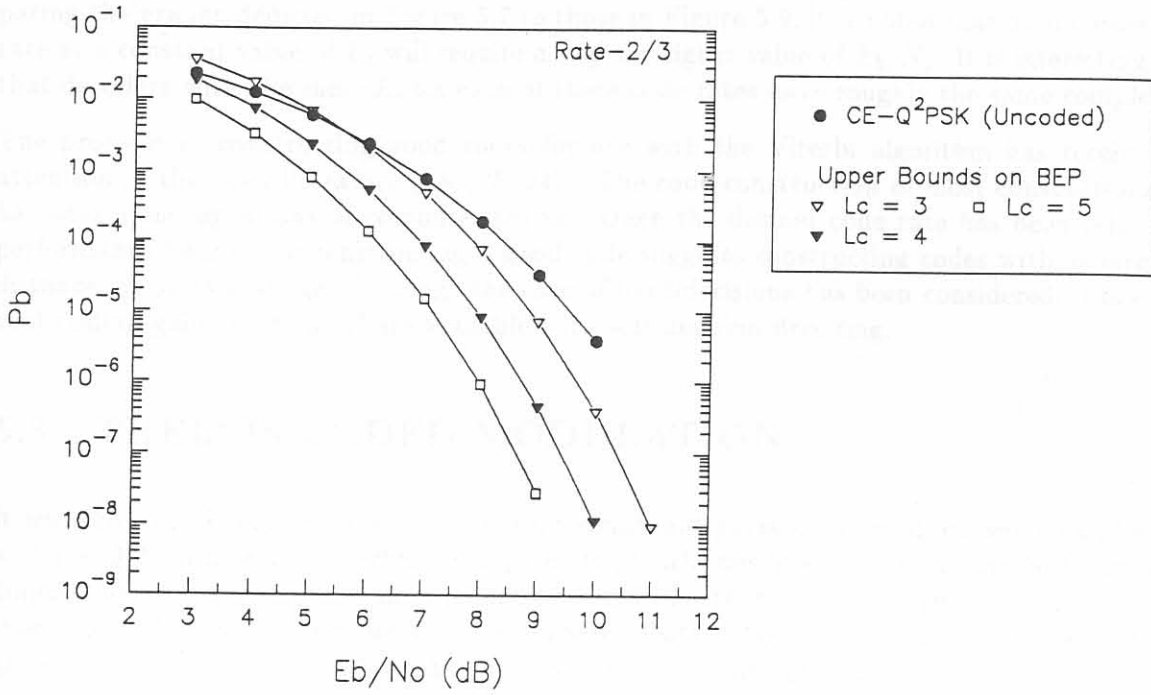


Figure 5.8: Bit error probability for Rate-2/3 codes with Viterbi decoding (Hard quantisation) and  $Q^2$ PSK modulation.

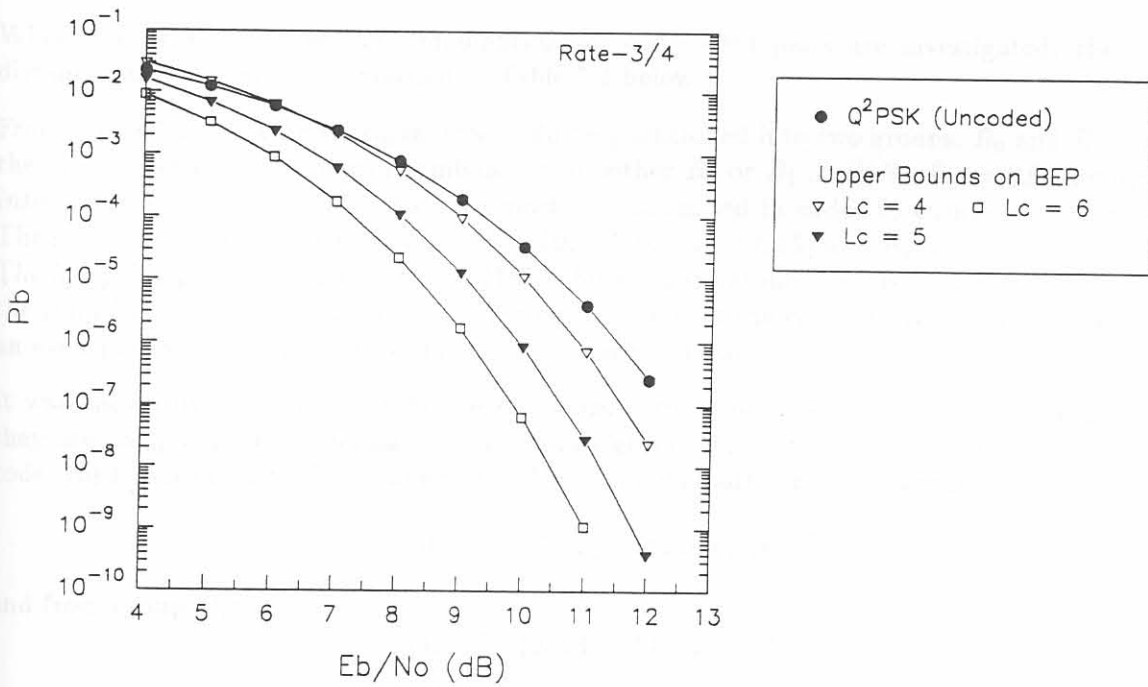


Figure 5.9: Bit error probability for Rate-3/4 codes with Viterbi decoding (Hard quantisation) and  $Q^2$ PSK modulation.

The BER performance are for a BSC (i.e., hard-decision decoding) in an AWGN channel. Comparing the graphs depicted in Figure 5.7 to those in Figure 5.9, it is noted that an increase in code rate at a constant value of  $L_c$  will require a slightly higher value of  $E_b/N_o$ . It is interesting to note that decoders with the same  $L_c$  for each of these code rates have roughly the same complexity.

The problem of constructing good codes for use with the Viterbi algorithm has received much attention in the open literature (see [25, 24]). The code construction of most convolutional codes has been done by means of computer search. Once the desired code rate has been selected, the performance bounds for constructing a good code suggests constructing codes with as large a free distance,  $d_{free}$  as possible. Although the case of hard-decisions has been considered, it is expected that coding gains up to 3 dB are available with soft-decision decoding.

### 5.3 TRELIS CODED MODULATION

It was shown in Chapter 2 (section 2.3) that significant gains in spectral efficiency can be gained with the Q<sup>2</sup>PSK modulation scheme compared to 2D schemes by exploiting all available signal space dimensions within the given transmission bandwidth. Furthermore, utilisation of all available signal space dimensions may bring about further improvements in the coding gain. Therefore, high coding gains are expected when TCM techniques are combined with Q<sup>2</sup>PSK.

The Minimum Squared Euclidean Distance (MSED),  $d_{free}^2$  between any pair of 4-tuples or code words  $(a_1 a_2 a_3 a_4)$ , say  $s_x$  and  $s_y$ , can be easily evaluated and is given by

$$d_{free}^2 = \sum_{i=1}^4 (a_i^{(x)} - a_i^{(y)})^2 \quad (5.3)$$

When the MSED between all combinations of code word pairs are investigated, the following distances are obtained (summarised in Table 5.1 below.)

From Table 5.1, the Q<sup>2</sup>PSK signal space can be partitioned into two groups,  $B_0$  and  $B_1$ , such that the MSED between any pair of symbols within either  $B_0$  or  $B_1$  is  $d^2(B_0, B_1) = 8E_b$ , known as the *intradistance* of a code. This distance must be maximised in order to ensure an optimum code. The resulting subgroups are given by  $B_0 = \{0, 3, 5, 6, 9, 10, 12, 15\}$  and  $B_1 = \{1, 2, 4, 7, 8, 11, 13, 14\}$ . The foregoing partitioning results in a MSED between subgroups,  $B_0, B_1$  of  $4E_b$ , which is known as the *interdistance* of the code. It is interesting to note that the code words from group  $B_0$  maintain an even parity, while the code words from  $B_1$  have odd parity.

It was shown by Saha in [12] that the minimum correlation among code words is achieved when they are antipodal. Considering the partitioned groups  $B_0$  and  $B_1$ , we identify four pairs of such code words out of each of the subgroups. These symbol pairs are, from group  $B_0$ :

$$\{0, 15\}, \{3, 12\}, \{5, 10\}, \{6, 9\} \quad (5.4)$$

and from group  $B_1$ :

$$\{1, 14\}, \{2, 13\}, \{4, 11\}, \{7, 8\} \quad (5.5)$$

Note that for these antipodal code word pairs the MSED is maximised. Therefore, we can partition subgroups  $B_0$  and  $B_1$  even further, such that the MSED between the antipodal symbol pair in any

Reference	$s_1$	$s_2$	$s_3$	$s_4$	$s_5$	$s_6$	$s_7$	$s_8$	$s_9$	$s_{10}$	$s_{11}$	$s_{12}$	$s_{13}$	$s_{14}$	$s_{15}$
$s_0$	4	4	8	4	8	8	12	4	8	8	12	8	12	12	16
$s_1$	—	8	4	8	4	12	8	8	4	12	8	12	8	16	12
$s_2$	—	—	4	8	12	4	8	8	12	4	8	12	16	8	12
$s_3$	—	—	—	12	8	8	4	12	8	8	4	16	12	12	8
$s_4$	—	—	—	—	4	4	8	8	12	12	16	4	8	8	12
$s_5$	—	—	—	—	—	8	4	12	8	16	12	8	4	12	8
$s_6$	—	—	—	—	—	—	4	12	16	8	12	8	12	4	8
$s_7$	—	—	—	—	—	—	—	16	12	12	8	12	8	8	4
$s_8$	—	—	—	—	—	—	—	—	4	4	8	4	8	8	12
$s_9$	—	—	—	—	—	—	—	—	—	8	4	8	4	12	8
$s_{10}$	—	—	—	—	—	—	—	—	—	—	4	8	12	4	8
$s_{11}$	—	—	—	—	—	—	—	—	—	—	—	12	8	8	4
$s_{12}$	—	—	—	—	—	—	—	—	—	—	—	—	4	4	8
$s_{13}$	—	—	—	—	—	—	—	—	—	—	—	—	—	8	4
$s_{14}$	—	—	—	—	—	—	—	—	—	—	—	—	—	—	4

Table 5.1: Minimum squared Euclidean distances between all pairs of Q<sup>2</sup>PSK code words.

group is  $16E_b$ , forming subgroups  $C_0, \dots, C_7$ , each containing an antipodal code word pair. These subgroups are defined by

$$\begin{aligned} B_0 &= \{C_0, C_1, C_2, C_3\} \\ B_1 &= \{C_4, C_5, C_6, C_7\} \end{aligned} \quad (5.6)$$

where

$$\begin{aligned} C_0 &= \{0, 15\}, C_1 = \{3, 12\}, C_2 = \{5, 10\}, C_3 = \{9, 6\} \\ C_4 &= \{1, 14\}, C_5 = \{2, 13\}, C_6 = \{4, 11\}, C_7 = \{8, 7\} \end{aligned} \quad (5.7)$$

as illustrated in Figures 5.10 and 5.11.

Symbol	$a_1$ $a_2$ $a_3$ $a_4$	$a_c$ $b_c$ $a_s$ $b_s$	4D Signal Components	4D Signal Space	Coder Output	
$C_0$	0	-1 -1 -1 -1	-1 -1 -1 +1	$s_{13} + s_{22}$		1
	15	+1 +1 +1 +1	+1 -1 +1 +1	$s_{11} + s_{24}$		-15
$C_1$	3	-1 -1 +1 +1	-1 +1 +1 -1	$s_{14} + s_{23}$		5
	12	+1 +1 -1 -1	+1 +1 -1 -1	$s_{12} + s_{21}$		-11
$C_2$	5	-1 +1 -1 +1	-1 +1 -1 -1	$s_{12} + s_{23}$		9
	10	-1 -1 +1 -1	+1 +1 +1 -1	$s_{14} + s_{21}$		-7
$C_3$	9	+1 -1 -1 +1	+1 -1 -1 +1	$s_{11} + s_{22}$		-3
	6	-1 +1 +1 -1	-1 -1 +1 +1	$s_{13} + s_{24}$		13

 Figure 5.10: Group  $B_0 = \{C_0, C_1, C_2, C_3\}$ : Even Parity



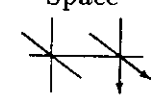
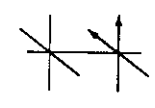
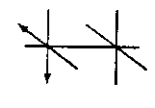
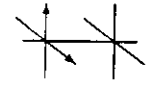
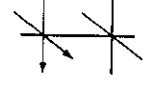
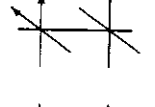
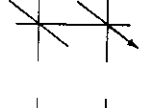
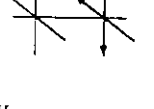
Symbol	$a_1$ $a_2$ $a_3$ $a_4$	$a_c$ $b_c$ $a_s$ $b_s$	4D Signal Components	4D Signal Space	Coder Output	
$C_4$	1	-1 -1 -1 +1	-1 +1 -1 +1	$s_{22} + s_{23}$		3
	14	+1 +1 +1 -1	+1 +1 +1 +1	$s_{21} + s_{24}$		-13
$C_5$	2	-1 -1 +1 -1	-1 -1 +1 -1	$s_{13} + s_{14}$		7
	13	+1 +1 -1 +1	+1 -1 -1 -1	$s_{11} + s_{12}$		-9
$C_6$	4	-1 +1 -1 -1	-1 -1 -1 -1	$s_{12} + s_{13}$		11
	11	+1 -1 +1 +1	+1 -1 +1 -1	$s_{11} + s_{14}$		-5
$C_7$	8	+1 -1 -1 -1	+1 +1 -1 +1	$s_{21} + s_{22}$		-1
	7	-1 +1 +1 +1	-1 +1 +1 +1	$s_{23} + s_{24}$		15

Figure 5.11: Group  $B_1 = \{C_4, C_5, C_6, C_7\}$ : Odd Parity

The foregoing set partitioning of the Q<sup>2</sup>PSK signal space is graphical displayed in Figure 5.12.

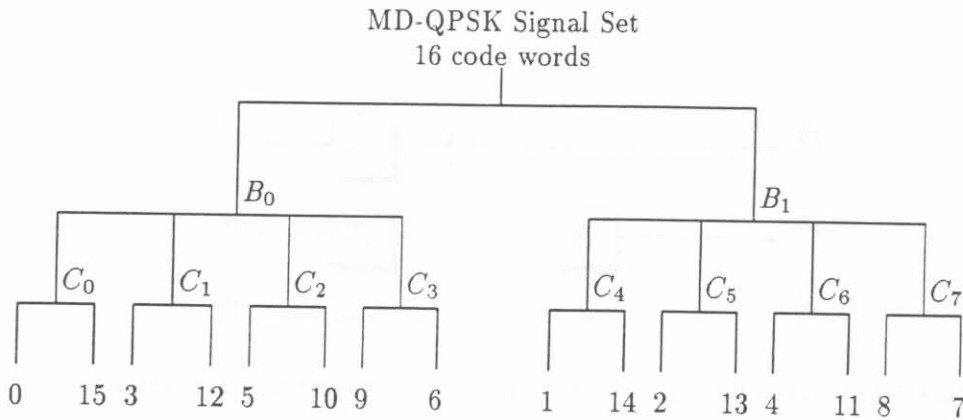


Figure 5.12: Q<sup>2</sup>PSK signal space partition tree.

In the design of the rate 3/4 and rate 2/4 Q<sup>2</sup>PSK trellis codes, the original 4D Q<sup>2</sup>PSK constellation (i.e. unexpanded) is utilised. Therefore, coding gains are obtained by sacrificing the effective data rate of the system.

For small code memory codes, the design can be produced "by hand", following the set partitioning concepts of Ungerboeck and then applying the analytical code design approach, presented in Appendix A. For more complex codes, say with more than 32 trellis states, a computer search for maximal free distance codes is definitely warranted. However, it will be shown that surprisingly large coding gains can be achieved with simple rate 3/4 and 2/4 TCM "hand" code designs.

### 5.3.1 Rate 3/4 Q<sup>2</sup>PSK/TCM

In the following section, the design of codes for rate 3/4 TCM are carried out. The 3/4 code rate implies that the information transmission rate is reduced by a factor of 3/4, resulting in a bandwidth efficiency of 1.5 *bits/s/Hz*, compared to the 2.0 *bits/s/Hz* of the uncoded case.

#### 5.3.1.1 8-State Code design

The code structure for the half-connected code is presented in Figure 5.13, defining the sliding block of source variables ( $b_1, b_2, b_3, b_4, b_5, b_6$ ). The trellis diagram illustrated in Figure 5.14, has been labeled with the Q<sup>2</sup>PSK code words (presented in Figures 5.10 and 5.11), and the variables of the sliding block, ( $b_1, b_2, \dots, b_6$ ) taking on the values 0 or 1. For the rate 3/4 code, the 3 input bits ( $b_1, b_2, b_3$ ) are input to the encoder, producing the 4 output bits ( $b_1, b_4, b_5, b_6$ ). The values of the output bits are not only determined by the current input bits, but also the encoder state formed by bits ( $b_4, b_5, b_6$ ). The 4-tuple code word ( $b_1, b_4, b_5, b_6$ ) produced, must then be converted to values of  $\pm 1$  instead of 0 and 1, producing a Q<sup>2</sup>PSK symbol being output as presented in Figures 5.10 and 5.11.

Substituting the coder output code words for the Q<sup>2</sup>PSK code words, and by using the Calderbank—Mazo algorithm (presented in Appendices A and B), the following solutions for the  $D$  matrix is

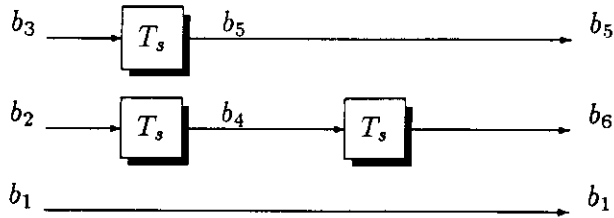


Figure 5.13: Inputs and state variables for the half-connected 8-state code.

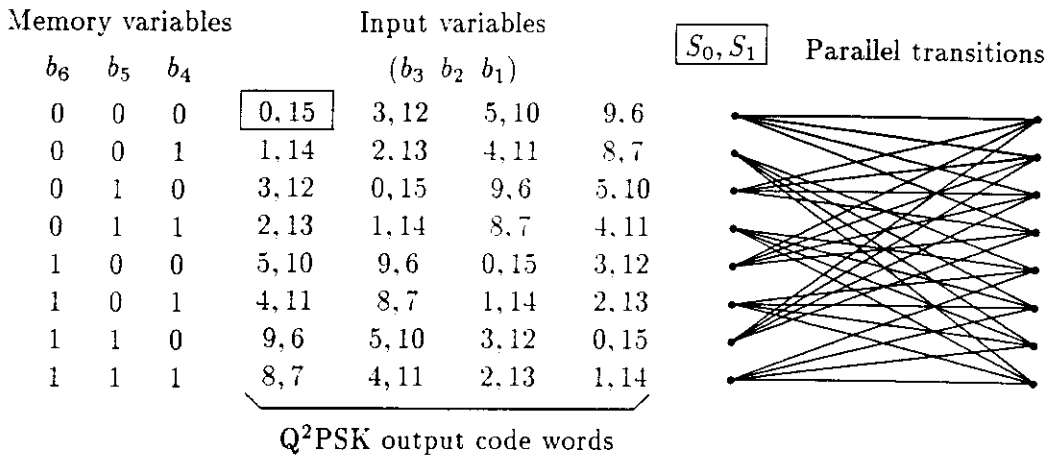


Figure 5.14: Half-connected  $R = 3/4$  8-state trellis code.

obtained:

$$d_1 = 8, d_4 = -1, d_{25} = -2, d_{36} = -4 \tag{5.8}$$

The analytical description of the encoder is:

$$X = 8b_1 - b_4 - 2b_2b_5 - 4b_3b_6 \tag{5.9}$$

where  $X$  denotes the coder output code word.

The achievable coding gain of the 8-state code is limited by parallel transitions which occur when two different symbols can cause a transition along the same trellis branch. The minimum free distance,  $d_{free}^2$  of the code is equal to  $d_{free,c}^2 = 8E_b$ , where  $E_b$  is the average energy per bit in the coded signals. (For uncoded Q<sup>2</sup>PSK the minimum free distance,  $d_{free,u}^2 = 4E_b$ ). Therefore an asymptotic coding gain (defined in (A.4)),  $\gamma_c = 10 \log_{10} d_{free,c}^2/d_{free,u}^2 = 10 \log_{10} 8E_b/4E_b = 3.01$  dB is obtained for the 8 state trellis codes, given by a length  $L = 1$  Error Event Path (EEP).

The code structure for the fully-connected code is presented in Figure 5.15, again defining the sliding block of source variables ( $b_1, b_2, b_3, b_4, b_5, b_6$ ). No parallel transition is included in the code structure. The corresponding trellis diagram is illustrated in Figure 5.16.

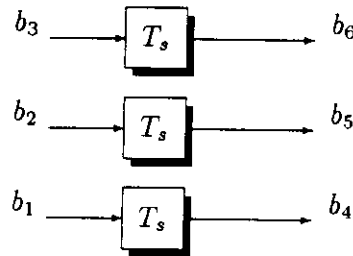


Figure 5.15: Inputs and state variables for fully-connected 8-state code.

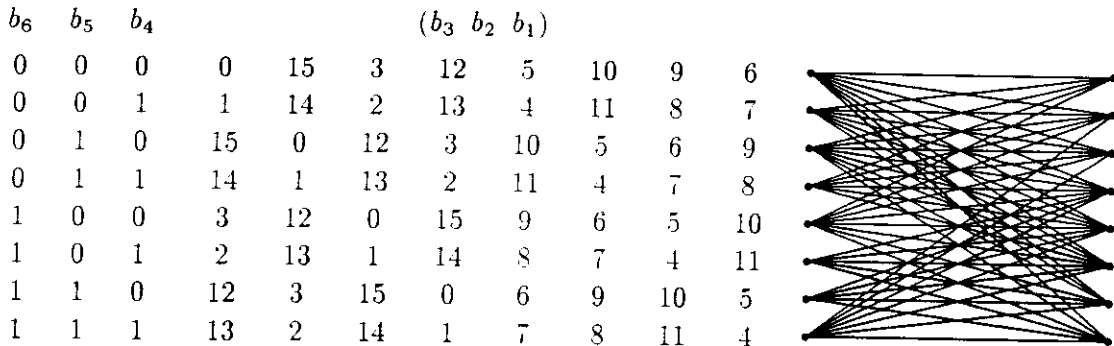


Figure 5.16: Fully-connected  $R = 3/4$  8-state trellis code.

The  $d_{free}^2$  of the code is equal to  $12E_b$ , representing an asymptotic coding gain of  $10 \log_{10} 12/4 = 4.77$  dB achievable with this 8 state trellis codes. The EEP is  $L = 3$ , since the code performance is not limited by parallel transitions.

### 5.3.2 Rate 2/4 Q<sup>2</sup>PSK/TCM

In the following discussion, the design of codes for rate 2/4 TCM are carried out. The information transmission rate is reduced by a factor of 2/4, resulting in a reduction in bandwidth efficiency to

1.0 bits/s/Hz. In the design of the new rate 2/4 Q<sup>2</sup>PSK trellis codes, selecting code words from the Q<sup>2</sup>PSK code words that maintain odd parity, a constant envelope Q<sup>2</sup>PSK signal is obtained which improves performance on non-linear channels.

Learning from the experience gained from the Rate-3/4 code designs, we consider in the following only coders excluding parallel transitions in their trellis structures. The code structures for the half-rate coders are presented in Figure 5.17, defining the sliding block of source variables ( $b_1, \dots, b_6$ ).

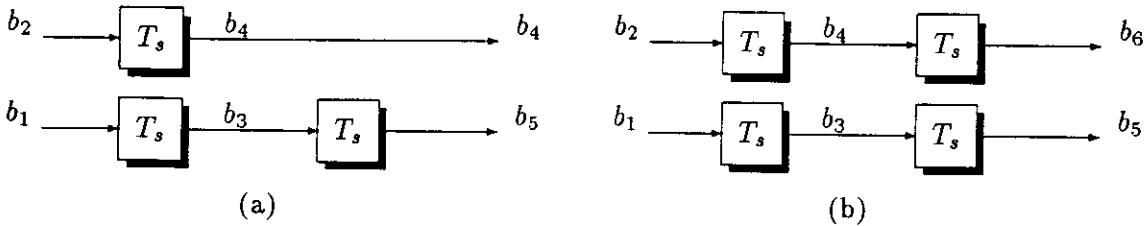


Figure 5.17: Code structures for half-rate trellis coders.

### 5.3.2.1 Non-Constant Envelope

$b_5$	$b_4$	$b_3$		$(b_2 \ b_1)$		
0	0	0	0	15	3	12
0	0	1	1	14	2	13
0	1	0	5	10	9	6
0	1	1	4	11	8	7
1	0	0	15	0	12	3
1	0	1	14	1	13	2
1	1	0	10	5	6	9
1	1	1	11	4	7	8

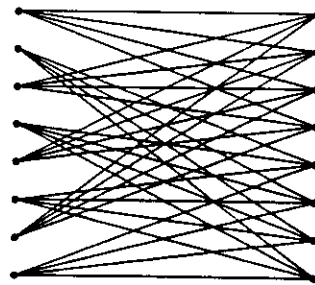


Figure 5.18: Half-connected  $R = 2/4$  8-state trellis code.

The trellis diagram of the 8-state code is illustrated in Figure 5.18, leading to the analytical description of the encoder, given by:

$$X = 8b_1b_5 - 4b_4 - 2b_2 - b_3 \tag{5.10}$$

The analytical description of the encoder, depicted in Figure 5.19 is given by:

$$X = 7b_1b_5 - 3b_4 - b_2b_6 - b_3 \tag{5.11}$$

Half rate trellis codes for Q<sup>2</sup>PSK signals have been reported by Saha and Acha [47, 23, 48], different 2, 8 and 16 state trellis codes were designed, and asymptotic coding gains up to 6.0 dB were calculated. However, a closer examination of the 2/4 rate codes proposed by Saha revealed a few

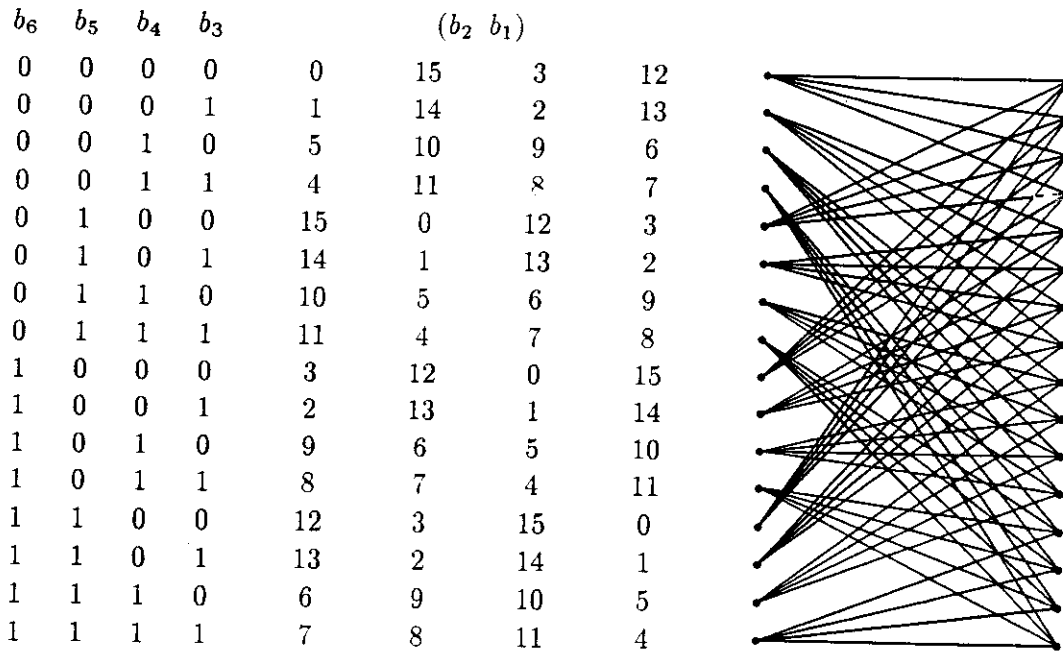


Figure 5.19: Quarter-connected  $R = 2/4$  16-state trellis code.

catastrophic deficiencies. Firstly, the trellis labeling proposed by Saha for the 2 state  $2/4$  rate code leads to catastrophic error propagation. This can be attributed to the fact that Saha incorporated no redundant information into the symbol sequences, resulting in infinite error propagation.

### 5.3.2.2 Constant Envelope

The analytical description of the encoder, depicted in Figure 5.20, is given as:

$$X = 7b_1b_5 - 3b_4 - b_2b_6 - b_3 \quad (5.12)$$

The squared minimum distance,  $d_{free}^2$  of this code is equal to  $24E_b$  resulting in an asymptotic coding gain of  $10 \log_{10} 16/4 = 6.02$  dB. Note, that the coding gain of this 8-state code is not limited by parallel transitions and that the number of nearest neighbors at a distance of  $d_{free}$ , is reduced from 4 to 2.

### 5.3.3 $Q^2$ PSK/TCM code performance

In this section the performance evaluation of TCM systems when utilised on AWGN channels are derived. The classical performance measure for TCM, is the asymptotic coding gain, which is directly determined by the MSED of the code (see Appendix A). While this is an indication of the limit of the code performance, it can be an unreliable measure to use under practical operational conditions. For this reason, performance evaluation of trellis coded systems are usually accomplished by derivation of the upper and lower bounds of the code if the convolutional coders are linear.

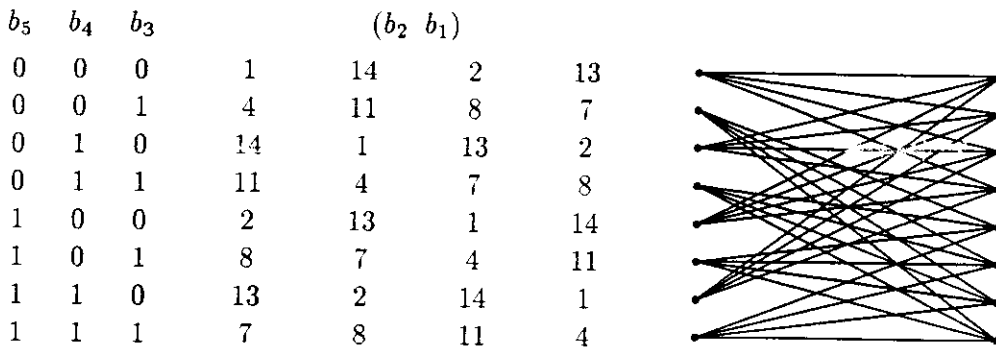


Figure 5.20: Half-connected  $R = 2/4$  8-state trellis code for Constant Envelope (CE)  $Q^2$ PSK.

If the code is non-linear theoretical performance calculation becomes extremely cumbersome, and computer simulations are commonly used to evaluate code performance.

In the following section upper bounds for TCM schemes are derived when employed on the AWGN channel based on the so-called transfer function bound [30]. Furthermore, we will discuss the application of a new algebraic algorithm for generating the transfer function of a trellis encoder, proposed by Chan and Norton [79] (presented in detail in Appendix C).

There are basically two ways to generate the transfer function. The first one is by graphical means — the state diagram is first drawn and properly labeled. The transfer function can then be found by a graph-reduction technique, or Mason's rule. The second approach is algebraic, i.e., solving state equations, or performing matrix inversion. All of these methods have a common difficulty: The complexity of calculation increases exponentially as the number of encoder states increases.

### 5.3.4 Analytical upper performance bounds for $Q^2$ PSK/TCM

As an example we consider the derivation of the tight upper bound on BEP for the 8-state fully-connected rate-3/4 trellis code presented earlier in this chapter (see section 5.3.1).

In order to calculate the transfer function one has to utilise the error weight profiles, and the trellis diagram showed in Figure 5.15. The error weights are easily calculated as defined according to (A.18) for the error vector  $\bar{e} = (e_1, e_2, e_3, e_4)$ , and are given by

$$\begin{aligned}
 W(0000) &= 1 & W(0001) &= D^4 & W(0010) &= D^4 & W(0011) &= D^8 \\
 W(0100) &= D^4 & W(0101) &= D^8 & W(0110) &= D^8 & W(0111) &= D^{12} \\
 W(1000) &= D^4 & W(1001) &= D^8 & W(1010) &= D^8 & W(1011) &= D^{12} \\
 W(1100) &= D^8 & W(1101) &= D^{12} & W(1110) &= D^{12} & W(1111) &= D^{16}
 \end{aligned} \tag{5.13}$$

Following the algebraic approach described in Appendix C, the transfer function of this encoder (after some intermediate algebra) is given by

$$T(D) = \frac{D^{20} + 24D^{36} - 16D^{18} + 48D^8 + 24D^{24}}{2 + 18D^4 - 8D^8 + D^{12}} \tag{5.14}$$

By substituting  $D = \exp(-E_b/N_o)$  in equation (5.14), one obtains the upper bound (UB1) to the BEP. The derivation of the tighter upper bound (UB2) requires knowledge of the minimum free distance,  $d_{free}$  of the code, which was computed by the algorithm proposed by Mulligan and Wilson [80], and discussed in Appendix B. The calculation gave  $d_{free} = 3.464$ . Substituting the values for  $D$  and  $d_{free}$  into equation (A.21), the tighter upper bound (UB2) is obtained.

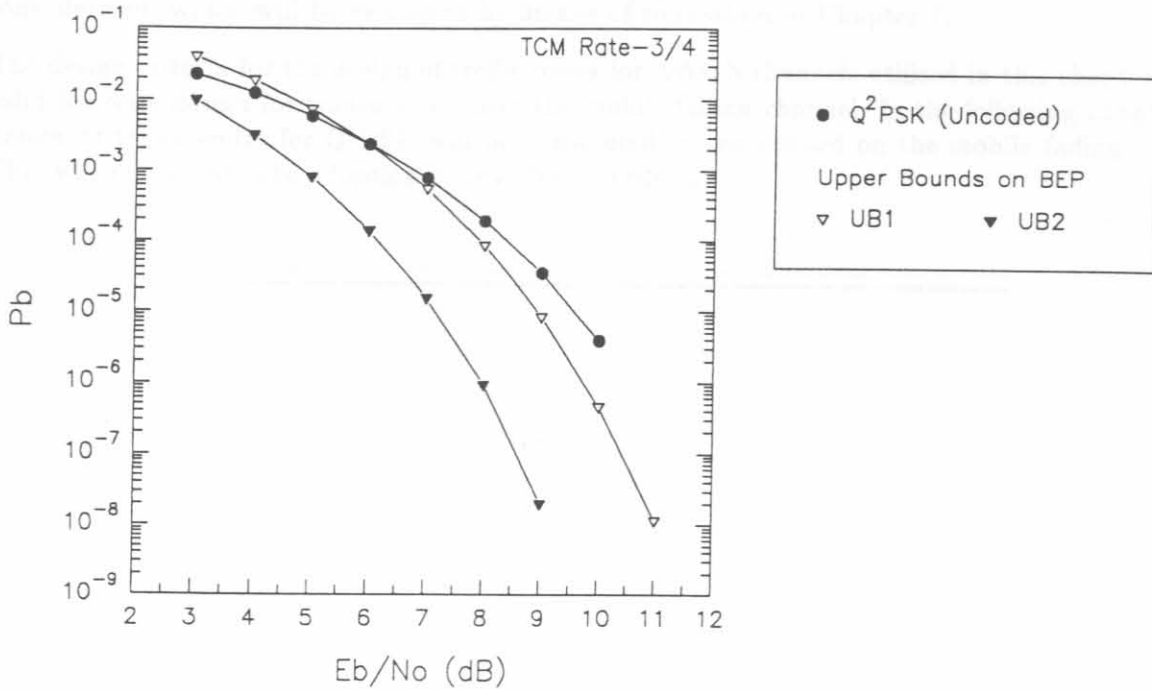


Figure 5.21: Upper bounds to bit error probabilities for 8-state rate-3/4 Q<sup>2</sup>PSK/TCM.

The calculated upper bounds to the BEP have been calculated for this trellis coder and are shown in Figure 5.21. The curve defined as UB1 denotes the upper bound calculated by equation (A.20), and that defined as UB2 corresponds to the bound calculated with (A.21), i.e., the tighter bound on the BEP.

## 5.4 CONCLUDING REMARKS: CHAPTER 5

In this chapter the designs of classical and TCM codes were carried out, performed for a Q<sup>2</sup>PSK system when utilised on the AWGN channel.

For the classical code designs, low-complexity sub-optimal convolutional encoding schemes were proposed for Q<sup>2</sup>PSK. Three coding schemes were presented: The first scheme employs a single rate-3/4 convolutional encoder, yielding a effective data rate of 3/4 uncoded Q<sup>2</sup>PSK. The second encoding scheme, with so called *dual-use* of conventional 2D signals, employs two rate-1/2 convolutional encoders. At the receiver two soft-decision Viterbi decoders are utilised in parallel. Finally, a third encoding scheme was proposed, employing a hybrid convolutional-block coding scheme. The encoder consists of a rate-2/3 convolutional encoder, followed by a simple block encoding scheme to produce a constant envelope. At the receiver a single soft-decision Viterbi decoder, together with a block decoding scheme, is employed. Performance estimates of these classical coders were



carried out based on the union bound technique. Upper bounds to BEP were derived. In Chapter 7 these bounds will be benchmarked against actual simulation curves.

The final sections of this chapter dealt with the design of TCM codes for  $Q^2$ PSK when utilised on the AWGN channel. For these channels, the parameter to be maximised, is the Euclidean distance of the TCM code. The designs and realisations for rate 3/4 and 2/4 "hand designed" trellis codes were presented. In addition, upper bounds on the BEP for a specific 8-state rate 3/4 trellis code were derived, which will be evaluated by means of simulation in Chapter 7.

The design criteria for the design of trellis codes for AWGN channels utilised in this chapter, is not valid for code design for transmission over the mobile fading channel. In the following chapter, the design of trellis codes for  $Q^2$ PSK will be considered, when utilised on the mobile fading channel. This will necessitate the adoption of new design criteria.

## DESIGN OF TCM AND MTCM FOR FADING CHANNELS

## CHAPTER 6

---

# DESIGN OF TCM AND MTCM FOR FADING CHANNELS

---

---

In this chapter the design of Multiple-Trellis Coded Modulation (MTCM) for Q<sup>2</sup>PSK is presented when transmitted over a fading channel. Although, both Rician and Rayleigh fading channels are considered, most of this section is concerned with the design for transmission over the Rician channel. The latter choice has been made in view of the fact that the distortion introduced by the Rayleigh channel requires the use of an adaptive equaliser which does not form part of this study.

Digital communications over mobile channels often suffers from multipath effects, which results in signal fading. Multipath fading plagues the propagation medium by imposing random amplitude and phase variations onto the transmitted waveform. It is well known that this fading degrades the performance of the communications systems. Therefore, this research is primarily concerned with the application of MTCM to Q<sup>2</sup>PSK in order to achieve superior performance on the fading channel, compared to that achievable by conventional (single channel symbol per trellis branch) TCM of the same throughput and decoder complexity.

Divsalar and Simon did some excellent work on the effects of fading in M-PSK signals [39, 81]. They showed that whereas maximising free Euclidean distance ( $d_{free}$ ) is the optimum criterion on the AWGN channel, in the case of fading channels (specifically Rician) with interleaving/deinterleaving, the asymptotic (high SNR) performance of TCM is dominated by several other factors. These factors are categorised as primary and secondary considerations and depends on the value of the Rician parameter,  $K$ . Specifically, for small values of  $K$ , the primary design criteria become

- the *length* of the shortest error event path (measured in number of symbols), and

- the *product* of branch distances along that path, with  $d_{free}$  a secondary consideration.

As  $K$  increases, the significance of these primary and secondary considerations shift relative to one another until  $K$  reaches infinity (AWGN channel), in which case optimum performance is once again achieved by trellis code designed solely to maximise  $d_{free}$ .

In this section attention is focused on implementing the foregoing considerations in the design and implementation of trellis codes for  $Q^2$ PSK to give optimum performance on the fading channel. The design of Multiple Trellis Coded Modulation (MTCM) codes is considered, since the diversity potential offered by the latter codes is fully exploited by the fading channel.

## 6.1 MULTIPLE TRELIS CODED MODULATION

Recall that with conventional trellis coding (i.e., one symbol per trellis branch), the length  $L$  of the shortest EEP is equal to the number of trellis branches along that path. Equivalently, if it is assumed that the all-zeros path in the trellis diagram represents the transmitted sequence,  $L$  is the number of branches in the shortest path to which a nonzero symbol is associated. Since a trellis diagram with parallel paths is constrained to have a shortest error event path of one branch, thus  $L = 1$ . This implies that asymptotic region of the graph of expected (average) bit error probability will vary *inverse linearly* with  $\overline{E}_s/N_o$  or  $E_s/N_o$ , since  $\overline{E}_s = E_s$  [30]. Therefore, from an error probability viewpoint it is undesirable to design conventional TCM codes to have parallel paths in their trellis diagrams. Unfortunately, for a convolutional code of rate  $m/(m+1)$ , when  $2^m$  exceeds the number of states, one is forced to utilise a trellis containing parallel paths.

When MTCM is employed, the option of designing a trellis diagram with parallel paths may again be considered, since achieving an asymptotic performance on the fading channel which varies inversely with  $\overline{E}_s/N_o$  at a rate faster than linear may now be achieved. The reason behind this lies in the fact that even if parallel paths exist in the trellis, it is now possible to have more than one coded symbol with nonzero Euclidean distance associated with an EEP branch of length,  $L = 1$ .

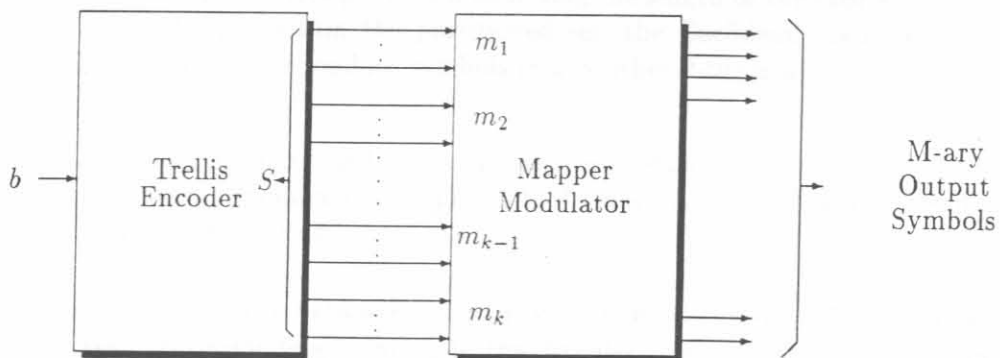


Figure 6.1: Generalised MTCM transmitter.

In its most general form, MTCM is implemented by an encoder with  $b$  binary input bits and  $s$  binary output bits that are mapped into  $k$   $Q^2$ -ary symbols in each transmission interval, illustrated in Figure 6.1. The parameter  $k$  is referred to as the *multiplicity* of the code, since it represents the number of  $Q^2$ -ary symbols allocated to each branch in the trellis diagram ( $k = 1$  corresponds to

conventional TCM). To produce such a result, the  $s$  binary encoder output bits are partitioned into  $k$  groups containing  $m_1, m_2, \dots, m_k$  symbols. Each of these groups, through a suitable mapping function, results in an  $Q^2$ -ary output symbol. The transmitter parameters are constrained such that

$$s = k \log_2 M \quad (6.1)$$

where  $M = 16$  for  $Q^2$ PSK, without expanded signal set (note that  $M = 32$  when an expanded signal set is utilised). The throughput of the MTCM transmitter is given by  $r = b/k$  bits/s/Hz, which is not necessarily integer-valued.

### 6.1.1 Ungerboeck Set Partitioning: From *Root-to-Leaf*

In the design of the trellis codes a procedure similar to that presented in [30], known as the *Ungerboeck: Root-to-Leaf* approach, has been followed. The method, makes use of  $k$ -fold Cartesian products of the sets found in Ungerboeck's original set-partitioning method for conventional trellis codes [27]. The set-partitioning procedure is started with a  $k$ -fold Cartesian product of the complete  $Q^2$ PSK signal set.

Attention is focused on the design of a code with multiplicity,  $k = 2$ . Let  $A_0$  denotes the complete  $Q^2$ PSK signal set (i.e., signal points  $0, 1, \dots, M-1 = 15$ ) and  $A_0 \otimes A_0$  denote the two-fold Cartesian product of  $A_0$  with itself. (Note, that for a multiplicity,  $k = 4$ , the process should have started with the four-fold Cartesian product set,  $A_0 \otimes A_0 \otimes A_0 \otimes A_0$ ). Thus, an element of the set  $A_0 \otimes A_0$  is a 2-tuple, denoted by  $(j_1, j_2)$ , with symbols chosen from the set  $A_0$ . The first step is to partition  $A_0 \otimes A_0$  into  $M$  signal sets defined by the ordered Cartesian product  $\{A_0 \otimes B_i\}$ ,  $i = 0, 1, \dots, M-1$ . The second element  $\{j_2\}$  of  $B_i$  is defined by  $nj + i \pmod{M}$ . Thus, the  $j$ -th 2-tuple from the product  $A_0 \otimes B_i$  is the ordered pair  $(j_1 = j, j_2 = nj + i)$ .

The first partitioning step has two purposes. These are summarised below [30]:

- Firstly, it guarantees that within any of the  $M$  partitions, each of the two symbol positions has distinct elements, from the viewpoint of maximising the length of the shortest error event path. That is, for a 2-tuple within the partitioned set, the Euclidean distance of each of the two symbols from the corresponding symbols in any other 2-tuple within the same set is nonzero.
- Secondly, it accomplishes a minimum Euclidean distance *product* between 2-tuples within the partitioned set (i.e., the minimum of the product of the distances between corresponding 2-tuple symbol pairs) is maximised.

Since the squared Euclidean distance between any pair of 2-tuples is the sum of the squared Euclidean distances between corresponding symbols in the 2-tuples, the set partitioning guarantees that the *intradistance* (i.e., distance between pairs within a specific set or partition) of all of the partitions  $A_0 \otimes B_i$  is identical. It is, therefore, sufficient to study the distance structure of  $A_0 \otimes B_0$ , referred to as the *generating set* by Biglieri et al.[30]. For this set, the minimum product of squared distances over all pairs of 2-tuples in  $A_0 \otimes B_0$ ,  $\prod d_i^2$ , must be maximised. This is done by choosing the odd integer multiplier,  $n$  such that it produces a *maximin* solution. A computer search for possible values of  $n$  to be utilised, revealed the solution as  $n = 11$ . In [30] it was stated that the *additive inverse* of  $n$ , denoted by  $n^* = M - n$ , could also have been used. However, in our design the solution for  $n^*$  does not produce optimum (i.e., maximum) intradistances. The ordered Cartesian

product set,  $A_0 \otimes A_0$ , together with the generating set,  $A_0 \otimes B_0$  are illustrated below for Q<sup>2</sup>PSK with  $M = 16$ .

$$A_0 \otimes A_0 = \begin{bmatrix} 0 & 0 & 8 & 8 \\ 1 & 1 & 9 & 9 \\ 2 & 2 & 10 & 10 \\ 3 & 3 & 11 & 11 \\ 4 & 4 & 12 & 12 \\ 5 & 5 & 13 & 13 \\ 6 & 6 & 14 & 14 \\ 7 & 7 & 15 & 15 \end{bmatrix} \quad A_0 \otimes B_0 = \begin{bmatrix} 0 & 0 & 8 & 8 \\ 1 & 11 & 9 & 3 \\ 2 & 6 & 10 & 14 \\ 3 & 1 & 11 & 9 \\ 4 & 12 & 12 & 4 \\ 5 & 7 & 13 & 15 \\ 6 & 2 & 14 & 10 \\ 7 & 13 & 15 & 5 \end{bmatrix} \quad (6.2)$$

The sets obtained by this first partition, each with minimum intradistance of  $8.0E_b$ , are illustrated in Appendix D, for  $n = 11$ . The *interdistances* (i.e., minimum distances between pairs of 2-tuples from different sets), for these sets are summarised in Table 6.1 below.

**Table 6.1:** Interdistances between partitioned subsets, with  $A_0 \otimes B_0$  used as reference.

Subset	Distance	Subset	Distance
$A_0 \otimes B_0$	—	$A_0 \otimes B_8$	$4.0E_b$
$A_0 \otimes B_1$	$4.0E_b$	$A_0 \otimes B_9$	$8.0E_b$
$A_0 \otimes B_2$	$4.0E_b$	$A_0 \otimes B_{10}$	$8.0E_b$
$A_0 \otimes B_3$	$8.0E_b$	$A_0 \otimes B_{11}$	$8.0E_b$
$A_0 \otimes B_4$	$4.0E_b$	$A_0 \otimes B_{12}$	$4.0E_b$
$A_0 \otimes B_5$	$8.0E_b$	$A_0 \otimes B_{13}$	$8.0E_b$
$A_0 \otimes B_6$	$8.0E_b$	$A_0 \otimes B_{14}$	$4.0E_b$
$A_0 \otimes B_7$	$8.0E_b$	$A_0 \otimes B_{15}$	$4.0E_b$

The second step in the set partitioning procedure for MTCM design also differs somewhat from the traditional set partitioning procedure. The second step should guarantee that the resulting sets, of dimensionality  $M/2$ , have an intradistance product structure equal to that achieved by the first-level partitioning in accordance with the requirement to achieve a *maximin* Euclidean distance. In the second step of set partitioning  $M$  is replaced by  $M/2$ .

In order to perform the set partitioning, another odd integer multiplier, denoted by  $n'$  is introduced such that it again results in a maximin solution. A computer search revealed the optimum solution for the second level multiplier as  $n' = 3$ . Note that if one of the solutions for  $n'$  (or its additive inverse  $n'^{-1}$ ) is equal to the solution of the first level multiple,  $n$ , when  $M$  is replaced by  $M/2$ , then the first two levels follow a *tree structure*. Since, this is not the case here, the sets formed by the second level partition have to be recalculated, repeating the procedure followed in the first partitioning. The two subsets,  $C_0 \otimes D_{0a}$  and  $C_0 \otimes D_{0b}$ , resulting from partitioning set  $A_0 \otimes B_0$ , are shown in (6.3); the complete partitioned subsets are given in Appendix D. The *interdistances* for these sets, with reference to subset  $C_0 \otimes D_{0a}$ , are summarised in Table 6.2 below. Each of the subsets have a minimum intradistance of  $8.0E_b$ , corresponding to the sets formed by the first partitioning step.

<sup>1</sup>Additive inverse,  $n'^{-1}$  is given as  $M - n'$ .

$$C_0 \otimes D_{0a} = \begin{bmatrix} 0 & 0 & 4 & 8 \\ 1 & 6 & 5 & 14 \\ 2 & 12 & 6 & 4 \\ 3 & 2 & 7 & 10 \end{bmatrix} \quad C_0 \otimes D_{0b} = \begin{bmatrix} 0 & 3 & 4 & 11 \\ 1 & 9 & 5 & 1 \\ 2 & 15 & 6 & 7 \\ 3 & 5 & 7 & 13 \end{bmatrix} \quad (6.3)$$

**Table 6.2:** Interdistances between partitioned subsets, with  $C_0 \otimes D_{0a}$  used as reference.

Subset	Distance	Subset	Distance
$C_0 \otimes D_{0a}$	—	$C_0 \otimes D_{0b}$	$12.0E_b$
$C_0 \otimes D_{1a}$	$4.0E_b$	$C_0 \otimes D_{1b}$	$12.0E_b$
$C_0 \otimes D_{2a}$	$4.0E_b$	$C_0 \otimes D_{2b}$	$16.0E_b$
$C_0 \otimes D_{3a}$	$8.0E_b$	$C_0 \otimes D_{3b}$	$12.0E_b$
$C_0 \otimes D_{4a}$	$4.0E_b$	$C_0 \otimes D_{4b}$	$16.0E_b$
$C_0 \otimes D_{5a}$	$8.0E_b$	$C_0 \otimes D_{5b}$	$12.0E_b$
$C_0 \otimes D_{6a}$	$4.0E_b$	$C_0 \otimes D_{6b}$	$12.0E_b$
$C_0 \otimes D_{7a}$	$4.0E_b$	$C_0 \otimes D_{7b}$	$8.0E_b$
$C_0 \otimes D_{8a}$	$0.0E_b$	$C_0 \otimes D_{8b}$	$12.0E_b$
$C_0 \otimes D_{9a}$	$4.0E_b$	$C_0 \otimes D_{9b}$	$12.0E_b$
$C_0 \otimes D_{10a}$	$4.0E_b$	$C_0 \otimes D_{10b}$	$16.0E_b$
$C_0 \otimes D_{11a}$	$8.0E_b$	$C_0 \otimes D_{11b}$	$12.0E_b$
$C_0 \otimes D_{12a}$	$4.0E_b$	$C_0 \otimes D_{12b}$	$16.0E_b$
$C_0 \otimes D_{13a}$	$8.0E_b$	$C_0 \otimes D_{13b}$	$12.0E_b$
$C_0 \otimes D_{14a}$	$4.0E_b$	$C_0 \otimes D_{14b}$	$12.0E_b$
$C_0 \otimes D_{15a}$	$4.0E_b$	$C_0 \otimes D_{15b}$	$8.0E_b$

The set partitioning procedure is illustrated in Figure 6.2 for  $k = 2$ . To extend the previous procedure to higher multiplicity of order  $k \geq 2$ , simply form the  $k/2$ -fold ordered Cartesian product of all the sets on a given partition level created by the procedure for  $k = 2$ . The result of this procedure is illustrated in Figure 6.3 for  $k = 4$ .

6.2 QPSK/TMCM CODE DESIGN

6.2.1 Design of 4-State Rate 1/2 Codes

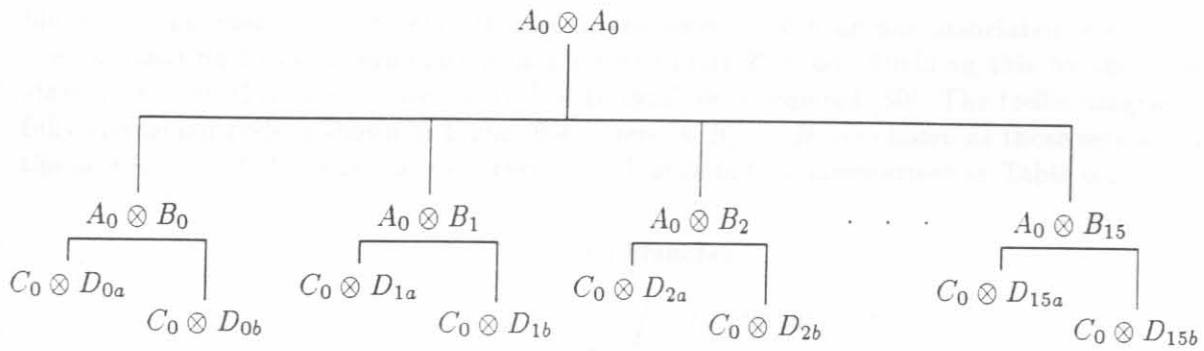


Figure 6.2: Set partitioning method for multiple ( $k = 2$ ) trellis codes on the fading channel.

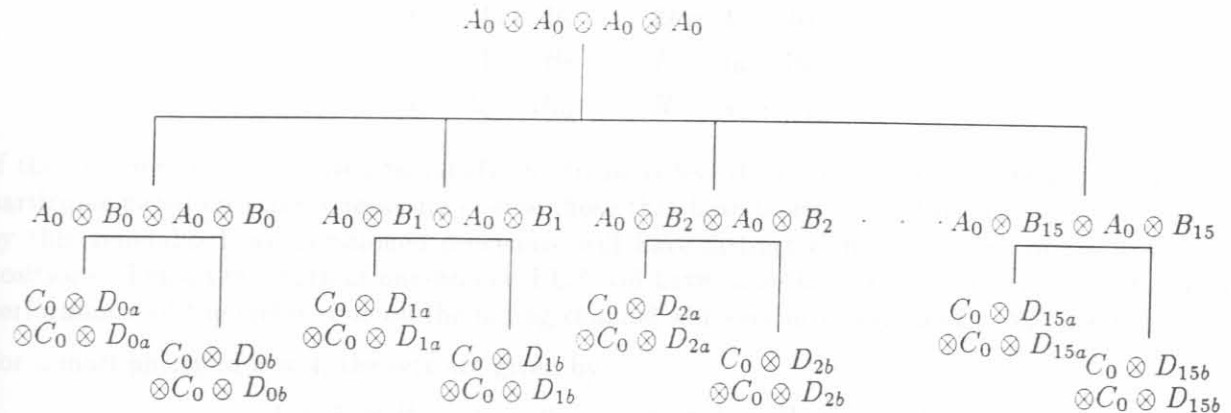


Figure 6.3: Set partitioning method for multiple ( $k = 4$ ) trellis codes on the fading channel.

## 6.2 Q<sup>2</sup>PSK/MTCM CODE DESIGN

### 6.2.1 Design of 4-State Rate 6/8 codes

In this section the design of a 4-state trellis code, with multiplicity  $k = 2, 4$ , is discussed. Two Q<sup>2</sup>PSK symbols are transmitted over the channel for each 6 bits accepted by the encoder. Hence, the throughput of the system is lowered by a factor 8/6, resulting in a spectral efficiency of 1.5 bits/s/Hz, compared to the 2.0 bits/s/Hz of the uncoded system.

Since, the number of input bits are  $b = 6$ , the number of branches associated with each state (i.e., emanating from or terminating in a node) equals  $2^6 = 64$ . Dividing this by the number of states, i.e., 4 in this case, a cardinality<sup>2</sup> of 16 symbols is required [30]. The trellis diagram of this fully-connected code is shown in Figure 6.4, where  $A, B, \dots, H$  are chosen as those sets which have the largest *interdistance* in the construction of Figure 6.2, as summarised in Table 6.1.

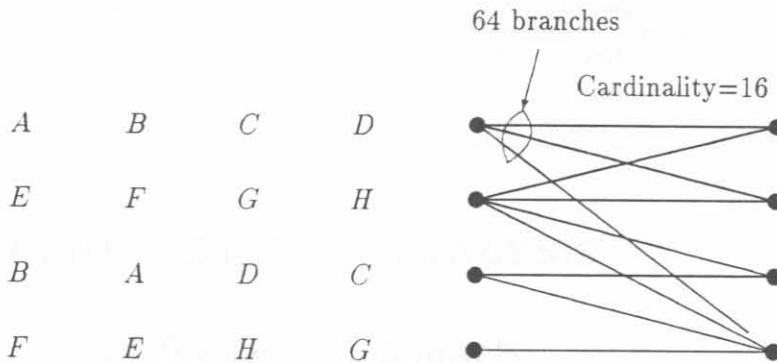


Figure 6.4: Rate-6/8 4-state Q<sup>2</sup>PSK/MTCM

Thus, for a multiplicity of  $k = 2$ , the sets are given by

$$\begin{aligned}
 A &= A_0 \otimes B_0 & B &= A_0 \otimes B_3 \\
 C &= A_0 \otimes B_5 & D &= A_0 \otimes B_6 \\
 E &= A_0 \otimes B_7 & F &= A_0 \otimes B_9 \\
 G &= A_0 \otimes B_{10} & H &= A_0 \otimes B_{11}
 \end{aligned} \tag{6.4}$$

If the number of sets required to satisfy the trellis is less than the number of sets generated on a particular partition leave, one would choose those that have largest *interdistance*. The sets formed by this generalised set-partitioned procedure will have distinct elements in any of the  $k$  symbol positions. Thus, the length of one-branch EEP will have value  $k$ , and hence the asymptotic BER performance of the trellis code on the fading channel will vary inversely as  $(\overline{E}_s/N_o)^n$ , with  $n \geq k$ .

For a multiplicity of  $k = 4$ , the sets are given by

$$\begin{aligned}
 A &= A_0 \otimes B_0 \otimes A_0 \otimes B_0 & B &= A_0 \otimes B_3 \otimes A_0 \otimes B_3 \\
 C &= A_0 \otimes B_5 \otimes A_0 \otimes B_5 & D &= A_0 \otimes B_5 \otimes A_0 \otimes B_6 \\
 E &= A_0 \otimes B_7 \otimes A_0 \otimes B_7 & F &= A_0 \otimes B_9 \otimes A_0 \otimes B_9 \\
 G &= A_0 \otimes B_{10} \otimes A_0 \otimes B_{10} & H &= A_0 \otimes B_{11} \otimes A_0 \otimes B_{11}
 \end{aligned} \tag{6.5}$$

<sup>2</sup>The cardinality is a number used to represent the size of a subset.



Several MTCM code designs were carried out. The designs are summarised in Table 6.3.

Table 6.3: Design summary for Q<sup>2</sup>PSK/MTCM.

Code Rate $R_c$	Branches per State	Number of States	Connectivity	Multiplicity $k$	Required Cardinality
6/8	64	4	Fully	2	$\geq 16$
5/8	32	4	Fully	2	$\geq 8$
4/8	16	4	Half	2	$\geq 8$
6/16	64	4	Fully	4	$\geq 16$
5/16	32	4	Fully	4	$\geq 8$
4/16	16	4	Half	4	$\geq 8$
6/8	64	8	Half	2	$\geq 8$
5/8	32	8	Half	2	$\geq 4$
4/8	16	8	Quarter	2	$\geq 4$
6/16	64	8	Half	4	$\geq 8$
5/16	32	8	Half	4	$\geq 4$
4/16	16	8	Quarter	4	$\geq 4$

## 6.3 PERFORMANCE ANALYSIS

### 6.3.1 TCM for fading channels

It was shown by Biglieri et al. [30] that the asymptotic pairwise error performance for coherent detection varies inversely with  $(E_s/N_0)^{L_\eta}$ .  $L_\eta$  is the smallest number of elements with non-zero pairwise distances between the symbols along its branches and those along the correct path. Evaluation of the pairwise probability depends on the proposed decoding metric, the presence or absence of Channel State Information (CSI), and the type of detection used. In [30] the relation between the asymptotic behavior of the pairwise error probability to that of the BEP is approximately given by

$$P_b \cong \frac{1}{b} C \left( \frac{(1+K)e^{-K}}{E_s/N_0} \right)^{L_\eta}, \quad E_s/N_0 \gg K \quad (6.6)$$

where  $b$  is the number of bits transmitted per branch in the trellis,  $K$  is the Rician parameter and  $C$  is a constant that depends on the distance structure of the code, defined as [30]

$$C = \begin{cases} 4^{L_\eta} \left[ \prod_{n \in \eta} |x_n = \hat{x}_n|^2 \right]^{-1} & \text{Coherent detection with ideal CSI} \\ \left( \frac{2e}{L_\eta} \right)^{L_\eta} \left( \prod_{n \in \eta} \frac{|x_n = \hat{x}_n|^2}{\left( \sum_{n \in \eta} |x_n = \hat{x}_n|^2 \right)^{1/2}} \right)^{-2} & \text{Coherent detection with no CSI} \end{cases} \quad (6.7)$$

From the above it may be concluded that the primary objective for good trellis code design on the fading channel is the maximisation of the number of symbols with non-zero ED between the error and correct paths, denoted by  $L_\eta$ .

As an example the rate-3/4 trellis coded Q<sup>2</sup>PSK with 8-state trellis diagram is considered, corresponding to the design carried out in the previous chapter (see Figure 5.14). Referring to the state diagram of Figure 5.14, the shortest EEP branches is of length,  $L = 3$ , and all of these have nonzero distance with respect to the branches of the correct path (assumed to be the all-zeros path). Thus the length  $L$  of the shortest EEP equals 3, or equivalently, the code has a diversity equal to 3.

For coherent detection with no CSI, the product of the squared branch distances need to be computed, normalised by the square root of their sum in accordance with  $C$  of (6.7). From Figure 5.14, the square of this ratio is easily computed as

$$\left( \prod_{n \in \eta} \frac{|x_n - \hat{x}_n|^2}{\left( \sum_{n \in \eta} |x_n - \hat{x}_n|^2 \right)^{1/2}} \right)^{-2} = \left[ \frac{4 \cdot 8 \cdot 4}{(4 + 8 + 4)^{3/2}} \right]^{-2} = \frac{1}{4} \quad (6.8)$$

Thus letting  $L_\eta = 3$  and  $b = 3$  in (6.6), the approximated average BEP in terms of  $E_b/N_o$  and  $K$  is

$$P_b \cong \frac{2e^3}{81} \left( \frac{(1+K)e^{-K}}{E_b/N_o} \right)^3 \quad (6.9)$$

for  $E_b/N_o \gg K$ .

For coherent detection with CSI, the product of the distances in accordance with  $C$  in (6.7) need to be computed. For the shortest EEP this product is easily computed as

$$\prod_{n \in \eta} |x_n - \hat{x}_n|^2 = 4 \cdot 8 \cdot 4 = 128 \quad (6.10)$$

Substituting this value for  $C$  into (6.6), the BEP is given by

$$P_b \cong \frac{1}{6} \left( \frac{(1+K)e^{-K}}{E_b/N_o} \right)^3 \quad (6.11)$$

### 6.3.2 MTCM for fading channels

The throughput of multiple trellis codes can be compared with the computational cutoff rate  $R_o$  of the decoding channel to determine the efficiency of the code design. The computation of  $R_o$ , which is very similar to the channel capacity  $C$  discussed in Chapter 2, is not at all straight forward. In fact, it is an extremely complex process. For this reason the theoretical analysis has been omitted. The efficiency of the MTCM designs will therefore only be evaluated by means of computer simulation. In the following chapter these MTCM coding designs will be subjected to extensive simulations.

## 6.4 CONCLUDING REMARKS: CHAPTER 6

Optimum design criteria for trellis coded Q<sup>2</sup>PSK systems on fading channels have been derived and presented in this chapter. These criteria were utilised in the designs of new multiple trellis coded Q<sup>2</sup>PSK systems.

Initially, the study model of the coded  $Q^2$ PSK system on the fading channel has been presented. Fading channel statistics have been analysed and utilised in the design of the trellis coded systems. Design criteria derivation has revealed that design of trellis coded  $Q^2$ PSK systems to achieve optimum performance on the Rician fading channel is guided by factors that differ from optimum code design on the AWGN channel. In particular, to minimise the error probability, the code has to maximise the length of symbols at nonzero Euclidean distance from the shortest EEP. The secondary objective is to maximise the product of the branch distances along the shortest EEP, normalised by the Euclidean distance if coherent detection is utilised. The final objective will be the maximisation of the free squared Euclidean distance of the code. However, the relative importance of these parameters varies with the variation of the Rician factor encountered on the Rician fading channel.

Several new TCM and MTCM trellis codes for  $Q^2$ PSK signals have been designed and constructed. In the next chapter these coding schemes will be subjected to extensive simulation tests on the AWGN channel, as well as to fading channel conditions, to establish comparative coding efficiencies.

---

---

CHAPTER 7

PERFORMANCE EVALUATION

## PART III

---

---

# Q<sup>2</sup>PSK Modulation and Coding: PERFORMANCE EVALUATION

---

---

7.1 INTRODUCTION

7.1.1 Introduction

7.1.2

7.1.3

7.1.4

7.1.5

7.1.6

7.1.7 Signal-to-Noise Ratio

7.1.8

7.1.9

7.1.10

## CHAPTER 7

---

# PERFORMANCE EVALUATION

---

---

This chapter presents the performance results of the Q<sup>2</sup>PSK and Constant Envelope Q<sup>2</sup>PSK modems in the presence of impairments due to AWGN, ISI from bandlimiting and fading, due to the mobile V/UHF radio communication environment. The integration and evaluation of the developed carrier tracking strategies are carried out. The validity and efficiency of the said algorithms are evaluated under typical mobile channel conditions. Furthermore, the bit error probability graphs are presented to compare the performance of the classical, trellis and multiple trellis codes designed in Part II of this study. The derived upper bounds on bit error probability are benchmarked under typical channel conditions based on the same criteria of equal complexity and throughput.

### 7.1 INTRODUCTION

The performance evaluations are started by investigation of the uncoded Q<sup>2</sup>PSK and constant envelope CE-Q<sup>2</sup>PSK by appropriate modem back-to-back tests in AWGN, followed by evaluations in the presence of phase and frequency uncertainties. Then the evaluation of the convolutional (Classic, TCM and MTCM) trellis codes under similar AWGN channel conditions will be carried out. The second half of this chapter deals with the performance evaluation of the uncoded and coded Q<sup>2</sup>PSK and CE-Q<sup>2</sup>PSK modem under mobile fading channel conditions.

#### 7.1.1 SNR versus $E_b/N_o$

Before the performance investigation is continued, probably the most important quantity in the evaluation of different communications systems, namely the required SNR measured in *dB*, is quantified. Conventional power requirements are concerned with the average carrier power *C*, and

the average noise power  $N$ . The ratio  $C/N$ , is however meaningless unless the noise bandwidth of the receiver is specified. For this reason it is necessary to normalise the ratio  $C/N$  so that it becomes independent of bandwidth. The result of this normalisation is the quantity  $E_b/N_o$ , which becomes the independent variable in all subsequent BER measurements.

By specifying the required  $E_b/N_o$  in *dB*, the correct scale factor is calculated by which the noise samples are weighted to produce the required noise variance  $\sigma_r^2$  [58, 82]. The noise is added to the output of the Q<sup>2</sup>PSK transmitter to produce the required  $E_b/N_o$  ratio. By introducing the signal bandwidth,  $W$  (taken to be 10.0 *kHz* in this study) the following relationship between SNR and  $E_b/N_o$  can be written for binary signals,

$$\begin{aligned} \text{SNR} \doteq P_s/P_n &= \frac{\sigma_s^2}{\sigma_r^2}, \text{ (In the bandwidth } W \text{ of the signal)} \\ &= \frac{E_b R_b}{N_o W} \end{aligned} \quad (7.1)$$

where

$$\begin{aligned} \sigma_s^2 &= \text{signal variance} \\ \sigma_r^2 &= \text{required noise variance} \\ E_b &= \text{nominal energy per bit} \\ R_b &= 1/T_b = \text{nominal bit rate} \\ N_o &= \text{Level of single-sided power spectral density of white noise} \end{aligned} \quad (7.2)$$

Equation (7.1) can be manipulated to obtain an expression for the required noise variance to obtain a specified  $E_b/N_o$  ratio. This produces

$$\sigma_r^2 = \frac{\sigma_s^2 \cdot W}{10 \left( \frac{E_b}{N_o} \frac{1}{10} \right) \cdot R_b} \quad (7.3)$$

where  $E_b/N_o$  has been specified in *dB*.

The noise generator used in the simulation is based on the Wichmann-Hill algorithm (see Byte, 1984), and employs the Marsaglia-Bray transformation to generate AWGN with variance  $\sigma_n^2 = N_n f_{\text{samp}}/2 = 1 \text{ Watt}$ , where  $f_{\text{samp}}$  is the sampling frequency. From this expression,  $N_n$  can be obtained

$$N_n = \frac{2}{f_{\text{samp}}} \quad (7.4)$$

Both  $\sigma_n^2$  and  $N_n$  will have to be weighted with a constant  $k_r$ , to obtain the required noise variance  $\sigma_r^2$  for a specified  $E_b/N_o$  ratio. This constant is obtained as follows:

$$k_r = \frac{\sigma_r^2}{\sigma_n^2} = \sigma_r^2, \text{ since } \sigma_n^2 = 1 \quad (7.5)$$

producing

$$k_r = \frac{\sigma_s^2 \cdot f_{\text{samp}}}{10 \left( \frac{E_b}{N_o} \frac{1}{10} \right) \cdot 2R_b} \quad (7.6)$$

The noise samples must finally be weighted by the square root of  $k_r$ , since  $k_r$  is a power scale factor, and noise samples are generated in *volt*. Since the Marsaglia-Bray algorithm produces noise samples with unit variance,  $\sigma_n^2 = 1 \text{ Watt}$ , scaling by  $\sqrt{k}$  will directly produce noise samples with variance  $\sigma_r^2$ , as required by (7.1) [82].

### 7.1.2 Simulation software

Detail concerning the implementation of the Q<sup>2</sup>PSK mobile communication system in software (written in C and C++), can be found in technical research reports of the Laboratory for Advanced Engineering at the University of Pretoria [83, 84, 85, 86, 87, 88]. Complete descriptions of the software developed over a long period of time, as well as the actual simulation software utilised in this study, are contained in these reports.

## 7.2 EVALUATION ON AWGN CHANNELS

The AWGN, or static (non-fading) channel is probably the most studied channel in communication system evaluation. In this section the modem's performance under these static channel conditions will be investigated.

Block diagrams of the digital Q<sup>2</sup>PSK modulator and demodulator were given and analysed in detail in Chapter 4. At the receiver the blocks labeled 'BPF', i.e., the bandpass filters, were implemented by modulating specific lowpass filter responses to the desired passband frequencies. For all the simulation results presented in this chapter the lowpass impulse responses were taken to be full Nyquist LPFs with roll-off factors of  $\alpha = 0.5$ . The Intermediate Frequency (IF) is chosen as 12.5 kHz.

The geometry of the Q<sup>2</sup>PSK hypercube is affected by bandlimiting since the orthogonality of the data shaping pulses,  $q_1(t)$  and  $q_2(t)$  may be partially lost in the process. The loss of orthogonality causes ISI, resulting in loss of system performance (i.e., a degradation of BER performance).

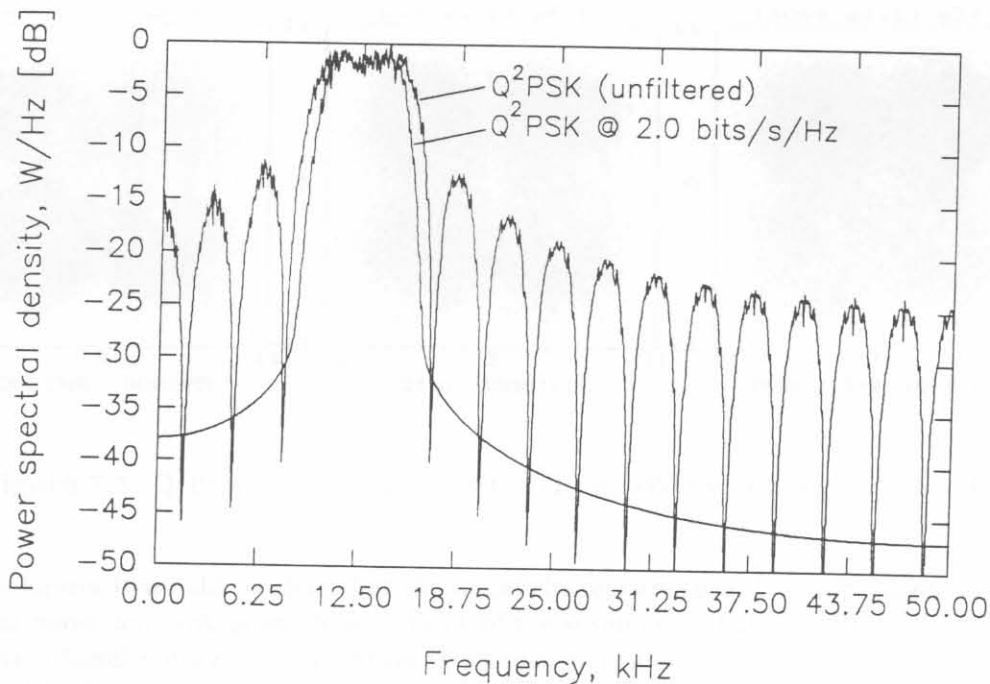


Figure 7.1: Power spectral densities of unfiltered and filtered Q<sup>2</sup>PSK (CE-Q<sup>2</sup>PSK).

Figure 7.1 shows the power spectral densities of unfiltered and filtered Q<sup>2</sup>PSK (CE-Q<sup>2</sup>PSK). The latter modem has an effective bandwidth efficiency,  $\eta_f = 2.0 \text{ bits/s/Hz}$ . It was shown by Saha [12] that under these bandlimiting conditions the effect of ISI interference on the Q<sup>2</sup>PSK signal is as mild as the effects of ISI on QPSK when operating at  $1.0 \text{ bit/s/Hz}$ .

An effective way of displaying the qualitative effects of ISI is to construct the signal space constellations in accordance with the discussion in Chapter 4 (see Figure 4.7). Figures 7.2 to 7.3 depict the bandlimited Q<sup>2</sup>PSK signal constellations operating at  $2.0 \text{ bits/s/Hz}$  in AWGN with  $E_b/N_o = 25.0$  and  $5.0 \text{ dB}$ , respectively.

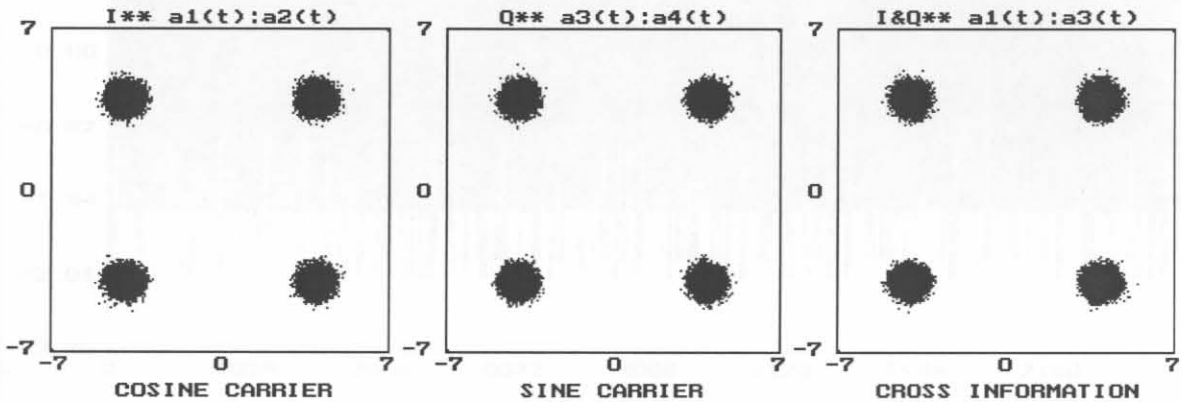


Figure 7.2: Q<sup>2</sup>PSK operating at  $2.0 \text{ bits/s/Hz}$  in AWGN with  $E_b/N_o = 25.0 \text{ dB}$ .

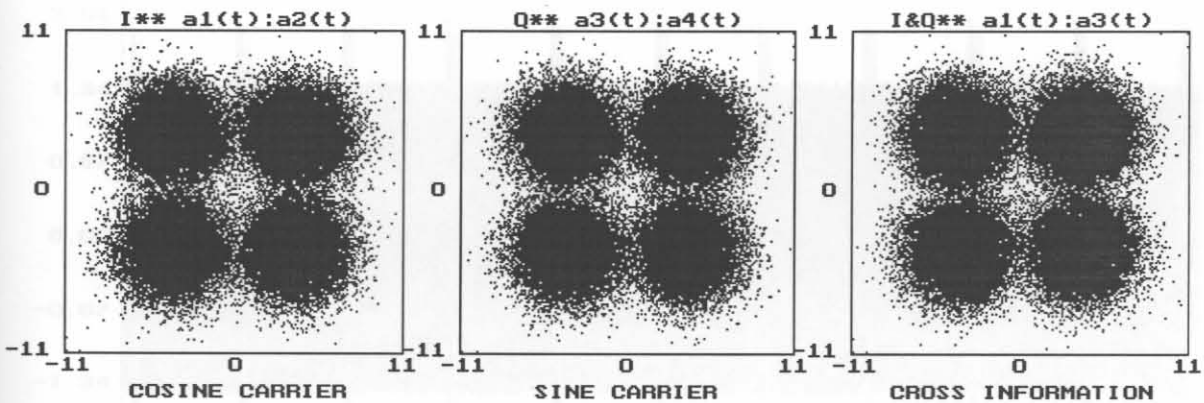


Figure 7.3: Q<sup>2</sup>PSK operating at  $2.0 \text{ bits/s/Hz}$  in AWGN with  $E_b/N_o = 5.0 \text{ dB}$ .

From these figures it should be clear that the signal clusters are spread out primarily as a result of the thermal noise, and not as much as a result of the severeness of the bandlimiting. In the case of more severe bandlimiting (i.e., operation at  $2.4 \text{ bits/s/Hz}$  and higher) the ISI is more severe and clusters tend to blend into neighboring signal points, as is to be expected. These figures show the correct phase positions, in the absence of any carrier phase or frequency offset. The former error will manifest itself as a constant phase offset of  $\theta_0 \text{ rad}$ , whereas the latter will result in a constant rotation of the phase symbols at a rate equal to the frequency difference between the local carrier



in-phase  $I$  and quadrature phase  $Q$  references, and the received  $Q^2$ PSK signal. These above results will serve as reference for the simulation tests to follow.

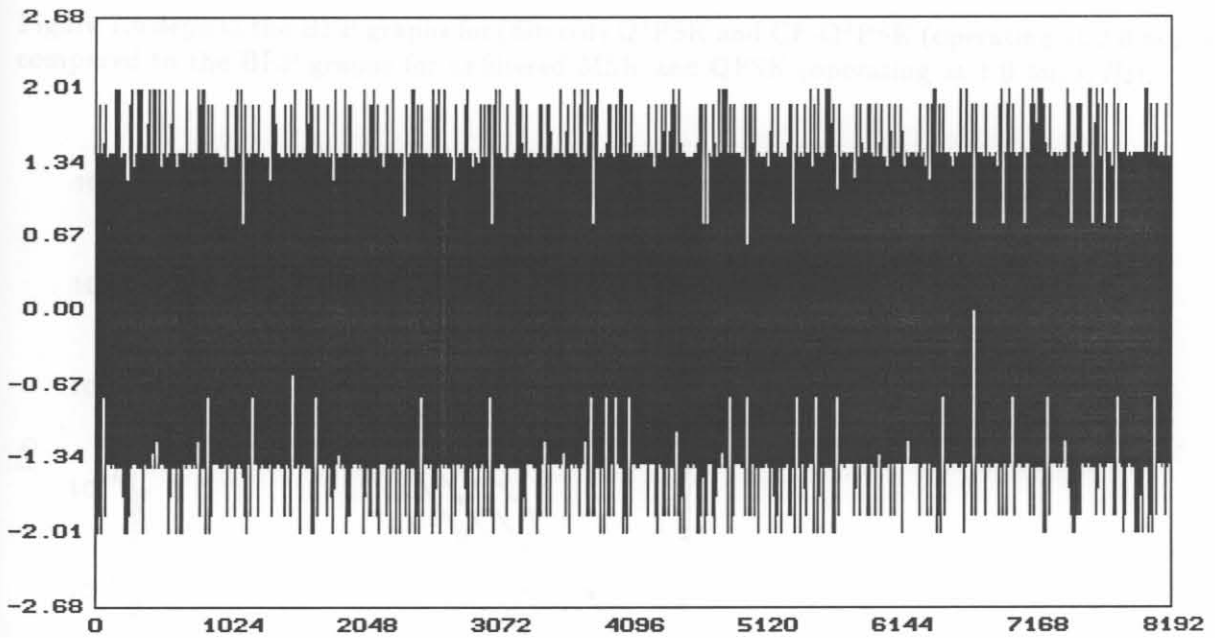


Figure 7.4:  $Q^2$ PSK signal under static channel conditions (X-axis: samples, Y-axis: volt).

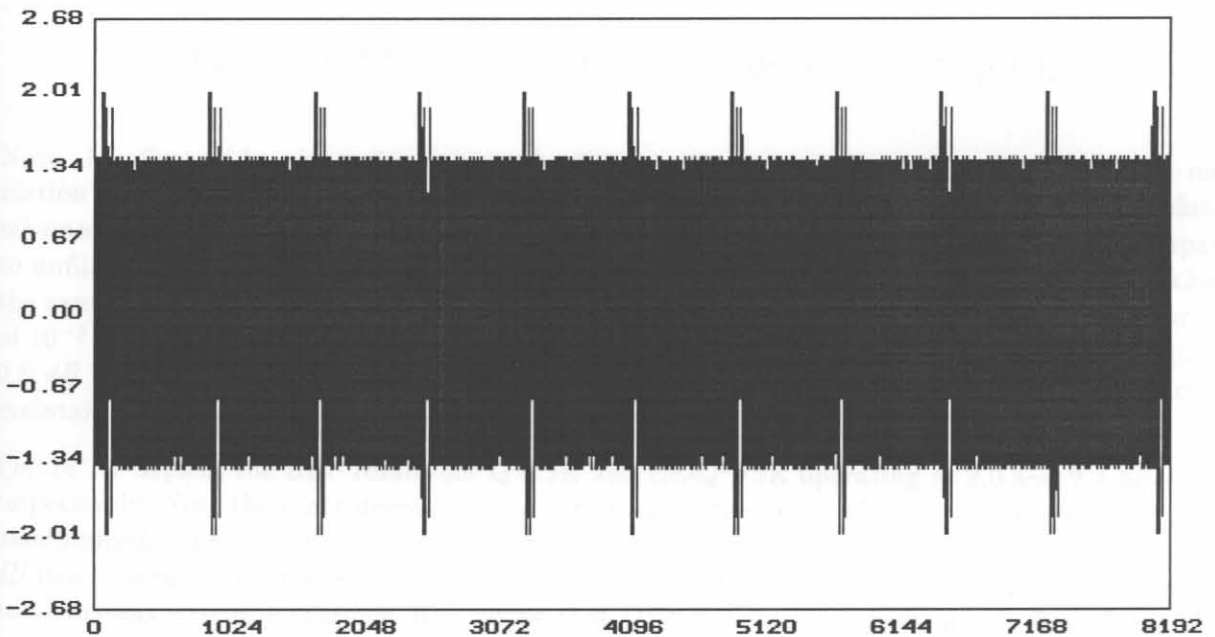


Figure 7.5: CE- $Q^2$ PSK signal under static channel conditions.

Figures 7.4 and 7.5 depict the discrete time (sampled) signals for  $Q^2$ PSK and CE- $Q^2$ PSK transmitted over the bandlimited AWGN channel, for a SNR of  $E_b/N_o = 35$  dB. Note the non-constant envelope of the  $Q^2$ PSK signal, whereas the CE- $Q^2$ PSK signal envelope is constant except over the

(8 or 16 symbol) header (designed for optimum correlation properties), preceding each data frame according to the block transmission strategy outlined in section 4.2, Figure 4.11.

Figure 7.6 depicts the BEP graphs for (filtered) Q<sup>2</sup>PSK and CE-Q<sup>2</sup>PSK (operating at 2.0 bits/s/Hz) compared to the BEP graphs for unfiltered MSK and QPSK (operating at 1.0 bit/s/Hz).

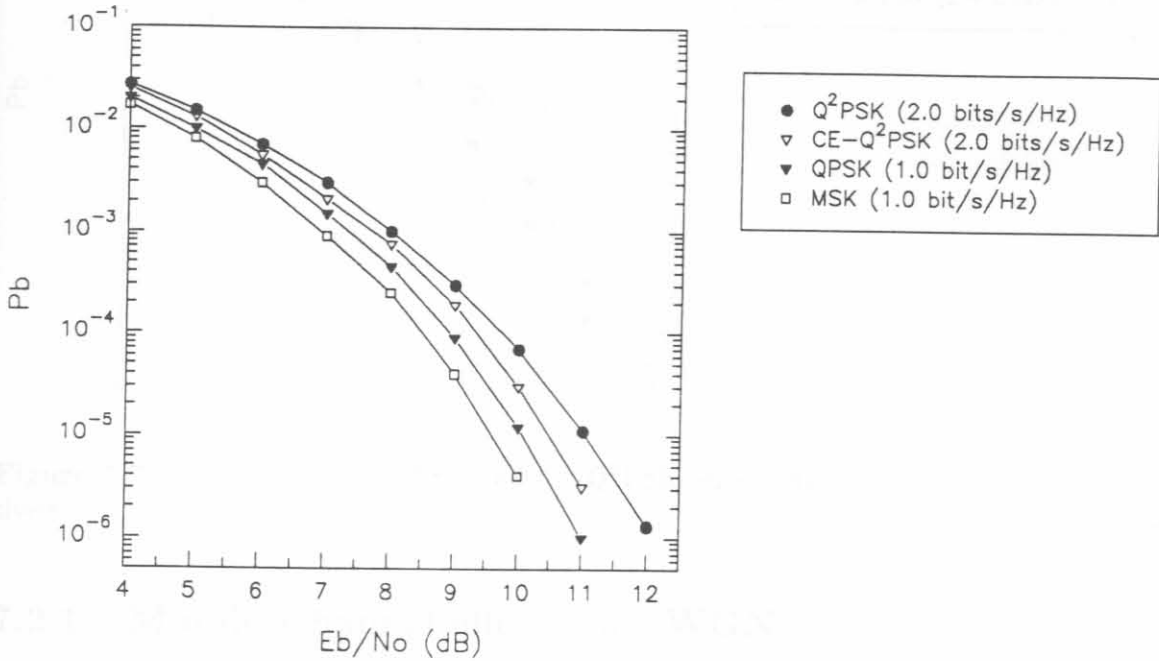


Figure 7.6: BEP curves for MSK, QPSK, Q<sup>2</sup>PSK, and CE-Q<sup>2</sup>PSK.

Note the effect of bandpass filtering on the BEP performance curves of the forementioned modulation schemes. Recall from the analysis carried out in Chapter 2 that all of the modulation schemes shown have exactly the same theoretical BEP. From Figure 7.6 it is noted that compared to unfiltered MSK and QPSK, Q<sup>2</sup>PSK requires, respectively 1.5 and 1.1 dB more energy to achieve the same error performance at  $P_b = 10^{-5}$ . Furthermore, Q<sup>2</sup>PSK requires to achieve a bit error rate of  $10^{-5}$ , an  $E_b/N_0$  of 11.1 dB, whereas CE-Q<sup>2</sup>PSK requires only 10.4 dB. This performance gain of 0.6 dB is a direct result of the inherent coding gain brought about by the block coding scheme to maintain a constant envelope signal.

Figure 7.7 depicts the BEP results for Q<sup>2</sup>PSK and CE-Q<sup>2</sup>PSK operating at 2.0 and 2.4 bits/s/Hz, respectively. Note the slight degradation in performance due to the effects of ISI as a result of severe bandlimiting. Specifically, Q<sup>2</sup>PSK operating at 2.0 bits/s/Hz requires 11.1 dB, while it requires 1.1 dB more energy per bit when operating at a bandwidth-efficiency of 2.4 bits/s/Hz. Comparing the non-constant envelope schemes, it is noted that Q<sup>2</sup>PSK requires approximately 0.9 dB more bit energy to achieve the same performance when operating at 2.4 bits/s/Hz, compared to operating at 2.0 bits/s/Hz.

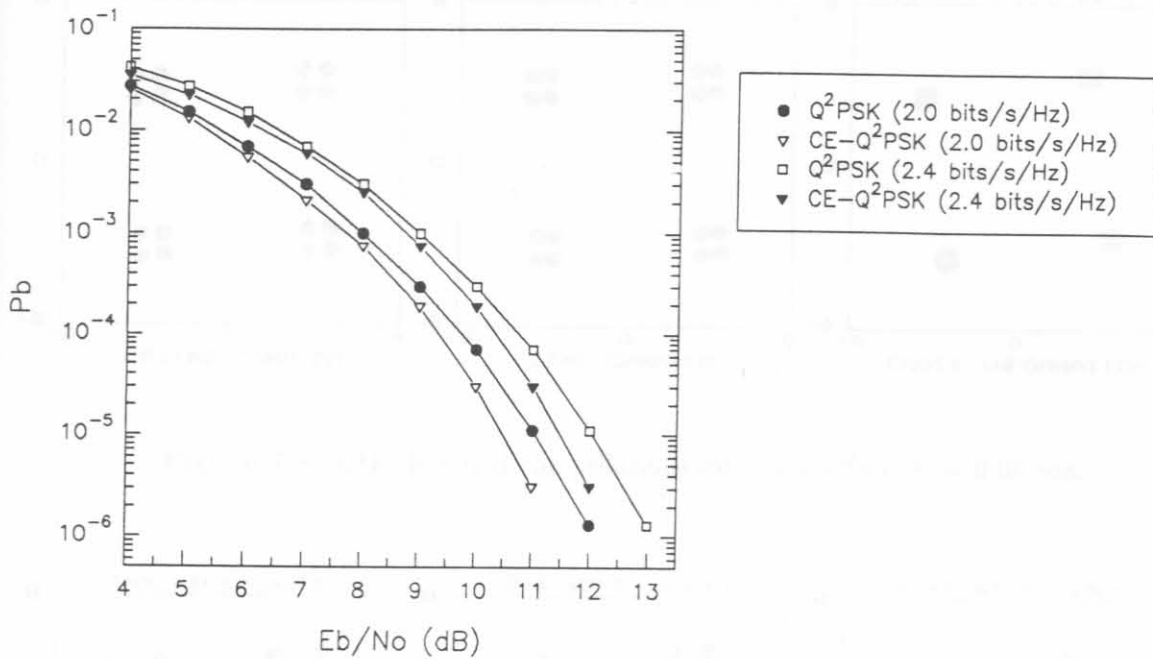


Figure 7.7: BEP curves for Q<sup>2</sup>PSK and CE-Q<sup>2</sup>PSK, operating at 2.0 and 2.4 *bits/s/Hz*, respectively.

### 7.2.1 Mobile Channel effects in AWGN

In this section the effects of mobile channel non-linearities will be investigated on the performance of the Q<sup>2</sup>PSK modem. The BEP performance curves are shown for values of phase and Doppler frequency normalised by the symbol rate,  $R_s = 1/T_s$ . The normalised phase offsets  $\theta_o T_s$  range from  $10 \times 10^{-6}$  to  $40 \times 10^{-6}$  at a bit rate of  $R_b = 20.0$  *kbits/s*, this range corresponds to phase offsets in the range 0.05 to 0.2 *rad*.

For vehicle speeds of 30, 60 and 120 *km/h*, and a carrier frequency of 900 *MHz*, the corresponding Doppler frequencies are 25, 50 and 100 *Hz*, respectively. For these vehicle speeds and bit rate, the normalised Doppler frequency,  $f_D T_s$ , ranges from  $5 \times 10^{-3}$  to  $20 \times 10^{-3}$ . In satellite mobile systems however, much higher Doppler frequencies will be experienced.

Figures 7.8 to 7.10 display the Q<sup>2</sup>PSK modem signal constellations for phase offsets  $\theta_o$  of 0.05, 0.1 and 0.2 *rad*, respectively, with  $E_b/N_o = 30$  *dB*. The phase offsets result in the signal constellation clusters to be rotated with an amount corresponding to the phase offset. Figures 7.11 to 7.13 display the Q<sup>2</sup>PSK modem signal constellations for Doppler frequencies,  $f_D$  of 25, 50 and 100 *Hz* and  $E_b/N_o = 30$  *dB*. The Doppler frequencies result in a constant rotation of the phase symbols at a rate equal to the frequency difference between the local carrier references, and the received Q<sup>2</sup>PSK signal, over one symbol period.

Figures 7.14 to 7.16 illustrates the effects of phase offsets on the CE-Q<sup>2</sup>PSK signal space constellations for values of  $\theta_o$  in the above ranges. Interestingly, when these constellations are compared with those presented in Figures 7.8 to 7.10, it is noted that the phase effects are restricted. This can easily be explained. Recall, in order to force a constant envelope signal, a block coder of rate-3/4 is utilised. The effect of this coder is to add an amount of redundancy to one of the four information carrying data streams, resulting in a 1/4 reduction in dimensionality. Therefore, the qualitative

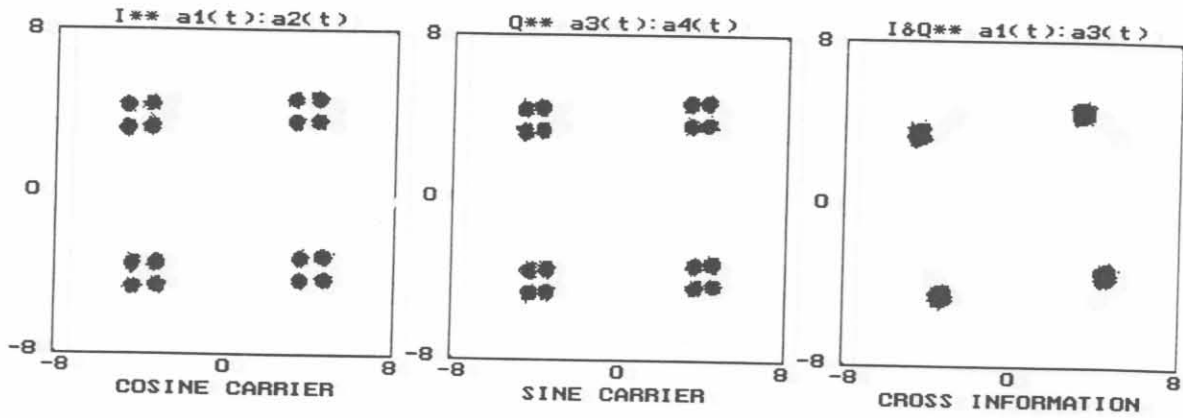


Figure 7.8:  $Q^2$ PSK signal constellations for phase offset,  $\theta_o = 0.05 \text{ rad}$ .

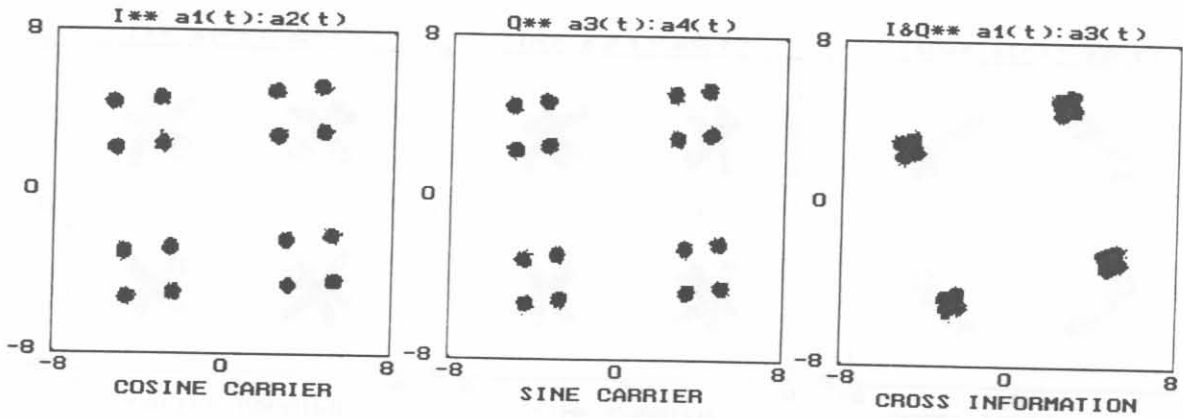


Figure 7.9:  $Q^2$ PSK signal constellations for phase offset,  $\theta_o = 0.1 \text{ rad}$ .

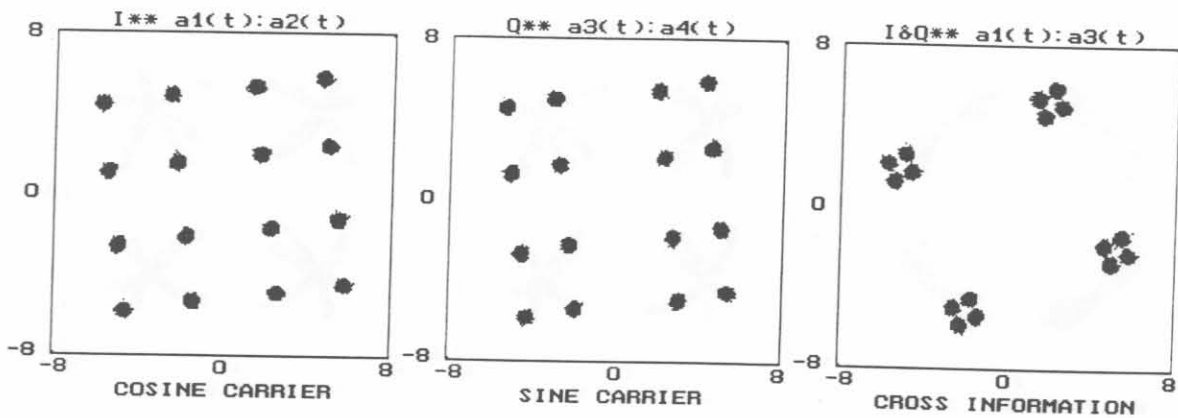


Figure 7.10:  $Q^2$ PSK signal constellations for phase offset,  $\theta_o = 0.2 \text{ rad}$ .

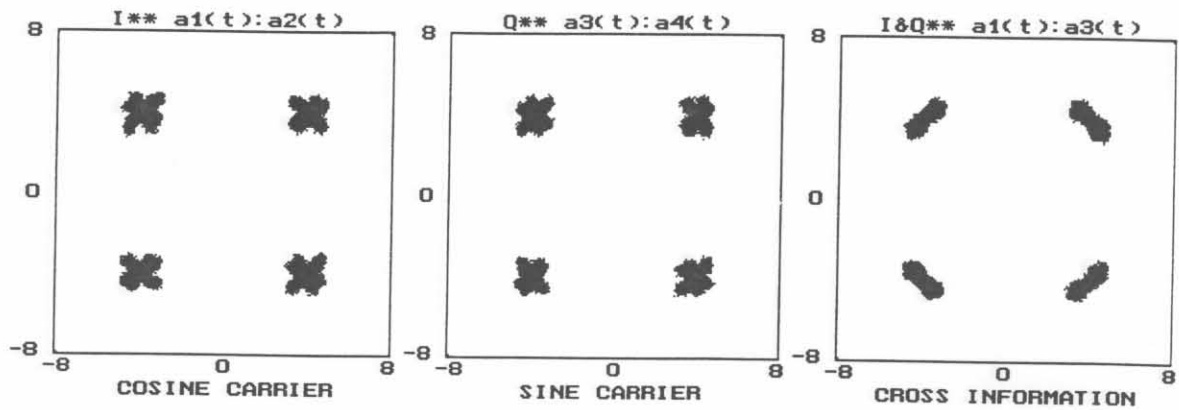


Figure 7.11:  $Q^2$ PSK signal constellations for Doppler frequency of 25 Hz at RF frequency of 900 MHz.

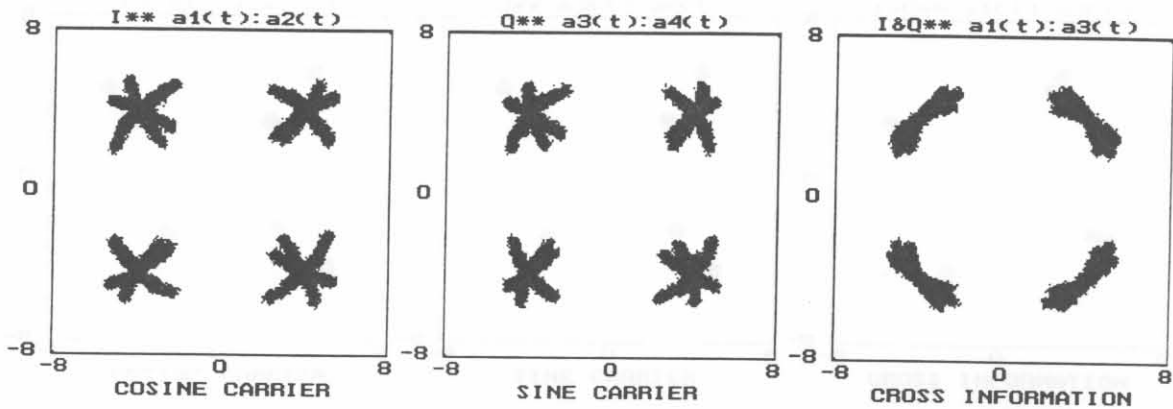


Figure 7.12:  $Q^2$ PSK signal constellations for Doppler frequency of 50 Hz.

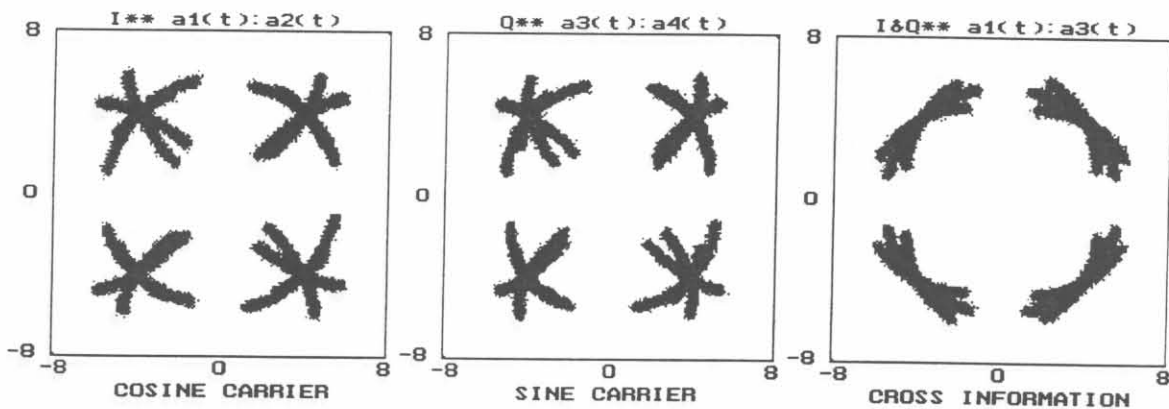


Figure 7.13:  $Q^2$ PSK signal constellations for Doppler frequency of 100 Hz.

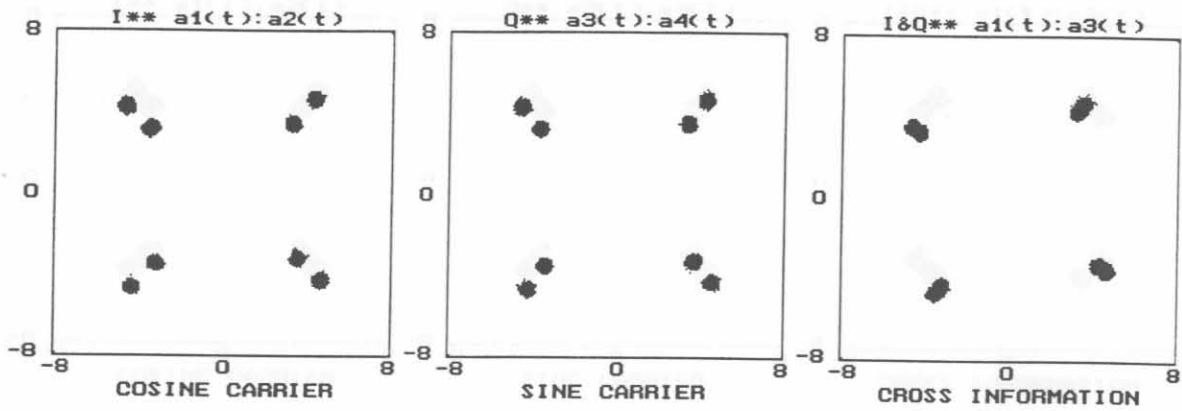


Figure 7.14: CE-Q<sup>2</sup>PSK signal constellations for phase offset,  $\theta_o = 0.01 \text{ rad}$ .

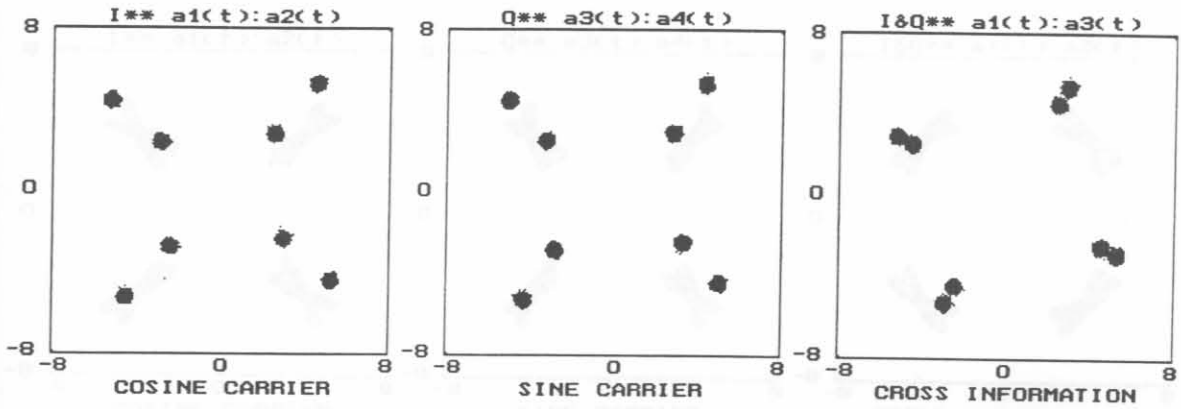


Figure 7.15: CE-Q<sup>2</sup>PSK signal constellations for phase offset,  $\theta_o = 0.1 \text{ rad}$ .

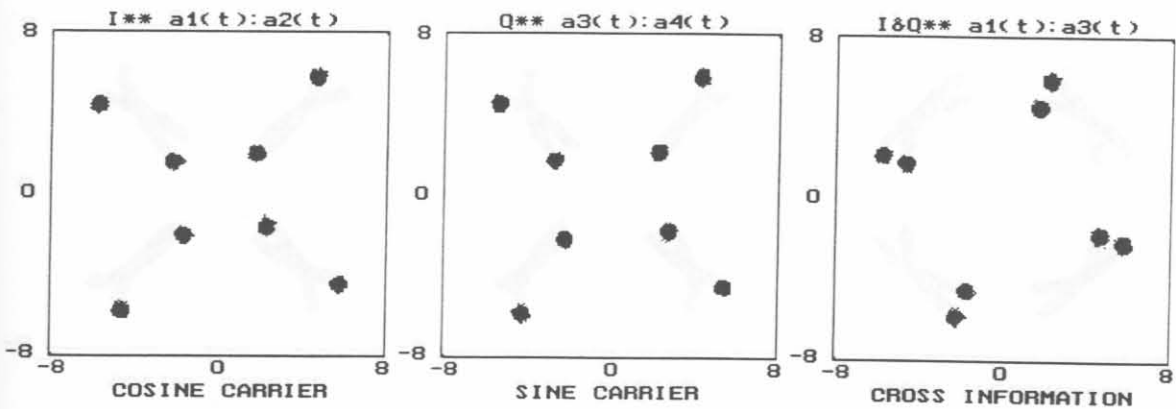


Figure 7.16: CE-Q<sup>2</sup>PSK signal constellations for phase offset,  $\theta_o = 0.2 \text{ rad}$ .

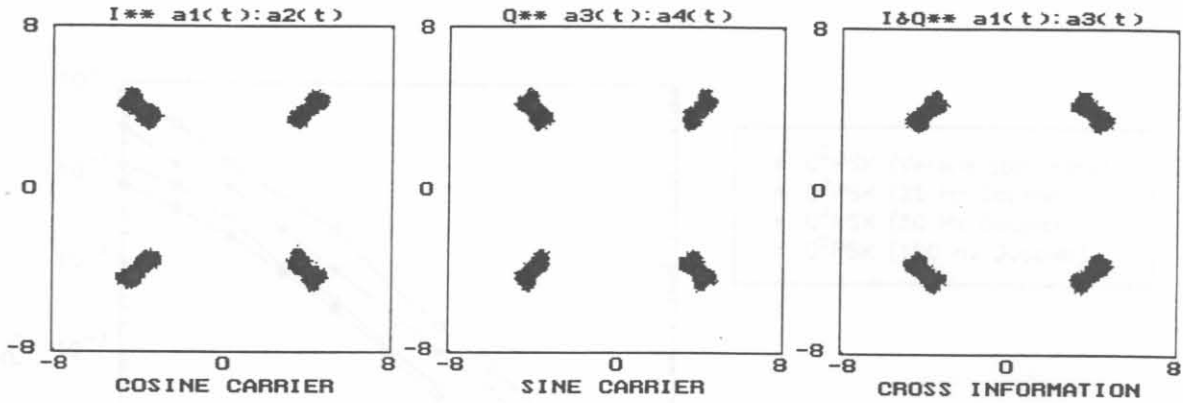


Figure 7.17: CE-Q<sup>2</sup>PSK signal constellations for Doppler frequency of 25 Hz at RF frequency of 900 MHz.

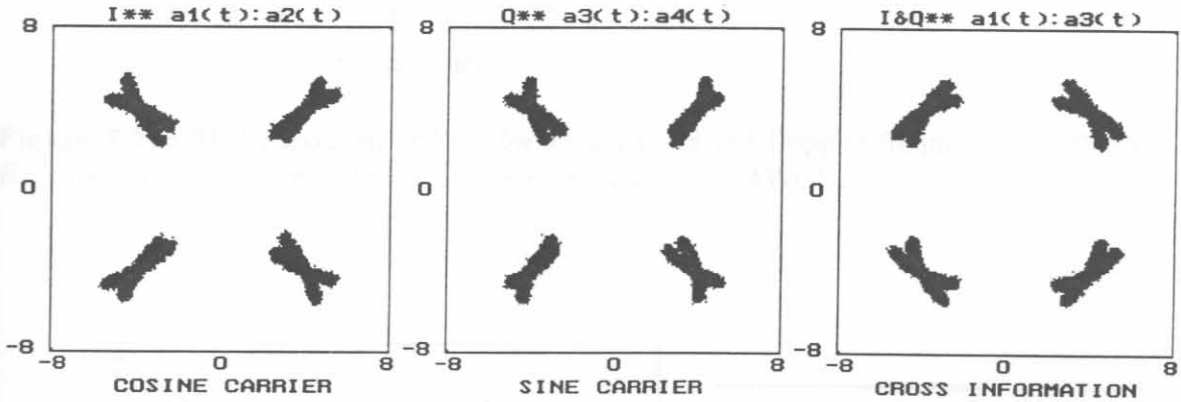


Figure 7.18: CE-Q<sup>2</sup>PSK signal constellations for Doppler frequency of 50 Hz.

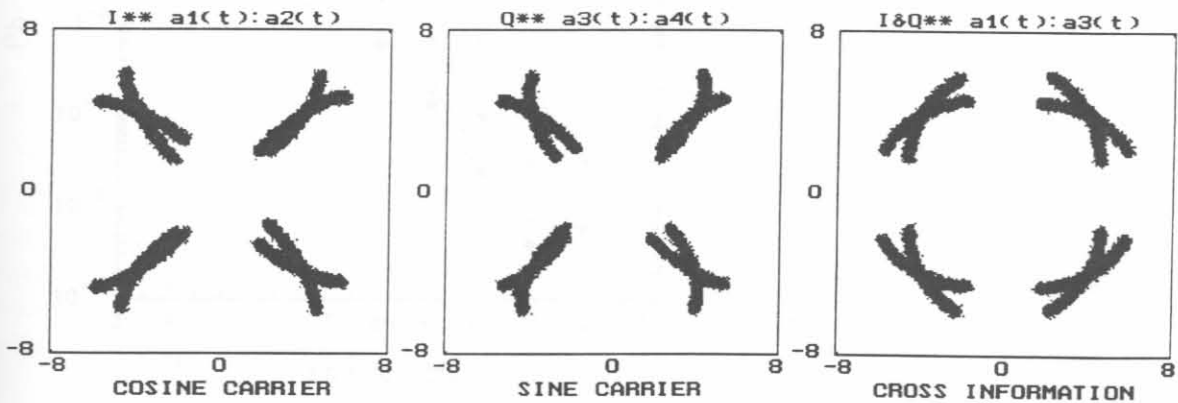


Figure 7.19: CE-Q<sup>2</sup>PSK signal constellations for Doppler frequency of 100 Hz.

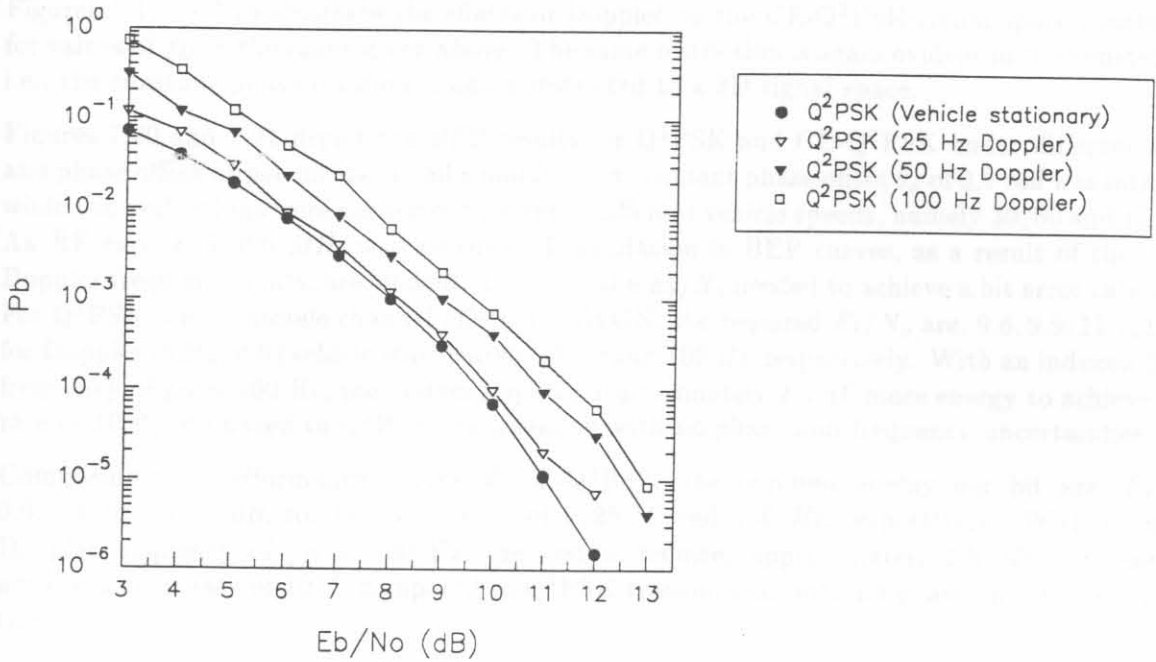


Figure 7.20: BEP curves for Q<sup>2</sup>PSK for  $\theta_o = 0.1$  rad and Doppler frequencies of 25, 50 and 100 Hz, compared to the ideal Q<sup>2</sup>PSK modem transmission in AWGN.

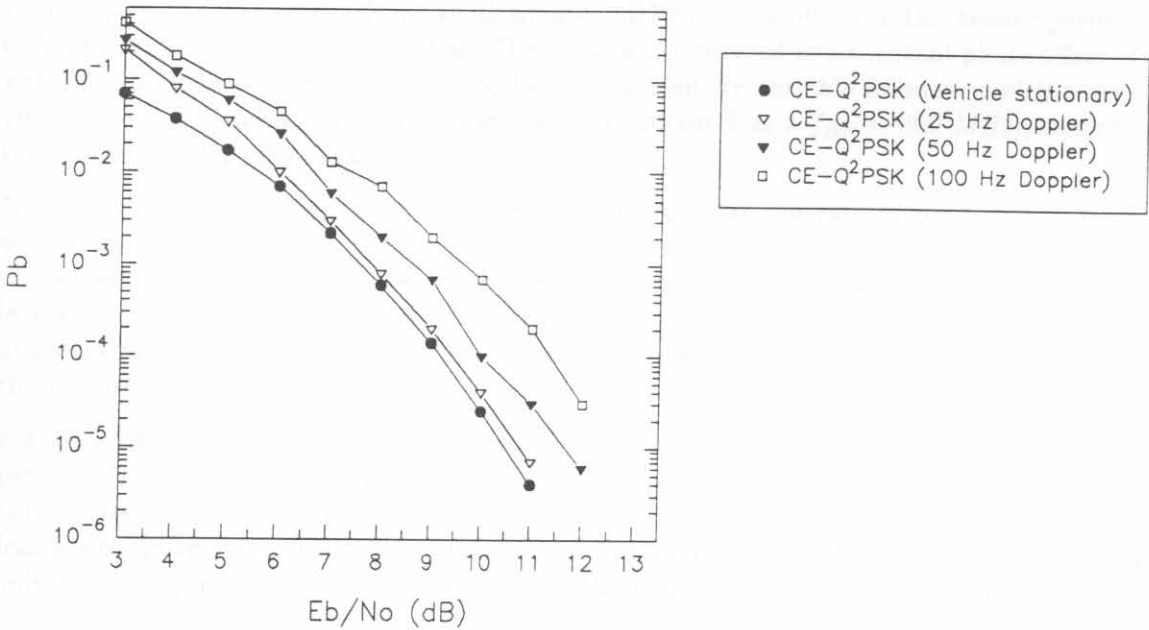


Figure 7.21: BEP curves for CE-Q<sup>2</sup>PSK for  $\theta_o = 0.1$  rad and Doppler frequencies of 25, 50 and 100 Hz, compared to the ideal CE-Q<sup>2</sup>PSK modem transmission in AWGN.



effects of phase non-linearities are restricted to a three-dimensional (3D) signal space.

Figures 7.17 to 7.19 illustrate the effects of Doppler on the CE-Q<sup>2</sup>PSK signal space constellations for values of  $f_D$  in the range given above. The same restriction is again evident in the constellations, i.e., the constant phase rotation is again restricted to a 3D signal space.

Figures 7.20 and 7.21 depict the BEP results for Q<sup>2</sup>PSK and CE-Q<sup>2</sup>PSK under different Doppler and phase offset impairments. In all simulations a constant phase offset  $\theta_o$  of 0.1 *rad* was introduced, while the evaluations were carried out for three different vehicle speeds, namely 30, 60 and 120 *km/h*. An RF carrier of 900 *MHz* was assumed. Degradation in BEP curves, as a result of the different Doppler frequency shifts, are evident. Consider the  $E_b/N_o$  needed to achieve a bit error rate of  $10^{-4}$ . For Q<sup>2</sup>PSK, under mobile channel effects in AWGN, the required  $E_b/N_o$  are, 9.6, 9.9, 11.1, 12.0 *dB*, for Doppler shifts of 0 (vehicle stationary), 25, 50 and 100 *Hz*, respectively. With an induced Doppler frequency of  $f_D = 100$  *Hz*, the system requires approximately 2.4 *dB* more energy to achieve a error rate of  $10^{-4}$ , compared to Q<sup>2</sup>PSK transmission with no phase and frequency uncertainties.

Comparing the performance curves of CE-Q<sup>2</sup>PSK, the required energy per bit are,  $E_b/N_o = 9.0, 9.3, 10.5, 11.5$  *dB*, for Doppler shifts of 0, 25, 50 and 100 *Hz*, respectively. With an induced Doppler frequency of  $f_D = 100$  *Hz*, the system requires approximately 2.5 *dB* more energy to achieve a error rate of  $10^{-4}$ , compared to Q<sup>2</sup>PSK transmission with no phase and frequency uncertainties.

## 7.2.2 Phase/Frequency Tracking and Correction

Some simulation results are presented to illustrate the capability of the carrier phase and Doppler frequency offset algorithms discussed in section 4.3, under typical mobile channel conditions.

Figure 7.22 depicts mesh plots of the frequency and phase Minimum Square Error (MSE) for the Dual Phase and Frequency Kalman Estimator (DPFKE), taken over the *header* period only, for different values of  $E_b/N_o$  as indicated. The modem is subjected to a constant phase offset of  $\theta_o = 0.1$  *rad*. The Doppler frequency is taken to be a cosinusoidally variable frequency with a maximum of 100 *Hz* (i.e., corresponding to a vehicle speed of 120 *km/h* at a  $f_{RF} = 900$  *MHz*), centered around the nominal (0 *Hz* offset) value.

Note from Figure 7.22(a) for the frequency MSE,  $\rho_k$ , that the rate of convergence at low values of  $E_b/N_o$  is not very fast. However, at higher values of  $E_b/N_o$ , i.e.,  $E_b/N_o > 15$  *dB*, the rate of convergence is significantly higher with acceptable results. Considering the phase MSE,  $\rho_l$ , depicted in Figure 7.22(b), it is noted that the DPFKE finds it difficult to effectively track any phase offsets at low values of  $E_b/N_o$ . Acceptable convergence rates are again achieved for values of  $E_b/N_o$  higher than 15 *dB*.

Figure 7.23 depicts the plots for the DPFKE frequency MSE,  $\rho_k$  taken over a part of the data period. The line plot clearly indicates, that at high  $E_b/N_o$  values, it is useful to track any possible carrier frequency variations over the data interval. Note, however that it does not seem to be feasible to do this at lower values of  $E_b/N_o$ . It is therefore concluded that carrier tracking should only be attempted under relatively good AWGN channel conditions (i.e.,  $E_b/N_o > 14$  *dB*).

### To Track or Not To Track

Figure 7.24 depicts the BEP graphs for the Q<sup>2</sup>PSK and CE-Q<sup>2</sup>PSK, under mobile channel conditions in AWGN, with the DPFKE activated. Note that the BEP curves are again given for different

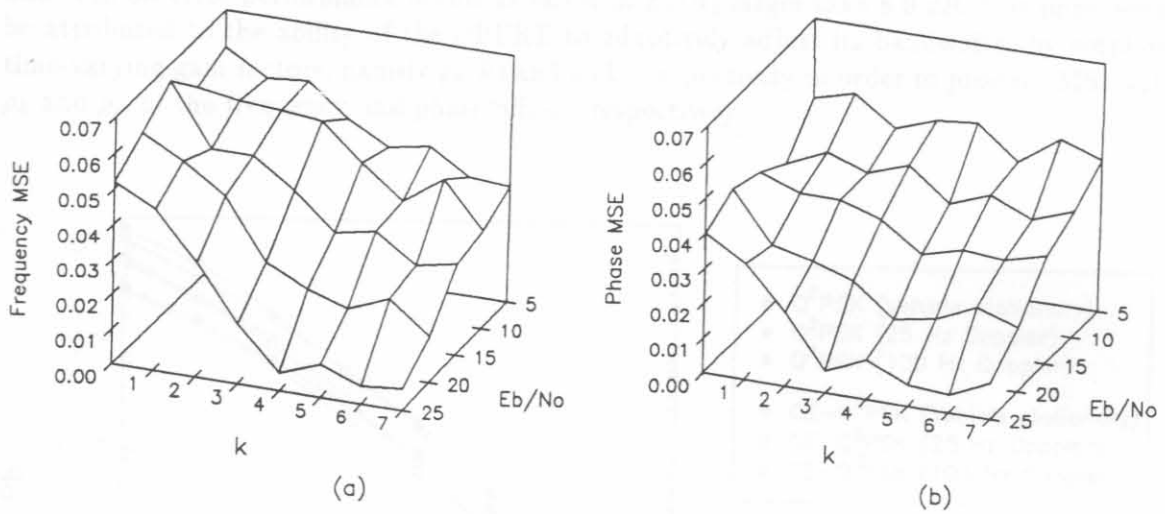


**Figure 7.22:** Minimum Squared Errors for DPFKE estimator tracking carrier phase and frequency uncertainties over the header period (a) Frequency MSE,  $\rho_k$  (b) Phase MSE,  $\rho_l$ .

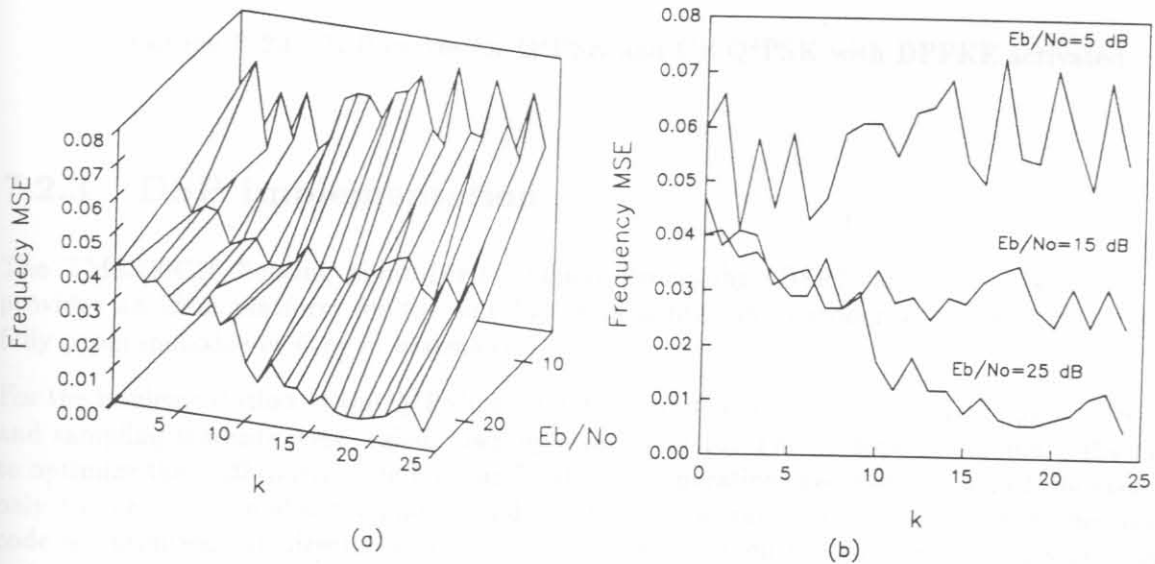


**Figure 7.23:** Frequency MSE for DPFKE estimator tracking carrier frequency uncertainties over the data period.

Doppler frequency shifts (0, 25, 50 and 100 Hz), and for a constant carrier phase error of  $\theta_0 = 0.1$  rad. From the BEP curves only a slight degradation in bit error rate performance at low values of  $E_b/N_o$ , for frequency shifts up to 100 Hz can be seen. Note also that hardly any noticeable degradation in bit error performance occurs at values of  $E_b/N_o$  larger than 8.0 dB. This improvement can be attributed to the ability of the DPFKE to adaptively adjust its bandwidth, by employing two time-varying gain factors, namely  $\rho_k(k)$  and  $\rho_l(k)$ , respectively in order to produce MSE estimates,  $\rho_k$  and  $\rho_l$ , of the frequency and phase offsets, respectively.

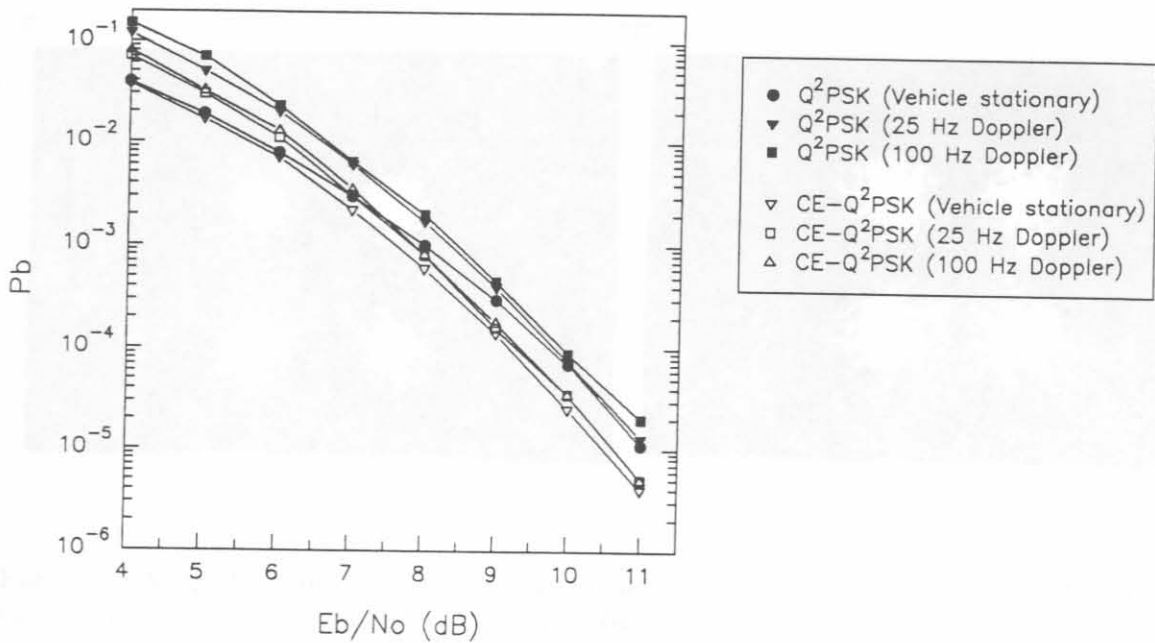


Figure 7.24: BEP curves for Q<sup>2</sup>PSK and CE-Q<sup>2</sup>PSK with DPFKE activated.

### 7.2.3 DSP implementation

The TMS320C30 floating point Digital Signal Processing (DSP) chip from Texas Instruments, provides an ideal platform for the suitable implementation of modems [89, 90, 91]. The DSP is fully programmable in *C* or in *assembler*.

For the implementation of the Q<sup>2</sup>PSK modulator and demodulator on the DSP, all the frequencies and sampling instants were scaled down by a factor of 10. This is done to eliminate the necessity to optimize the *C30* source code for true "real time" operation, because the aim of the exercise was only to verify the modulator and demodulator implementation principles. When the simulation code is optimized, or directly written in assembler and then cross-compiled to produce machine code, a speed-up factor of at least 10 times can easily be achieved.

Figures 7.25(a) and (b) depict the two 2D Q<sup>2</sup>PSK signal constellations associated with the cosine-carrier information (see Figure 4.7) under static AWGN channel conditions, for values  $E_b/N_o$  of 20.0 and 15.0 dB, respectively. Figures 7.26 to 7.27 similarly depict the two 2D Q<sup>2</sup>PSK signal constellations associated with the cosine-carrier information under mobile channel conditions at a RF

carrier frequency of 900 MHz. Specifically the constellation depicted by Figure 7.26(a) correspond to the cosine-carrier for a constant phase uncertainty  $\theta_o$  of 0.1 rad, while Figure 7.26(b) corresponds to a Doppler frequency of 100.0 Hz, both for a  $E_b/N_o$  of 25.0 dB. Note that these figures correspond well to that obtained by computer simulation (refer to Figures 7.11 to 7.19). The constellations depicted in Figure 7.27 corresponds to the Q<sup>2</sup>PSK signal space constellations associated with the cosine-carrier information (see Figure 7.27(a)) and cosine-sine-carrier information associated with shaping function  $q_1(t)$  (see Figure 7.27(a)) for a constant phase offset  $\theta_o = 0.1$  rad, a Doppler frequency  $f_D = 50.0$  Hz and  $E_b/N_o = 15.0$  dB.

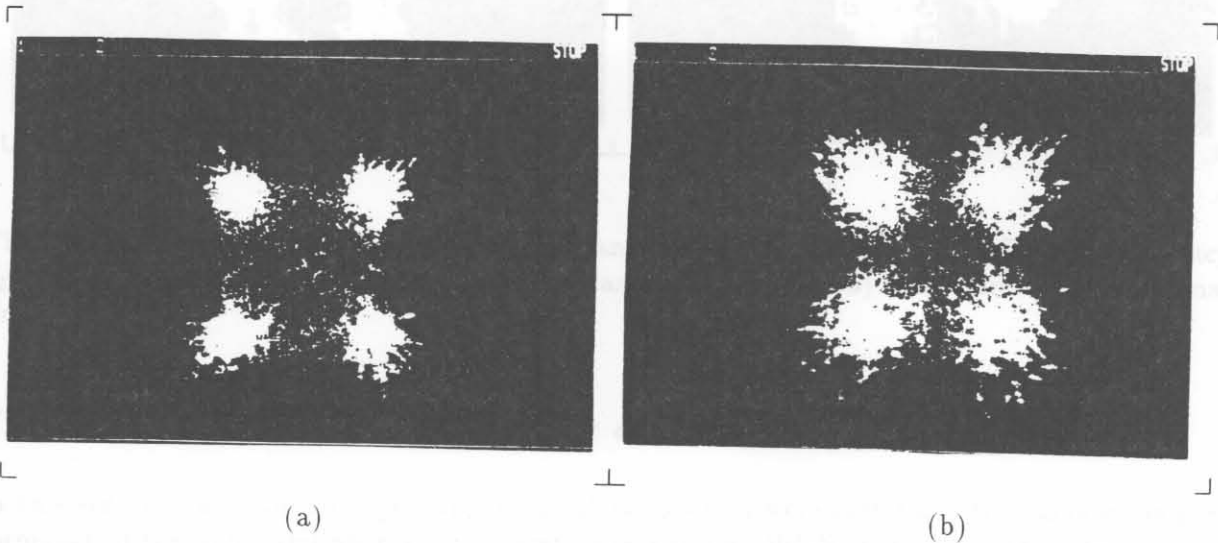


**Figure 7.25:** Q<sup>2</sup>PSK constellations (cosine-carrier information) under static AWGN channel conditions (a)  $E_b/N_o = 20.0$  dB (b)  $E_b/N_o = 15.0$  dB.

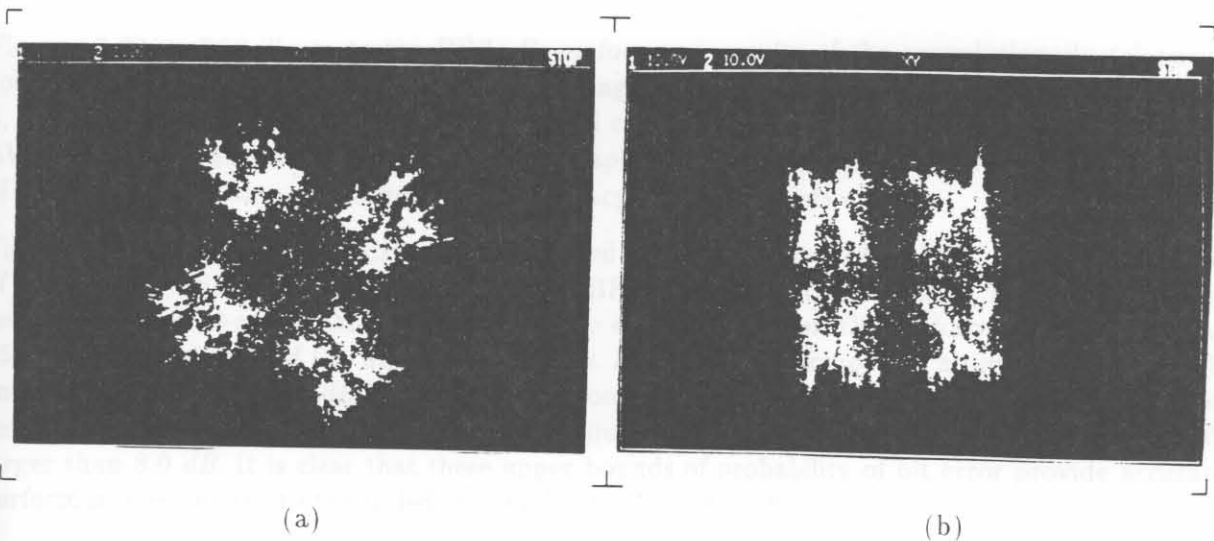


**Figure 7.26:** Q<sup>2</sup>PSK constellations (cosine-carrier information) under mobile channel impairments for  $E_b/N_o = 25$  dB (a) carrier phase offset  $\theta_o = 0.1$  rad (b) Doppler frequency  $f_D = 100.0$  Hz.

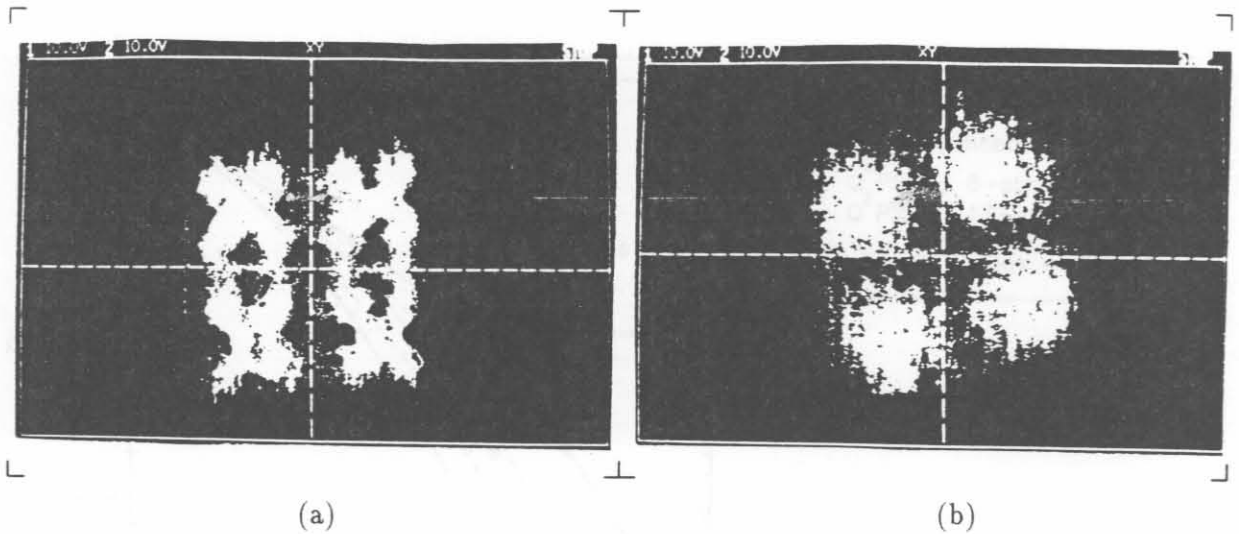


**Figure 7.27:** Q<sup>2</sup>PSK constellations for a constant phase offset  $\theta_o = 0.1 \text{ rad}$ , a Doppler frequency  $f_D = 50.0 \text{ Hz}$  and  $E_b/N_o = 15.0 \text{ dB}$  (a) cosine-carrier information (b) cosine-sine-carrier information.

## 7.2.4 Classical and TCM error correction in AWGN

In this section, the results of the software simulations which were performed to evaluate the performance of the coded Q<sup>2</sup>PSK systems operating in a static AWGN channel are presented. For all the simulation tests, perfect carrier and time synchronisation were assumed.

### 7.2.4.1 Classical error correction

Figures 7.28 to 7.30 illustrate the BER,  $P_b$  performance results of the convolutionally (classical) coded Q<sup>2</sup>PSK and CE-Q<sup>2</sup>PSK systems. Employing the Union bound approach described in Chapter 5, the performance of the different convolutional coded Q<sup>2</sup>PSK systems have been evaluated in an AWGN channel. These results, presented in Chapter 5 are repeated in the BEP results as a means of comparison in order to benchmark the accuracy of these bounds.

Figure 7.28 illustrates the BEP results obtained for coded rate 1/2 Q<sup>2</sup>PSK, compared to that of uncoded Q<sup>2</sup>PSK and the upper bounds to BEP presented in Figure 5.7. For the simulation tests two 8- and 16-state rate-1/2 encoders were employed. When the performance curves of the 16-state coder to that of the uncoded system at  $P_b = 10^{-5}$  are compared, an improvement in bit energy requirement of 2.0 dB is seen. Furthermore, it is noted from the figure that the simulation curves correspond well to the derived bounds (illustrated by the dashed lines) for values of  $E_b/N_o$  larger than 8.0 dB. It is clear that these upper bounds of probability of bit error provide accurate performance estimates to the coded system for  $E_b/N_o > 8.0 \text{ dB}$ .

Figure 7.29 illustrates the BER performance results obtained for coded hybrid rate 1/2 constant envelope CE-Q<sup>2</sup>PSK, compared to that of uncoded CE-Q<sup>2</sup>PSK. As was the case for Q<sup>2</sup>PSK, the simulation tests were performed employing 8- and 16-state coders, the only difference being that a single rate-2/3 convolutional coder, together with the block coder to force a constant envelope, was employed (see Figures 5.3 and 5.6).

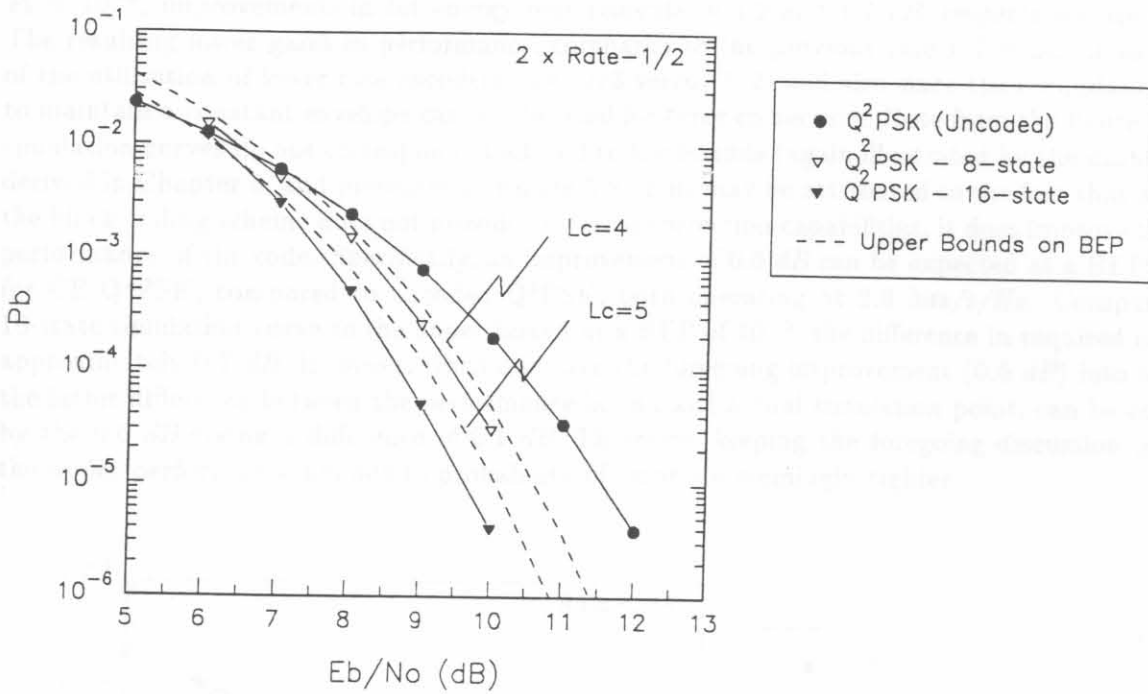


Figure 7.28: BEP graphs 8- and 16-state rate-2/4  $Q^2$ PSK, compared to uncoded  $Q^2$ PSK and the upper bounds to BEP.

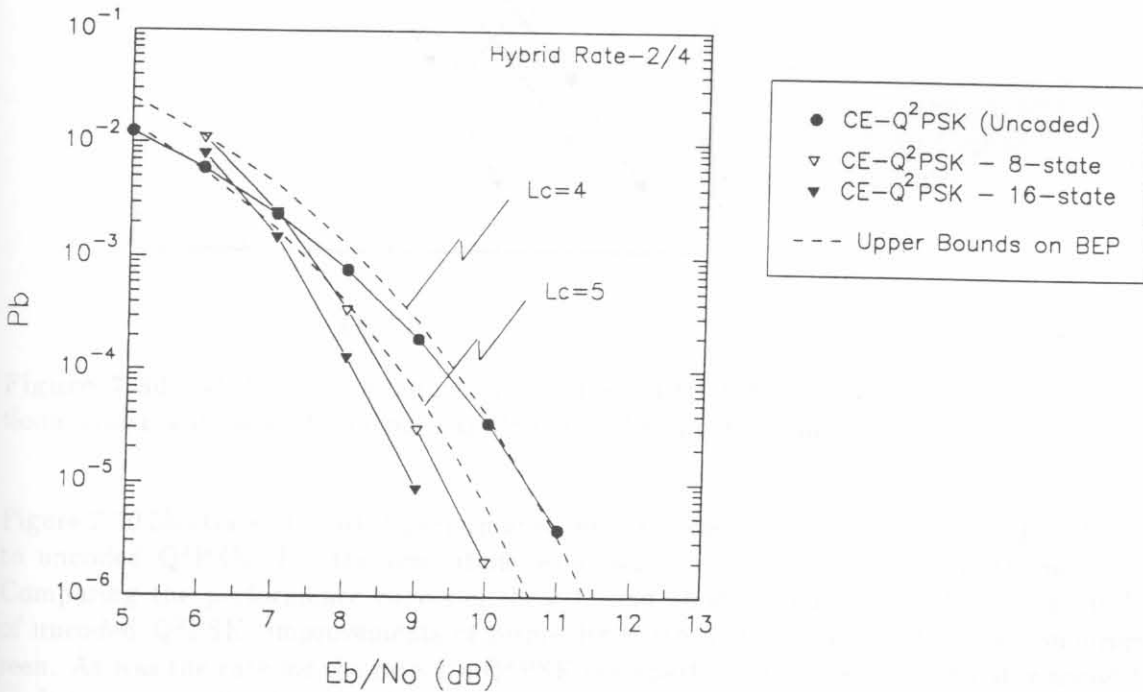
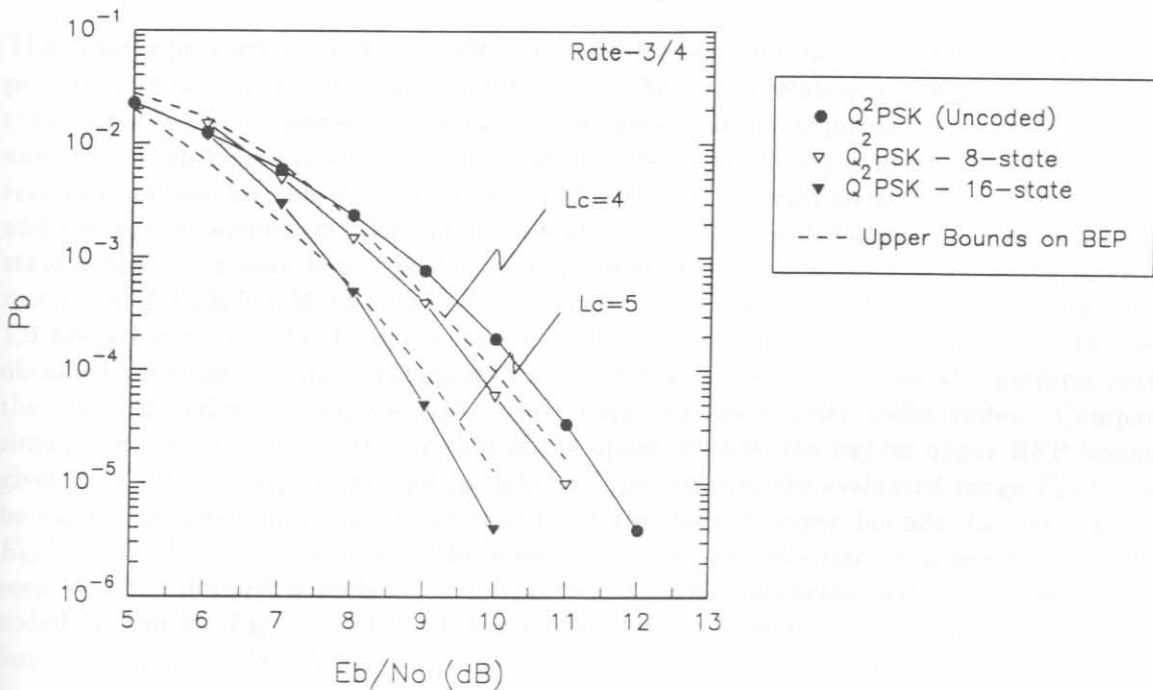


Figure 7.29: BEP graphs 8- and 16-state hybrid rate-2/4  $Q^2$ PSK employing a single rate-2/3 convolutional coder, compared to uncoded CE- $Q^2$ PSK and the upper bounds to BEP.

Comparing the performance curves of the 8- and 16-state coders to that of the uncoded system at  $P_b = 10^{-5}$ , improvements in bit energy requirements of 1.2 and 1.7 dB, respectively are evident. The resulting lower gains in performance, compared to the previous rate-1/2 coder, is as a result of the utilisation of lower rate encoders, (i.e. 2/3 versus 1/2) and also since the redundancy added to maintain a constant envelope can not be used for error correction. Note from the figure that the simulation curves do not correspond at all well to the bounds (again illustrated by the dashed lines) derived in Chapter 5, and presented in Figure 5.8. This may be attributed to the fact that although the block coding scheme does not provide any error correction capabilities, it does improve the noise performance of the code. Specifically, an improvement of 0.6 dB can be expected at a BEP of  $10^{-5}$  for CE-Q<sup>2</sup>PSK, compared to uncoded Q<sup>2</sup>PSK, both operating at 2.0 bits/s/Hz. Comparing the 16-state simulation curve to the upper bound at a BEP of  $10^{-5}$ , the difference in required energy is approximately 0.7 dB. However, when one take the foregoing improvement (0.6 dB) into account, the latter difference between the performance bound and actual simulation point, can be corrected by the 0.6 dB giving a difference of 0.1 dB. Therefore, keeping the foregoing discussion in mind, the upper performance bounds to probability of error are seemingly tighter.



**Figure 7.30:** BEP graphs 8- and 16-state rate-3/4 Q<sup>2</sup>PSK employing a single rate-3/4 convolutional coder, compared to uncoded Q<sup>2</sup>PSK and the upper bounds to BEP.

Figure 7.30 illustrates the BER performance results obtained for coded rate-3/4 Q<sup>2</sup>PSK, compared to uncoded Q<sup>2</sup>PSK. For the simulation tests, 8- and 16-state rate-3/4 encoders were employed. Comparing the performance curves of these 8- and 16-state codes at a BEP,  $P_b = 10^{-5}$  to that of uncoded Q<sup>2</sup>PSK, improvements of respectively, 0.6 and 1.8 dB in bit energy requirement are seen. As was the case for the rate-2/4 Q<sup>2</sup>PSK code performance (Figure 7.29), it is noted from the performance results that the simulation curves correspond well to the derived upper bounds (see Figure 5.9) for values of  $E_b/N_0$  larger than 8.0 dB.

From the BER graphs shown it is clear that reasonable coding gains can be achieved by employing

simple low-complexity sub-optimal encoding and decoding strategies for Q<sup>2</sup>PSK and its constant envelope CE-Q<sup>2</sup>PSK version. Recall that the effective coding gain,  $G_c$ , is the dB decrease in signal energy per bit-to-noise power density ratio ( $E_b/N_o$ ) to maintain the same error performance as uncoded transmission.

#### 7.2.4.2 Evaluation of TCM strategies

Simulation results of the trellis codes for Q<sup>2</sup>PSK/TCM on the static AWGN channel are shown in Figures 7.31 to 7.32. Figure 7.31 illustrates the BEP results obtained for rate-2/4 trellis coded Q<sup>2</sup>PSK/TCM and CE-Q<sup>2</sup>PSK/TCM, compared to that of uncoded Q<sup>2</sup>PSK. For the simulation tests 4- and 8-state trellis codes were evaluated. Comparing the performance curves at a BEP of  $P_b = 10^{-5}$ . Comparing the simulation results of Q<sup>2</sup>PSK/TCM to that of the uncoded system, coding gains of 1.6 and 2.6 are achieved for the 4- and 8-state encoders, respectively. Comparing this with the results obtained with the classical techniques, it is noted that the trellis codes perform better than the classical codes (see Figure 7.28). Furthermore, these improvements are brought about with lower order trellis codes and therefore also lower complexity.

The same improvements in BEP results are evident when the trellis coded CE-Q<sup>2</sup>PSK/TCM system performance is compared to the uncoded system. Note that relative to the uncoded Q<sup>2</sup>PSK system (this curve is not displayed in the figure), improvements in required bit energy in excess of 1.3 and 2.5 dB can be expected, for 4- and 8-state codes, respectively. Figure 7.32 illustrates the BEP results obtained for rate-3/4 trellis coded Q<sup>2</sup>PSK/TCM, compared to that of uncoded Q<sup>2</sup>PSK and the upper bounds on BEP for the 8-state code (derived in Chapter 5). As before, 4- and 8-state trellis codes were evaluated for the performance simulation tests. Comparing the simulation results of Q<sup>2</sup>PSK/TCM to that of the uncoded system at  $P_b = 10^{-5}$ , coding gains of 0.5 and 1.9 are achieved for the 4- and 8-state encoders, respectively. Comparing this with the results obtained with the classical techniques, it is noted that these trellis codes also perform better than the classical codes (see Figure 7.30), while requiring lower order trellis codes. Comparing the simulation curves of the 8-state to that of the upper bounds, the tighter upper BEP bound (UB2) given by (A.21) is surprisingly not as tight as expected over the evaluated range  $E_b/N_o$ . This can be easily explained in terms of the validity of the derived upper bounds, i.e. at high values of  $E_b/N_o$ . By close investigation of the simulation curve and the tighter upper bound (UB2), it is seen that the derived bounds can be expected to provide accurate performance estimates to the coded system for  $E_b/N_o > 11.0$  dB. For values of  $E_b/N_o$  lower than 11.0 dB, the less tight upper bound, UB1 (given by (A.20) should be used as performance estimate.

### 7.3 EVALUATION ON FADING CHANNELS

We consider a typical mobile channel, which is both power-limited and bandwidth-limited. In a mobile channel the available bandwidth is constraint to accommodate a large number of users in a given transmission bandwidth, and power is constrained by the flux density limitation of the mobile (radio or satellite) transmitter's transmission and the physical size of the mobile's antenna. In addition to the usual additive thermal noise background, the mobile channel is also impaired by Doppler frequency shift due to vehicle motion, the potential of a nonlinear channel due to nonlinear amplifiers in the transmitter, voice delay, multipath fading and shadowing. The latter two are most definitely the most serious, whereas for reliable performance the system must be able to be robust under short fades and recover quickly from long fades.



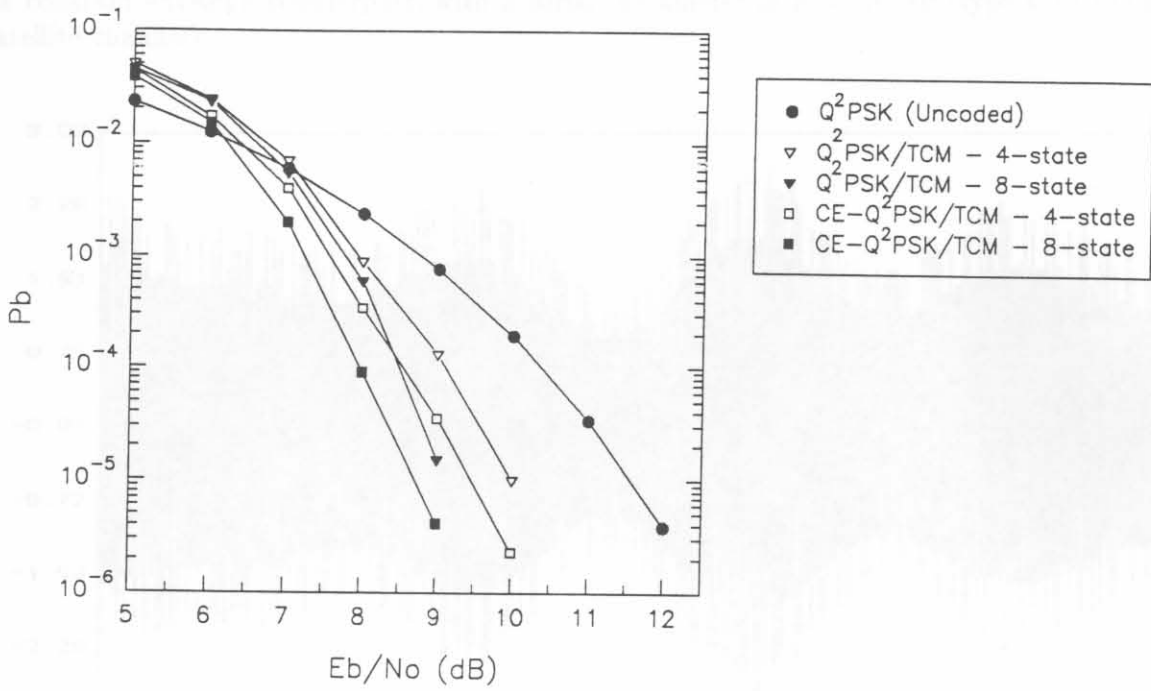


Figure 7.31: BEP graphs 8- and 16-state rate-2/4  $Q^2$ PSK/TCM and CE- $Q^2$ PSK/TCM compared to uncoded  $Q^2$ PSK.

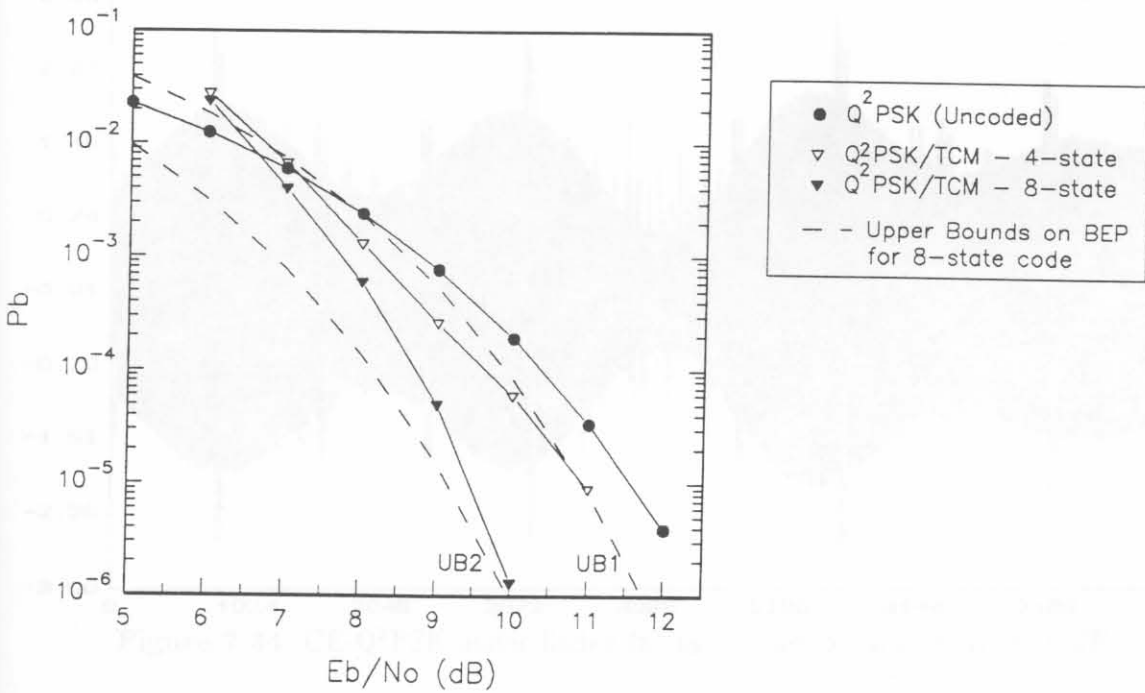


Figure 7.32: BEP graphs 8- and 16-state rate-3/4  $Q^2$ PSK/TCM, compared to uncoded  $Q^2$ PSK.

Figures 7.33 and 7.34 depict the Rician faded discrete time (i.e., sampled) signals for Q<sup>2</sup>PSK and its constant envelope counterpart, with a Rician parameter of  $K = 10$  dB (typical of the mobile satellite channel).

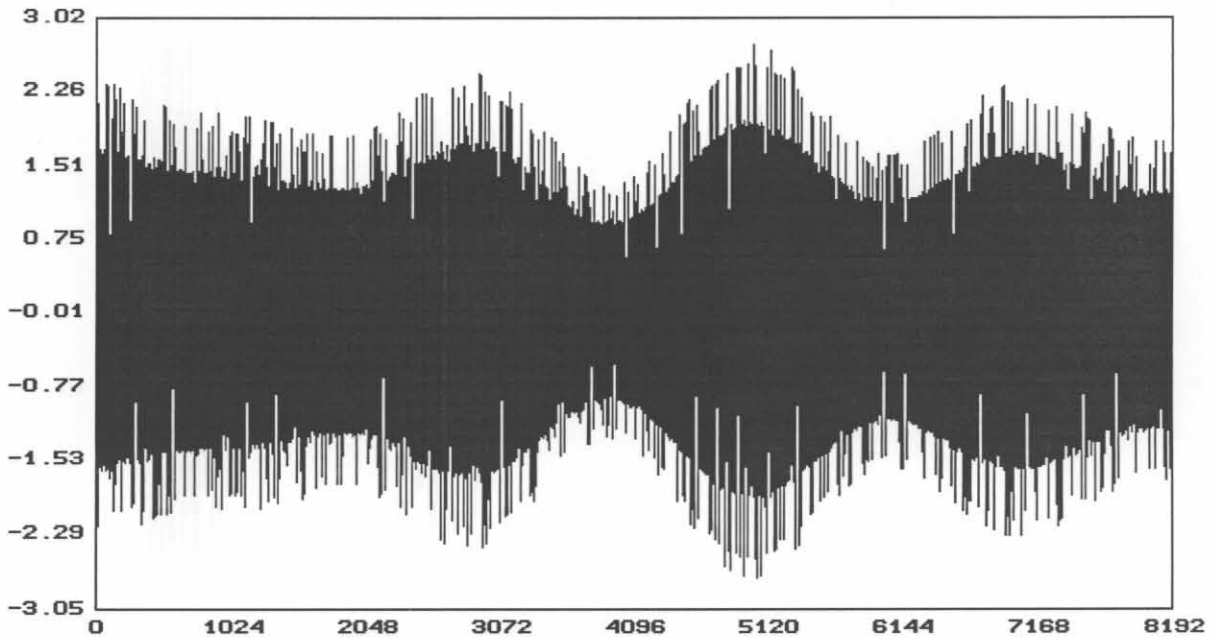


Figure 7.33: Q<sup>2</sup>PSK under Rician fading channel conditions,  $K = 10$  dB.

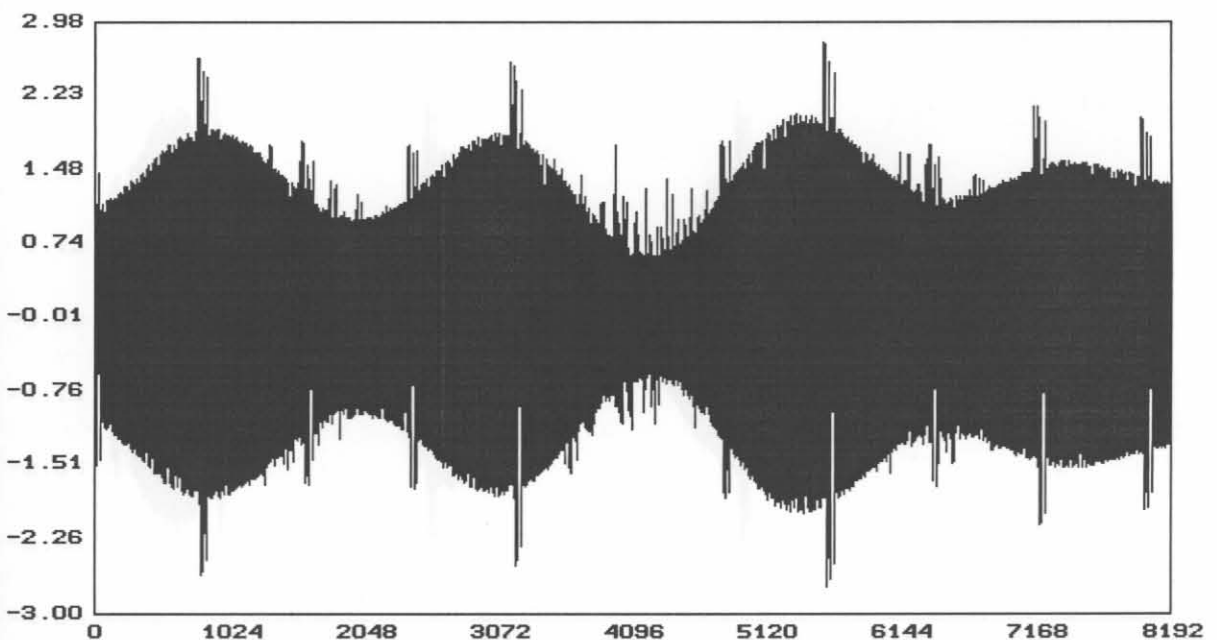


Figure 7.34: CE-Q<sup>2</sup>PSK under Rician fading channel conditions,  $K = 10$  dB.

Figures 7.35 and 7.36 depict the Rayleigh faded discrete time signals for Q<sup>2</sup>PSK and CE-Q<sup>2</sup>PSK, with a Rician parameter of  $K = 0$  dB. For these channel conditions, the Line-of-Sight (LOS) (coherent) component is totally blocked out (typical of the land mobile channel).

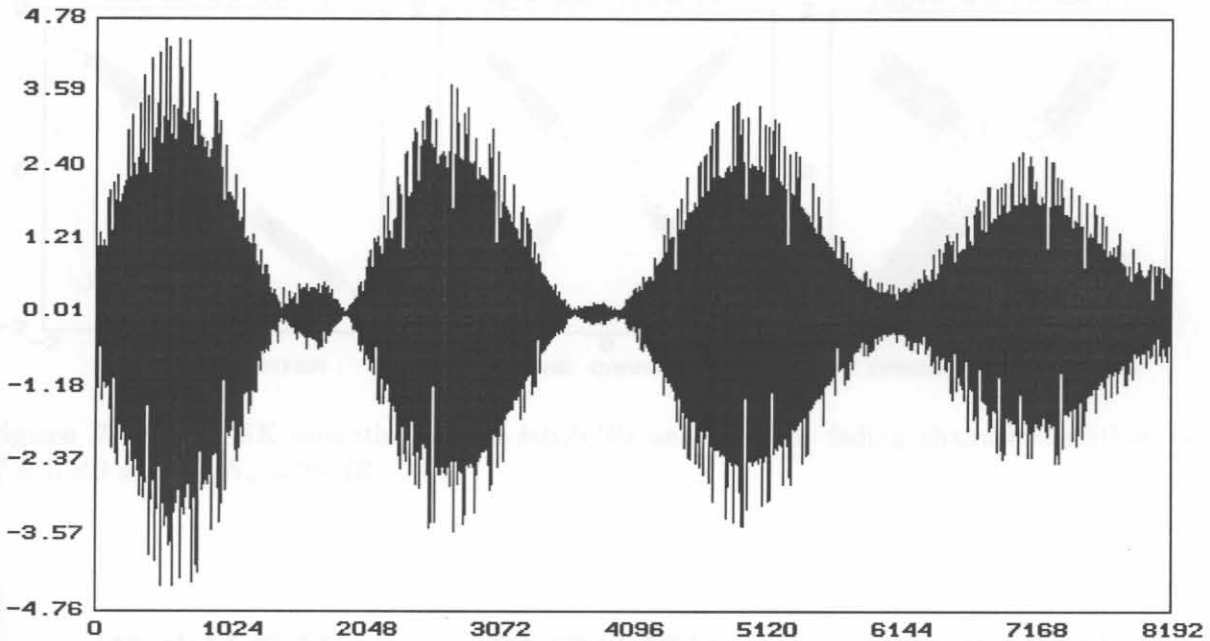


Figure 7.35: Q<sup>2</sup>PSK under Rayleigh fading channel conditions,  $K = 0$  dB.

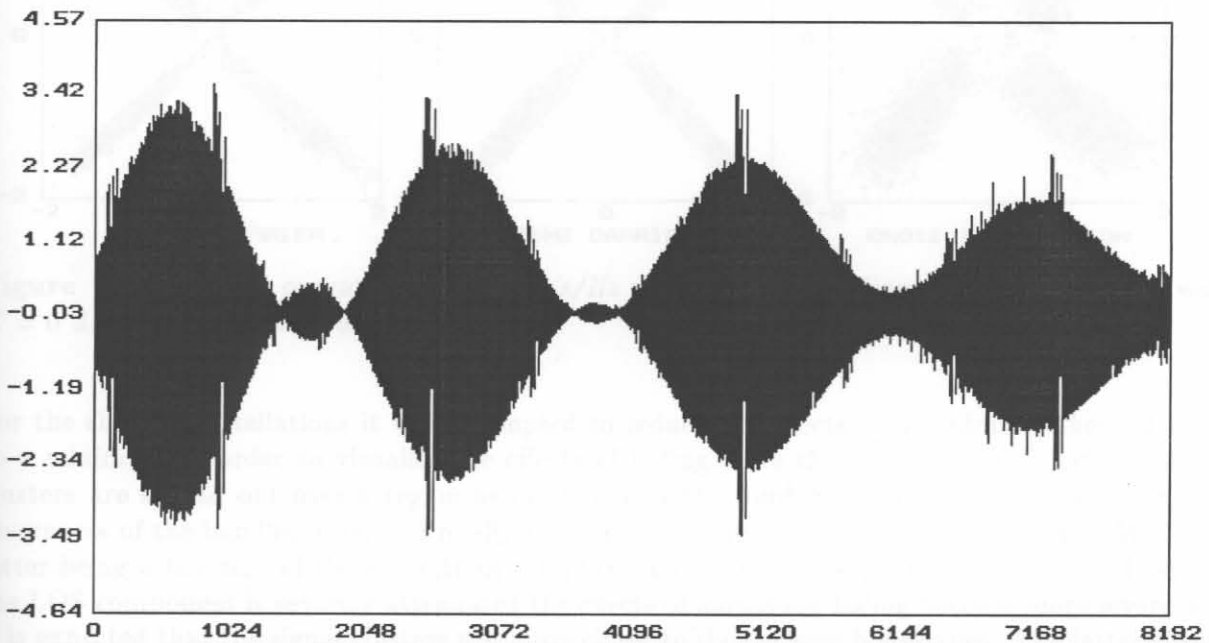


Figure 7.36: CE-Q<sup>2</sup>PSK under Rayleigh fading channel conditions,  $K = 0$  dB.

We again consider the signal space constellations as an effective way of displaying the detrimental effects of mobile fading channels. Figures 7.37 to 7.38 show the bandlimited Q<sup>2</sup>PSK signal constel-

lations operating at 2.0 bits/s/Hz under typical mobile fading channel conditions in AWGN with  $E_b/N_o = 25.0$ .

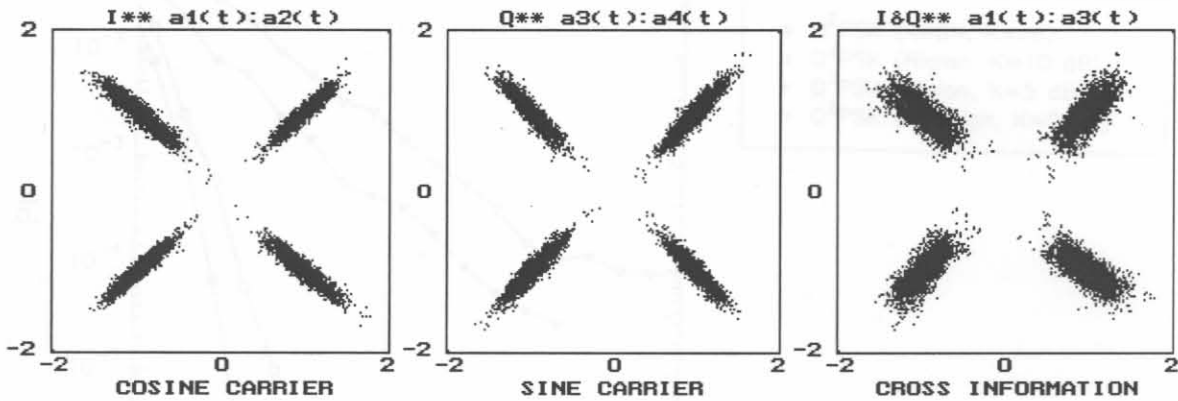


Figure 7.37: Q<sup>2</sup>PSK operating at 2.0 bits/s/Hz under Rician fading channel conditions with  $K = 5$  dB and  $E_b/N_o = 25$  dB.

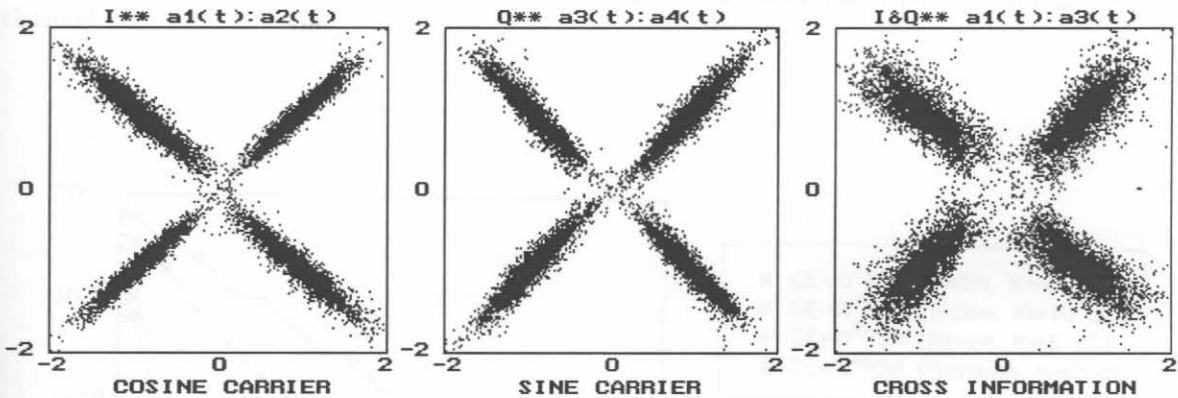


Figure 7.38: Q<sup>2</sup>PSK operating at 2.0 bits/s/Hz under Rayleigh fading channel conditions with  $K = 0$  dB and  $E_b/N_o = 25$  dB.

For the shown constellations it was attempted to reduce the effects of the additive thermal noise to a minimum in order to visualise the effects of fading more clearly. It is seen that the signal clusters are spread out over a region associated with the combined effects of thermal noise, the severeness of the bandlimiting, and finally the effects of mobile channel amplitude fades. With the latter being a function of the strength of the LOS component in the fading channel model. When the LOS component is severely attenuated the effects of amplitude fading become more severe and it is expected that the signal clusters will move closer to the decision boundaries. The latter effects are clearly visible on the constellations depicted in Figure 7.38 where the LOS component power is taken to be equal to the power in the scatter components (i.e., dual equal amplitude propagation model [63]).

Figures 7.39 to 7.40 show the BER results of the Q<sup>2</sup>PSK and CE-Q<sup>2</sup>PSK modem operating at

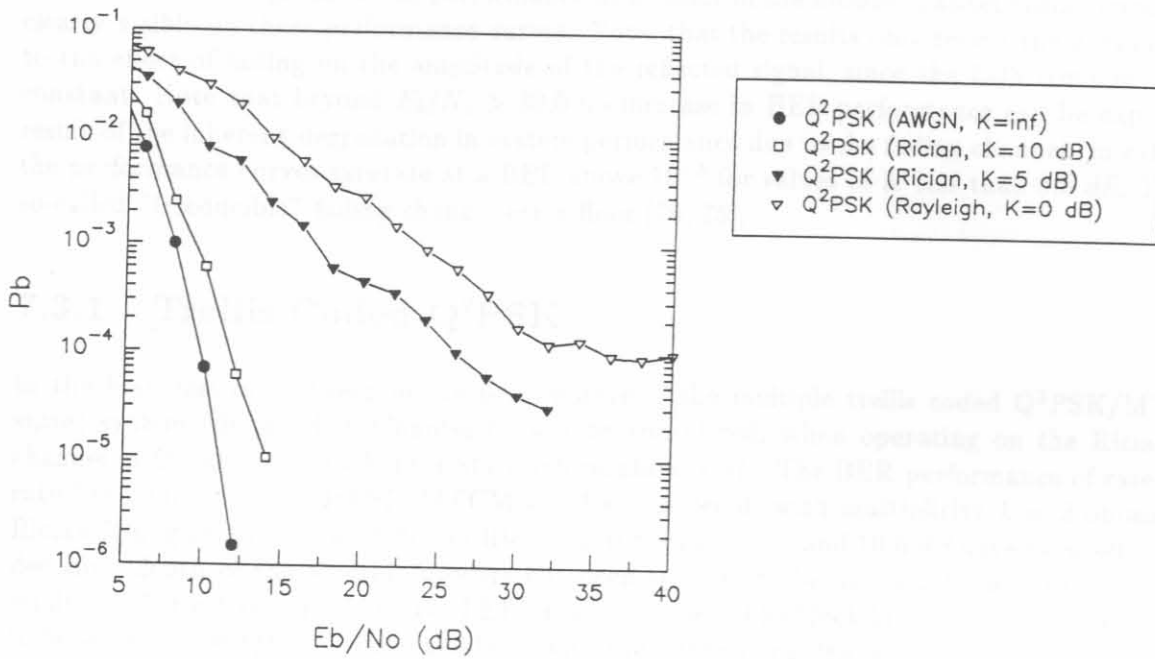


Figure 7.39: BER results for Q<sup>2</sup>PSK modem operating on AWGN, Rician and Rayleigh fading channel.

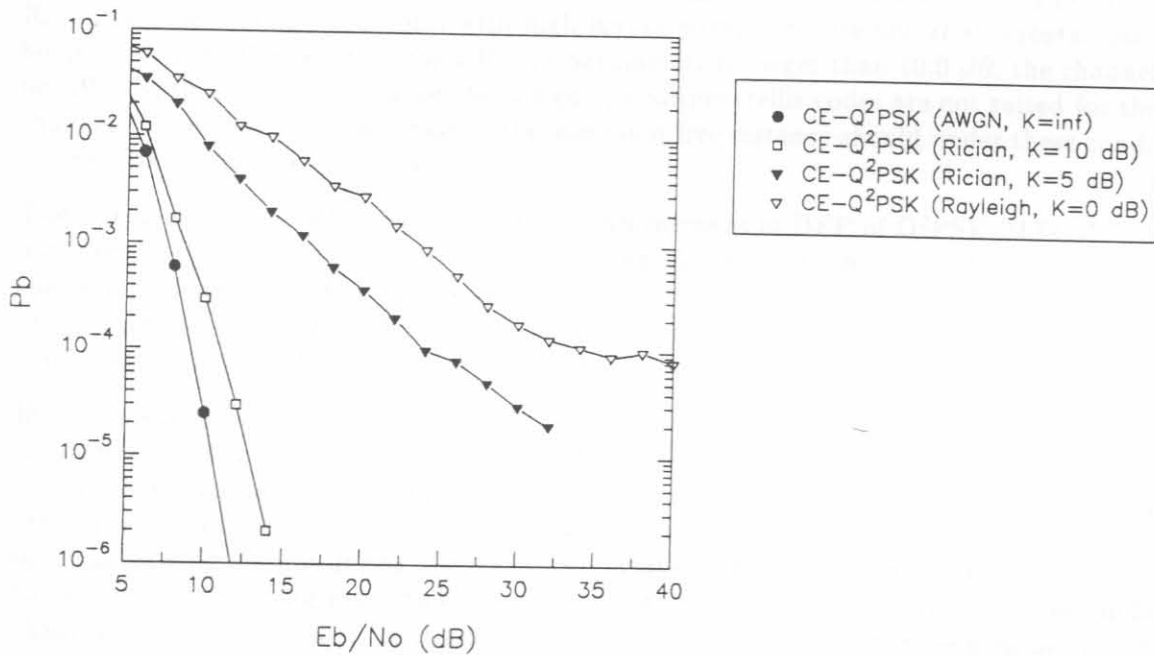


Figure 7.40: BER results for CE-Q<sup>2</sup>PSK modem operating on AWGN, Rician and Rayleigh fading channel.

2.0 bits/s/Hz, under AWGN, Rician ( $K = 5, 10$  dB), and Rayleigh ( $K = 0$  dB) fading channel conditions. The degradation in performance as a result of the mobile channel fading conditions are clearly visible on these performance curves. Note, that the results only reflect the degradation due to the effect of fading on the amplitude of the reflected signal, since the LOS component is kept constant. Note that beyond  $E_b/N_o > 30.0$  no increase in BEP performance can be expected as a result of the inherent degradation in system performance due to the fading channel. In other words the performance curves saturate at a BEP above  $10^{-5}$  for values of  $K$  less than 5.0 dB. This is the so-called "irreducible" fading channel error floor [76, 75].

### 7.3.1 Trellis Coded Q<sup>2</sup>PSK

In the first part of this section the performance of the multiple trellis coded Q<sup>2</sup>PSK/MTCM (4-state) system (designed in Chapter 6) will be considered, when operating on the Rician fading channel in the absence of Channel State Information (CSI). The BER performance of rate-6/8 and rate-5/8 coded 4-state Q<sup>2</sup>PSK/MTCM will be considered, with multiplicity  $k = 2$  obtained on a Rician fading channel. Two different Rician factors of  $K = 5.0$  and 10.0 dB have been selected. The decoding depth of the Viterbi decoders has been selected to be at least 4 times the length of the minimum Error Event Probability (EEP) in all the cases. The block bit interleaving size was chosen to be equal to 196 Q<sup>2</sup>PSK coded symbols, with the interleaving depth equal to 16 symbols (64 bits), and the interleaver span equal to 12 symbols (48 bits). This will cause a worst case-delay (due to the block interleaver) of 768 coded Q<sup>2</sup>PSK information bits. When one considers a transmission rate of  $R_b = 20.0$  kbits/s, the worst case-delay will be 38.4 ms, which is quite acceptable for the transmission of digitally encoded speech [58, 76].

Results of the Rician fading channel for  $K = 10$  dB are shown in Figure 7.41. The important point made in this figure is that the improvement in achievable BEP performance for MTCM codes under Rician channel fading conditions, with high Rician parameter, are not at all substantial. This can be attributed to the fact that for a Rician parameter,  $K$  larger than 10.0 dB, the channel tends to be AWGN, that is the criteria for the design of multiple trellis codes are not suited for these fading channels. Therefore, maximisation of the minimum free distance should under these conditions still be the primary design objective.

The foregoing is clear when we consider the improvement in BEP of Q<sup>2</sup>PSK/MTCM compared to uncoded Q<sup>2</sup>PSK, operating on the Rician fading channel with  $K = 5$  dB. Importantly, we note that the probability of error for the rate-6/8 and 5/8 codes varies inversely with  $(E_s/N_o)^2$ , because of the length of the shortest EEP (or code diversity) is equal to 2. Note that when the multiplicity is increased to  $k = 4$ , the probability of error is expected to vary inversely with  $(E_s/N_o)^4$ .

In the foregoing discussion no CSI was available during the demodulation process. Recall, that the metric chosen for the Viterbi decoder depends on whether or not CSI can be obtained. As discussed in Chapter 3 (see Figure 3.3), a measure of CSI can be obtained from the channel state extractor. For our application, the use of the magnitudes of the complex correlation function at the optimum timing instant during the frame and symbol synchronisation period, has been considered to determine the fading magnitude over the header interval, This is used as a direct indication of channel state or reliability. In general, any other measure could have been employed. Consider, for instance the utilisation of a channel estimator based on a recursive Least Mean Square (LMS) estimator. The latter technique was found to be as effective as the correlation-magnitude method, but at a much higher complexity.

Employing the correlation-magnitude as an indication of CSI, i.e., the reliability or state of the

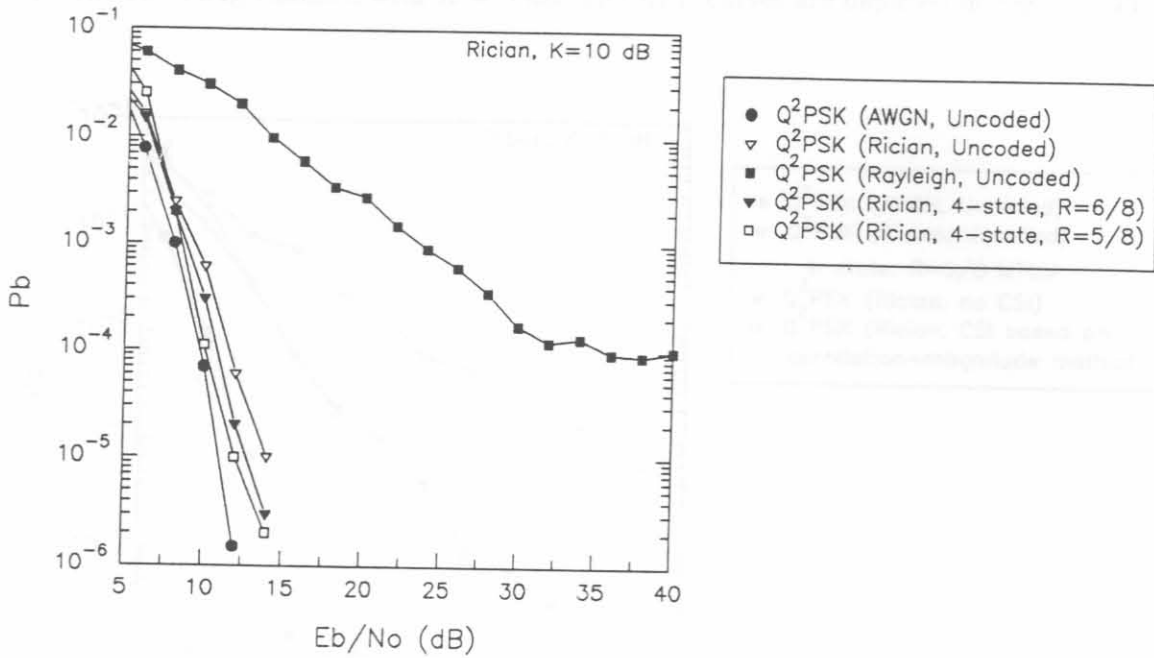


Figure 7.41: BER results for 4-state rate-6/8 and rate-5/8 Q<sup>2</sup>PSK/MTCM operating on Rician ( $K = 10$  dB) fading channel.

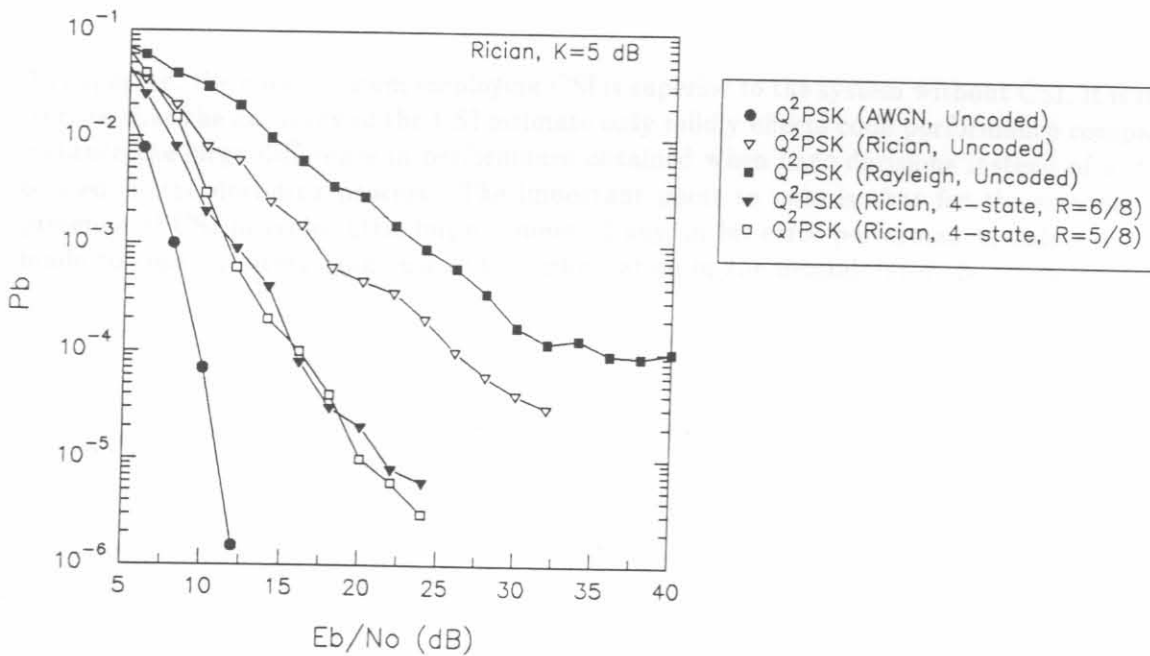
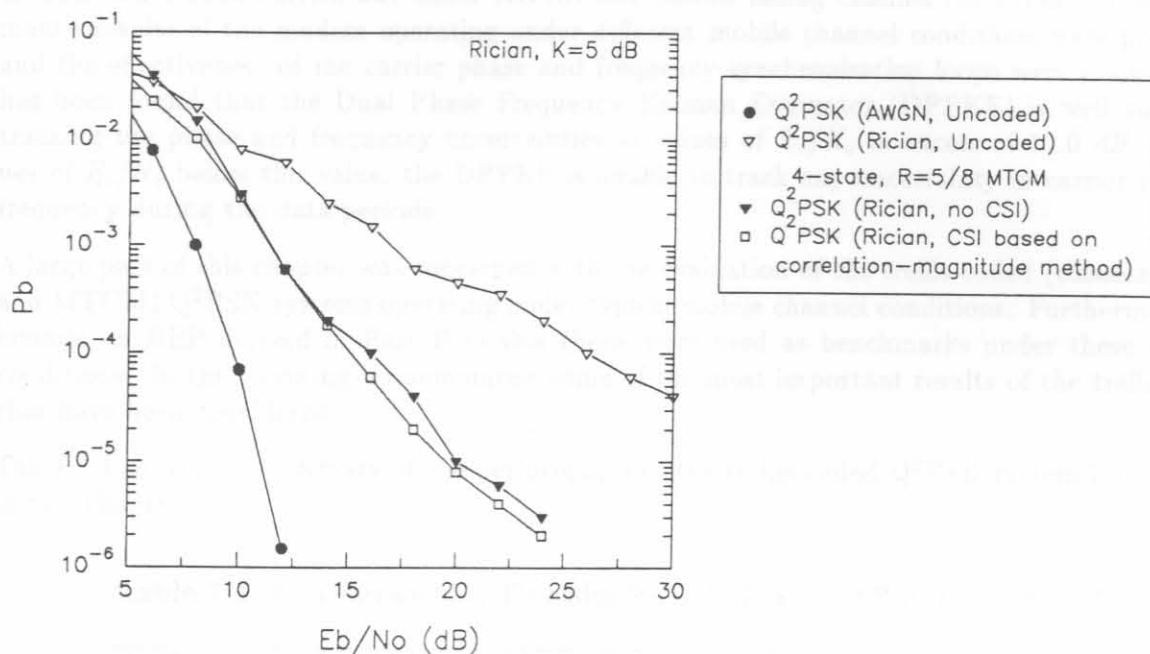


Figure 7.42: BER results for 4-state rate-6/8 and rate-5/8 Q<sup>2</sup>PSK/MTCM modem operating on Rician ( $K = 5$  dB) fading channel.

channel, the performance of the 4-state rate-5/8  $Q^2$ PSK/MTCM coded system was evaluated on the Rician fading channel, with  $K = 5$  dB. The BEP curves are depicted in Figure 7.43.



**Figure 7.43:** BER results for 4-state rate-5/8  $Q^2$ PSK/MTCM modem operating on Rician ( $K = 5$  dB) fading channel without and with CSI based on the correlation-magnitude of the frame and symbol synchronisation process.

As expected, the coded system employing CSI is superior to the system without CSI. It is interesting to note that the accuracy of the CSI estimate only mildly effects code performance compared to for instance the large difference in performance obtained when hard decisions instead of soft decisions is used in the decoding process. The important point to note is that for the uncoded case, the presence of CSI provides little improvement, if any, in bit error performance, unless an attempt is made to constructively make use of this information in the demodulator/detection process.



## 7.4 CONCLUDING REMARKS: CHAPTER 7

In this chapter an extensive simulation performance evaluation of the Q<sup>2</sup>PSK and CE-Q<sup>2</sup>PSK modems have been carried out under AWGN and mobile fading channel conditions. The performance results of the modem operating under different mobile channel conditions were presented, and the effectiveness of the carrier phase and frequency synchronisation loops were evaluated. It has been found that the Dual Phase Frequency Kalman Estimator (DPFKE) is well suited for tracking the phase and frequency uncertainties at values of  $E_b/N_o$  in excess of 10.0 dB. For values of  $E_b/N_o$  below this value, the DPFKE is unable to track any uncertainty in carrier phase or frequency during the data periods.

A large part of this chapter was concerned with the evaluation of the trellis coded (classical, TCM and MTCM) Q<sup>2</sup>PSK systems operating under typical mobile channel conditions. Furthermore, the bounds on BEP derived in Part II of this thesis were used as benchmarks under these channel conditions. In the following we summarise some of the most important results of the trellis codes that have been considered.

Table 7.1 provides a summary of the performance of the trellis coded Q<sup>2</sup>PSK system investigated in this chapter.

**Table 7.1:** Comparison of trellis codes for Q<sup>2</sup>PSK at a BEP of  $P_e = 10^{-5}$  dB.

Trellis Code	Code Rate, $R_c$	No. of states	$E_b/N_o$ for $P_e \leq 10^{-5}$	Channel	Gain, $G_c$ over uncoded Q <sup>2</sup> PSK
Classical	2/4	8	10.3 dB	AWGN	1.1 dB
Classical	2/4	16	9.4 dB	AWGN	2.0 dB
Classical	2/4(CE)	8	9.6 dB	AWGN	1.8 dB
Classical	2/4	16	9.0 dB	AWGN	2.4 dB
Classical	3/4	8	10.9 dB	AWGN	0.5 dB
Classical	3/4 (CE)	16	9.7 dB	AWGN	1.7 dB
TCM	2/4	4	10.0 dB	AWGN	1.4 dB
TCM	2/4	8	9.0 dB	AWGN	2.4 dB
TCM	2/4 (CE)	4	9.6 dB	AWGN	1.8 dB
TCM	2/4 (CE)	8	8.7 dB	AWGN	2.7 dB
TCM	3/4 (CE)	4	11.0 dB	AWGN	0.4 dB
TCM	3/4 (CE)	8	9.6 dB	AWGN	1.8 dB
MTCM	6/8	4	13.0 dB	Rician ( $K = 10$ )	1.5 dB
MTCM	5/8	4	12.0 dB	Rician ( $K = 10$ )	2.5 dB
MTCM	6/8	4	22.0 dB	Rician ( $K = 5$ )	> 13.0 dB
MTCM	5/8	4	20.0 dB	Rician ( $K = 5$ )	> 15.0 dB
MTCM (CSI)	5/8	4	17.5 dB	Rician ( $K = 5$ )	> 17.5 dB

The performance is compared to the corresponding performance of uncoded Q<sup>2</sup>PSK, expressed as a coding gain,  $G_c$  in dB. From the table it can be seen that the low rate classical convolutional codes provided good performance, compared to their relative complexity. The hybrid rate-2/4 code, employing the single rate-2/3 convolutional encoder, provides the best performance of all the classical error correction strategies considered. This is in spite of the lower expected performance of

the rate-2/3 encoder, when compared to that of the rate-1/2 encoders of the non-constant envelope Q<sup>2</sup>PSK system. It should therefore be clear that the choice of constant envelope coded scheme should be strongly considered for application on non-linear channels.

When we compare the performance of the trellis coded modulation codes, similar observations are made. Specifically, the performance of the rate-2/4 trellis coded constant envelope Q<sup>2</sup>PSK provides the best performance under AWGN channel conditions. The rate-3/4 trellis codes also provide relatively high coding gains, compared to that of the uncoded Q<sup>2</sup>PSK system, without a substantial reduction in throughput rate.

Finally, we compare the multiple-trellis codes, specifically designed for transmission over the fading channel, with and without the availability of CSI.

In the first part of this section the performance of the multiple trellis coded Q<sup>2</sup>PSK/MTCM (4-state) system operating on the Rician fading channel in the absence of Channel State Information (CSI) was considered. For all the simulation results a block interleaver was employed with bit interleaving size was chosen to be equal to  $16 \times 12 = 196$  Q<sup>2</sup>PSK coded symbols. We have considered the bit error rate performance of rate-6/8 and rate-5/8 coded 4-state Q<sup>2</sup>PSK/MTCM, with multiplicity  $k = 2$  obtained on a Rician fading channel for two different Rician factors of 5.0 and 10.0 dB.

From the results of the Rician fading channel for  $K = 10$  dB, shown in Figure 7.41, it can be seen that the coding gains achieved by the 4-state MTCM are not as high as one may have expected. The important point to keep in mind when considering these results, is that the trellis codes which are optimum for the AWGN channel, will also be optimum for the Rician channel, when  $K$  is greater than 5.0 dB. This can be attributed to the fact that a Rician channel,  $K$  larger than 5.0 dB strongly resembles an AWGN channel.

Comparing the results of the 4-state Q<sup>2</sup>PSK/MTCM, at the same code rates operating on the Rician fading channel for  $K = 5$  dB, a large increase in coding gains is noted. Recall, that for a code multiplicity  $k = 2$ , the probability of error of the 4-state rate-6/8 and 5/8 codes varies inversely with  $(E_s/N_o)^2$ , since the length of the shortest EEP is equal to  $k = 2$ .

Therefore, it is concluded that some of the optimum codes specially designed for the AWGN channel, may also be very suitable for application over fading channels with Rician parameter in excess of 5.0 dB. This is true, since in channels with  $K$  large, the diversity factor does not significantly influence the BEP behavior of the codes.

---

---

## CHAPTER 8

---

# CONCLUSIONS AND FUTURE RESEARCH

---

---

In this chapter a summary of the research work performed during this study is presented. Furthermore, we present future research areas of interest. Finally, the chapter is concluded with a discussion and dissertation conclusions.

First of all a brief summary of the research work carried out during this study, is presented.

The research covered in this dissertation was presented in three parts. In Chapter 1 the overall introduction and literature survey on specific topics related to four-dimensional modulation, demodulation, synchronisation and coding were presented. In the first part of this dissertation, Chapter 2, 3 and 4, the most important theories and general communication system concepts were given. More specifically, we have considered in Chapter 2 the principles of four-dimensional  $Q^2$ PSK signalling, as well as the advantages of multidimensional signal space utilisation. Furthermore, considerations of energy and bandwidth efficiency, and capacity have been given. In Chapter 3 we have presented detail concerning the mobile digital communication system, as well as the fading channel model adopted for evaluation purposes. In Chapters 4 the three main topics of modulation, demodulation and synchronisation of the digital  $Q^2$ PSK and CE- $Q^2$ PSK communication system operation were treated and discussed in detail. The digital modulation and demodulation block diagrams were presented and analysed in detail. A novel frame synchronisation procedure for  $Q^2$ PSK was presented. Furthermore, investigations into the effects of carrier phase and frequency uncertainties were investigated. The final parts of Chapter 4 considered the problems concerning the design and implementation of carrier phase and frequency tracking loops for the  $Q^2$ PSK system.

In the second part the concepts of trellis coding have been considered, including classical, TCM and MTCM error correction techniques, for application into the  $Q^2$ PSK modem. In Chapter 5 specific designs of trellis codes for  $Q^2$ PSK for transmission over the AWGN channel have been considered.

The design and implementation of forward error correction codes, based on classical convolutional error correction were carried out, as possible solutions when complexity (low computational load) and cost are the primary design objectives. Furthermore, the state of the art TCM techniques were compared to the classical techniques with a view of achieving even better BEP performance. Appendix A presents the general theories of channel coding, with specific reference to the concepts of TCM. The Ungerboeck and analytical (Calderbank—Mazo) code descriptions, the decoding procedure and finally the very important issues of code performance evaluation are considered. The trellis codes designed and analysed were derived from the original unexpanded Q<sup>2</sup>PSK signal set. Throughout this part of the dissertation, theoretical performance bounds on bit error probability were derived, when feasible, i.e. for codes of low complexity.

In Chapter 6 the designs of trellis codes (TCM and MTCM) have been carried out for Q<sup>2</sup>PSK transmission over the mobile fading channel, again employing the original (unexpanded) Q<sup>2</sup>PSK signal constellation. Therefore, the coding gains are obtained at the expense of the information data rate. We have concentrated on the design for Rician fading channels, with high Rician factors, i.e.  $K \geq 5$  dB.

The final part of this dissertation was concerned with the extensive performance evaluation of the proposed modem, synchronisation and coding techniques presented in the foregoing chapters. Chapter 7 dealt with this performance evaluation by means of computer simulation. The coded and uncoded Q<sup>2</sup>PSK signals have been evaluated on the AWGN, non-linear channel, and typical mobile fading channel conditions. For the non-linear channel, we have considered the effects of carrier phase and Doppler frequency effects in AWGN. Our system was evaluated under typical non-linear mobile conditions, where a maximum Doppler frequency  $f_D = 100.0$  Hz and maximum phase offset  $\theta_o = 0.2$  rad were simulated. The effects of phase fading on the received signal, typical of frequency selective multipath fading channels, have not been investigated in this dissertation, since the latter require the implementation of a multidimensional complex equaliser.

## 8.1 FUTURE RESEARCH

The work presented in this dissertation has brought about many new questions and possible areas of future research.

### 8.1.1 Design and implementation of a multidimensional equaliser

In this dissertation we have only considered the effects of amplitude fading on the received signal. In general, in a land mobile channel characterised by multipath effects, fading causes severe distortion of the transmitted waveform, i.e., random amplitude and phase variations and accordingly long, densely packed noise bursts. These effects cause phase and amplitude uncertainties, which result in Intersymbol Interference (ISI) and distortion of the signal space geometry. In order to maintain the signal space geometry as closely as possible to the original one, equalisation is required. As long as two orthogonal baseband signals are present in each of the in-phase and quadrature-phase signals, which is the case for four-dimensional Q<sup>2</sup>PSK, a multidimensional complex equalisation procedure is required. At this point in time the design of such an equaliser, remains a subject for future research.

### 8.1.2 Application of a burst-error correcting Viterbi decoder

Interleaving random-error-correcting codes to combat burst noise is a standard technique that can be applied to any bursty channel. Interleaving randomises error clusters by spreading the erroneous bits in a burst so far apart that the bursty channel is effectively transformed into a random-error channel, i.e. a memoryless Additive White Noise (AWGN) channel. In general, the interleaving mechanism is robust in that changes in the channel statistics do not influence the system's performance appreciably [30, 92, 42].

The burst-error-correction Viterbi decoder, proposed by Schlegel and Herro [93], combines maximum-likelihood decoding with a burst error detection scheme and can be considered as an alternative coding method for bursty channels. As proposed by Schlegel and Herro, the burst-error-correction strategy combines maximum-likelihood decoding with a burst error Viterbi detection scheme. The decoder nominally operates as a Viterbi decoder and switches to a burst-error-correcting mode when the receiver detects incoming error patterns the Viterbi decoder is unable to correct, i.e., the dual-mode decoder automatically switches modes according to the state of the channel.

The strength of using the Viterbi decoder in this dual-mode configuration lies in its undiminished error-correcting power when the channel is in the random-error state. Most known burst correction schemes sacrifice error-correcting power in order to detect bursts, which makes them unsuitable for use on random-error channels plagued by occasional deep fades and associated error bursts. The proposed burst-error-correcting algorithm could therefore be investigated as an alternative to the standard interleaving strategies usually employed on digital communication systems utilising the Viterbi algorithm.

## 8.2 Design of Ungerboeck-type codes for fading channels

Under certain conditions it is possible to reduce a multiple trellis code with parallel paths, to an Ungerboeck-type code (multiplicity  $k = 1$ ) with no parallel paths, but an increased number of states. We first note that in order for an Ungerboeck-type code with rate  $b/(b + 1)$  and no parallel paths to achieve diversity  $L$ , the smallest number of states required is

$$2^v = 2^{b(L-1)} \quad (8.1)$$

For example, for  $b = 3$ , the minimum number of states required to achieve  $L = 4$  would be  $N_s = 2^{3(4-1)} = 2^{512}$ . The application of these codes to the Q<sup>2</sup>PSK modem operating on fading channels needs to be investigated on merits, with considerations on application, bandwidth constraints, cost and complexity.

### 8.3 CONCLUDING REMARKS: CHAPTER 8

In this dissertation the problem of modulation, demodulation, synchronisation and coding of a four-dimensional signalling digital modem have been addressed for the mobile digital communication environment. Evaluation of the Q<sup>2</sup>PSK communication system was carried out by means of extensive computer simulations under typical mobile communication channel conditions. Two different cases were considered, namely the conventional Q<sup>2</sup>PSK and the constant envelope version. In most cases the CE-Q<sup>2</sup>PSK system achieved superior performance to that of the non-constant envelope system.

Concerning, the synchronisation aspects of the Q<sup>2</sup>PSK system, it was found that the novel frame synchronisation procedure yielded good performance under AWGN channels, as well as under fading channel conditions. The complex correlation-magnitude information obtained during frame synchronisation can furthermore be used to provide a means of Channel State Information (CSI). It was shown by means of simulation that this channel reliability information can lead to improved bit error performance under fading channel conditions when a coded system is utilised. It should, however, be mentioned that for the uncoded systems, the presence of CSI provide no improvement in performance. The designed carrier phase and frequency tracking loops performed well under specific non-ideal channel conditions in AWGN. It was found however, that the Dual Phase and Frequency Kalman Estimator (DPFKE) is not well suited for typical mobile fading conditions. This can be mainly attributed by the fact that the phase tracking loop in this DPFKE is unable to track the effects of phase non-linearities due to fading. It should, however be mentioned that the application of a complex equaliser may prove advantageous in estimating these carrier phase and frequency uncertainties.

For the uncoded Q<sup>2</sup>PSK system operating over the fading channel, it was found that the system performed poorly in the Rayleigh and Rician mobile fading channels, with all of the performance curves saturating at a BEP above  $10^{-5}$ , except for the cases of high Rician channel factors, i.e.  $K \geq 5.0$  dB.

Several design criteria in the design of optimum trellis coded system on the fading channel have been derived. Design criteria revealed that the design of trellis coded Q<sup>2</sup>PSK systems aimed to achieve optimum performance on the Rician fading channel is guided by a factor that differs from the optimum trellis code design on the AWGN channel. In particular, the primary objective to minimise the bit error probability of the code, requires the maximisation of the number of symbols at non-zero Euclidean distance to the shortest error event path. The secondary objective is to maximise the product of the branch distances along the shortest error event path normalised by the Euclidean distance. Following the criteria derived, different multiple trellis codes were designed, aided by computer searches to find the optimum Q<sup>2</sup>PSK/MTCM codes. The 4-state rate-5/8 and 6/8 trellis codes were evaluated on Rician fading channels with  $K = 5$  and  $K = 10$  dB. Results on the Rician fading channel with  $K = 5$  dB have shown the importance of the multiplicity or diversity factor of the trellis coded system under these channel conditions. On the contrary, the results obtained for Rician fading channels with  $K = 10$  dB, demonstrate that for these channel situations, the diversity of the code does not constitute the primary objective for optimum performance. This is true since the free Euclidean distance of the code dominated the performance of the trellis coded system.

In conclusion, it should be kept in mind that the best error correction strategies discussed in this dissertation are probably good in overall terms, but that better schemes do exist if unlimited complexity is allowed. The existence of possibly better schemes of similar complexity cannot be proved or denied. The problem is that there is no unified theory for the design of error correction

codes — the design of new codes should be the result of long term research and the application of the experienced gained in the field over time. Evaluation of the coded and uncoded Q<sup>2</sup>PSK mobile digital communication system was accomplished on the AWGN and typical mobile fading conditions. It was shown that this four-dimensional modulation scheme may be advantageously utilised for digital communications over these mobile channels at data rates exceeding that of for instance the American adopted  $\pi/4$ -QPSK modulation scheme under identical channel bandwidth and propagation conditions.

---

---

---

---

# APPENDICES

---

---

## APPENDIX A

### A TUTORIAL ON TCM

---

---

#### A.1 INTRODUCTION

TCM is a traditional Chinese medical system of diagnosis and healing, known as 1. The development of TCM is a long process, and it is believed that TCM has evolved over a period of 2,000 years. The purpose of this tutorial is to provide a comprehensive overview of TCM, including its history, theory, and practice. The tutorial is divided into several sections, each covering a different aspect of TCM. The first section, 'Introduction', provides an overview of TCM and its history. The second section, 'Theory', discusses the fundamental principles of TCM, including the concepts of Yin and Yang, Qi, and the Five Phases. The third section, 'Diagnosis', describes the various methods used in TCM to diagnose a patient's condition, such as pulse diagnosis, tongue diagnosis, and observation. The fourth section, 'Treatment', discusses the various methods used in TCM to treat a patient's condition, including acupuncture, herbal medicine, and dietary therapy. The fifth section, 'Conclusion', summarizes the key points of the tutorial and provides a brief overview of the future of TCM.

The idea of TCM is to provide a holistic approach to medicine, one that considers the whole person, not just the symptoms. TCM is based on the idea that the body is a complex system, and that the health of the body depends on the balance of its various parts. TCM practitioners believe that the body has a natural ability to heal itself, and that the role of the practitioner is to support this natural healing process. TCM is a highly effective and safe form of medicine, and it is becoming increasingly popular around the world. The World Health Organization (WHO) has recognized TCM as a traditional medicine, and it is now included in the World Health Organization's International Classification of Diseases (ICD-10). TCM is also recognized by the World Bank as a traditional medicine, and it is now included in the World Bank's International Classification of Diseases (ICD-10). TCM is a highly effective and safe form of medicine, and it is becoming increasingly popular around the world.



The design was based on Euclidean distance rather than on Hamming distance. The choice of the modulation of the signal constellation was performed separately. First, the detection process was made soft rather than hard. Second, the detection process was made soft rather than hard. The transmitted symbols they contained.

## A.1 Fundamentals of TCM

# APPENDIX A

---

# A TUTORIAL ON TCM

---

---

This appendix presents a tutorial on trellis codes as applied to  $Q^2$ PSK. Specifically, the general concepts of trellis coded modulation are discussed, including some fundamental principles, decoding and evaluation.

## A.1 INTRODUCTION

In this appendix the techniques of combined modulation and coding, known as Trellis Coded Modulation (TCM) are introduced. Over the last 2 decades TCM has emerged as an efficient and reliable coding scheme used for data communication with the purpose of gaining noise immunity over uncoded transmission without altering the data rate. Stated in other words, TCM is a combined coding and modulation scheme for improving the reliability of a digital transmission system without increasing the transmitted power or the required bandwidth. In a power-limited environment, the desired system performance should be achieved with the smallest possible power. One solution is the use of error-correcting codes, which increase the power efficiency by adding extra bits to the transmitted symbol sequence. This procedure requires the modulator to operate at a higher data rate and hence requires a larger bandwidth. In a bandwidth-limited environment, increased efficiency in frequency utilization can be obtained by choosing higher-order modulation schemes (e.g. 8-PSK instead of QPSK), but larger signal power would be needed to maintain the same signal separation and hence the same error probability.

The idea is indeed not new, since multilevel modulation of convolutionally encoded symbols was a known concept before the introduction of TCM. The innovative aspect of TCM is the concept that convolutional encoding and modulation should not be treated as separate entities, but rather, as a combined operation. The parameter governing the performance of the transmission system is consequently not the *free Hamming distance* of the convolutional code, but rather, over the additive Gaussian noise channel, the *free Euclidean distance* between transmitted signal sequences. Thus

the optimization of the TCM design will be based on Euclidean distances rather than on Hamming distances, so that the choice of the code and of the signal constellation will both be performed separately. Finally, the detection process will involve *soft* rather than *hard* decisions (i.e., received signals are processed before making decisions as to which transmitted symbol they correspond.)

### A.1.1 Fundamentals of TCM

Assume here a discrete-time, continuous-amplitude model for the transmission of data on the additive white Gaussian noise channel. In this communications model, independently introduced by the Russian scholar Kotel'nikov and by C.E. Shannon, the messages to be delivered to the user are represented by points, or vectors, in an  $N$ -dimensional Euclidean space  $\mathbf{R}^N$ , called the *signal space*. When the vector  $x$  is transmitted, the received signal is represented by the vector

$$z = x + \nu \quad (\text{A.1})$$

where  $\nu$  is a noise vector whose components are independent Gaussian random variables with mean zero and the same variance  $N_o/2$ . The vector  $x$  is chosen from  $\Omega'$  consisting of  $M'$  vectors, known as the *signal constellation*. The average square length

$$E' = E_{s,u} = \frac{1}{M'} \sum_{x \in \Omega'} \|x\|^2 \quad (\text{A.2})$$

will be referred to as the average signal *energy* of the uncoded transmission. This parameter is very important when analyzing TCM schemes, since it is used in quantifying the effective coding gain of the coding scheme.

Consider now the transmission of a sequence  $\{x_i\}_{i=1}^L$  of  $L$  signals, where the subscript  $i$  denotes discrete time. The receiver that minimises the average error probability over the sequences operates as follows. It first observes the received signal  $y_1, \dots, y_L$ , and then decides that  $X_1, \dots, X_L$  was transmitted if the squared Euclidean distance

$$d^2 = \sum_{i=1}^L \|y_i - x_i\|^2 \quad (\text{A.3})$$

is minimised for  $x_i = X_i, i = 1, \dots, L$ , or, in other words, if the sequence  $X_1, \dots, X_L$  is closer to the received sequence than to any other allowable signal vector sequence. The resulting error probability, as well as the symbol error probability, is upper bounded, at least for high SNR, by a decreasing function of ratio  $d_{min}^2/N_o$ , where  $d_{min}^2$  is the Minimum Squared Euclidean Distance (MSED) between two allowable signal vector sequences.

One way of improving the system performance is that of removing the assumption that the signals are independent. This can be done by restricting the transmitted sequences to a subset of  $\Omega'^K$ . Now, to do this, the transmission rate will also be reduced. To avoid this unwanted reduction, one may choose to increase the size of  $\Omega'$ . For example, if  $\Omega'$  is changed into  $\Omega \supset \Omega'$  and  $M'$  into  $M.M'$ , and select  $M'^K$  sequences as subset of  $\Omega^K$ , one can have sequences that are less tightly packed and hence increase the minimum distance between them.

In conclusion, a minimum distance  $d_{free}$  between two possible sequences is obtained that turns out to be greater than the minimum distance  $d_{min}$  between signals in  $\Omega'$ , i.e., the constellation from which they were drawn. Hence use of ML sequence detection will yield a *distance gain*  $d_{free}^2/d_{min}^2$ .

On the other hand, to avoid a reduction of the value of the transmission rate, the constellation is expanded from  $\Omega'$  to  $\Omega$ . This may entail an increase in the average signal energy from  $E' = E_{s,u}$  to  $E = E_{s,c}$ , and hence an "energy loss"  $E/E' = E_{s,c}/E_{s,u}$ . Thus the *asymptotic coding gain* of a TCM scheme is defined as

$$\gamma_c = \frac{d_{free,c}^2/E_{s,c}}{d_{free,u}^2/E_{s,u}} = 10 \log_{10} \frac{d_{free,c}^2}{d_{free,u}^2} \quad (\text{A.4})$$

where  $E_{s,u}$  and  $E_{s,c}$  are the average energies associated with uncoded and coded transmission, respectively.

The introduction of interdependencies among the signals and the expansion of the signal set are two of the basic ideas underlying trellis-coded modulation, another is *set partitioning* introduced by Ungerboeck [27, 29].

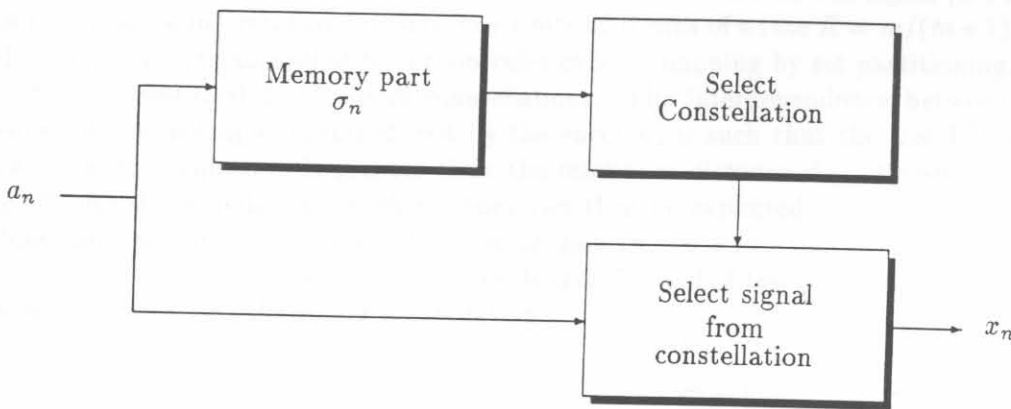


Figure A.1: General model for TCM.

Assume that the signal  $x_n$  transmitted at discrete time  $n$  depends not only on the source symbol  $a_n$  transmitted at the same time instant (as it would be with memoryless modulation), but also on a finite number of previous source symbols:

$$x_n = f(a_n, a_{n-1}, \dots, a_{n-L}). \quad (\text{A.5})$$

By defining

$$\sigma_n = (a_{n-1}, \dots, a_{n-L}). \quad (\text{A.6})$$

as the *state* of the encoder at time  $n$ , can be rewritten (A.5) in the more compact form

$$\begin{aligned} x_n &= f(a_n, \sigma_n) \\ \sigma_{n+1} &= g(a_n, \sigma_n). \end{aligned} \quad (\text{A.7})$$

Equations A.7 can be interpreted as follows. The function  $f(\cdot, \cdot)$  describes the fact that each channel symbol depends not only on the corresponding source symbol, but also on the encoder state parameter,  $\sigma_n$ . In other words, at any time instant the transmitted symbol is chosen from a constellation that is selected by the encoder state,  $\sigma_n$  at time instant  $n$ . The function  $g(\cdot, \cdot)$  describes the *memory part* of the encoder and shows the evolution of the modulator states. The general model for TCM is shown in Figure A.1.

## A.2 HEURISTIC AND ANALYTIC REPRESENTATION OF TCM

In this section the two different approaches to code design are examined, the first proposed by Ungerboeck, consisting of modeling the memory part of the TCM encoder through a convolutional encoder [27, 29], and the second introduced by Calderbank and Mazo [31, 30], where the output channel signals are directly expressed in terms of a sliding block of input bits.

### A.2.1 Ungerboeck Codes

Ungerboeck proposed a channel coding technique that achieves remarkable coding gains, without sacrificing the data rate or expanding the bandwidth of the transmitted signal [27, 29]. The basic idea is to encode  $m$  information bits into  $m + 1$  bits by means of a rate  $R = m/(m + 1)$  convolutional encoder, which selects according to certain rules called "mapping by set partitioning," points from one of the conventional  $2^{m+1}$  signal constellations. The interdependence between the resulting sequences of channel signals, introduced by the encoder, is such that the free ED,  $d_{free}$  between any two possible sequences is greater than the minimum distance  $d_{min}$  between any two points in the  $2^m$  signal constellation. Such memory can then be exploited by the ML decoder, yielding a coding gain,  $\gamma_c$  defined in (A.4). The coding gain ( $\gamma_c$ ) is a function of the amount of memory introduced by the encoder, i.e., the constraint length  $L_c$ , and of the positioning of the signal points in the signal space, i.e., the signal constellation.

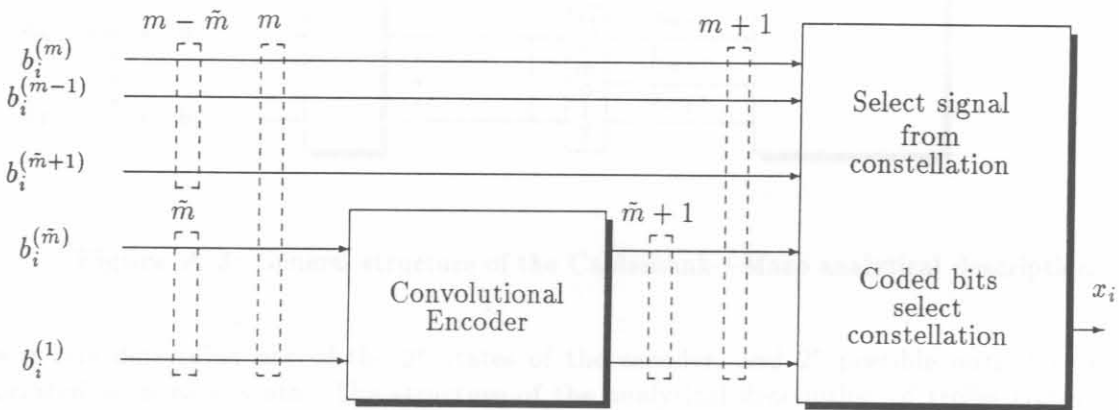


Figure A.2: Block diagram of an Ungerboeck code ( $m = \log_2 M$ ).

It is convenient to represent an Ungerboeck code by the scheme depicted in Figure A.2. At every time instant  $i$ , the rate  $\tilde{m}/(\tilde{m} + 1)$  convolutional encoder receives  $\tilde{m}$  input bits and generates  $\tilde{m} + 1$  coded bits. These, in return, determine the subconstellation from which the transmitted signal has to be chosen. Furthermore, these coded bits move the encoder to the next state. In the figure, the  $m - \tilde{m}$  source bits left uncoded are explicitly shown. The presence of uncoded bits causes parallel transitions.

Ungerboeck's codes or variations of these codes have received a great deal of attention in that they are readily implemented, and considered as standards for high-speed modems on the voiceband

data channel.

### A.2.2 Calderbank—Mazo Codes

The analytic description of the trellis codes was developed for one dimensional modulation, and channel signals have to be real numbers for the analytic process. Basically, the output channel signals are directly expressed in terms of a sliding block of input bits, with the intermediate step of output coded bits being irrelevant for analytical described trellis codes.

When a trellis code is used to encode data at a rate of  $r$  bit per channel symbol, each channel input  $x$  will depend not only on the most recent block of  $k$  bits that enter the encoder but will also depend on the  $\nu$  bits preceding this block. Formally [31, 30]:

$$X_j = x(a_{jr}, a_{jr-1}, \dots, a_{jr-(r-1)}; a_{(j-1)r}, \dots, a_{(j-1)-(\nu-1)}) \tag{A.8}$$

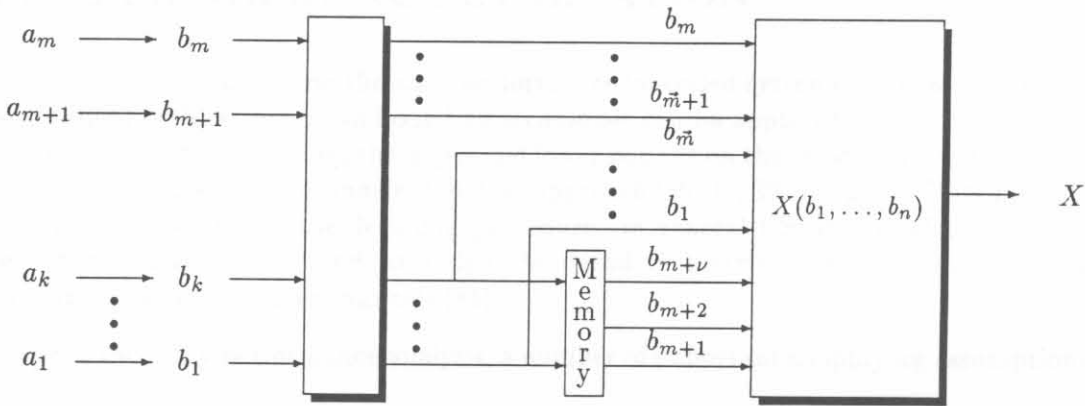


Figure A.3: General structure of the Calderbank—Mazo analytical description

The  $\nu$  bits determine one of the  $2^\nu$  states of the encoder, and  $2^r$  possible output symbols are associated with each state. The structure of the analytical description of trellis codes is shown in Figure A.3, and then the output symbol may be determined by solving the set of equations resulting from all the input bit combinations:

$$\begin{aligned}
 x(b_1, b_2, \dots, b_n) &= \sum_{i=1}^n d_i b_i + \sum_{i,j=1; j>i}^n d_{ij} b_i b_j + \\
 &+ \sum_{i,j,l=1; l>j>i}^n d_{ijl} b_i b_j b_l + \dots + d_{12\dots n} b_1 b_2 \dots b_n
 \end{aligned} \tag{A.9}$$

or by solving its equivalent matrix equation, describing the encoder function as follows:

$$X = Bd \tag{A.10}$$

where  $b_i = 1 - 2a_i$ ,  $X$  is the channel signal matrix,  $B$  is the Hadamard matrix with elements  $\pm 1$  and  $d$  the matrix of constants which determines the code.

In order to calculate the coefficients of the matrix  $d$ , the matrix of the channel symbols is calculated from the trellis diagram and the solution for  $d$  is obtained from:

$$d = \frac{B^T X}{2^n} \quad (\text{A.11})$$

where  $X$  is the channel signal matrix,  $B$  is the Hadamard matrix with elements  $\pm 1$ , and  $d$  is the matrix of constants to be determined. In (A.10) one has  $X = X(b_1, b_2, \dots, b_n)$  which present the modulation output  $X$  for the input information and memory bits  $b_1, b_2, \dots, b_n$ , which denote the  $k$ -th row of the  $(1 \times n')$  matrix  $B$  given by  $B_k = (b_1, b_2, \dots, b_n, b_1 b_2, \dots, b_1 b_2 \dots b_n)$ ;  $d^T$  will be a  $(1 \times n')$  matrix given by  $d^T = (d_1, d_2, \dots, d_n, d_{12}, \dots, d_1 d_2 \dots d_n)$ , where  $n' = 2^n - 1$ ,  $n$  being the number of input bits per interval plus the number of memory bits of the encoder.

The discussion of the Calderbank—Mazo algorithm, together with the  $C$  software listing can be found in Appendix B.

### A.3 PERFORMANCE EVALUATION

In order to obtain bounds on the error performance for coded systems used on memoryless channels, the Chernoff or Bhattacharyya bounding techniques can be applied to trellis coded communication systems [30]. In the following, the upper and lower bounds on the error probability of a coded system are discussed, based on the transfer function approach [75, 33, 30]. Channel State Information (CSI) may also be available in the decoding procedure. In general CSI is the information derived from the channel that can be used to design the decoding metric to give improved performance for communication over fading channels [81].

In order to simplify performance analysis, a number of important simplifying assumptions are made:

- First, assume perfect coherent detection and consider the effects of amplitude fading only,
- In order to ensure independent fading of adjacent demodulated signals, infinite interleaving/deinterleaving depth is assumed. This permits a memoryless channel approximation, which in turn makes *analytical* performance analysis feasible.
- Third, an infinite decoding delay is assumed in the decoding (Viterbi) process.
- Finally, it is assumed that fading over a single signalling interval may be represented by a single fading amplitude.

The assumptions made here are consistent with those in [61].

#### A.3.1 Analytical Upper Bound to the Error Probability of Q<sup>2</sup>PSK

The discussion is started by expressing a coded sequence of transmitted Q<sup>2</sup>PSK channel signals of length  $L$  by  $\mathbf{x}_L = (\overline{x}_1, \overline{x}_2, \dots, \overline{x}_L)$ , where  $\overline{x}_k$ ,  $k = 1, 2, \dots, L$ , are Four-Dimensional (4D) representations of the allowable Q<sup>2</sup>PSK channel signals. Corresponding to  $\mathbf{x}_L$ , is the channel output sequence  $\mathbf{y}_L = (\overline{y}_1, \overline{y}_2, \dots, \overline{y}_L)$  where  $\overline{y}_k$ ,  $k = 1, 2, \dots, L$ , is the 4D continuous random variable,

$$\overline{y}_k = \overline{\rho}_k \overline{x}_k + \overline{n}_k \quad (\text{A.12})$$

where  $\overline{\rho_k}$  represents a (normalised) random fading amplitude, and where  $\overline{n_k}$  is a 4D additive Gaussian noise process with zero mean and variance  $\sigma^2$  in each of the four dimensions.

Based on a suitable decoding metric, the receiver will make a decision on the transmitted sequence  $\mathbf{x}_L$ , which is called  $\mathbf{x}'_L$ , which leads to the definition of a pairwise error probability [61],

$$P_e(\mathbf{x}_L \rightarrow \mathbf{x}'_L) = Pr(m(\mathbf{y}_L, \mathbf{x}'_L) \geq m(\mathbf{y}_L, \mathbf{x}_L) | \mathbf{x}_L) \quad (\text{A.13})$$

where

$$m(\mathbf{y}_L, \mathbf{x}_L) = \sum_{k=1}^L m(\overline{y}_k, \overline{x}_k)$$

$$m(\overline{y}_k, \overline{x}_k) = \begin{cases} -|\overline{y}_k - \overline{\rho}_k \overline{x}_k|^2 & , \text{ ideal CSI} \\ -|\overline{y}_k - \overline{x}_k|^2 & , \text{ no CSI} \end{cases} \quad (\text{A.14})$$

is the decoding metric [61, 30].

In the case of ideal CSI, the receiver is assumed to have exact knowledge of  $\overline{\rho}_k$ ,  $k = 1, 2, \dots, L$ , and the decoding metric is then ML. On the other hand, when no CSI is available at the receiver, the decoding metric is no longer ML and this introduces an additional weakness into the bounding procedure [94, 95].

A tight upper bound on the average bit error probability can be obtained from

$$P_b \leq \frac{k_0}{bN} T(D) |_{D=Z} \quad (\text{A.15})$$

where  $N$  is the number of trellis states;  $b$  is the number of information symbols associated with each branch in the trellis;  $k_0$  is a factor that depends on the type of channel, the type of demodulation and the code structure; and  $Z = \exp\{-E_s/4N_o\}$  is the so-called Bhattacharyya parameter. For AWGN with optimum coherent demodulation,  $k_0$  is given by

$$k_0 = Q \left\{ \sqrt{\frac{E_s}{N_o} d_{free}^2} \right\} D^{-d_{free}^2} \quad (\text{A.16})$$

which means to compute  $k_0$ , knowledge of  $d_{free}$  is required, the minimum free distance. As a consequence, availability of fast algorithms to evaluate  $d_{free}$  is of crucial importance. The software listing of the program written in *C* to calculate  $d_{free}$  is presented in Appendix B.

In (A.15),  $T(D)$  a function of  $D$ , is the (scalar, closed loop) *transfer function* of the error state diagram, where its power generally represents the distance (Hamming or Euclidean) between two code words. In this study a new algebraic algorithm for the derivation of the transfer function for a trellis encoder, originally introduced by Chan and Norton [79], is utilised. This algebraic algorithm is discussed in detail in Appendix C. Alternatively, the computational algorithm introduced by Biglieri et al. [30], based on matrix-algebra could have been used with equally good affect.

From the analysis by Biglieri et al. [30] for the symbol error probability, the SEP is given as

$$P_s \leq T(D) |_{D=Z} \quad (\text{A.17})$$

where  $T(D) = \sum_{\bar{e}} W(\bar{e})$ ,  $Z = \exp(-E_b/N_o)$  is the so-called Bhattacharyya parameter, and  $\bar{e}$  is the error vector.  $T(D)$  is called the (scalar) *transfer function* of the error-state diagram.

Define  $W(\bar{\epsilon})$  as the *weight profile* given by

$$W(\bar{\epsilon}) = \frac{1}{M} \sum_{\bar{\epsilon}_i}^M D^{d^2(\bar{\epsilon}_i, \bar{\epsilon}_i \oplus \bar{\epsilon})} \quad (\text{A.18})$$

where  $M$  is the number of Q<sup>2</sup>PSK symbols in a subset after set-partitioning,  $\bar{\epsilon}_i$  denotes the  $M$  symbol vectors constituting the subset, and  $d^2(\cdot)$  is the MSED between two symbol vectors separated by the error vector  $\bar{\epsilon}$ .

A better upper bound on  $P_s$  than (A.17) can be derived by knowledge of the free distance,  $d_{free}$  of the code and is given by

$$P_s \leq Q \left\{ \sqrt{\frac{d_{free}^2 E_b}{N_o}} \right\} \exp\left(\frac{d_{free}^2 E_b}{4N_o}\right) T(D) |_{D=Z} \quad (\text{A.19})$$

From (A.17) the upper bound on the BEP is easily found and given by

$$P_b \leq \frac{1}{b} T(D) |_{D=Z} \quad (\text{A.20})$$

where  $b$  is the number of source (input) bits per trellis transition.

Yet, another tighter upper bound can be found from (A.19), given by

$$P_b \leq \frac{1}{b} Q \left\{ \sqrt{\frac{d_{free}^2 E_b}{N_o}} \right\} \exp\left(\frac{d_{free}^2 E_b}{4N_o}\right) T(D) |_{D=Z} \quad (\text{A.21})$$

A discussion of the Chan—Norton algebraic algorithm utilised for generating the transfer function of the trellis encoder may be found in Appendix B.

### A.3.2 Lower Bound to Error Probability

An lower bound to the average bit error probability is given by

$$P_b \geq \frac{\psi}{m} Q \left\{ \frac{d_{free}}{\sqrt{N_o}} \right\} \quad (\text{A.22})$$

where  $\psi$  is the probability that at any time, a trellis path chosen at random has another path splitting from it at that time, and remerging later, such that the Euclidean distance is  $d_{free}$ . In (A.22)  $m$  denotes the number of information bits at any node.

### A.3.3 Union Bound techniques

Before proceeding with the union bound, consider the case of comparing the correct path with another path that differs from it in  $q$  positions. Denote the probability of error in this comparison by  $P_q$ . For the BSC with channel symbol error rate  $\rho$ , the probability of error in this computation is simply the probability that more than  $q/2$  errors occur plus  $1/2$  the probability that  $q/2$  error occur [24].



An union bound on the probability of a first-event error,  $P_e$  at branch  $i$  may be obtained by summing the error probabilities for all possible paths that merge with the all-zero path at this point. This overbound is then given by

$$P_e < \sum_{q=0}^{\infty} n_q P_q \quad (\text{A.23})$$

Furthermore, an union bound on the probability of bit error,  $P_b$  may be obtained from (A.23) by weighting each term by the corresponding number of bit errors, i.e. the information weight for each path). However, for a rate- $k/n$  code there are  $k$  symbols decoded on each branch. Thus,  $P_b$  is bounded by

$$P_b < \frac{1}{k} \sum_{q=0}^{\infty} w_q P_q \quad (\text{A.24})$$

The evaluation of (A.23) and (A.24) requires knowledge of the path weight distribution of the code. One can also perform various manipulations with the transfer functions to provide approximate closed-form expressions for bounds on  $P_e$  and  $P_b$ . Observe that (A.23) and (A.24) would be identical if the term  $P_q$  could be written in the form  $a^q$ . This is possible for a few channels. For example, it can be shown that for the BSC,  $P_q$  is over-bounded by [96]:

$$P_j < \left\{ 2[\rho(1-\rho)]^{1/2} \right\}^q \quad (\text{A.25})$$

Thus, from (A.23) and (A.25) one may write the bound on the symbol error probability as

$$P_e < T(D, N) \Big|_{N=1, D=2[\rho(1-\rho)]^{1/2}} \quad (\text{A.26})$$

In a similar fashion, from (A.24) and (A.25) one can write the bit error probability as

$$P_b < \frac{1}{k} \frac{\delta T(D, N)}{\delta N} \Big|_{N=1, D=2[\rho(1-\rho)]^{1/2}} \quad (\text{A.27})$$

A union bound which is valid for demodulator soft decisions may be similarly established [96]. Bounds similar to (A.26) and (A.27) can also be obtained for more general channel models than the BSC. For a binary input AWGN channel with no output quantization, the bounds respectively become

$$P_e < T(D, N) \Big|_{N=1, D=e^{R_c E_b / N_0}} \quad (\text{A.28})$$

and

$$P_b < \frac{1}{k} \frac{\delta T(D, N)}{\delta N} \Big|_{N=1, D=e^{R_c E_b / N_0}} \quad (\text{A.29})$$

where  $R_c$  is the code rate.

## A.4 DECODING TCM

In this section the Viterbi algorithm as applied to decoding TCM signals is considered. If the TCM signal is described by using a trellis, whose branches are associated with transitions between encoder states and with signals transmitted over the channel, the task of the TCM decoder is to

estimate the path that the encoded signal sequence traverses through the trellis. This is done by associating with each branch of the trellis a number, called the *branch metric*, and looking for the path whose total metric is minimum. This path corresponds to the transmitted sequence. Thus the decoding problem can be split into two parts:

- Definition of a branch metric, and its computation based on the observed values of the received signal.
- Evaluation of the minimum-metric path.

In this section, the Viterbi Algorithm (VA) is considered for decoding TCM. This decoding algorithm, introduced by Viterbi in 1967 [96], uses the trellis structure of the code and determines the ML estimate of the transmitted sequence that has the largest metric.

ML decoding implies finding the path with largest metric through the trellis by comparing the metrics of all branch paths entering each state with the corresponding level elements of the received sequence in an iterative manner. In the decoding process, if at some level it is found that a path cannot possibly yield the largest metric, then the path is discarded by the decoder. In this manner, a decoder that compares the metrics of all paths entering a state and only retains the survivor path at that state will yield a most likely path if the operation is repeated for all distinct states at each level. This simple iterative process is known as the Viterbi Algorithm (VA), described by Dr. A.J. Viterbi in the late 1960's [96].

Viterbi decoding consists fundamentally of three processes. The first step in the decoder process is to generate a set of correlation measurements, known as *branch metrics*, for each  $n$ -tuple of codewords input from the communication channel (where  $k$  and  $n$  are, respectively the number of bits input and output to a rate  $k/n$  convolutional coder. These branch metric values indicate the correlation between received codewords and the  $2^m$  possible codeword combinations.

The Viterbi decoder determines the state of the  $L_c$ -bit (where  $L_c$  is the constraint length) memory at the encoder using a maximum likelihood technique. Once the value of the encoder is determined, the original information is known, since the encoder memory is simply information that is a function of the state (value) of the encoder. To determine the encoder state, the second step in the Viterbi algorithm generates a set of  $2^{L_c-1}$  *state metrics* which are measures of the occurrence probability for each of the  $2^{L_c-1}$  possible encoder memory states. For this reason, the exponential growth of the decoding effort is related to the encoder memory order,  $L_c - 1$ . As the state metrics are computed, a binary decision is formed for each of the  $2^{L_c-1}$  possible states as to the most probable path taken to arrive at that particular state. These binary decision are stored in a *path memory*.

Step three computes the decoded output data. To do this, the *path* from the current state to some point in the finite past is traced back by *chaining* the binary decisions stored in the path memory during step 2 from state to state. The effects caused by noise to the one and only correct result are mitigated as the paths within the *chainback* memory converge after some history. The greater the *decoding depth* of the chainback process the more likely that the final decoded result will be error free. As a result, higher code rates and constraint lengths require longer chainback depths for best performance. The chainback memory of the Viterbi decoder traces the history of the previous states to arrive at the most probable state of the encoder in the past, and thus determine the transmitted data.

## A.5 CONCLUDING REMARKS: APPENDIX A

In the classical approach to channel encoding, the two functions of coding and modulation are regarded as separate operations. It was seen that in TCM these two functions are combined at the trellis decoder. However, the code design goal is to exploit the redundancy (whether in the form of parity bits or an enlarged signal space) to maximize the minimum distance (Hamming or Euclidean) between different codewords.

---



---

## APPENDIX B

### TCM CODE DESIGN — Utility Software

#### B.1 (1/4)-rank - Maze Description of trellis codes

The procedure for the design of a trellis code is as follows:

Appendix A describes the design of a trellis code for a given rate and distance.

where  $k$  is the number of information bits per symbol,  $n$  is the number of bits per symbol,  $D$  is the minimum distance of the code, and  $M$  is the number of states in the trellis. The trellis code is designed by first choosing a trellis structure and then choosing a set of states of the trellis which are separated by a minimum distance of  $D$ . The trellis code is then defined as the set of states of the trellis which are separated by a minimum distance of  $D$ .

where  $X$  is the channel signal matrix,  $B$  is the Hadamard matrix with elements  $\pm 1$ , and  $D$  is the matrix of constants to be determined. Here  $n$  is  $k + p$ , where  $k$  is the number of data bits and  $p$  is the number of parity elements for the trellis code.

In the following the computer software to calculate the coefficients of  $D$  is presented. The method is based on simple matrix algebra, from which an analytical description can be derived. The design of a trellis representation of a code, by knowing the input bits and the corresponding signal and evaluation signal set.

## APPENDIX B

# TCM CODE DESIGN — Utility Software

The evaluation of the coefficients of the analytical description and finding  $d_{free}$  are the two main tasks in the design procedure, and compliments the results presented in Chapter 7. In this appendix a discussion of the analytical description of trellis codes proposed by Calderbank and Mazo, and the utility software developed for computing the coefficients of the analytical equation are presented. In the second part of this appendix the computational algorithm proposed by Mulligan and Wilson for the computation of  $d_{free}$  is considered. The software code written in C is discussed.

### B.1 Calderbank—Mazo Description of trellis codes

The general theory of the Calderbank—Mazo [31] formulation of trellis codes was presented in Appendix A. The structure of the analytical description of trellis codes may be determined by solving its equivalent matrix equation, describing the encoder function as follows [30]:

$$X = BD \quad (\text{B.1})$$

where  $b_i = 1 - 2a_i$ ,  $X$  is the channel signal matrix,  $B$  is the Hadamard matrix with elements  $\pm 1$  and  $D$  the matrix of constants which determines the code. Calderbank and Mazo show that  $B$  is an orthogonal matrix. Therefore, in order to calculate the coefficients of the matrix  $D$ , the matrix of the channel symbols is calculated from the trellis diagram and the solution for  $D$  is obtained from:

$$D = \frac{B^T X}{2^n} \quad (\text{B.2})$$

where  $X$  is the channel signal matrix,  $B$  is the Hadamard matrix with elements  $\pm 1$ , and  $D$  is the matrix of constants to be determined. Here  $n = k + \nu$ , where  $k$  is the number of input bits and  $\nu$  is the number of memory elements for the trellis code.

In the following the computer software to calculate the coefficients of  $D$  is presented. The program is based on simple matrix algebra, from which an analytical description can be derived by means of a trellis representation of a code, by knowing the input bits and the corresponding signals in the modulation signal set.

```

1 // =====
2 // Program Name: ANALYTIC.CPP
3 //
4 // Description:  EVALUATION OF
5 //                CALDERBANK-MAZO ANALYTICAL
6 //                DESCRIPTION OF TCM
7 //
8 // =====

9 #include <iostream.h>
10 #include <conio.h>
11 #include <stdio.h>
12 #include <stdlib.h>
13 #include "matrix_d.h"      // Includes the matrix algebra routines
14 #include "mathstat.h"     // Includes general mathematical and statistical
15                          // functions

16 void main(int argc, char *argv[])
17 {
18     Matrix B, A;
19     Matrix f, d;
20     FILE    *Config;      // Configuration file

21     int      i[K], P[K];
22     int      a, b, m, n, o, p, q, s, t, r;
23     int      N, R, C;
24     double  element;

25     clrscr();
26     if (argc != 2)
27     {
28         cout << "Usage: Analytic Configuration_File"; exit(1);
29     }
30     Config = fopen(argv[1], "rt");
31     fscanf(Config, "%d", &N);
32     R = pow(2, N);
33     for (a = 0; a < K; a++) P[a] = 999;

```

```

34     C = 0;
35     for (a = 1; a <= N; a++)
36     {
37         // C is the number of columns in matrix B
38         // (i.e. the number of possible solutions of D)
39         // It is given by
40         //     Sum of all the combinations of N and a, where a=1,...,N

41         P[a-1] = Combination(N,a);
42         C += P[a-1];
43     }
44     // Initialisation of matrices
45     B.Set_dimension(R,C);
46     A.Set_dimension(C,R);
47     f.Set_dimension(R,1);
48     d.Set_dimension(1,C);

49     // Obtain trellis structure from configuration file
50     for (a = 1; a <= R; a++)
51     {
52         fscanf(Config,"%d", &t);
53         f(a,1) = t;
54     }
55     fcloseall(); // Close configuration file
56     r = 1;
57     for (a = 0; a < N; a++) // initialise the sliding block input-output
58                             // bits to initial condition (-1,-1,...,-
59         i[a] = -1;
60     clrscr();
61     cout << "CALDERBANK-MAZO: Analytical Description of TCM coders (c)dvw96\n\n";
62     cout << "C: = " << C << "\n";
63     for (a = 0; a < N; a++)
64         cout << P[a] << " + ";
65     cout << "\n\n";

66     //=====
67     // INITIALISATION OF MATRIX --- B
68     //=====

69     for (a = R; a > 0; a--)
70     {
71         // L = 1
72         for (m = 0; m < N; m++)
73             B(a,r++) = i[m];
74         // L = 2
75         for (m = 0; m < N-1; m++)
76             for (n = m+1; n < N; n++)
77                 B(a,r++) = i[m]*i[n];
78         // L = 3

```

```

79     for (m = 0; m < N-2; m++)
80         for (n = m+1; n < N-1; n++)
81             for (o = n+1; o < N; o++)
82                 B(a,r++) = i[m]*i[n]*i[o];
83     // L = 4
84     for (m = 0; m < N-3; m++)
85         for (n = m+1; n < N-2; n++)
86             for (o = n+1; o < N-1; o++)
87                 for (p = o+1; p < N; p++)
88                     B(a,r++) = i[m]*i[n]*i[o]*i[p];
89     // L = 5
90     for (m = 0; m < N-4; m++)
91         for (n = m+1; n < N-3; n++)
92             for (o = n+1; o < N-2; o++)
93                 for (p = o+1; p < N-1; p++)
94                     for (q = p+1; q < N; q++)
95                         B(a,r++) = i[m]*i[n]*i[o]*i[p]*i[q];
96     // L = 6
97     for (m = 0; m < N-5; m++)
98         for (n = m+1; n < N-4; n++)
99             for (o = n+1; o < N-3; o++)
100                 for (p = o+1; p < N-2; p++)
101                     for (q = p+1; q < N-1; q++)
102                         for (s = q+1; s < N; s++)
103                             B(a,r++) = i[m]*i[n]*i[o]*i[p]*i[q]*i[s];
104     // L = 7
105     for (m = 0; m < N-6; m++)
106         for (n = m+1; n < N-5; n++)
107             for (o = n+1; o < N-4; o++)
108                 for (p = o+1; p < N-3; p++)
109                     for (q = p+1; q < N-2; q++)
110                         for (s = q+1; s < N-1; s++)
111                             for (t = s+1; t < N; t++)
112                                 B(a,r++) = i[m]*i[n]*i[o]*i[p]*i[q]*i[s]*i[t];
113     for (m = 0; m < N; m++)
114     {
115         i[m] += 2;
116         if (i[m] == 1) break;
117         else i[m] = -1;
118     }
119     r = 1;
120 }
121 //=====
122 // SOLVE MATRIX --- D
123 //=====
124 d = T(T(B)*f/R); // Solve for D
125 printf("\n\nSolution for coefficients of D:\n* ");
126 for (a = 1; a <= C; a++)

```

```

127         cout << d(1,a);
128         cout << "\n\n*** FIN ***";
129     }

```

## B.2 Mulligan—Wilson Algorithm for computation of $d_{free}$

In this study it was shown to what extent the Euclidean free distance of a TCM and MTCM defines the asymptotic coding gain of the scheme. Furthermore, it was shown that  $d_{free}$  plays a central role in determining tighter bounds on system performance. It is stated in the book by Biglieri *et al.* that if a single parameter is to be used to assess the quality of a trellis coded scheme,  $d_{free}$  is the only sensible one that comes to mind. Therefore, it makes sense to look at an algorithm to compute this parameter.

The algorithm for computation of  $d_{free}$  is described, as derived by Mulligan and Wilson [80]. Our presentation here follows from [30] (pp. 128-131). Consider the trellis description of the TCM scheme. Every pair of branches in a section of the trellis defines one distance between the signals labeling the branches. If there are parallel transitions, every branch will be associated with an entire subconstellation (partitioned subset). In this case, only the minimum distance between any two signals extracted from the pair of subconstellations will be used. The squared distance between the signal sequences associated with two paths in the trellis is obtained by summing the individual squared distances. The algorithm is based on the update of the entries of a matrix  $D$ , which are the minimum squared distances between all pairs of paths diverging from any initial state and reaching a specific pair of states at discrete time  $n$ .

In the following we present the computer program to calculate  $d_{free}$ . The program requires the number of states  $N_s$ , the number of branches leaving a state or re-emerging at a state and the number of parallel transitions. The signals are sequentially assigned in an configuration input file, with the signal order corresponding exactly to the signal assignment of the trellis. Following the signals, there are  $N_s$  additional entries, specifying the trellis structure (e.g. fully, half- or quarter-connected trellis).

---

```

1 // =====
2 // Program Name: DMIN.CPP
3 //
4 // Description:  EVALUATION OF MINIMUM FREE
5 //                EUCLIDEAN DISTANCE
6 //
7 // =====

8 #include <conio.h>
9 #include <stdio.h>
10 #include <stdlib.h>
11 #include <iostream.h>
12 #include <math.h>
13 #include <mem.h>

```



```

14 #define FALSE 0
15 #define TRUE 1

16 // =====
17 // GLOBALS
18 // =====
19 float **X, **PT, **CDT, **TEMP;

20 // =====
21 // PROCEDURE MAIN
22 // =====
23 void main(int argc, char *argv[])
24 {
25     FILE *Config;
26     int S, K, KT, D;
27     int TOTAL1, TOTAL2, TOTAL3, TOTAL4, TOTAL5, TOTAL6;
28     unsigned int FIRST, STILL;
29     int TD, SN;
30     int C1, C2, C3; // Counters
31     int p, q, Y, Z, ROWPT, ROW, COL;
32     float MIN, DIST, DMIN, TEMPO;
33     int i, j, k, l, m, n, r, Itemp;
34     float Ftemp;

35     clrscr();
36     if (argc != 2)
37     {
38         cout << "Usage: Dmin Configuration_File";
39         exit(1);
40     }
41     cout << "Mulligan & Wilson Computational Algorithm";
42     cout << " - (c) dvw96";
43     cout << "\n\nAssuming Configuration File: " << argv[1];
44     Config = fopen(argv[1], "rt");
45     fscanf(Config, "%d", &S);
46     fscanf(Config, "%d", &K);
47     fscanf(Config, "%d", &KT);
48     fscanf(Config, "%d", &D);

49     // =====
50     // INITIALISATION
51     // =====
52     TOTAL1 = S*pow(2,K);
53     TOTAL2 = S*pow(2,KT);
54     TOTAL3 = pow(2,KT);
55     TOTAL4 = pow(2,K-KT);
56     TOTAL5 = pow(2,2*KT);
57     TOTAL6 = S*S;

```

```

58 // =====
59 // MEMORY ALLOCATION
60 // =====
61 Memory_Allocation();

62 // X[TOTAL1][D]
63 // CDT[S][S]
64 // TEMP[S][S]
65 // PT[TOTAL6][TOTAL5][2]

66 Y = Z = 0; // Position indexes

67 // =====
68 // Input channel signals into matrix X
69 // =====

70 for (i = 0; i < TOTAL1; i++)
71     for (j = 0; j < D; j++)
72     {
73         fscanf(Config, "%f", &Ftemp);
74         X[i][j] = Ftemp;
75     }
76 for (i = 0; i < S; i++)
77     for (j = 0; j < S; j++)
78     {
79         if (i == j)
80         {
81             CDT[i][j] = 0.0;
82             TEMP[i][j] = 0.0;
83         }
84         else
85         {
86             CDT[i][j] = 1000.0;
87             TEMP[i][j] = 1000.0;
88         }
89     }
90 // =====
91 // Initialize Pair-state Table (PT)
92 // =====
93 TD = 0; // Trellis-Depth = 0
94 C1 = 0;
95 for (n = 0; n < S; n++)
96 { // 10
97     fscanf(Config, "%d", &C2);
98     C2 = C2 - 1;
99     C3 = 0;
100    SN = 0;
101    j = 0; // loop-control variable for column

```

```

102     for (m = 0; m < TOTAL2; m++)
103     { // 20
104         for (l = 0; l < TOTAL3; l++)
105         { // 30
106             MIN = 1000.0;
107             for (p = 0; p < TOTAL4; p++)
108             { // 35
109                 for (q = 0; q < TOTAL4; q++)
110                 { // 38
111                     DIST = 0.0;
112                     for (r = 0; r < D; r++)
113                         DIST = DIST + pow(X[Y+p][r] - X[Z+q][r], 2.0);
114                     if (DIST < MIN) MIN = DIST;
115                 } // 38
116             } // 35
117             Z = Z + TOTAL4;
118             if (Z >= TOTAL1)
119             {
120                 Z = 0;
121                 Y = Y + TOTAL4;
122             }
123             PT[C1 * S + SN][C3 * TOTAL3 + 1][0] = MIN;
124             PT[C1 * S + SN][C3 * TOTAL3 + 1][1] = C2*S+(j+1);
125             j = j + 1;
126             if (j == S) j = 0;
127         } // 30
128         SN = SN + 1;
129         if (SN == S)
130         {
131             SN = 0;
132             C2 = C2 + 1;
133             C3 = C3 + 1;
134         }
135     } // 20
136     C1 = C1 + 1;
137 } // 10

138 // =====
139 // Compute TEMP for the next trellis depth
140 // =====

141 FIRST = TRUE;
142 DMIN = 1000.0;
143 do
144 {
145     for (i = 0; i < S; i++)
146     { // 70
147         for (j = 0; j < S; j++)
148         { // 80

```

B.2. MULLIGAN—WILSON ALGORITHM FOR COMPUTATION OF  $D_{FREE}$ 

```

149         if ((CDT[i][j] != 0.0 || FIRST == TRUE) &&
150             (CDT[i][j] < 1000.0))
151         { // If 1
152             for (l = 0; l < TOTAL5; l++)
153             { // 90
154                 ROWPT = i*S + j;
155                 TEMPO = CDT[i][j] + PT[ROWPT][l][0];
156                 ROW = (int) (PT[ROWPT][l][1] - 1.0)/S;
157                 COL = (((int) PT[ROWPT][l][1]) % S)-1;
158                 if (COL == -1) COL = S-1;
159                 if ((TEMPO < TEMP[ROW][COL]) || (TEMP[ROW][COL] == 0.0))
160                     TEMP[ROW][COL] = TEMPO;
161                 // =====
162                 if ((ROW == COL) && (TEMP[ROW][ROW] > 0.0) && (TEMP[ROW][ROW]
163                     DMIN = TEMP[ROW][COL];
164             } // 90
165         } // If 1
166     } // 80
167 // =====
168 // Update CDT from TEMP
169 // =====

170     STILL = FALSE;
171     FIRST = FALSE;

172     for (i = 0; i < S; i++)
173     { // 120

174         for (j = 0; j < S; j++)
175         { // 130

176             CDT[i][j] = TEMP[i][j];

177             if (i == j) TEMP[i][j] = 0.0;
178             else TEMP[i][j] = 1000.0;

179             if (CDT[i][j] < DMIN) STILL = TRUE;

180         } // 130
181     } // 120

182     TD = TD + 1;
183     } while ((STILL == TRUE) && (TD < 100));

184 // =====
185 // Presentation of Results
186 // =====
187 highvideo();
188 cprintf("\r\n\nResults:\n\r");

```

B.2. MULLIGAN—WILSON ALGORITHM FOR COMPUTATION OF  $D_{FREE}$ 

```

189     if (TD >= 100)
190     {
191         cout << "The code appears to be catastrophic after a ";
192         cout << "trellis depth of 100\n";
193     }
194     else
195     {
196         cout << "Minimum Squared Euclidean Distance, Dmin: " << DMIN << "\n";
197         cout << "Trellis Depth = " << TD << "\n";
198     }
199     fcloseall();

200     // =====
201     // Free memory
202     // =====
203     Free_Memory();
204 }

```

---

## APPENDIX C

# TRANSFER FUNCTION DERIVATION

This appendix the Chan—Norton algebraic algorithm for generating the transfer function of a trellis code is presented. The algebraic method is presented as an alternative to the better known transfer function derivation by means of graphical means, i.e. by graph-reduction of Mason's rule.

The Chan—Norton algorithm for transfer function derivation is presented [79]. In order to find the transfer function representing all paths (except the loop at 0, i.e. the modified transfer function is considered) starting from state 0 and ending at state  $0'$ . Firstly the trellis diagram of the encoder is drawn. Then each branch of the trellis is labeled. The labels can be in general expressed as a finite sum  $\sum_i a_i x^{n_i}$ , which is the weight profile (defined in Chapter 6). The summation accounts for parallel transitions,  $x$  is a dummy variable whose exponent  $n_i$  is the number of bits in error for that transition and  $a_i$  is a scalar which could be a function of the SNR or Euclidean distance.

The transfer function  $T(x)$  is a quotient of two polynomials,  $T(x) = f(x)/g(x)$ , say. From the discussion in [79], the successive coefficients of the transfer function form a linear recurring sequence, and the denominator of minimal degree can be used using the Extended Euclidean Algorithm (XEA). The next step is to generate the *adjacency matrix*  $A = A(x)$  of the encoder from the trellis diagram. For an  $N_s$  state encoder,  $A$  is matrix of dimension  $(N_s + 1) \times (N_s + 1)$ , and  $A_{ij}$  represents the paths with starting state  $i$ , ranging from states  $0, 1, 2, \dots, N_s, 0'$ , and ending in state  $j$  also ranging from states  $0, 1, 2, \dots, N_s, 0'$ .

Importantly, the entries of the matrix will be the labels on the trellis diagram. If the two states are not joined on the trellis diagram, the entry will be zero in the adjacency matrix. The column  $0'$  represents the *first output column*. The  $A_{00'}$  entry represents the path starting from state 0 and ending at state  $0'$ . (Note that the first column and last row in  $A$  are zero.)

If  $p$  is a polynomial, let  $\delta p$  denote the degree of  $p$ . Then determine the upper bound for  $\delta \det(I - A)$ ,

where  $I$  is the identity matrix. An upper bound is found by taking the sum of the maximum of the degrees of each of the columns in  $I - A$ , and adding one. Denote this upper bound by  $M$ . Next all the paths starting from state 0 and ending at state  $0'$  with degree of  $x$  less than  $2M$ , i.e.,  $T(x) \bmod x^{2M}$  need to be summed. One method is by repeated multiplication of  $A$  with the output column vector. The sum of the first entries in the resulting column vectors is the answer we are looking for. Let  $e(x) = T(x) \bmod x^{2M}$ . Apply the XEA to  $x^{2M}$  and  $e(x)$  until  $\delta r_{n+1} < M$ ; letting  $r_{-1} = x^{2M}$ ,  $r_0 = e(x)$ ,  $r_{i+1} = r_{i-1} - q_{i+1} \cdot r_i$  is obtained, where  $\delta r_{i+1} < \delta r_i$ , i.e.,  $q_{i+1}$  is the quotient obtained from dividing  $r_{i-1}$  by  $r_i$  with remainder  $r_{i+1}$  for  $0 \leq i \leq n$ . The transfer function is then given by  $T(x) = r_{n+1}/t_{n+1}$ .

It is important to note that the general complexity of this algebraic algorithm, as is the case with the graph-reduction method, increases exponentially with the number of states of the encoder. In the following detail concerning the derivation of the transfer function of the rate-3/4 8-state trellis code given in Chapter 6 is presented.

The trellis code structure for the fully-connected rate-3/4 trellis code designed in Chapter 6, is repeated here for convenience. The trellis diagram is illustrated in Figure C.1.

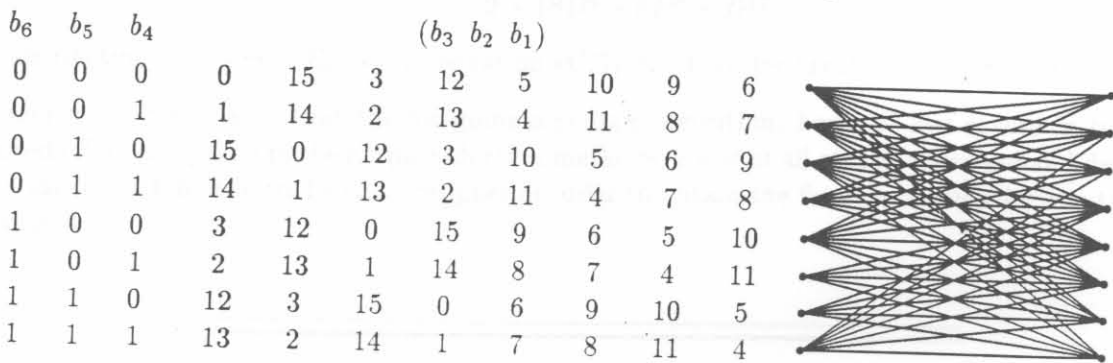


Figure C.1: Fully-connected  $R = 3/4$  8-state trellis code.

The adjacency matrix, of dimensions  $(9 \times 9)$  for the 8-state trellis code in Figure C.1 is

$$A(x) = \begin{bmatrix} S_0 & S_1 & S_2 & S_3 & S_4 & S_5 & S_6 & S_7 & S_{0'} \\ 0 & D_{15}x & D_3x & D_{12}x^2 & D_5x & D_{10}x^2 & D_9x^2 & D_6x^3 & D_0 \\ 0 & D_{14}x & D_2x & D_{13}x^2 & D_4x & D_{11}x^2 & D_8x^2 & D_7x^3 & D_1 \\ 0 & D_0x & D_{12}x & D_3x^2 & D_{10}x & D_5x^2 & D_6x^2 & D_9x^3 & D_{15} \\ 0 & D_1x & D_{13}x & D_2x^2 & D_{11}x & D_4x^2 & D_7x^2 & D_8x^3 & D_{14} \\ 0 & D_{12}x & D_0x & D_{15}x^2 & D_9x & D_6x^2 & D_5x^2 & D_{10}x^3 & D_3 \\ 0 & D_{13}x & D_1x & D_{14}x^2 & D_8x & D_7x^2 & D_4x^2 & D_{11}x^3 & D_2 \\ 0 & D_3x & D_{15}x & D_0x^2 & D_6x & D_9x^2 & D_{10}x^2 & D_5x^3 & D_{12} \\ 0 & D_2x & D_{14}x & D_1x^2 & D_7x & D_8x^2 & D_{11}x^2 & D_4x^3 & D_{13} \\ 0 & 0 & 0 & 0 & 0 & 0 & 0 & 0 & 0 \end{bmatrix} \quad (C.1)$$

where  $D_0 \dots D_{15}$  are nonzero scalar labels of the trellis diagram. An upper bound,  $M$  for  $\delta \det(I - A)$  is easily found as the sum of the maximum of the degrees of each of the columns in  $(I - A)$ , and adding one. The bound is  $M = (1 + 1 + 2 + 1 + 2 + 2 + 2 + 3 + 0) + 1 = 14$ . Therefore, we need to

find all the paths from  $S_0$  to  $S_{0'}$ , that have degree less than  $2M = 28$ . This is found by repeated multiplication of matrix  $A$  with an output column vector, for instance

$$C_1 = A \cdot \begin{bmatrix} D_0 \\ D_1 \\ D_{15} \\ D_{14} \\ D_3 \\ D_2 \\ D_{12} \\ D_{13} \\ 0 \end{bmatrix} \quad (C.2)$$

We continue this multiplication until the order of the polynomial in the first row is of order  $\delta < 2M$ . Since, the computational complexity of this specific code design is quite high it is necessary to consider the use of computer utilities to assist in the computations.

After some mathematics (computer mathematics by means of "Mathematica" [97]) the transfer function of this trellis code is given by (see (5.14))

$$T(D) = \frac{D^{20} + 24D^{36} - 16D^{18} + 48D^8 + 24D^{24}}{2 + 18D^4 - 8D^8 + D^{12}} \quad (C.3)$$

By substituting  $D = \exp(-E_b/N_o)$  in equation (C.3), the transfer function is readily obtained.

In conclusion, it is stated that the foregoing algebraic algorithm, however less severe in terms of required effort compared to the graph-reduction methods, is not at all straight forward and demands still a lot of work by the trellis code designer in order to obtain the final expression for the transfer function.



## APPENDIX D

# SET PARTITIONING FOR Q<sup>2</sup>PSK/MTCM CODE DESIGN

In this appendix the subsets obtained from the first and second partition levels, for the multiplier integer  $n = 11$  as required in the MTCM analysis of Chapter 6, section 6.1.1, are presented. Only the subsets obtained for a multiplicity,  $k = 2$  are presented. Recall, that the subsets for the codes of higher multiplicity is easily derived from the subsets with code multiplicity of 2.

### D.1 CODE CARDINALITY OF 16

$$A_0 \otimes B_0 = \begin{bmatrix} 0 & 0 & 8 & 8 \\ 1 & 11 & 9 & 3 \\ 2 & 6 & 10 & 14 \\ 3 & 1 & 11 & 9 \\ 4 & 12 & 12 & 4 \\ 5 & 7 & 13 & 15 \\ 6 & 2 & 14 & 10 \\ 7 & 13 & 15 & 5 \end{bmatrix} \quad A_0 \otimes B_1 = \begin{bmatrix} 0 & 1 & 8 & 9 \\ 1 & 12 & 9 & 4 \\ 2 & 7 & 10 & 15 \\ 3 & 2 & 11 & 10 \\ 4 & 13 & 12 & 5 \\ 5 & 8 & 13 & 0 \\ 6 & 3 & 14 & 11 \\ 7 & 14 & 15 & 6 \end{bmatrix} \quad (D.1)$$

$$A_0 \otimes B_2 = \begin{bmatrix} 0 & 2 & 8 & 10 \\ 1 & 13 & 9 & 5 \\ 2 & 8 & 10 & 0 \\ 3 & 3 & 11 & 11 \\ 4 & 14 & 12 & 6 \\ 5 & 9 & 13 & 1 \\ 6 & 4 & 14 & 12 \\ 7 & 15 & 15 & 7 \end{bmatrix} \quad A_0 \otimes B_3 = \begin{bmatrix} 0 & 3 & 8 & 11 \\ 1 & 14 & 9 & 6 \\ 2 & 9 & 10 & 1 \\ 3 & 4 & 11 & 12 \\ 4 & 15 & 12 & 7 \\ 5 & 10 & 13 & 2 \\ 6 & 7 & 14 & 13 \\ 7 & 0 & 15 & 8 \end{bmatrix} \quad (D.2)$$

$$A_0 \otimes B_4 = \begin{bmatrix} 0 & 4 & 8 & 12 \\ 1 & 15 & 9 & 7 \\ 2 & 10 & 10 & 2 \\ 3 & 5 & 11 & 13 \\ 4 & 0 & 12 & 8 \\ 5 & 11 & 13 & 3 \\ 6 & 6 & 14 & 14 \\ 7 & 1 & 15 & 9 \end{bmatrix} \quad A_0 \otimes B_5 = \begin{bmatrix} 0 & 5 & 8 & 13 \\ 1 & 0 & 9 & 8 \\ 2 & 11 & 10 & 3 \\ 3 & 6 & 11 & 14 \\ 4 & 1 & 12 & 9 \\ 5 & 12 & 13 & 4 \\ 6 & 7 & 14 & 15 \\ 7 & 2 & 15 & 10 \end{bmatrix} \quad (D.3)$$

$$A_0 \otimes B_6 = \begin{bmatrix} 0 & 6 & 8 & 14 \\ 1 & 1 & 9 & 9 \\ 2 & 12 & 10 & 4 \\ 3 & 7 & 11 & 15 \\ 4 & 2 & 12 & 10 \\ 5 & 13 & 13 & 5 \\ 6 & 8 & 14 & 0 \\ 7 & 3 & 15 & 11 \end{bmatrix} \quad A_0 \otimes B_7 = \begin{bmatrix} 0 & 7 & 8 & 15 \\ 1 & 2 & 9 & 10 \\ 2 & 13 & 10 & 5 \\ 3 & 8 & 11 & 0 \\ 4 & 3 & 12 & 11 \\ 5 & 14 & 13 & 6 \\ 6 & 9 & 14 & 1 \\ 7 & 4 & 15 & 12 \end{bmatrix} \quad (D.4)$$

$$A_0 \otimes B_8 = \begin{bmatrix} 0 & 8 & 8 & 0 \\ 1 & 3 & 9 & 11 \\ 2 & 14 & 10 & 6 \\ 3 & 9 & 11 & 1 \\ 4 & 4 & 12 & 12 \\ 5 & 15 & 13 & 7 \\ 6 & 10 & 14 & 2 \\ 7 & 5 & 15 & 13 \end{bmatrix} \quad A_0 \otimes B_9 = \begin{bmatrix} 0 & 9 & 8 & 1 \\ 1 & 4 & 9 & 12 \\ 2 & 15 & 10 & 7 \\ 3 & 10 & 11 & 2 \\ 4 & 5 & 12 & 13 \\ 5 & 0 & 13 & 8 \\ 6 & 11 & 14 & 3 \\ 7 & 6 & 15 & 14 \end{bmatrix} \quad (D.5)$$

$$A_0 \otimes B_{10} = \begin{bmatrix} 0 & 10 & 8 & 2 \\ 1 & 5 & 9 & 13 \\ 2 & 0 & 10 & 8 \\ 3 & 11 & 11 & 3 \\ 4 & 6 & 12 & 14 \\ 5 & 1 & 13 & 9 \\ 6 & 12 & 14 & 4 \\ 7 & 7 & 15 & 15 \end{bmatrix} \quad A_0 \otimes B_{11} = \begin{bmatrix} 0 & 11 & 8 & 3 \\ 1 & 6 & 9 & 14 \\ 2 & 1 & 10 & 9 \\ 3 & 12 & 11 & 4 \\ 4 & 7 & 12 & 15 \\ 5 & 2 & 13 & 10 \\ 6 & 13 & 14 & 5 \\ 7 & 8 & 15 & 0 \end{bmatrix} \quad (D.6)$$

$$A_0 \otimes B_{12} = \begin{bmatrix} 0 & 12 & 8 & 4 \\ 1 & 7 & 9 & 15 \\ 2 & 2 & 10 & 10 \\ 3 & 13 & 11 & 5 \\ 4 & 8 & 12 & 0 \\ 5 & 3 & 13 & 11 \\ 6 & 14 & 14 & 6 \\ 7 & 9 & 15 & 1 \end{bmatrix} \quad A_0 \otimes B_{13} = \begin{bmatrix} 0 & 13 & 8 & 5 \\ 1 & 8 & 9 & 0 \\ 2 & 3 & 10 & 11 \\ 3 & 14 & 11 & 6 \\ 4 & 9 & 12 & 1 \\ 5 & 4 & 13 & 12 \\ 6 & 15 & 14 & 7 \\ 7 & 10 & 15 & 2 \end{bmatrix} \quad (D.7)$$

$$A_0 \otimes B_{14} = \begin{bmatrix} 0 & 14 & 8 & 6 \\ 1 & 9 & 9 & 1 \\ 2 & 4 & 10 & 12 \\ 3 & 15 & 11 & 7 \\ 4 & 10 & 12 & 2 \\ 5 & 5 & 13 & 13 \\ 6 & 16 & 14 & 8 \\ 7 & 11 & 15 & 3 \end{bmatrix} \quad A_0 \otimes B_{15} = \begin{bmatrix} 0 & 15 & 8 & 7 \\ 1 & 10 & 9 & 2 \\ 2 & 5 & 10 & 13 \\ 3 & 0 & 11 & 8 \\ 4 & 11 & 12 & 3 \\ 5 & 6 & 13 & 14 \\ 6 & 1 & 14 & 9 \\ 7 & 12 & 15 & 4 \end{bmatrix} \quad (D.8)$$

## D.2 CODE CARDINALITY OF 8

$$C_0 \otimes D_{0a} = \begin{bmatrix} 0 & 0 & 4 & 8 \\ 1 & 6 & 5 & 14 \\ 2 & 12 & 6 & 4 \\ 3 & 2 & 7 & 10 \end{bmatrix} \quad C_0 \otimes D_{0b} = \begin{bmatrix} 0 & 11 & 4 & 3 \\ 1 & 1 & 5 & 9 \\ 2 & 7 & 6 & 15 \\ 3 & 13 & 7 & 5 \end{bmatrix} \quad (D.9)$$

$$C_0 \otimes D_{1a} = \begin{bmatrix} 0 & 1 & 4 & 9 \\ 1 & 7 & 5 & 15 \\ 2 & 12 & 6 & 5 \\ 3 & 3 & 7 & 11 \end{bmatrix} \quad C_0 \otimes D_{1b} = \begin{bmatrix} 0 & 12 & 4 & 4 \\ 1 & 1 & 5 & 10 \\ 2 & 8 & 6 & 0 \\ 3 & 14 & 7 & 6 \end{bmatrix} \quad (D.10)$$

$$C_0 \otimes D_{2a} = \begin{bmatrix} 0 & 2 & 4 & 10 \\ 1 & 8 & 5 & 0 \\ 2 & 14 & 6 & 6 \\ 3 & 4 & 7 & 12 \end{bmatrix} \quad C_0 \otimes D_{2b} = \begin{bmatrix} 0 & 13 & 4 & 5 \\ 1 & 3 & 5 & 11 \\ 2 & 9 & 6 & 1 \\ 3 & 15 & 7 & 7 \end{bmatrix} \quad (D.11)$$

$$C_0 \otimes D_{3a} = \begin{bmatrix} 0 & 3 & 4 & 11 \\ 1 & 9 & 5 & 1 \\ 2 & 15 & 6 & 7 \\ 3 & 0 & 7 & 8 \end{bmatrix} \quad C_0 \otimes D_{3b} = \begin{bmatrix} 0 & 14 & 4 & 6 \\ 1 & 4 & 5 & 9 \\ 2 & 10 & 6 & 2 \\ 3 & 0 & 7 & 8 \end{bmatrix} \quad (D.12)$$

$$C_0 \otimes D_{4a} = \begin{bmatrix} 0 & 4 & 4 & 12 \\ 1 & 10 & 5 & 2 \\ 2 & 0 & 6 & 8 \\ 3 & 6 & 7 & 14 \end{bmatrix} \quad C_0 \otimes D_{4b} = \begin{bmatrix} 0 & 15 & 4 & 7 \\ 1 & 5 & 5 & 13 \\ 2 & 11 & 6 & 3 \\ 3 & 1 & 7 & 9 \end{bmatrix} \quad (D.13)$$

$$C_0 \otimes D_{5a} = \begin{bmatrix} 0 & 5 & 4 & 13 \\ 1 & 11 & 5 & 3 \\ 2 & 1 & 6 & 9 \\ 3 & 7 & 7 & 15 \end{bmatrix} \quad C_0 \otimes D_{5b} = \begin{bmatrix} 0 & 0 & 4 & 8 \\ 1 & 6 & 5 & 14 \\ 2 & 12 & 6 & 4 \\ 3 & 2 & 7 & 10 \end{bmatrix} \quad (\text{D.14})$$

$$C_0 \otimes D_{6a} = \begin{bmatrix} 0 & 6 & 4 & 14 \\ 1 & 12 & 5 & 4 \\ 2 & 2 & 6 & 10 \\ 3 & 8 & 7 & 0 \end{bmatrix} \quad C_0 \otimes D_{6b} = \begin{bmatrix} 0 & 1 & 4 & 9 \\ 1 & 7 & 5 & 15 \\ 2 & 13 & 6 & 5 \\ 3 & 3 & 7 & 11 \end{bmatrix} \quad (\text{D.15})$$

$$C_0 \otimes D_{7a} = \begin{bmatrix} 0 & 7 & 4 & 15 \\ 1 & 13 & 5 & 5 \\ 2 & 3 & 6 & 11 \\ 3 & 9 & 7 & 1 \end{bmatrix} \quad C_0 \otimes D_{7b} = \begin{bmatrix} 0 & 2 & 4 & 10 \\ 1 & 8 & 5 & 0 \\ 2 & 14 & 6 & 6 \\ 3 & 4 & 7 & 12 \end{bmatrix} \quad (\text{D.16})$$

$$C_0 \otimes D_{8a} = \begin{bmatrix} 0 & 8 & 4 & 0 \\ 1 & 14 & 5 & 6 \\ 2 & 4 & 6 & 12 \\ 3 & 10 & 7 & 2 \end{bmatrix} \quad C_0 \otimes D_{8b} = \begin{bmatrix} 0 & 3 & 4 & 11 \\ 1 & 9 & 5 & 1 \\ 2 & 15 & 6 & 7 \\ 3 & 5 & 7 & 13 \end{bmatrix} \quad (\text{D.17})$$

$$C_0 \otimes D_{9a} = \begin{bmatrix} 0 & 9 & 4 & 1 \\ 1 & 15 & 5 & 7 \\ 2 & 5 & 6 & 13 \\ 3 & 11 & 7 & 3 \end{bmatrix} \quad C_0 \otimes D_{9b} = \begin{bmatrix} 0 & 4 & 4 & 12 \\ 1 & 10 & 5 & 2 \\ 2 & 0 & 6 & 8 \\ 3 & 6 & 7 & 14 \end{bmatrix} \quad (\text{D.18})$$

$$C_0 \otimes D_{10a} = \begin{bmatrix} 0 & 10 & 4 & 2 \\ 1 & 0 & 5 & 8 \\ 2 & 6 & 6 & 14 \\ 3 & 12 & 7 & 4 \end{bmatrix} \quad C_0 \otimes D_{10b} = \begin{bmatrix} 0 & 5 & 4 & 13 \\ 1 & 11 & 5 & 3 \\ 2 & 1 & 6 & 9 \\ 3 & 7 & 7 & 15 \end{bmatrix} \quad (\text{D.19})$$

$$C_0 \otimes D_{11a} = \begin{bmatrix} 0 & 11 & 4 & 3 \\ 1 & 1 & 5 & 9 \\ 2 & 7 & 6 & 15 \\ 3 & 13 & 7 & 5 \end{bmatrix} \quad C_0 \otimes D_{11b} = \begin{bmatrix} 0 & 6 & 4 & 14 \\ 1 & 12 & 5 & 4 \\ 2 & 2 & 6 & 10 \\ 3 & 8 & 7 & 0 \end{bmatrix} \quad (\text{D.20})$$

$$C_0 \otimes D_{12a} = \begin{bmatrix} 0 & 12 & 4 & 4 \\ 1 & 2 & 5 & 10 \\ 2 & 8 & 6 & 0 \\ 3 & 14 & 7 & 6 \end{bmatrix} \quad C_0 \otimes D_{12b} = \begin{bmatrix} 0 & 7 & 4 & 15 \\ 1 & 13 & 5 & 5 \\ 2 & 3 & 6 & 11 \\ 3 & 9 & 7 & 1 \end{bmatrix} \quad (\text{D.21})$$

$$C_0 \otimes D_{13a} = \begin{bmatrix} 0 & 13 & 4 & 5 \\ 1 & 3 & 5 & 11 \\ 2 & 9 & 6 & 1 \\ 3 & 15 & 7 & 7 \end{bmatrix} \quad C_0 \otimes D_{13b} = \begin{bmatrix} 0 & 8 & 4 & 0 \\ 1 & 14 & 5 & 6 \\ 2 & 4 & 6 & 12 \\ 3 & 10 & 7 & 2 \end{bmatrix} \quad (\text{D.22})$$

$$C_0 \otimes D_{14a} = \begin{bmatrix} 0 & 14 & 4 & 6 \\ 1 & 4 & 5 & 12 \\ 2 & 10 & 6 & 2 \\ 3 & 0 & 7 & 8 \end{bmatrix} \quad C_0 \otimes D_{14b} = \begin{bmatrix} 0 & 9 & 4 & 1 \\ 1 & 15 & 5 & 7 \\ 2 & 5 & 6 & 13 \\ 3 & 11 & 7 & 3 \end{bmatrix} \quad (\text{D.23})$$

$$C_0 \otimes D_{15a} = \begin{bmatrix} 0 & 15 & 4 & 7 \\ 1 & 5 & 5 & 13 \\ 2 & 11 & 6 & 3 \\ 3 & 1 & 7 & 9 \end{bmatrix} \quad C_0 \otimes D_{15b} = \begin{bmatrix} 0 & 10 & 4 & 2 \\ 1 & 0 & 5 & 8 \\ 2 & 6 & 6 & 14 \\ 3 & 12 & 7 & 4 \end{bmatrix} \quad (\text{D.24})$$

- [1] S. Haykin, *Digital Communications*, Wiley, New York, 1994.
- [2] W. D. Costas, *IEEE Transactions on Communications*, vol. 34, no. 3, pp. 282-283, March 1986.
- [3] J. G. Proakis and R. D. Yeh, "A new spread-spectrum service for INTELSAT global services," *IEEE Spectrum*, vol. 24, pp. 46-55, 1987.
- [4] D. Chavakis, "ISAT (Intelsat Satellite) changed capacity versus earth performance," *IEEE Transactions on Communications Technology*, vol. 31(1), pp. 10-16, 1983.
- [5] S. D. Stalling, "A new spread spectrum system for digital satellite radio services," *IEEE Transactions on Communications*, vol. 31(2), pp. 105-110, February 1983.
- [6] J. G. Proakis, "A new spread spectrum system architecture for PCS services," *IEEE Journal on Selected Areas in Communications*, vol. 10(2), pp. 105-110, February 1992.
- [7] D. S. Costas, *Frequency, Angle and Time-Frequency Processing*, Prentice-Hall, Englewood Cliffs, New Jersey, 1991.
- [8] J. G. Proakis, "A new spread spectrum system architecture for PCS services," *IEEE Journal on Selected Areas in Communications*, vol. 10(2), pp. 105-110, February 1992.
- [9] C. E. Ruck, "A new spread spectrum system architecture for PCS services," *IEEE Journal on Selected Areas in Communications*, vol. 10(2), pp. 105-110, February 1992.
- [10] J. G. Proakis, *Digital Communications*, Wiley, New York, 1991.
- [11] P. D. Smith, "A new spread spectrum system architecture for PCS services," *IEEE Transactions on Communications*, vol. 42, pp. 105-110, February 1994.
- [12] J. G. Proakis and R. D. Yeh, "A new spread spectrum system architecture for PCS services," *IEEE Journal on Selected Areas in Communications*, vol. 10(2), pp. 105-110, February 1992.

## BIBLIOGRAPHY

- [1] S. Haykin, *Digital Communications*. Wiley, 1988.
- [2] W. D. Gregg, *Analog and Digital Communication*. John Wiley and Sons, New York, 1977.
- [3] J. G. Puente and A. M. Werth, "Demand-assigned service for INTELSAT global network," *IEEE Spectrum*, pp. 59–69, January 1971.
- [4] D. Chakraborty, "INTELSAT IV satellite system (voice) channel capacity versus earth-station performance," *IEEE Transactions on Communication Technology*, vol. COM-19, pp. 355–362, June 1971.
- [5] H. Hasemi, "The indoor radio propagation channel," *Proceedings of the IEEE*, vol. 81, pp. 941–968, July 1993.
- [6] C. L. Lui and K. Feher, " $\pi/4$ -QPSK modems for satellite sound/data broadcast systems," *IEEE Transactions on Broadcasting*, vol. 37, pp. 1–8, March 1991.
- [7] S. Chennakeshu and G. J. Saulnier, "Differential detection of  $\pi/4$ -Shifted-DQPSK for digital cellular radio," *IEEE Transactions on Vehicular Technology*, vol. 42, pp. 46–57, February 1993.
- [8] K. Murota and K. Hirade, "GMSK modulation for digital mobile radio telephony," *IEEE Transactions on Communications*, vol. COM-29, pp. 1044–1050, July 1981.
- [9] Y. Guo and K. Feher, "A new FQPSK modem/radio architecture for PCS and mobile satellite communications," *IEEE Journal on Selected Areas in Communications*, vol. 13, February 1995.
- [10] D. N. Chorafas, *Telephony: Today and Tomorrow*. Prentice-Hall, 1984.
- [11] D. Saha and T. G. Birdsall, "Quadrature-Quadrature Phase-Shift Keying," *IEEE Transactions on Communications*, vol. 37, pp. 437–448, May 1989.
- [12] D. Saha, *Quadrature-Quadrature Phase Shift Keying*. PhD thesis, University of Michigan, 1986.
- [13] C. E. Shannon, "Communications in the presence of noise," *IRE Proceedings*, vol. 37, pp. 10–21, January 1949.
- [14] J. G. Proakis, *Digital Communications*. McGraw-Hill, third ed., 1989.
- [15] D. Slepian, "Bounds on communications," *Bell Systems Technology Journal*, vol. 42, pp. 681–707, 1963.
- [16] S. G. Wilson and H. A. Sleeper, "Four-dimensional modulation and coding — An alternative to frequency-reuse," Tech. Rep. UVA/528200/EE83/107, Communications Systems Laboratory, University of Virginia, Charlottesville, Va., September 1983.

- 
- [17] G. R. Welter and S. L. Lee, "Digital transmission with coherent four-dimensional modulation," *IEEE Transactions on Information Theory*, vol. IT-20, pp. 397–402, July 1974.
- [18] L. Zetterberg and H. Brändström, "Codes for combined phase and amplitude modulated signals in four-dimensional signal space," *IEEE Transactions on Communications*, vol. COM-25, pp. 943–950, September 1977.
- [19] S. G. Wilson, H. A. Sleeper II, P. J. Schottler, and M. T. Lyons, "Rate 3/4 Convolutional Coding of 16-PSK: Code design and Performance Study," *IEEE Transactions on Communications*, vol. COM-32, pp. 1308–1315, December 1984.
- [20] E. Biglieri and M. Elia, "Multidimensional modulation and coding for bandlimited digital channels," *IEEE Transactions on Information Theory*, vol. IT-34, pp. 803–809, July 1988.
- [21] A. Gersho and V. B. Lawrence, "Multidimensional signal constellations for voiceband data transmission," *IEEE Selected Areas in Communications*, vol. SAC-2, pp. 687–702, September 1984.
- [22] J. M. Wozencraft and I. M. Jacobs, *Principle of Communication Engineering*. New York: Wiley, 1965.
- [23] V. Acha and R. A. Carrasco, "A new digital implementation of quadrature-quadrature phase shift keying," in *Third IEE Conference on telecommunications*, (Edinburg, Scotland), pp. 29–34, March 1991.
- [24] G. C. Clark and J. Bibb Cain, *Error-Correction Coding for Digital Communications*. Plenum Press, 1988.
- [25] S. Lin and D. J. Costello, Jr, *Error control coding - Fundamentals and Applications*. Prentice-Hall, 1983.
- [26] J. L. Massey, "Coding and modulation in digital communications," *Proceedings 1974 International Zurich Seminar on Digital Communications*, pp. E2(1)–E2(4), 1974.
- [27] G. Ungerboeck, "Channel coding with Multilevel/Phase signals," *IEEE Transactions on Information Theory*, vol. IT-28, pp. 55–67, January 1982.
- [28] G. Ungerboeck, "Trellis-Coded Modulation with redundant signal sets - Part 1:Introduction," *IEEE Communications*, vol. 25, pp. 5–11, February 1987.
- [29] G. Ungerboeck, "Trellis-Coded Modulation with redundant signal sets - Part II:State of the art," *IEEE Communications Magazine*, vol. 25, pp. 12–21, February 1987.
- [30] E. Biglieri, D. Divsalar, P. J. McLane, and M. K. Simon, *Introduction to Trellis-Coded Modulation with Applications*. Macmillan, 1991.
- [31] R. Calderbank and J. E. Mazo, "A new description of trellis codes," *IEEE Transactions on Information Theory*, vol. IT-30, pp. 784–791, November 1984.
- [32] R. Fang and W. Lee, "Four-Dimensional coded PSK systems for combating effects of severe ISI and CCI," in *Globecom '93*, pp. 1–7, 1983.
- [33] E. Biglieri, "High-level modulation and coding for nonlinear satellite channels," *IEEE Transactions on Communications*, vol. COM-32, pp. 616–626, May 1984.
-

- [34] L. F. Wei, "Rotationally invariant convolutional channel coding with expanded signal space - Part I and Part II," *IEEE Journal on Selected Areas in Communications*, vol. SAC-2, pp. 659–686, September 1984.
- [35] L. F. Wei, "Trellis coded modulation with multidimensional constellations," *IEEE Transactions on Information Theory*, vol. IT-33, pp. 483–501, July 1987.
- [36] D. Divsalar and M. K. Simon, "Trellis Coding with Asymmetric modulations," *IEEE Transactions on Communications*, vol. COM-35, February 1987.
- [37] A. R. Calderbank and J. A. Sloane, "New Trellis Codes based on Lattices and Cosets," *IEEE Transactions on Information Theory*, vol. IT-33, pp. 177–195, March 1987.
- [38] S. Benedetto, M. A. Marsan, G. Albertengo, and E. Giachin, "Combined coding and modulation: Theory and Applications," *IEEE Transactions on Information Theory*, vol. 34, pp. 223–236, March 1988.
- [39] D. Divsalar and M. K. Simon, "The design of Trellis Coded MPSK for fading channels: Performance Criteria," *IEEE Transactions on Communications*, vol. 36, pp. 1004–1012, September 1988.
- [40] D. Divsalar and M. K. Simon, "The design of Trellis Coded MPSK for fading channels: Set Partitioning for optimum code design," *IEEE Transactions on Communications*, vol. 36, pp. 1013–1021, September 1988.
- [41] D. Divsalar and M. K. Simon, "Multiple Trellis Coded Modulation (MTCM)," *IEEE Transactions on Communications*, vol. 36, pp. 410–419, April 1988.
- [42] D. Divsalar and M. K. Simon, "The use of interleaving for reducing noisy reference loss in Trellis-Coded Modulation systems," *IEEE Transactions on Communications*, vol. 38, pp. 1190–1198, August 1990.
- [43] P. G. Farrell and L. H. Lee, "Coded modulation for fading channels," in *Second Bangor Symposium on Communications*, (Bangor, Wales), 23-24 May 1990.
- [44] E. Zehavi, "8-PSK Trellis Codes for a Rayleigh channel," *IEEE Transactions on Communications*, vol. 40, pp. 873–884, May 1992.
- [45] S. S. Peryalwar and M. Fleisher, "Trellis-Coded frequency and phase modulation," *IEEE Transactions on Communications*, vol. 40, pp. 1038–1046, June 1992.
- [46] D. Saha, "Trellis Coded Quadrature-Quadrature Phase Shift Keying," *Proceedings IEEE MIL-COM*, pp. 44.4.1–44.4.5, October 1987.
- [47] D. Saha, "Channel coding with Quadrature-Quadrature Phase Shift-Keying ( $Q^2$ PSK) signals," *IEEE Transactions on Communications*, vol. 38, pp. 409–417, April 1990.
- [48] V. Acha and R. A. Carrasco, "Trellis coded  $Q^2$ PSK signals - Part 1: AWGN and nonlinear satellite channels," *IEE Proceedings in Communications*, pp. 151–158, June 1994.
- [49] V. Acha and R. A. Carrasco, "Trellis coded  $Q^2$ PSK signals - Part 2: Land mobile satellite fading channels," *IEE Proceedings in Communications*, pp. 159–167, June 1994.
- [50] G. J. Foschini, R. D. Gitlin, and S. B. Weinstein, "Optimization of Two-dimensional signal constellation in the presence of Gaussian noise," *IEEE Transactions on Communications*, January 1974.



- [51] J. H. Conway and N. J. A. Sloane, "Voronoi Regions of Lattices," *IEEE Transactions of Information Theory*, March 1982.
- [52] B. E. Rimoldi, "A decomposition approach to CPM," *IEEE Transactions of Information Theory*, vol. 34, pp. 260–270, March 1988.
- [53] D. K. Asano, H. Leib, and S. Pasupathy, "Phase smoothing functions for continuous phase modulation," *IEEE Transactions on Communications*, vol. 42, pp. 1040–1049, February/March/April 1994.
- [54] J. Huber and W. Liu, "An alternative approach to reduced-complexity CPM-receivers," *IEEE Journal on Selected Areas in Communications*, vol. 7, pp. 1437–1449, December 1989.
- [55] R. De Gaudenzi and M. Luise, "Carrier and clock reference recovery for quadrature-quadrature PSK signals," in *Globecom '90*, pp. 599–603, December 1990.
- [56] W. C. Lindsey and M. K. Simon, *Telecommunication System Engineering*. Prentice-Hall, 1973.
- [57] F. G. Stremler, *Introduction to Communication Systems*. Addison-Wesley, third ed., 1990.
- [58] B. Sklar, *Digital Communications — Fundamentals and Applications*. Prentice-Hall, Englewood Cliffs, New Jersey, 1988.
- [59] D. Verhulst, M. Mouly, and J. Szpirglas, "Slow frequency hopping multiple access for digital cellular radiotelephone," *IEEE Transactions on Vehicular Technology*, vol. VT-33, pp. 179–190, August 1984.
- [60] D. J. van Wyk and L. P. Linde, "Multidimensional frame synchronisation for 4D-Q<sup>2</sup>PSK," *Electronics Letters*, pp. 2077–2078, November 1995.
- [61] D. Divsalar and M. K. Simon, "Trellis-coded modulation systems for 4800 and 9600 bps transmission over a fading satellite channel," *IEEE Journal on Selected Areas in Communications*, vol. SAC-5, pp. 162–175, February 1987.
- [62] A. P. R. Opperman, "VHF/UHF channel simulator for mobile digital communication," Master's thesis, University of Pretoria, South Africa, October 1995.
- [63] W. C. Jakes, *Microwave Mobile Communications*. Wiley-Interscience Publication, 1974.
- [64] P. J. van Gerwen, "Microprocessor implementation of high-speed data modems," *IEEE Transactions on Communications*, vol. COM-25, pp. 238–250, February 1977.
- [65] A. J. Viterbi, *Principles of Coherent Communication*. New York: McGraw-Hill, 1966.
- [66] R. de Buda, "Coherent demodulation of frequency-shift keying with low deviation ratio," *IEEE Transactions on Communications*, pp. 429–435, June 1972.
- [67] R. L. Frank and S. A. Zadoff, "Phase shift pulse codes with good periodic correlation properties," *IRE Transactions on Information Theory*, vol. IT-7, pp. 381–382, October 1962.
- [68] W. O. Alltop, "Complex sequences with low periodic correlations," *IEEE Transactions on Information Theory*, vol. IT-26, pp. 350–354, May 1980.
- [69] B. Kim, "Digital carrier recovery with adaptive dual loop DPLL for mobile communication applications," *IEEE Transactions on Communications*, pp. 29 – 32, 1989.

- [70] A. Aghamohammad, H. Meyr, and G. Ascheid, "Adaptive synchronization and channel parameter estimation using an Extended Kalman filter," *IEEE Transactions on Communications*, pp. 1212–1218, 1989.
- [71] S. M. Bozic, *Digital and Kalman Filtering*. Edward Arnold, 1979.
- [72] S. Aguirre and S. Hinedi, "Two novel automatic frequency tracking loops," *IEEE Transactions on Aerospace and Electronic Systems*, vol. 25, pp. 749–760, September 1989.
- [73] L. P. Linde, "Derivation of scalar Kalman estimator." Lecture notes - 1995.
- [74] D. J. van Wyk and L. P. Linde, "Phase and frequency tracking techniques for 4D-Q<sup>2</sup>PSK modem." Submitted for publication in *The Transactions of the SAIEE*, 1996.
- [75] A. J. Viterbi and J. K. Omura, *Principles of Digital Communication and Coding*. McGraw-Hill, 1979.
- [76] W. C. Y. Lee, *Mobile Communications Engineering*. McGraw-Hill, 1982.
- [77] M. Y. Rhee, *Error-Correcting Coding Theory*. McGraw-Hill, 1989.
- [78] D. J. van Wyk and L. P. Linde, "Half rate convolutional coding for 4D-QPSK," in *COMSIG '95: South African Symposium on Communications and Signal Processing*, (Pretoria, South Africa), pp. 27–34, November 1995.
- [79] K. Y. Chan and G. H. Norton, "A new algebraic algorithm for generating the transfer function of a trellis encoder," *IEEE Transactions on Communications*, vol. 43, pp. 1866–1867, May 1995.
- [80] M. M. Mulligan and S. G. Wilson, "An improved algorithm for evaluating trellis phase codes," *IEEE Transactions on Information Theory*, vol. IT-30, pp. 846–851, November 1984.
- [81] D. Divsalar and M. K. Simon, "The design of trellis codes for fading channels," Tech. Rep. MSAT-X Report 147, JPL Publication, Pasadena, Calif., November 1987.
- [82] L. P. Linde, "SNR calibration." Lecture notes - 1995.
- [83] D. J. van Wyk and L. P. Linde, "Development of a MD-QPSK modem for application in mobile communication - Item 400: Literature Study," Tech. Rep. 94/026, Laboratory for Advanced Engineering, August 1994.
- [84] D. J. van Wyk and L. P. Linde, "Development of a MD-QPSK modem for mobile communication - Item 600: Theoretical Design," Tech. Rep. 94/027, Laboratory for Advanced Engineering, November 1994.
- [85] D. J. van Wyk and L. P. Linde, "Development of a MD-QPSK modem for application in mobile communication - Item 800: Evaluation," Tech. Rep. 95/001, Laboratory for Advanced Engineering, February 1995.
- [86] D. J. van Wyk and L. P. Linde, "Development of a error-correction strategies for MD-QPSK modem for application in mobile communication - Item 5: Literature Study," Tech. Rep. 95/034, Laboratory for Advanced Engineering, August 1995.
- [87] D. J. van Wyk and L. P. Linde, "Development of a error-correction strategies for MD-QPSK modem for application in mobile communication - Item 6: Design and preliminary Evaluation," Tech. Rep. 95/043, Laboratory for Advanced Engineering, November 1995.

- 
- [88] D. J. van Wyk and L. P. Linde, "Development of a error-correction strategies for MD-QPSK modem for application in mobile communication - Item 7: Evaluation under typical channel conditions," Tech. Rep. 96/009, Laboratory for Advanced Engineering, March 1996.
- [89] Texas Instruments, *TMS320C30 C Compiler*, 1990.
- [90] Texas Instruments, *TMS320C30 Assembly Language Tools*, 1988.
- [91] R. Chassaing, *Digital Signal Processing with C and the TMS320C30*. John-Wiley and Sons, 1992.
- [92] A. J. Viterbi and A. M. Viterbi, "Nonlinear estimation of PSK modulated carrier phase with application to burst digital transmission," *IEEE Transactions on Information Theory*, vol. IT-32, pp. 543-551, July 1983.
- [93] C. Schlegel and M. A. Herro, "A Burst-Error-Correcting Viterbi Algorithm," *IEEE Transactions on Communications*, vol. 38, pp. 285-291, March 1990.
- [94] M.-C. Lin and S.-C. Ma, "A coded modulation scheme with interblock memory," *IEEE Transactions on Communications*, vol. 42, pp. 911-916, February/March/April 1994.
- [95] C.-H. Chuang and L.-S. Lee, "A coded modulation design with equal utilization of signal dimensions using a simple convolutional code," in *International Symposium on Information Theory and its Applications*, (Sydney, Australia), pp. 469-473, November 1994.
- [96] A. J. Viterbi, "Error bounds for convolutional codes and an asymptotically optimum decoding algorithm," *IEEE Transactions on Information Theory*, vol. IT-13, pp. 260-269, April 1967.
- [97] S. Wolfram, *Mathematica — A system for doing mathematics by computer*. Addison-Wesley Publishing Company, Inc., 1991.